Thermodynamics and Solitonic Excitations of a Strongly-Interacting Fermi Gas

by

Mark Jen-Hao Ku

Submitted to the Department of Physics
in partial fulfillment of the requirements for the degree of

Doctor of Philosophy

at the

MASSACHUSETTS INSTITUTE OF TECHNOLOGY

June 2015

Signature redacted

Author .....
Department of Physics
May 22, 2015

Signature redacted

Certified by .....
Martin W. Zwierlein
Silverman Career Development Professor of Physics
Thesis Supervisor

Signature redacted

Accepted by .....
Nergis Mavalvala
Curtis and Kathleen Marble Professor of Astrophysics
Associate Department Head for Education

Thermodynamics and Solitonic Excitations of a Strongly-Interacting Fermi Gas

by

Mark Jen-Hao Ku

Submitted to the Department of Physics
on May 22, 2015, in partial fulfillment of the
requirements for the degree of
Doctor of Philosophy

Abstract

In this thesis, I present experiments that study the thermodynamics and solitonic excitations of a strongly-interacting Fermi gas, realized with ^{6}Li atoms at a Feshbach resonance where the scattering length is large. The strongly-interacting Fermi gas, also called the unitary Fermi gas, exhibits a novel superfluidity that is a crossover of the Bose-Einstein condensation of molecules and Bardeen-Cooper-Schrieffer superfluid of long-ranged Cooper pairs, with a high critical temperature and a small healing length. The unitary Fermi gas serves as a model for other strongly correlated fermions, such dilute neutron matter in the crust of neutron stars.

The homogeneous equation of state of a unitary Fermi gas was measured with high precision via a method that requires no theoretical input nor external thermometer. The measurement provides an accurate value of the critical temperature and the Bertsch parameter that characterizes the ground state energy. The equation of state is then used to provide a prediction for the higher collective modes. I also describe a method to obtain the equation of state of global thermodynamic quantitites of harmonically trapped gases from their column density.

In another set of experiments, long-lived solitonic excitation was generated via a one-sided phase imprinting. The excitation's slow oscillation within the trapped superfluid indicates a large ratio of the inertial mass to the gravitational mass. Tomographic imaging identifies the excitation to be a solitonic vortex. The precession period in the BEC-BCS crossover was measured, and good agreement is found with predictions from a hydrodynamic model. Prior to the formation of the vortex, the evolution of the superfluid after the phase imprint was investigated. A dark planar soliton was observed to emerge after the phase imprint, undergo snake instability, subsequently decay into a ring defect, and eventually convert into a single vortex. The growth rate of the transverse modes during the snake instability was measured.

Thesis Supervisor: Martin W. Zwierlein
Title: Silverman Career Development Professor of Physics

To Tai-Hua, Marie, Martin, and Matthew, my dearest family,

Guan-Ting, the woman I love,

and Jesus Christ my shepherd, in whom I find the Way, the Truth, and the Life

Acknowledgments

It is fair to say that one of the most worthwhile aspects of my time at MIT is the friendship, mentorship, and support I have received from many individuals, both in and outside of Boston.

First of all, I am greatly indebted to my doctoral advisor, Martin Zwierlein. In him I find a mentor who embodies brilliance in physics and tremendous care for those in his team. Besides having learned a great deal of physics from him, I have also learned to deal with challenges with a fearless attitude.

Throughout the years, I have been fortunate to work alongside and receive mentorship from senior members of the BEC 1 team. Andre Schirotzek was the first student to graduate from the group. Though I only overlapped with him for one semester, he quickly took me under his wing and taught me two valuable lessons - a trick for fiber coupling that shall not be named, and the truth that the machine will return love when it receives a lot of attention. Ariel Sommer is a wonderful co-worker and is like a big brother to me in the lab. I enjoy very much his easy-going nature and optimism. Besides spending time in the lab, we have also gone on numerous conference trips together, leaving me with many fond memories. Postdoc Tarik Yefsah and I worked closely during the time when I was the senior student in the lab. I would say we make a great team like Batman and Robin. He is gracious to be the recipient of much poking fun from me. His presence has ensured that the work we do is high-quality, and I have benefited very much from his mentorship.

What makes working in BEC 1 so enjoyable is the many excellent members one gets to work with. Lawrence Cheuk made an immense contribution as soon as he joined the lab, and he has been instrumental in the progress in BEC 1 until he switched full time to Fermi 2. I am very excited for their realization of the Fermi microscope. Wenjie Ji, Biswaroop Mukherjee, Zhenjie Yan, and Parth Patel are all brilliant students who started to contribute to the lab as soon as they arrived. Undergraduate researcher Elmer Guardado-Sanchez "works as a grad student" (in the word of Martin) both in terms of effort as well as productivity. Postdoc Julian

Struck has brought solid AMO expertise to the lab and has done a fantastic job in leading the new students.

The members of the other teams of the Zwierlein group, Fermi 1 and Fermi 2, have also played important roles in my time at MIT. I want to thank postdocs Peynman Ahmadi and Sebastian Will and fellow classmate Peter Park who have offered me much help and knowledge. I want to thank Melih Okan for exposing me to good Turkish food and for the many stimulating conversations we have had. My gratitude also goes to postdoc Thomas Lompe and fellow student Matthew Nichols for allowing me to frequently "raid" Fermi 2 for parts. I am very excited for the recent accomplishments of these two teams, seeing that years of hard work have finally paid off. I want to congratulate the team of Fermi 1 - Sebastian, Peter, Jennifer Schloss, Zoe Zan, and Huanquian Loh - for their recent success in generating ground state molecules of NaK. I also want to congratulate Fermi 2 - Lawrence, Thomas, Matthew, Melih, and Katherine Lawrence - for their recent realization of the Fermi microscope. I look forward to hearing about the exciting physics that will build on these two successes.

I also want to give my thanks to Wolfgang Ketterle. He has offered valuable advice to our work at BEC 1 throughout the years. In addition, I have learned tremendously from his AMO 1 and 2 classes, and have had the pleasure to work as a teaching assistant for a semester of his AMO 1 class.

I am fortunate to be in the environment of the Center for Ultracold Atoms. The camaraderie and friendship of close to about a hundred of researchers have provided a very pleasant working environment. I am glad to reunite with fellow TRIUMF interns Tout Wang and Alexei Bylinskii in CUA. Tout has provided much encouragement as a fellow Christian in the field of physics. I am grateful for the discussion about job search I have had with Alexei as both of us are near the end of our PhD. I have had the pleasure to be roommate with classmates Wujie Huang and Molu Shi. There are many others who have played a part during my time at CUA, and though I am not able to name everyone, I want to express my sincere gratitude to them.

Many researchers outside of MIT have also made an impact on my work. Giacomo Roati from LENS, Florence spent about half a year in BEC 1 and significantly

contributed to the spin-transport experiment. It was fun working with him, and I am grateful for his hospitality when Ariel and I visited LENS. I had the pleasure to work closely with Felix Werner on the joint theoretical-experimental project in obtaining the equation of state of the normal phase of the unitary Fermi gas. We continue to have frequent conversations after the project, which have been highly valuable to my research. His hospitality when Ariel and I were in Paris for the ICAP 2012 made that trip a highly memorable one. I also thank the others on the theory team of the project, Kris Van Houcke, Evgeny Kozik, Nikolay Prokofev, and Boris Svistunov, for a great collaboration and stimulating conversations. The collaboration with Sandro Stringari and Yan-Hua Hou was also highly enjoyable. I have known Michael McNeil Forbes since my time at UBC and we have had numerous stimulating conversations in conferences as well as via remote correspondence. We in BEC 1 have benefited much from frequent discussions with Wilhelm Zwerger, Gabriel Ferrari, and David Huse.

Many friends outside of CUA have been a vital part of my life in Boston. I want to thank John Liu, Gerald Pho, and Thomas Chiasson for our brotherhood and mutual support and accountability. I have had the pleasure to live with Dawsen Hwang for the past 3 years, and we have had a blast. I am grateful for Stuart and Hsuan DeLorme, who have been spiritual parents to me in Boston over the past six years. My immense gratitude goes to the many brothers and sisters at the MIT Graduate Christian Fellowship and Park Street International Fellowship for their prayer and support.

I cannot express my gratitude enough to my parents, Tai-Hua and Marie, who have taught me valuable wisdom in life, who have provided me a stable environment during the course of my growing up and education, and who have given me unconditional support in my pursuit of a career in physics. I must also thank my brothers, Martin and Matthew, who have given me tremendous inspiration, who have accompanied me through both fun and tough times, and who have been my best friends in the course of my life. To them are my many thanks and prayers.

I am excited that I will soon start a new life with the woman I love, Guan-

Ting Liao. She has been a source of much joy. She has supported me both with encouragement and also with tangible care such as her wonderful cooking, and what she has taken on and accomplished with planning of our wedding and future life is impressive. I am very grateful to God for bringing this strong and capable woman into my life, and I look forward to a new journey with her together as I complete my journey at MIT.

Contents

List of Figures

List of Tables

Chapter 1

Introduction

A century ago, the study of atomic spectra helped to usher in the discovery of quantum mechanics. Since then, quantum mechanics has become a necessary theory in the description of many fields of modern physics. Although a century has passed since its discovery, there seems to be no end to the vast world of quantum phenomena to be investigated. While a quantum system in the absence of interactions is relatively easy to understand, the challenge grows manyfold as soon as interactions enter into the picture. The problem is even more intractable if one considers a fermionic system with strong interactions leading to strong correlations. The presence of fermionic statistics often leads to the so-called sign problem which plagues computation. With strong interactions, there is no small parameter in which one can expand the theory describing the system, and one often has to resort to approximations without the ability to systematically improve the accuracy of the theory. Nevertheless, many important systems in nature belong to this class of interacting quantum matter: high-T_c superconductors, nuclear matter, and superfluid helium, among others.

Within this quest to understand strongly correlated systems, one finds an intersection between atomic physics and many-body physics. A century after the discovery of quantum mechanics, physicists have refined their understanding of and ability to control neutral atoms and ions. These highly-controllable, well-understood quantum systems have come to be recognized as "Lego® pieces" to realize a Hamiltonian that one wishes to study [24, 33]. Where the Hamiltonian may be intractable to compute

theoretically, one can perform experiments to ask nature itself about properties of the system described by this Hamiltonian - the program known as quantum simulation [76].

In the case of neutral atoms[1], the quantum simulation program took off about two decades ago with the realization of Bose-Einstein condensation (BEC) of atomic gases [5, 52]. Since then, experimental techniques have been refined and developed to enable a host of features in cold atom experiments: Feshbach resonances for the control of interactions [48], optical lattices [86], single-site imaging [12, 205], spin-orbit coupling [46, 138, 233], and artificial gauge fields [137, 3], to name a few. Some of the ongoing quantum simulation programs include the study of the Hubbard model (for a review, see for example [81, 24]), large synthetic magnetic fields [3, 2, 153], and low-dimensional systems [89, 211, 72].

One model system that has received widespread attention is the spin-$1/2$ Fermi gas with short-range interactions and infinite scattering length [246]. This can be realized with a spin-mixture of fermionic alkali atoms, such as ^{6}Li and ^{40}K, at a Feshbach resonance where the scattering length diverges. The magnitude of the scattering amplitude is then at the unitary limit, $|f(k)| = 1/k^2$, the largest value allowed by quantum mechanics. For this reason, the strongly-interacting Fermi gas is also called the unitary Fermi gas. On the side of the Feshbach resonance where $a > 0$, fermions of different spins pair up to form bosonic molecules, and the ground state of the system is a Bose-Einstein condensate of molecules. On the other side of the Feshbach resonance where $a < 0$, an isolated bound state of a spin-up and a spin-down fermions does not form. However, in the presence of a Fermi sea, fermions with opposite spins near the Fermi surface form long-range Cooper pairs as a consequence of many-body effects. From the Bardeen-Cooper-Schrieffer (BCS) theory [14], we know that as long as an attractive interaction is present, the ground state is a condensate of Cooper pairs. On resonance, where the scattering length diverges, one encounters a novel superfluid which is a crossover between the BEC of molecules and a BCS superfluid

[1]Ions have also proven to be a versatile platform as a quantum simulator [117, 15, 106] for spin models.

of Cooper pairs.

The unitary Fermi superfluid has a number of intriguing properties. Because of the absence of interaction-dependent length scales, the Fermi momentum $k_F = (3\pi^2 n)^{1/3}$, where n is the density, is the only length scale for the system at zero temperature. Therefore, the critical temperature T_c is expected to be on the order of the Fermi temperature $T_F = E_F/k_B$, where the Fermi energy is given by $E_F = \hbar^2 k_F^2/(2m)$. Indeed, BCS theory gives $T_c = 0.61 T_F e^{-\pi/(2k_F|a|)}$, and naively taking $1/|a| = 0$ gives $T_c = 0.61 T_F$. While this clearly would not be accurate since the BCS theory is a weakly-interacting theory, one expects this result to give the correct order of magnitude. This is among the highest known critical temperatures (relative to the Fermi temperature). In high-T_c superconductors, the critical temperatures are $\sim 100\,\mathrm{K}$, while the typical Fermi temperature in a metal is $\sim 10^4\,\mathrm{K}$, leading to $T_c/T_F \approx 0.01$. The phase coherence length ξ_0, which is a generalization of the healing length in a BEC and the BCS coherence length in BCS superfluidity [175], is smallest (compared to $1/k_F$) near unitarity [147], with $\xi_0 \sim 1/k_F$. This implies that the critical velocity $v_c \sim 1/\xi_0$ is largest (compared to the Fermi velocity v_F) near unitarity, indicating highly robust superfluidity.

The normal phase of the unitary Fermi gas also highly interesting open questions. The limit of a single minority fermion in a sea of majority fermions - the Fermi polaron - has been shown to be well-described by Landau Fermi liquid theory [200], an effective description of the system in terms of weakly interacting quasiparticles. Experiments with a spin-balanced gas reveal that the thermodynamics of the normal phase contains signatures of a Fermi liquid [158, 129], though the results are not conclusive. Finding a Fermi liquid in the normal phase would be remarkable; it would show that it is possible to treat the system as being composed of weakly-interacting quasiparticles of renormalized mass and energy, despite the strong interaction. Close to the phase transition, one expects to observe a window in the phase diagram where preformed pairs exist that are not yet condensed. In the BCS limit, pairing coincides with condensation, while in the BEC limit, there is a large window above the condensation temperature T_c where molecules exist, up to a temperature T^* above which

the molecules are destroyed by thermal fluctuations. Because the unitary Fermi gas is at the middle of the BEC-BCS crossover, it is expected to contain the regime of preformed pairs, also known as the pseudogap [134] in analogy to the Nernst regime in the phase diagram of high-T_c superconductors. Finally, the normal phase is a strongly collisional normal fluid which exhibits extremely low viscosity and elliptic flow [162], analogous to the hydrodynamics of a quark-gluon plasma [120, 207]. It has been suggested that the unitary Fermi gas may attain the quantum minimum of viscosity, and experiment indeed shows that the unitary Fermi gas comes close to the limit of minimum viscosity [50], and hence may be considered as a model of a "perfect fluid".

Interest in the unitary Fermi gas began even before the realization of degenerate Fermi gases of atoms. Nuclear physicists recognized that to leading order, a spin-1/2 Fermi system with short-range, unitarity-limited interaction serves as a model for dilute nuclear matter, such as that found in the crust of neutron stars. The neutron-neutron scattering length is $\sim -19\,\text{fm}$ [83], while the interparticle spacing of neutrons in the crust of a neutron star is $\sim 1\,\text{fm}$ [96], much smaller than the scattering length. G. Bertsch in 1999 posed a famous problem regarding the unitary Fermi gas [23]. One formulation of his problem is as follows: what is the ground state energy of the unitary Fermi gas? The lack of an interaction-dependent length scale means that only the density sets the scale, just like the non-interacting case, and hence the ground state energy should be given by that of the non-interacting gas, $\frac{3}{5}NE_F$, up to a universal factor - now famously known as the Bertsch parameter ξ_B.

The realization of degenerate Fermi gases of ^{40}K [53, 192] and ^{6}Li [85, 90, 224, 201, 108] in 1999 and the early 2000s paved the way to experimentally study fermionic many-body physics with cold atoms. The observation of Feshbach resonances [57, 141, 163, 109] in 2002 provided the necessary tool to create a Fermi gas with strong interactions. By sweeping the magnetic field across the Feshbach resonance, one can produce Feshbach molecules [187]. This led to the first realizations of condensates of fermionic atoms - Bose-Einstein condensation of molecules in 2003 [108, 87, 250]. In the following year, condensation in the BEC-BCS crossover was observed [186, 251].

Finally, in 2005, the observation of a vortex lattice [249] provided an unambiguous signature of the existence of superfluidity in the BEC-BCS crossover.

Since then, the properties of strongly-interacting Fermi gases have been studied extensively. The phase diagram of an imbalanced Fermi gas at unitarity was probed [206], revealing the signature of a first-order phase transition when the temperature is below a tricritical point. A first thermodynamic measurement was made with trap-averaged energy and entropy [143, 144], obtaining $T_c \approx 0.2T_F$ and $\xi_B = 0.41(2)$ [144]. Radio-frequency experiments enabled the observation of Fermi polarons [200] and their identification as quasiparticles in a Landau Fermi liquid. The superfluid pairing gap was also determined by radio-frequency measurement [199]. Non-equilibrium dynamics have also been investigated. Early studies of collective modes have been conducted [118, 241, 190]. The speed of sound [110] and the critical velocity [151] were measured in the BEC-BCS crossover.

The unitary Fermi gas has also received considerable theoretical attention because of its interesting physics, its challenges, and its relevance to the study of other strongly correlated fermionic systems. Numerous Monte Carlo calculations have investigated the zero-temperature equation of state of the balanced and imbalanced gas [37, 10, 39]. *Ab initio* lattice calculations have provided a finite-temperature equation of state [27]. Bogoliubov de Gennes simulations have generated insights into defects such as vortices and solitons [203, 7]. A new method of diagrammatic Monte Carlo calculation [179] was developed and has demonstrated its promise through a successful application on the Fermi polaron problem [180, 181].

This is a brief summary of our understanding of the strongly interacting Fermi gas when I joined the Zwierlein group in 2009. By this time, the community had developed a good qualitative understanding of the physics of the unitary Fermi gas, and accurate quantitative knowledge was starting to accumulate. The next step was to develop a more precise quantitative knowledge which would allow us to validate strongly-interacting theories; this is the theme of the work reported in this thesis.

To provide a theoretical background, I present some elementary theory regarding thermodyanmics and solitonic excitations of interacting fermions in Chapter 2. These

are the two major topics explored in this thesis. In Chapter 3, I briefly describe the experimental apparatus used for the Fermi gas experiments.

To improve the quantitative knowledge of the unitary Fermi gas, a natural starting place is to obtain a detailed understanding of the thermodynamics. The thermodynamic equation of state provides a suitable platform where one can benchmark many-body theories. Thermodynamics is important even in the study of non-equilibrium physics, because it is often needed as an input to dynamical theories, and it allows one to obtain important quantities such as the temperature of the cloud. The two equation of state measurements [158, 101] were reported in 2010 underscore the importance of a precise thermodynamic measurement. When I came to MIT, a collaboration between the Zwierlein group and the theory group at Amherst had just been established to perform a joint theoretical-experimental study of the thermodynamics of the unitary Fermi gas. The theory group would employ diagrammatic Monte Carlo (DMC) calculations to obtain the equation of state in the normal phase, while the experimental group would perform precision measurements to validate the theory. Such a validation would establish the DMC as a trustworthy technique for the further study of strongly correlated fermions. While I worked on the thermodynamic measurement, I also participated in concurrent spin-transport experiments [209, 210] and dimensional crossover experiments [211] led by my colleague Ariel Sommer.

The thermodynamic measurement turned out to be very fruitful, and is reported in Chapter 4. The experimental measurement and theoretical calculation of the equation of state of the normal phase agree excellently. This work is reported in [226]. In order to obtain a measurement of the equation of state across the superfluid transition, we developed a novel method that does not require a fitting procedure nor an external thermometer. The resulting measurement, reported in [129], clearly reveals the signature of the superfluid transition: a peak in the heat capacity, reminiscent of the λ-transition of superfluid helium. We obtained the critical temperature $T_c/T_F = 0.167(13)$ and the Bertsch parameter $\xi_B = 0.376(4)$.

In Chapter 5, I discuss two works that build upon this thermodynamic measurement. We developed a technique to obtain global thermodynamic quantities of the

entire trapped cloud from the column density [126]. This enables the measurement of the equation of state and thermometry for an experimental setup whose cloud has a large aspect ratio, and hence obtaining the local density from the inverse Abel transform is impractical. In another work, we participated in a joint theoretical-experimental collaboration to study the temperature dependence of the collective modes [222] with the Innsbruck group and the Trento group. The theory group at Trento developed a theory from Landau's equations, which involves the equation of state as an input. We participated in the calculation led by the Trento group to yield a prediction for the temperature dependence of the collective modes. This theoretical prediction has good agreement with the experimental measurement provided by the Innsbruck group.

Knowledge of the thermodynamics provides important information for our understanding of the unitary Fermi gas. However, there is also much physics that is not contained in the thermodynamic equations. For example, we do not yet know the wave equation that governs the matter wave in the superfluid phase. An example of such a wave equation exists in both limits of the BEC-BCS crossover: the Gross-Pitaevskii equation (GPE) for the weakly-interacting BECs, and the Bogoliubov-de Gennes (BdG) equation[2] for the BCS limit. Theories for the strongly-interacting Fermi superfluid exist, such as the time-dependent superfluid local density approximation (TSLDA) [31] and the time-dependent Ginzburg-Landau equation [198], but they remain to be validated.

In order to probe the superfluid wave function, we turned our attention to solitonic excitations, such as solitons and vortices. These objects are also called solitary waves, analogous to the solitary waves that exist in classical physics, fiber optics, and conducting polymers [95]. Solitonic excitations in a superfluid are defects in the phase of the superfluid. They are localized quasiparticles with well-defined mass and energy, and can be considered as particles emerging out of the background field of matter waves. They therefore serve as excellent probes of the underlying medium.

[2]In fact, the BdG equation can be extended along the crossover, though as a mean-field theory, it does not accurately describe the strongly-interacting regime. It reduces to the GPE describing BECs of molecules in the BEC limit, however with an incorrect molecule-molecule interaction strength.

Furthermore, in the case of a fermionic superfluid, these defects are known to host localized fermionic bound states called Andreev bound states [40], which play a crucial role in the physics of weak links in superconductors. Therefore, solitonic excitations in a fermionic superfluid would serve as a resource for the study of Andreev states. Solitons and vortices have been extensively studied experimentally [34, 54] and numerically [26, 25, 122] in weakly interacting BECs. However, for Fermi gases, theoretical work has begun only recently [7, 203, 204]. Prior to our experiments, only a vortex lattice had been observed in a Fermi gas [249], and there had been no experimental study of the dynamics and evolution of individual solitons and vortices.

In Chapter 6, I report on the first observation of a solitonic vortex in a fermionic superfluid. The excitation was generated via phase imprinting. The resulting object, which we at first interpreted as a planar soliton, was long-lived and had a long oscillation period compared to the period of atoms in the trap, implying a large ratio of its inertial to bare mass [243]. Both of these observations are counter-intuitive for a planar soliton. This study attracted interest from theorists, and soon several theory works suggested that the object we observed was a vortex ring [237, 30, 188]. To clarify the identity of the object, we performed tomographic imaging by selectively imaging slices of the cloud. Using this method, we identified the object to be not a vortex ring but a solitonic vortex [127] - a crossover between a conventional vortex and a planar soliton [25, 122]. We developed a hydrodynamic description of the vortex period and found it to agree well with the measured period in the BEC-BCS crossover.

The solitonic vortex is an object that emerges about half a second after phase imprinting. It is highly likely that after the phase imprint but prior to developing this steady-state object, the superfluid undergoes significant evolution. Such evolution would reveal the microscopic, beyond-hydrodynamic physics that plays a part in the dynamics of solitonic excitations. In Chapter 7, I report on an experiment studying the cascade of solitary waves, from a planar soliton to a ring defect and finally, to a single vortex line [128]. Using tomographic imaging, we confirmed the existence of a planar soliton during the first 10 ms after the imprint. The soliton subsequently

underwent snake instability - the undulation of the soliton plane - as a result of a dynamical instability in an effectively 3D geometry. We were able to track the nodal surface and observe its decay via a puncture of the initial soliton plane. In the intermediate stages, we found evidence for more exotic structures resembling Φ-solitons [155]. We studied the growth rate of the transverse modes of the snake instability and found a hierarchy in the growth rate.

During the course of the aforementioned studies, it became increasingly clear that the density inhomogeneity arising from the non-uniform trapping potential was hindering us from studying a wide range of physics - for example, the study of pseudogap physics, the measurement of the phase-velocity relation of a planar soliton, and the study of solitons in an imbalanced Fermi gas which may lead to the observation of the Larkin-Ovchinnikov state, to name a few. It is natural to pursue the creation of tailored potentials for Fermi gases as the next step. In the Conclusion, I summarize the work contained in this thesis, and discuss the diverse, exciting physics that could be studied with a Fermi gas in a tailored trapping potential.

Chapter 2

Many-body physics of Fermions with strong interactions

In this chapter, I present some elementary theory of interacting fermions to provide a theoretical background of the studies presented in this thesis.

2.1 Quantum statistics

The difference in particle statistics is one aspect that distinguishes quantum mechanics from classical physics. In classical mechanics, all particles are considered distinguishable. In quantum mechanics, particles of the same type are indistinguishable. Let us consider an ensemble of N identical particles in states ν_i, with $i = 1, ..., N$ being the labels of the particles. Since the particles are indistinguishable, exchanging two particles does not affect the probability amplitude,

$$|\Psi(..., \nu_i, ..., \nu_j, ...)|^2 = |\Psi(..., \nu_j, ..., \nu_i, ...)|^2 , \tag{2.1}$$

where Ψ is the wave function of the system. Therefore, exchanging two identical particles leads to the wave function acquiring a complex constant η whose amplitude is unity, $|\eta|^2 = 1$:

$$\Psi(..., \nu_i, ..., \nu_j, ...) = \eta\Psi(..., \nu_j, ..., \nu_i, ...) . \tag{2.2}$$

Now, let us consider exchanging the i^{th} and the j^{th} particle once more. In 3D, this is equivalent to doing nothing, so the wavefunction itself must be unaffected. Therefore, $\eta^2 = 1$, and the only two values possible for this exchange factor are $\eta = \pm 1$. The case $\eta = 1$ is for particles following Bose-Einstein statistics (bosons), and $\eta = -1$ is for particles following Fermi-Dirac statistics. The spin-statistics theorem [169] from quantum field theory tells us that a particle's spin determines which statistics it follows: particles with integer spins are bosons, and particles with half-integer spins are fermions. Correspondingly, the occupation probability of state ν of bosons and fermions at finite temperatures T obeys the following distributions

$$\langle n_\nu \rangle = \frac{1}{e^{\beta(E_\nu - \mu)} \mp 1}, \tag{2.3}$$

where $\beta = 1/(k_B T)$, k_B is the Boltzmann constant, E_ν is the energy of the state, and μ is the chemical potential. The upper (minus) sign gives the Bose-Einstein disbrituion for bosons, and the lower (plus) sign gives the Fermi-Dirac distribution for fermions. This is in contrast to the Maxwell-Boltzmann distribution for classical particles, $\langle n_\nu \rangle = \frac{1}{e^{\beta(E_\nu - \mu)}}$, which the Bose-Einstein and Fermi-Dirac distributions reduce to at high temperatures and in the low density limit.

In the case of fermions, an important consequence of the wave function being anti-symmetric upon particle exchange is the Pauli exclusion principle, which states that no two identical fermions can occupy the same quantum state. To demonstrate this, let us assume one can place two identical fermions in the same quantum state i. Eq. 2.2 with $\eta = -1$ then implies $\Psi(..., \nu, ..., \nu, ...) = -\Psi(..., \nu, ..., \nu, ...)$, and consequently $\Psi = 0$. The Pauli exclusion principle can also be seen in that the Fermi-Dirac distribution is always less than or equal to unity.

2.2 Ideal Bose and Fermi gas

The ideal (non-interacting) Bose and Fermi gas provides an example of the consequence of quantum statistics. In this section, we examine the ideal Bose and Fermi

gas at equilibrium. For free particles, $E_k = \frac{\hbar k^2}{2m}$, where $\mathbf{k}$ is the momentum and m is the particle mass. The density distribution for the non-condensed gas is then given by $n = \frac{1}{\mathcal{V}} \sum_{\mathbf{k}} \langle n_{\mathbf{k}} \rangle$, where $\mathcal{V}$ is the volume of the system. In the absence of macroscopic occupation, one can replace the sum with the integral $\int \frac{\mathrm{d}^3 k}{(2\pi)^3}$ times the volume. The density of the non-condensed gas is then given by

$$n = \int \frac{\mathrm{d}^3 k}{(2\pi)^3} \frac{1}{e^{\beta(\frac{p^2}{2m} - \mu)} \mp 1} = \pm \frac{1}{\lambda^3} \mathrm{Li}_{3/2} \left(\pm e^{\beta\mu} \right) , \tag{2.4}$$

where $\lambda = \sqrt{\frac{2\pi\hbar^2}{m k_B T}}$ is the thermal de Broglie wavelength, and $\mathrm{Li}_n(z)$ is the n^{th}-order Polylogarithm defined as[1]

$$\mathrm{Li}_n(z) = \sum_{j=1}^{\infty} \frac{z^j}{j^n} . \tag{2.5}$$

In the high temperature $\beta\mu \to -\infty$ limit, we recover the Boltzmann gas

$$n = \lambda^{-3} e^{\beta\mu} . \tag{2.6}$$

Gibbs-Duhem relation at constant temperature $\mathrm{d}P = n \mathrm{d}\mu$ tells us that the density is related to the pressure by $n = \left(\frac{\partial P}{\partial \mu} \right)_T$, and hence

$$P = k_B T \lambda^{-3} e^{\beta\mu} . \tag{2.7}$$

Therefore, we recover the ideal gas law

$$P = n k_B T . \tag{2.8}$$

[1]The Polylogarithm function also has the integral definition $\mathrm{Li}_n(z) \equiv \frac{1}{\pi^2} \int \mathrm{d}^{2n} r \frac{1}{e^{r^2}/z - 1} = \frac{1}{\Gamma(n)} \int_0^\infty \mathrm{d}q \frac{q^{n-1}}{e^q/z - 1}$

2.2.1 Ideal Bose gas at low temperatures: Bose-Einstein condensation

The Bose-Einstein distribution diverges or becomes negative if $\epsilon_0 \leq \mu$, where ϵ_0 is the energy of the lowest single-particle state. Therefore, for a non-condensed ideal Bose gas, one necessarily has $\mu < \epsilon_0$. As the temperature is lowered, the chemical potential rises but cannot exceed ϵ_0. Therefore, the occupation probability of any excited state is bounded from above by $\frac{1}{e^{\beta(E_\nu - \epsilon_0)}-1}$. If the total particle number in the excited states is less than the total number of the system N, the rest of the particles must be in the ground state. This phenomenon is the Bose-Einstein condensation. In the thermodynamic limit, the particles in the ground state make a macroscopic contribution to the density. Because of particle indistinguishability, the particles condensed in the ground state behave as a single matter wave. In a homogeneous system, the critical temperature at which condensation occurs is

$$T_c = \frac{2\pi\hbar^2}{mk_B}\left(\frac{n}{\zeta(3/2)}\right)^{2/3}, \tag{2.9}$$

where ζ is the Riemann Zeta function, with $\zeta(3/2) = 2.6124$. The relation between temperature and the condensate density n_0 is given by

$$\frac{n_0}{n} = 1 - \left(\frac{T}{T_c}\right)^{3/2}. \tag{2.10}$$

At $T = 0$, all the particles are condensed in the ground state.

2.2.2 Ideal Fermi gas at low temperatures: Fermi sea

The ground state of an ideal Fermi gas at zero temperature is very simple to understand: due to Pauli exclusion, fermions fill all the available energy levels, and each energy level is occupied by only one particle per species. The outermost occupied energy level is the Fermi energy. One can see it from the Fermi-Dirac distribution at $T = 0$, which is $\langle n_{\sigma,k}\rangle = \Theta(\mu - E_k)$, where $\sigma = \uparrow, \downarrow$ is the spin, and Θ is the Heaviside-

theta function. Here we consider a spin 1/2 system with equal population of both spin states $n_\uparrow = n_\downarrow$ and total density $n = n_\uparrow + n_\downarrow$. The Fermi energy of an ideal Fermi gas is then the same as the chemical potential, $E_F = \mu$. For a homogeneous system, the density of each spin state is given by $n_\sigma = \int \frac{\mathrm{d}^3k}{(2\pi)^3}\Theta\left(E_F - \frac{\hbar^2k^2}{2m}\right) = \frac{(2mE_F)^{3/2}}{6\pi^2\hbar^3}$. Therefore, we have $E_F = \frac{\hbar^2k_F^2}{2m}$, where the Fermi wave vector is $k_F = (3\pi^2 n)^{1/3}$. The Fermi temperature is the temperature scale associated with the Fermi energy, $T_F = E_F/k_B$.

For a Fermi gas at finite temperatures or with interactions, the Fermi surface is no longer sharp; however, one can still define the Fermi energy, Fermi temperature, and Fermi wave vector simply using the density, as defined above.

2.3 Tuning interactions with a Feshbach resonance

What makes a quantum many-body system interesting - and challenging to investigate - is interaction. In particular, interaction endows Bose-Einstein condesates with the property of superfluidity[2] and facilitates pairing in a Fermi gas to enable condensation of fermion pairs. In atomic gases, atomic interaction can be tuned via Feshbach resonances. This is the versatile knob that enables the study of interacting fermions, and in particular, fermions with strong interactions.

2.3.1 Quantum mechanical description of binary scattering of atoms

At large distances, atoms experience a van der Waals interaction $\sim -C_6/r^6$. At short ranges, atomic interaction is dominated by a repulsive core which arises from the deformation of electronic orbitals. The exact description of the atomic interaction is complicated. However, the gas in the experiment is dilute, with typical interatomic distances of $n^{-1/3} \approx 1\,\mu$m being much larger than the van der Waals length $b = (mC_6/\hbar^2)^{1/4} \sim 40\,a_0 \approx 2\,$nm. Hence the atoms do not explore the short-range

[2]The Landau criterion for superfluidity indicates that the critical velocity is $v_c = \min\left(\frac{|\varepsilon(\mathrm{p})|}{p}\right)$ and for an ideal Bose gas it leads to $v_c = 0$. In a weakly-interacting BEC, the critical velocity is non-zero, $v_c = c = \sqrt{gn/m}$, where c is the speed of sound and g is the coupling constant.

details of the interaction. In addition, the low temperature of the system ensures that scattering is purely s-wave (see the discussion on the Wigner threshold law later in this subsection). Therefore, scattering events in an atomic gas can be characterized by one single quantity, the s-wave scattering length a.

We first consider general elastic scattering of two particles via a central potential $V_{\text{int}}(r)$, where r is the distance between the two particles. The interaction does not affect the center-of-mass motion. Therefore, we can consider the scattering problem in terms of the relative coordinate r in the center-of-mass frame. The Schroedinger equation in the center-of-mass frame is

$$\left(\frac{\hbar^2}{2m_r}\nabla^2 + V_{\text{int}}(r)\right)\Psi_{\mathbf{k}} = E_k\Psi_{\mathbf{k}}\,, \tag{2.11}$$

where $m_r = m/2$ is the relative mass, and $E_k = \frac{\hbar^2 k^2}{2m_r}$, with $\mathbf{k}$ being the relative momentum of the two particles. Far away from the scattering potential, the wave function will be given by the sum of the incident wave and the scattered wave,

$$\Psi_{\mathbf{k}}(\mathbf{r}) = e^{i\mathbf{k}\cdot\mathbf{r}} + f(\mathbf{k},\mathbf{k}')\frac{e^{ikr}}{r}\,, \tag{2.12}$$

where $f(\mathbf{k},\mathbf{k}')$ is the scattering amplitude for scattering an incident plane wave with $\mathbf{k}$ into the direction $\mathbf{k}'$. Energy conservation requires $k = k'$. The scattering amplitude gives the differential cross section,

$$\frac{d\sigma}{d\Omega} = |f|^2\,, \tag{2.13}$$

the probability per unit time for the scattered particle to traverse the solid angle $d\Omega$, normalized by incident flux. Since we are dealing with a central potential, the resulting wave function must be axisymmetric with respect to the direction of $\mathbf{k}$. We can therefore set the z-axis to be along $\mathbf{k}$ and denote the azimuthal angle between $\mathbf{k}$ and $\mathbf{k}'$ to be θ. We can then expand the wave function in the basis of spherical

harmonics. In the large r limit, we have

$$\Psi_{\mathbf{k}}(\mathbf{r}) \to \frac{1}{kr} \sum_{l=0}^{\infty} c_l P_l(\cos\theta) \sin\left(kr - \frac{l\pi}{2} + \delta_l\right) , \tag{2.14}$$

where l is the angular momentum quantum number, c_l are expansion coefficients, and δ_l are the partial-wave phase shifts. In the absence of interaction, $\delta_l = 0$ solves the radial wave equation, i.e. gives the expansion of the incident wave. This result shows that the effect of the interaction is simply to add a phase shift δ_l to each spherical wave of angular momentum l. The scattering amplitude is then given by

$$f(k,\theta) = \sum_{l=0}^{\infty} P_l(\cos\theta) f_l(k) \tag{2.15}$$

$$f_l(k) = \frac{2l+1}{k(\cot\delta_l - i)} . \tag{2.16}$$

The analysis so far assumes two distinguishable particles. For identical particles, the scattering states also obey the same exchange statistics, namely $\Psi(\mathbf{r}) = \eta\Psi(-\mathbf{r})$. The consequence is $f(k,\theta) = \eta f(k,\pi-\theta)$, which then sets the condition that $f_l = 0$ when $(-1)^l\eta = -1$. Therefore, identical bosons do not scatter with odd l, and identical fermions do not scatter with even l. In the absence of a resonance, $\delta_l \sim k^{2l+1}$ for small k in a finite-range potential [131], and hence the scattering cross section for each partial wave follows the Wigner threshold law $\sim E^{l+1/2}$. Therefore, at low temperatures where the energy involved in scattering is low, identical fermions do not interact. In order to have interacting fermions, one needs to have a mixture of distinguishable fermions, so that they can undergo s-wave collisions. In this case, the above analysis of distinguishable particles applies directly.

With a mixture of two species of fermions, in the low temperature (and hence low energy) regime, we only consider the dominant $l = 0$ s-wave scattering. The s-wave phase shift scales as $\delta_0 \sim k$. We therefore define the s-wave scattering length as follows:

$$\frac{1}{a} = -\lim_{k\to 0} k\cot[\delta_0(k)] . \tag{2.17}$$

The scattering length is the zero crossing of the asymptotic scattering wave function. It therefore characterizes how much the interaction modifies the scattering wave function, and is thus a measure of the strength of the interaction

A typical expansion for $k \cot \delta_0$ beyond the zeroth order has the form

$$k \cot \delta_0 = -\frac{1}{a} + \frac{1}{2} r_e k^2 + \mathcal{O}(k^4) , \tag{2.18}$$

where r_e is the effective range. Therefore, the s-wave amplitude in the small k limit is given by

$$f_0 = \frac{1}{-\frac{1}{a} + \frac{1}{2} r_e k^2 + \mathcal{O}(k^4) - ik} . \tag{2.19}$$

2.3.2 Feshbach resonance

A Feshbach resonance is a versatile tool to control atomic interactions. Here, I provide a simple outline of the physical origin of a Feshbach resonance. Let us consider two molecular potentials. A Feshbach resonance arises when a bound state in a closed channel (closed means that the continuum states of this channel are not available as final scattering states due to energy conservation) is resonantly coupled to the open channel. In the case of ^{6}Li atoms at a typical magnetic field above 500 G, the electronic spin is essentially aligned in the same direction for the lowest three hyperfine states. Two ^{6}Li atoms in the lowest two hyperfine states $|1\rangle$ and $|2\rangle$, for example, would collide with a triplet configuration. The open channel is then the triplet potential, and the closed channel is the singlet potential. Due to hyperfine interaction, the two channels are coupled, and the atoms can also explore the closed (singlet) potential. The finite difference in the magnetic moment of the two channels means the energy difference between the two potentials can be tuned by the magnetic field. Resonance arises when the detuning is close to zero, and this leads to strong mixing between the two channels. The scattering between the two atoms in the two hyperfine states therefore depends on this detuning, and the scattering length is tunable by controlling the background magnetic field B. Near such a Feshbach resonance, one can obtain

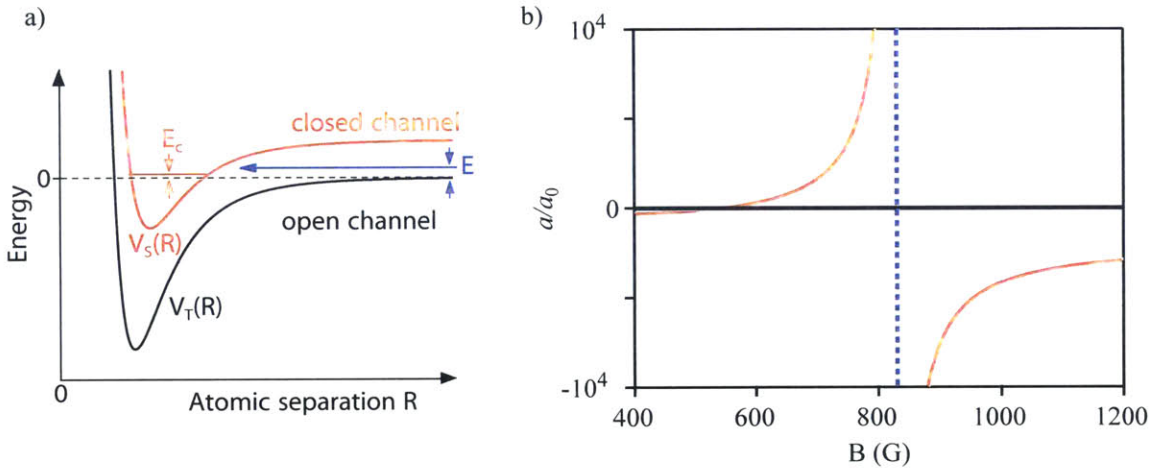

Figure 2-1: (a) A basic two-channel model for a Feshbach resonance. The model consists of a closed channel and an open channel. In the case of atoms, this corresponds to the singlet potential V_S and the triplet potential V_T respectively. Zero energy is taken to be the asymptotic value of the open channel. The two atoms collide at energy E in the open channel, and the closed channel supports a molecular bound state with energy E_c. A Feshbach resonance occurs when the open channel is resonantly coupled to the bound state. Since ultracold collisions take place at $E \to 0$, resonant coupling is realized by tuning E_c near zero. If there is a difference in the magnetic moment between the two channels, the tuning can be achieved by adjusting the magnetic field B. This figure is taken from Ref. [48]. (b) Scattering length (in units of the Bohr radius a_0) between the lowest two hyperfine states of ^{6}Li as a function of the magnetic field. A wide Feshbach resonance exists near 830 G, with a width of $\sim$ 300 G. The values of the scattering lengths shown here are from the measurement of Ref. [245], which obtained the location of the resonance to be $B_0 = 832.18(8)$ G

large scattering lengths. A comprehensive review for Feshbach resonances in atoms can be found in [48]. Here, I will simply state the results relevant to the thesis. The scattering length near a Feshbach resonance is well-modeled by the expression [16]

$$a = a_{\mathrm{bg}} \left(1 + \frac{\Delta B}{B - B_0}\right) (1 + \alpha(B - B_0)) , \tag{2.20}$$

where B_0 is the location of the resonance, ΔB is the width, a_{bg} is the background scatering length, and α is a correction parameter. There is a wide Feshbach resonance for scattering between the lowest two hyperfine states of ^{6}Li centered around ~ 830 G, with a width of ~ 300 G. This makes ^{6}Li a very versatile platform to study interacting Fermi systems. This Feshbach resonance was first precisely determined in Ref. [16] to be 834.15 ± 1.5 G. This was the value used in the MIT thermodynamic measurement, reported in Chapter 4. Given the precision of the thermodynamic measurement, knowledge of the Feshbach resonance becomes the limiting factor in the quantitative understanding of the strongly interacting Fermi gas. A subsequent new measurement gives $B_0 = 832.18(8)$ G [245].

On the side of the Feshbach resonance with $a > 0$, a bound state between two fermions of different species exists. In the vicinity of the resonance, the binding energy is

$$E_b = \frac{\hbar^2}{ma^2} . \tag{2.21}$$

The resulting bosonic molecules interact with each other with molecular scattering length $a_{\mathrm{bb}} = 0.6a$ [173].

2.4 Unitarity and scale invariance

At a Feshbach resonance, the scattering amplitude reaches the maximum value possible, $|f(k)| = 1/k^2$, as allowed by quantum mechanics - the unitary limit. In this section, I discuss the condition for a Fermi gas to reach the unitary limit and the property of scale invariance.

2.4.1 Unitarity

Obviously, the first criterion for having a unitary Fermi gas is for the system to be a gas. A gas is a dilute system whose interparticle spacing is large compared to the interaction range b of the potential, $nb^3 \ll 1$. For atoms, the interaction range is given by the Van der Waals range.

Since a gas is dilute, the probability that more than two particles come within a volume b^3 is negligible (assuming Efimov physics is absent, which is the case for fermions when there is no mass imbalance). Therefore, the particles mainly interact via binary scattering described in the previous section, Here, we derive the limit on the scattering amplitude assuming only isotropic, low energy scattering. Let us consider the scattering amplitude $f(\mathbf{k})$ of two particles, where $\mathbf{k}$ is the relative momentum. In the case of a fermionic mixture of a pseudo-spin 1/2 system at low temperatures, higher-order partial waves are suppressed, the particles scatter via s-wave scattering, and the scattering amplitude is isotropic, $f(k)$. To see what is the limit quantum mechanics places on the scattering amplitude, let us first consider the optical theorem, $\sigma_{\text{tot}} = \frac{4\pi}{k}\text{Im}[f(k)]$, where σ_{tot} is the total cross section. Since $\sigma_{\text{tot}} = 4\pi|f(k)|^2$, this then implies $|f(k)|^2 = \frac{\text{Im}[f(k)]}{k}$. Dividing both sides by $|f(k)|^2$ and making use of $f^*/|f|^2 = 1/f$ gives us $\text{Im}(1/f) = -k$. Therefore, quantum mechanics requires the scattering amplitude to have the form

$$f(k) = -\frac{1}{ik + u(k)}\,, \tag{2.22}$$

where $u(k)$ is a real function. The upper bound is then $|f(k)| \leq k^{-1}$, and the unitary limit is

$$f_{\text{unitary}}(k) = -\frac{1}{ik}\,. \tag{2.23}$$

For an ensemble to be at the unitary limit, we would like the above condition to hold for all relevant k, which requires $u(k)/k \ll 1$. To see what is the range of validity for this condition, we now adopt the usual expansion for $u(k)$ in the case of s-wave

scattering (by identifying $u(k) = -k\cot(\delta_0)$ where δ_0 is the phase shift),

$$u(k) = \frac{1}{a} - \frac{1}{2}r_e k^2 + \mathcal{O}(k^4)\,, \tag{2.24}$$

where a is the s-wave scattering length, and r_e is the effective range. Let us for now assume that the $\mathcal{O}(k^4)$ terms are negligible if $kb \ll 1$. Then the condition $u(k)/k \ll 1$ for unitarity is the following limit for all k

$$kb,\ k|r_e| \ll 1 \ll k|a|\,. \tag{2.25}$$

For a degenerate Fermi gas $T/T_F \lesssim 1$, the typical momentum is $k \lesssim k_F \sim n^{1/3}$. Therefore, in order to meet the above condition for every particle in a Fermi gas, one arrives at the following requirement for unitarity:

$$k_F b,\ k_F|r_e| \ll 1 \ll k_F|a|\,. \tag{2.26}$$

The analysis is so far general, and we had to make use of a plausible but unjustified assumption that $\mathcal{O}(k^4)$ terms are negligible if $kb \ll 1$. In the case of cold atoms interacting via an open channel and a closed channel potential, the conditions for unitarity may be achieved at a Feshbach resonance, near which the scattering length is modeled by Eq. 2.20. In this case, one can form a length scale R_*, which is related to the background scattering length $a_{\rm bg}$ and the width of the resonance ΔB [172],

$$R_* \equiv \frac{\hbar^2}{m\Delta B|a_{\rm bg}\mu_{\rm B,mol}|}\,, \tag{2.27}$$

where $\mu_{\rm B,mol}$ is the magnetic moment of the closed-channel molecule and is twice the magnetic moment of an atom in the open channel. For ^{6}Li near the resonance $B \sim 830\,\mathrm{G}$, one finds $\mu_{\rm B,mol} \simeq 2\mu_{\rm B}$, where $\mu_{\rm B}$ is the Bohr magneton. Physically, R_* is related to the effective range r_e as follows near a Feshbach resonance [239]:

$$r_e = -2R_*\left(1 - \frac{a_{\rm bg}}{a}\right)^2 + \frac{4b}{\sqrt{\pi}} - \frac{2b^2}{a}\,. \tag{2.28}$$

The sufficient condition for unitarity (see for example Ref. [42]) is then given by

$$b\,,R_*\,,(|a_{\rm bg}|R_*)^{1/2} \ll k_F^{-1} \ll |a| \tag{2.29}$$

In the case of ^{6}Li at the broad Feshbach resonance near 830 G, we have $b = 2.1\,\text{nm}$, $a_{\rm bg} = -74\,\text{nm}$, and $R_* = 0.027\,\text{nm}$, leading to $\sqrt{|a_{\rm bg}|R_*} = 1.4\,\text{nm}$, all of which are small compared to $1/k_F \approx 1\,\mu\text{m}$ [16].

At higher temperatures $T_F \lesssim T$, the typical momentum is on the order of the thermal de Broglie wavelength λ, and one replaces k_F with λ^{-1} for the appropriate condition for unitarity. The high-temperature regime admits a virial expansion in terms of the fugacity $e^{\beta\mu}$, $P\lambda^3/(k_BT) = 2\left(e^{\beta\mu} + b_2e^{2\beta\mu} + b_3e^{3\beta\mu} + ...\right)$. The virial expansion for the unitary Fermi gas is known up to the third order [140], which is accurate up to $T/T_F \approx 1.5$, as benchmarked by the experimentally measured equation of state and the diagrammatic Monte Carlo calculation. This high-temperature regime can therefore be considered as understood. The interesting regime for experiments is therefore in the degeneracy $T < T_F$.

2.4.2 Scale invariance

In the absence of interaction-related length scales, the only length scale that remains (at $T = 0$) is the interparticle spacing $n^{-1/3}$ given by the density, just as in the case of the non-interacting system. Therefore, any thermodynamic quantity is given by the corresponding quantity for an ideal gas at the same density, up to a universal factor. At finite temperatures, the thermal de Broglie wavelength λ enters as another length scale. The universal factor is replaced with a universal function that depends on $\lambda n^{1/3}$, or in other words, T/T_F.

Formally, the scaling of thermodynamic quantities mentioned above is a consequence of scale invariance, which I will briefly discuss here. For a detailed treatment, one can refer to Ref. [42]. To model the interaction in the unitary Fermi gas, there are two approaches. One is to take a model with an interaction that has a finite range b and a fixed scattering length a, and takes the $b \to 0$ limit. The other approach is to

use the zero-range model (see e.g. Ref. [41]). In this model, the interaction operator acts on the wave function as

$$V_{\text{int}}\Psi = \sum_{i\neq j} g\delta(r_{ij}) \lim_{r_{ij}\to 0} \frac{\partial}{\partial r_{ij}}(r_{ij}\Psi)\,, \tag{2.30}$$

where r_{ij} is the distance between particles i and j and $g = 4\pi\hbar^2 a/m$ is the coupling constant. If particles i and j are in different spin states, the wave function then has a $1/r_{ij}$ singularity. Therefore, the wave function satisfies the Wigner-Bethe-Peierls contact boundary conditions:

$$\Psi(\mathbf{r}_1, ..., \mathbf{r}_N) = A_{ij}(\mathbf{R}_{ij}; \{\mathbf{r}_k; k \neq i, j\})(r_{ij}^{-1} - a^{-1}) + \mathcal{O}(r_{ij})\,, \tag{2.31}$$

where $\mathbf{R}_{ij} = (\mathbf{r}_i + \mathbf{r}_j)/2$, and A_{ij} is some function. This means that in the short-range model, an interacting system can be described by the same Hamiltonian of the ideal system, but with a different domain - one that is restricted to functions that satisfy the contact boundary conditions.

Let us now consider a rescaling of coordinates $\mathbf{r}_i \to \eta\mathbf{r}_i$ in a homogeneous system. The corresponding rescaled wave function is

$$\Psi_\eta(\mathbf{r}_1, ..., \mathbf{r}_N) = \frac{\Psi(\mathbf{r}_1/\eta, ..., \mathbf{r}_N/\eta)}{\eta^{3N/2}}\,. \tag{2.32}$$

It is clear that for $1/a = 0$, if a wave function Ψ belongs to the domain of the Hamiltonian (i.e. satisfies the contact conditions), then the rescaled wave function also belongs to the domain. This is the formal mathematical definition of scale invariance. On the other hand, if a wave function Ψ obeys the contact conditions for a finite a, Ψ_η does not obey the contact conditions. It is also trivial to see that the invariance of the domain is satisfied for the non-interacting case.

How does the change of scale affect the Hamiltonian? Since we can now consider a free Hamiltonian acting on a domain given by the contact conditions, we only need to consider the kinetic energy term. The contribution from the kinetic energy $\hbar^2\nabla^2/(2m)$ will be rescaled by $1/\eta^2$, and hence $H \to H/\eta^2$. Therefore, the eigenenergies E_ν scale

as $E_\nu \to E_\nu/\eta^2$.

Let us now consider an ensemble of N particles in volume $\mathcal{V}$, with $N, \mathcal{V} \to \infty$ and $N/\mathcal{V} = n$. Spatial rescaling changes the volume from $\mathcal{V} = L^3$ to $\eta^3\mathcal{V}$, and hence $n \to n/\eta^3$. To keep $E_\nu/(k_BT)$ constant and hence occupation of eigenstates constant, the temperature is to be scaled by $T \to T/\eta^2$. Let us now consider the Helmholtz free energy density $\mathcal{F} = F/\mathcal{V}$, an intensive quantity and a function of density and temperature only (see 4.2.1 and Eq. 4.17). Then, scale invariance means

$$\mathcal{F}(n/\eta^3, T/\eta^2) = \mathcal{F}(n, T)/\eta^5 \,. \tag{2.33}$$

At $T = 0$, $\mathcal{F} = E/\mathcal{V} - TS/\mathcal{V}$ reduces to the ground state energy density $E_0/\mathcal{V}$ and depends on n only. The above scaling relation indicates[3] $\mathcal{F} \sim n^{5/3} \sim nE_F$ at $T = 0$, just as in the case of the ideal Fermi gas whose $T = 0$ free energy density is $\mathcal{F}_0 = E_0/\mathcal{V} = \frac{3}{5}nE_F$. Therefore, for $F = \mathcal{F}\mathcal{V}$, one has

$$F(n, T = 0) = \xi_B E_0 = \xi_B \frac{3}{5} N E_F \,, \tag{2.34}$$

where ξ_B is a universal number. This number is known as the Bertsch parameter, named after G. Bertsch who proposed the unitary Fermi gas as a model for the dilute neutron matter and posed the challenge to understand the ground state properties of this system [23]. Since $\mu = \left(\frac{\partial F}{\partial N}\right)_{T,\mathcal{V}}$ and $P = -\left(\frac{\partial F}{\partial \mathcal{V}}\right)_{T,N}$, the same type of relation holds for the chemical potential and pressure,

$$\mu(n, T = 0) = \xi_B \mu_0 = \xi_B E_F \tag{2.35}$$

$$P(n, T = 0) = \xi_B P_0 = \xi_B \frac{2}{5} n E_F \,. \tag{2.36}$$

At finite temperatures, a similar analysis using Eq. 2.33 implies that one can normalize the temperature by a scale that depends on the density as $n^{2/3}$ to obtain a universal form. The natural choice is the Fermi temperature $T_F = E_F/k_B$, and normalizing T

[3] One way to show this rigorously is to use Euler's homogeneous function theorem, which states $f(\eta x) = \eta^\gamma f(x) \to x f'(x) = \gamma f(x)$

by T_F gives the following functional form

$$F = \tilde{F}\left(\frac{T}{T_F}\right)\frac{3}{5}NE_F\,. \tag{2.37}$$

Similarly, the chemical potential and pressure follow the form

$$\mu = \tilde{\mu}\left(\frac{T}{T_F}\right)E_F \tag{2.38}$$

$$P = \tilde{p}\left(\frac{T}{T_F}\right)\frac{2}{5}nE_F\,. \tag{2.39}$$

In general, scale invariance means that one can compare one system with another system at a vastly different scale, as long as they are both in the universal regime. With the correct normalization, one obtains the same result in both systems. For example, the dilute neutron matter in the crust of neutron star is a spin-1/2 system whose scattering length $a \approx -19\,\text{fm}$ [83] is large compared to the neutron-neutron spacing $\approx 1\,\text{fm}$ [96]. Though the effective range is comparable to the interparticle spacing, $r_e \approx 3\,\text{fm}$ [231], the system is close to the universal regime. Therefore, for systems such as the dilute crust of neutron stars, which are conjectured to be modeled well by the unitary Fermi gas [23, 11, 96], a strongly-interacting Fermi gas can provide insights about these systems even though its density and temperature are orders of magnitude lower. There are also similarities between the unitary Fermi gas and other strongly-correlated fermionic systems, such as nuclei and quark gluon matter (see for example Ref. [246]).

2.5 BEC-BCS crossover and the strongly interacting Fermi gas

In the regime of positive a, the bosonic molecules formed by fermion pairs can condense to form a Bose-Einstein condensate of molecules at low temperatures. As the density increases, there comes a point where the Pauli pressure of the fermionic constituents becomes important. This occurs when the the interparticle spacing $\sim k_F^{-1}$ is

much smaller than the size of the molecules, which is on the order of a. On the side of $a < 0$, bound pairs between two isolated particles do not form, but any attractive interaction induces an instability in the Fermi sea to many-body pairing, and at low temperatures, one obtains a condensate of Cooper pairs, described by the Bardeen-Cooper-Schrieffer (BCS) theory. On resonance, one has a novel superfluid of fermion pairs that is a crossover of tightly-bound molecules and long-range pairs. Based on the early works of Keldysh [115], Popov [178], and Eagles [65], Leggett realized that the crossover from BCS to BEC superfluidity is smooth [135]. At $T = 0$, the ground state advances from a condensate of molecules to a condensate of Cooper pairs as one tunes the interaction, without any phase transition occuring in between. This is because in the presence of the Fermi sea, one simply crosses over from a regime where the pair size is much larger than the interparticle spacing to the regime where one has tighly bound molecules.

The regime where the scattering length is large, $a \gg k_F^{-1}$, for example as realized by Fermi gases right at a Feshbach resonance, is of particular interest along the crossover, as discussed previously. The absence of a small parameter and the sign problem associated with fermionic many-body systems make the theoretical study of strongly interacting fermions notoriously difficult. For this reason, the program called quantum simulation was proposed by Feynman [76], in which one realizes the model system in question with well-controlled constituents (in our case, atoms), and asks nature itself for the answer regarding the properties of the model system. Nevertheless, a theoretical approach that has proven useful to provide insight is the mean-field theory. A well-known formulation is based on Leggett's work [135], with extension to finite temperatures by Nozieres and Schmitt-Rink [161]. A detailed description of this approach can be found in reviews such as [116]. Here I will simply outline the result to gain intuition.

The many-body Hamiltonian in the second quantization notation is

$$H = \sum_{k,\sigma} \varepsilon_k c^\dagger_{k,\sigma} c_{k,\sigma} + \frac{g}{\mathcal{V}} \sum_{k,k',q} c^\dagger_{k+\frac{q}{2},\uparrow} c^\dagger_{-k+\frac{q}{2},\downarrow} c_{k'+\frac{q}{2},\downarrow} c_{-k'+\frac{q}{2},\uparrow}\,, \tag{2.40}$$

where $c_{k,\sigma}$ is the annhilation operator of a particle at momentum k and spin σ, $\varepsilon_k = \hbar^2 k^2/(2m)$ is the kinetic energy, and g is the coupling constant. The interaction term is a momentum-conserving contact interaction.

The key ingredient in the mean-field approach is to neglect interactions between pairs at non-zero momenta. This leads to the following approximate Hamiltonian,

$$H_{\rm BCS} = \sum_{k,\sigma} \varepsilon_k c^\dagger_{k,\sigma} c_{k,\sigma} + \frac{g}{\mathcal{V}} \sum_{k,k'} c^\dagger_{k,\uparrow} c^\dagger_{-k,\downarrow} c_{k',\downarrow} c_{-k',\uparrow} \,. \tag{2.41}$$

This is the famous BCS Hamiltonian. The coupling g is related to the observable quantity a using the formal prescription

$$\frac{1}{g} = \frac{m}{4\pi\hbar^2 a} - \frac{m}{\hbar^2} \int \frac{d^3q}{(2\pi)^3} \frac{1}{q^2} \,. \tag{2.42}$$

The exact solution to the BCS Hamiltonian of Eq. 2.41 is the celebrated BCS wave function

$$|\Psi_{\rm BCS}\rangle = \prod_k (u_k + v_k c^\dagger_{k,\uparrow} c^\dagger_{-k,\downarrow}) |0\rangle \tag{2.43}$$

where u_k, v_k are scalar functions of k. Minimizing the free energy $\langle H - \mu N \rangle$ leads to

$$\begin{aligned} v_k^2 &= \frac{1}{2}\left(1 - \frac{\xi_k}{E_k}\right) && (2.44) \\ u_k^2 &= \frac{1}{2}\left(1 + \frac{\xi_k}{E_k}\right) && (2.45) \\ \xi_k &\equiv \varepsilon_k - \mu && (2.46) \\ E_k &= \sqrt{\xi_k^2 + \Delta^2} \,, && (2.47) \end{aligned}$$

where the gap Δ is defined as

$$\Delta \equiv \frac{g}{\mathcal{V}} \sum_k \langle c_{k,\uparrow} c_{-k,\downarrow} \rangle \,, \tag{2.48}$$

With the BCS wave function, the gap equation becomes $\Delta = -\frac{g}{\mathcal{V}} \sum_k u_k v_k = -\frac{g}{\mathcal{V}} \sum_k \frac{\Delta}{2E_k}$. It follow then that $-1/g = \int \frac{d^3k}{(2\pi)^3} \frac{1}{2E_k}$. To replace the coupling g with the scattering

length a, one uses the prescription Eq. 2.42 and obtains

$$-\frac{m}{4\pi\hbar^2 a} = \int \frac{d^3k}{(2\pi)^3}\left(\frac{1}{2E_k} - \frac{1}{2\varepsilon_k}\right). \tag{2.49}$$

An additional constraint is given by the number equation

$$n = \frac{N}{\mathcal{V}} = 2\int \frac{d^3k}{(2\pi)^3} v_k^2. \tag{2.50}$$

The solutions are given by [164]

$$-\frac{1}{k_F a} = \frac{2}{\pi}\left(\frac{2}{3I_2(\frac{\mu}{\Delta})}\right)^{1/3} I_1\left(\frac{\mu}{\Delta}\right) \tag{2.51}$$

$$\frac{\Delta}{E_F} = \left(\frac{2}{3I_2(\frac{\mu}{\Delta})}\right)^{2/3}, \tag{2.52}$$

where the functions $I_1(z)$ and $I_2(z)$ are defined as

$$I_1(z) \equiv \int_0^\infty \mathrm{d}x\, x^2\left(\frac{\mathrm{i}}{\sqrt{(x^2-z)^2+1}} - \frac{1}{x^2}\right) \tag{2.53}$$

$$I_2(z) \equiv \int_0^\infty \mathrm{d}x\, x^2\left(1 - \frac{x^2-z}{\sqrt{(x^2-z)^2+1}}\right). \tag{2.54}$$

2.5.1 Thermodynamics at zero temperature

In the BCS limit of weak attractive interaction $k_F a \to 0_-$, the chemical potential and the gap are given by

$$\mu \approx E_F \tag{2.55}$$

$$\Delta \approx \frac{8}{e^2} e^{-\pi/(2k_F|a|)}. \tag{2.56}$$

The gap is exponentially suppressed, indicating that Cooper pairing is fragile in the weakly-interacting limit.

In the BEC limit, we have

$$\mu = -\frac{\hbar^2}{2ma^2} + \frac{\pi\hbar^2 a}{m} n \tag{2.57}$$

$$\Delta \approx \sqrt{\frac{16}{3\pi}} \frac{E_F}{\sqrt{k_F a}} . \tag{2.58}$$

The chemical potential is simply the binding energy per fermion, plus a mean field contribution describing the repulsive interaction between molecules. The second term is half of the chemical potential of a molecule $\mu_{\rm mol}$. For a weakly-interacting gas of molecules, $\mu_{\rm mol} = g_{\rm bb} n_B$, where $n_B = n/2$ is the density of the molecules, and $g_{\rm bb} = 4\pi\hbar^2 a_{\rm bb}/m_B$ is the boson-boson coupling constant, with $m_B = 2m$ the mass of the molecule. This then gives a boson-boson scattering length of $2a$. It should be noted that the mean-field treatment neglects correlations between different pairs, or between one fermion and a pair, and hence this is not the correct result. An exact calculation for the interaction between four fermions shows that $a_{\rm bb} = 0.6a$ [173].

For $\mu > 0$, the single-particle spectrum (Eq. 2.47) has a minimum of Δ at $\varepsilon_k = \mu$, while for $\mu \leq 0$, which occurs for $0.553 \leq 1/(k_F a)$, the minimum is $\sqrt{\mu^2 + \Delta^2}$ and is located at $k = 0$. For $\mu > 0$, Δ is the gap in the excitation spectrum. As soon as $\mu \leq 0$, there is no longer a gap at non-zero k. There, the quantity Δ itself does not represent the binding energy of molecules nor the gap in their excitation spectrum. So Δ itself does not play a role in the BEC regime. Rather, it is the ratio $\Delta^2/|\mu|$ that is important. From Eqs. 2.57 and 2.58, one sees that in the BEC limit,

$$\frac{\Delta^2}{2|\mu|} = \frac{4\pi\hbar^2}{m} na , \tag{2.59}$$

which is two times the molecular mean field.

The isentropic index, defined as

$$\gamma = \frac{\mu}{n} \frac{\partial n}{\partial \mu} , \tag{2.60}$$

gives the scaling of the density with respect to the chemical potential, $n \propto \mu^\gamma$. It

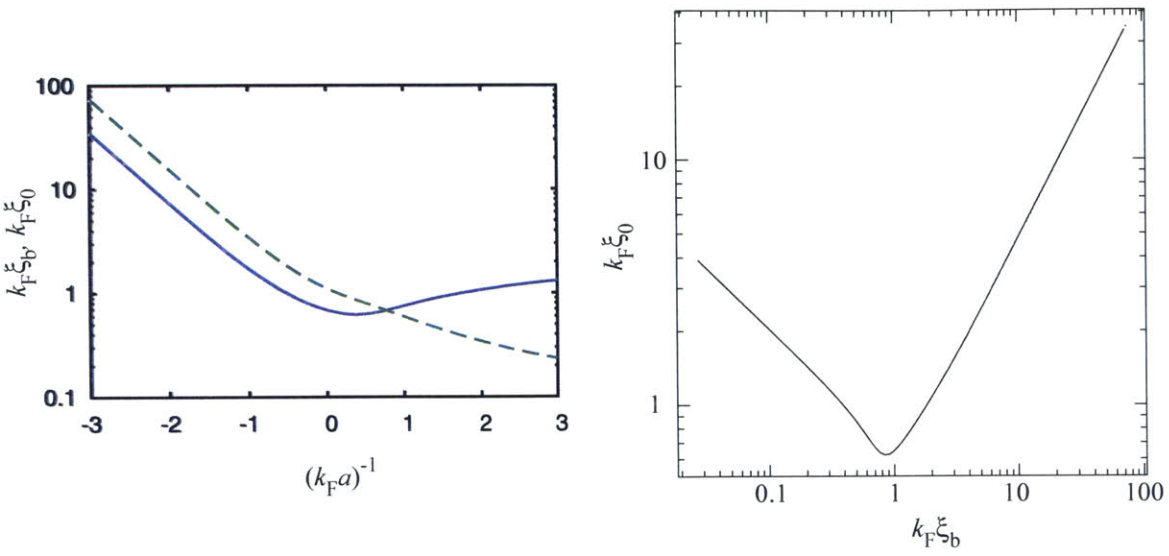

Figure 2-2: Phase coherence length ξ_0 and pair correlation length ξ_b in the BEC-BCS crossover. (a) ξ_0 (solid curve) and ξ_b (dashed curve) as a function of $(k_F a)^{-1}$, normalized by $1/k_F$. The pair correlation length monotonically decreases with increasing $(k_F a)^{-1}$, indicating an increasingly small pair as one moves towards the BEC limit. This figure is taken from Ref. [246]. (b) $\xi_0 k_F$ as a function of $\xi_b k_F$. The two quantities coincide in the BCS limit. This figure is taken from Ref. [147].

takes on the bosonic value $\gamma = 1$ in the BEC limit and the fermionic value $\gamma = 3/2$ on the BCS side. On resonance, universality demands also $\gamma = 3/2$.

An important quantity that characterizes the crossover is the two-particle correlation length ξ_b, defined as $\xi_b^2 = \frac{\langle\psi(\mathbf{r})|r^2|\psi(\mathbf{r})\rangle}{\langle\psi(\mathbf{r})|\psi(\mathbf{r})\rangle}$, where ψ is the BCS wave function. In BCS limit, one has

$$\xi_b \approx \xi_{\rm BCS} \equiv \frac{\hbar v_F}{\pi\Delta} \gg 1/k_F\,. \tag{2.61}$$

Here, $v_F = \hbar k_F/m$ is the Fermi velocity. The quantity $\xi_{\rm BCS}$ is the BCS coherence length. In the BEC limit, one has $\xi_b \sim a$, as one would expect from intuition. This length scale should be distinguished from the phase coherence length ξ_0 associated with spatial fluctuations of the order parameter. The phase coherence length and the pair correlation length coincide in the BCS limit (up to a trivial numerical factor) and are given by $\xi_{\rm BCS}$, but differ in the BEC limit, where the phase coherence length is given by the healing length $\xi = \sqrt{\hbar^2/(2n_B g_{\rm bb})}$. Fig. 2-2 shows the dependence of

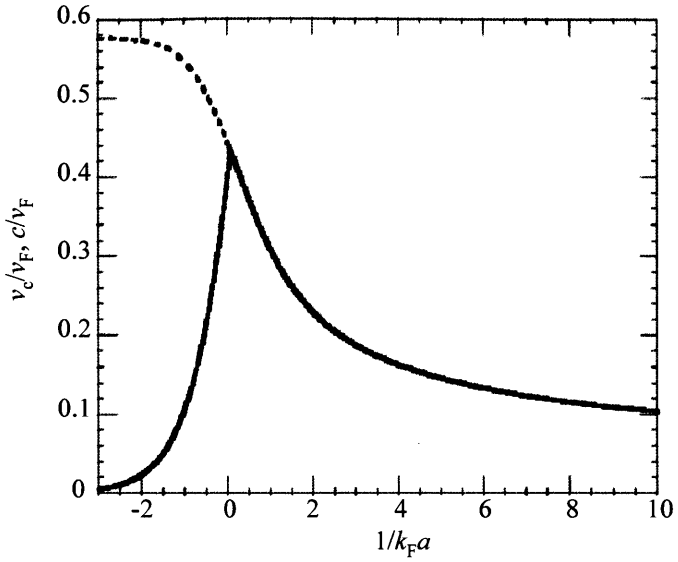

Figure 2-3: Critical velocity in the BEC-BCS crossover. The critical velocity v_c (solid curve) is plotted as a function of $(k_Fa)^{-1}$, normalized by the Fermi velocity v_F. For comparison, the sound velocity c (dashed curve), normalized by k_F, is also shown. The sound velocity reaches the limiting value of the Bogoliubov-Anderson mode of the BCS regime $c/v_F = 1/\sqrt{3} = 0.577$ for large $(k_Fa)^{-1}$. This figure is taken from Ref. [51].

ξ_b and ξ_0 in the BEC-BCS crossover. The pair correlation length $\xi_b k_F$ monotonically decreases with increasing $(k_Fa)^{-1}$, indicating the trend of decreasing pair size as one moves towards the BEC limit. Therefore, the quantity $\xi_b k_F$ is also a useful measure of where one is along the crossover, besides $(k_Fa)^{-1}$. On the other hand, the phase coherence length $\xi_0 k_F$ reaches a minimum near unitarity. It is the length scale that determines the size of defects in the superfluid such as solitons and vortex cores. It can be thought of as the generalization of the healing length in the BEC-BCS crossover. In this thesis, I will be using the term healing length (and the notation ξ) interchangably with the phase coherence length.

A quantity related to the phase coherence length is the critical velocity. The Landau criterion gives a critical velocity v_c beyond which it becomes energetically

favorable to transfer momentum from a moving superfluid to excitations:

$$v_c = \min\left(\frac{E_k}{\hbar k}\right) . \tag{2.62}$$

On the BCS side, the single-particle excitation spectrum gives the critical velocity of $v_{c,\mathrm{BCS}} = \frac{\Delta}{\hbar k_F}$. On the BEC side, the critical velocity is the speed of sound of the Bogoliubov dispersion, $c = \sqrt{\mu_{\mathrm{mol}}/m_B} = \frac{v_F}{\sqrt{3\pi}}\sqrt{k_F a}$. The phase coherence (healing) length is related to the critical velocity by $\xi \propto 1/v_c$. The evolution is shown in Fig. 2-3. The peak in the critical velocity around resonance reflects the narrow transition from the regime where excitation of sound prohibits superfluid flow, to the regime where pair breaking dominates. This peak indicates that the superfluid is most stable near the Feshbach resonance.

2.5.2 Finite temperatures

At finite temperatures, thermal excitations of the quasiparticles modify the gap and number equations. The Bogoliubov quasiparticle operators are

$$\gamma_{k,\uparrow} = u_k c_{k,\uparrow} - v_k c^\dagger_{-k,\downarrow} \tag{2.63}$$

$$\gamma^\dagger_{-k,\downarrow} = u_k c^\dagger_{-k,\downarrow} + v_k c_{k,\uparrow} . \tag{2.64}$$

These fermionic quasiparticles obey the Fermi-Dirac distribution $\langle \gamma^\dagger_{k,\sigma}\gamma_{k,\sigma}\rangle = \frac{1}{e^{E_k/(k_BT)}+1}$. Therefore, at finite temperatures, the expectation value for the pairing field becomes $\langle c_{k,\uparrow}c_{-k,\downarrow}\rangle = -u_k v_k\left(1 - \sum_\sigma \langle \gamma^\dagger_{k,\sigma}\gamma_{k,\sigma}\rangle\right) = -u_k v_k\left(1 - 2(1+e^{E_k/(k_BT)})^{-1}\right)$. The gap equation Eq. 2.49 then becomes

$$-\frac{m}{4\pi\hbar^2 a} = \int \frac{d^3k}{(2\pi)^3}\left(\frac{1}{2E_k}\tanh\left(\frac{E_k}{2k_BT}\right) - \frac{1}{2\varepsilon_k}\right) . \tag{2.65}$$

If one is interested in the temperature regime above the condensation temperature, for example in the calculation of the pair-formation temperature T^*, then one has a

normal Fermi gas with $\Delta = 0$, and the number equation becomes

$$n = 2 \int \frac{d^3k}{(2\pi)^3} \frac{1}{1 + e^{\xi_k/(k_B T^*)}} \,. \tag{2.66}$$

In the BEC regime, at low temperatures, the gas forms a condensate of molecules. At temperatures above the critical temperature T_c, condensation ceases, but the fermions remain paired as molecules. At even higher temperatures, thermal fluctuations destroy the pairs. The temperature of pair formation is denoted as T^*. In the BEC regime, one has

$$T^*_{\mathrm{BEC}} \approx \frac{1}{3} \frac{|E_b|}{W\left[\left(\frac{\pi}{6}\right)^{1/3} \frac{|E_b|}{2E_F}\right]} \tag{2.67}$$

$$T_{c,\mathrm{BEC}} = \frac{\pi\hbar^2}{m} \left(\frac{n}{2\zeta(3/2)}\right)^{2/3} = 0.22 E_F \tag{2.68}$$

where $W(x)$ is Lambert W-function. The critical temperature here is the same as the critical temperature of a non-interacting BEC of boson with mass $2m$ and density $n/2$. For stronger interactions, there is a small correction $T_c/T_{c,\mathrm{BEC}} = 1 + 1.31 n_B^{1/3} a_{\mathrm{bb}}$ [114].

On the BCS side, the pair formation and condensation coincides, as in BCS theory:

$$T_{c,\mathrm{BCS}} = T^*_{\mathrm{BCS}} = \frac{e^{\gamma_{\mathrm{E}}}}{\pi} \frac{8}{e^2} e^{-\pi/(2k_F|a|)} = \frac{e^{\gamma_{\mathrm{E}}}}{\pi} \Delta_0 \,, \tag{2.69}$$

where γ_{E} is Euler's constant, and Δ_0 is the gap at $T = 0$.

In the BCS regime, the critical temperature is exponentially suppressed. Naively taking the same expression to unitarity, one obtains $T_c = 0.61 T_F$. If indeed the critical temperature at unitarity is on the order of the Fermi temperature - the measurement that I will report in Chapter 4 will confirm that this is the case - it is a large value for fermionic superfluidity, considering that in metals the Fermi temperature is around many ten thousands of Kelvins.

Another observation is that in the crossover, there are regions in the phase diagram in which T_c and T^* are different. Between these two temperatures, we expect pairs that are not yet condensed. In the deeply BEC limit, this is not surprising,

but given the qualitative picture of the crossover, we also expect to find a region where uncondensed pairs exist, both at unitarity and in the BCS side close to resonance. These preformed pairs also occur in a part of the phase diagram of high-T_c superconductors, the Nernst regime of the pseudogap [134]. Therefore, the regime of preformed pairs is also commonly called the pseudogap. At the present time, there is no conclusive experimental evidence of preformed pairs above T_c. Thermodynamic signature of preformed pairs is not found in our thermodynamic measurement (see Chapter 4). Momentum-resolved radio-frequency spectroscopy [217] suggests that the single-particle excitation is gapped above T_c, but the result is not conclusive. Clear evidence may be obtained through a local measurement of the spin susceptibility, either with a Bragg scattering experiment [100] or with a thermodynamic measurement of the spin-imbalanced Fermi gas.

Fig. 2-4 is the well-known phase diagram that qualitatively describes the phases in the BEC-BCS crossover. The calculation of T_c and T^* is taken from Ref. [194] and not from the mean-field crossover theory presented previously.

2.5.3 Non-equlibrium dynamics of the pair condensate in the crossover

Since the condensate behaves as a single matter wave, the study of non-equilibrium dynamics simplifies dramatically when there exists a description of the single wavefunction in which the particles (and holes in the case of BCS superfluidity) participate, rather than an equation that involves all the particles individually. One such example is the well-known Gross-Pitaevski equation (GPE) for the description of weakly-interacting BECs. In a weakly-interacting BEC trapped in a potential V and with interaction g, the GPE governs the evolution of the superfluid wave function ψ:

$$i\hbar\frac{\partial\psi}{\partial t} = -\frac{\hbar^2\nabla^2}{2m_B}\psi + V\psi + g|\psi|^2\psi\,. \tag{2.70}$$

Here, m_B is the mass of the boson that forms the condensate. In the case of bosonic atoms, $m_B = m$ is simply the particle mass, while in the case of BEC of molecules

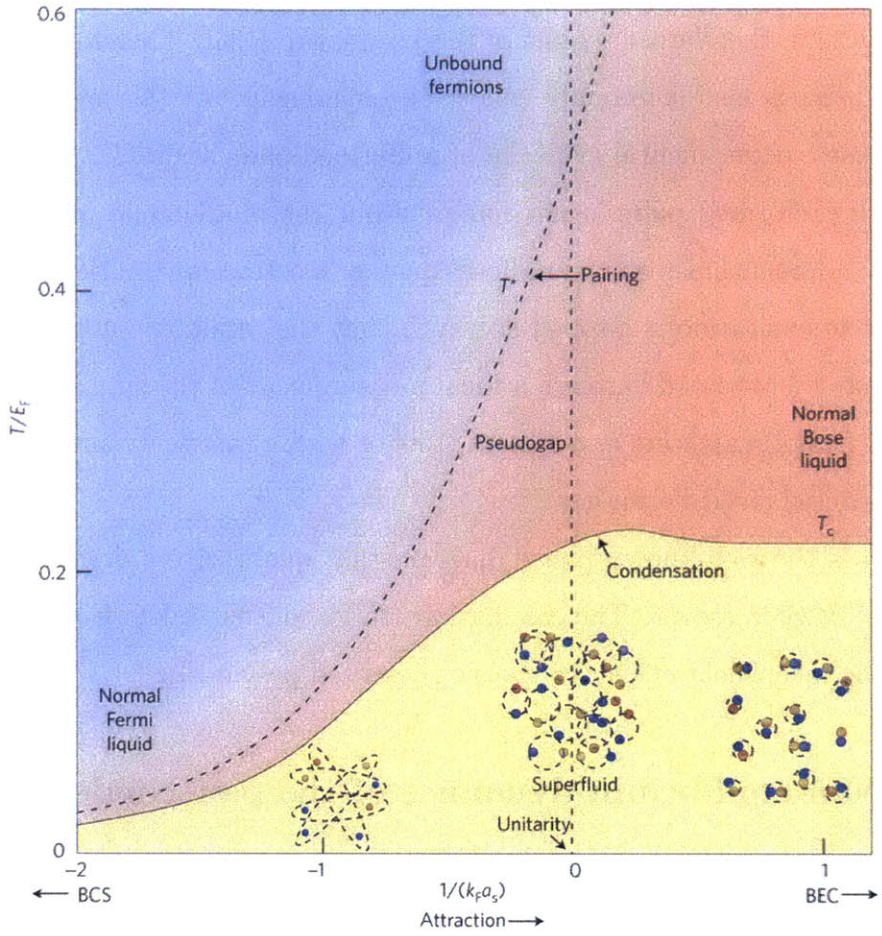

Figure 2-4: Phase diagram of a spin-balanced Fermi gas in the BEC-BCS crossover. In the BEC limit, fermions pair to form tightly bound bosonic molecules below the pairing temperature T^*. Above T^*, the molecules are destroyed by thermal fluctuations. In between T^* and T_c, one has a thermal gas of molecular bosons. The molecules condense below T_c to form BEC. As one approaches the BCS side, the window of pre-formed pairs - the pseudogap - becomes smaller, while both T^* and T_c decrease as pairing becomes less and less robust. T_c/T_F reaches a maximum value close to unitarity. In the deep BCS regime, the condensation and pairing occur at the same temperature. The figure is taken from Ref. [184], which makes use of the result in [194].

formed by pairing of fermions, the particle mass is replaced by the molecular mass $m_B = 2m$. A stationary solution is obtained by substituting $\psi(t, \mathbf{r}) = e^{-i\mu t/\hbar}\psi(\mathbf{r})$. The time-independent GPE looks just like above, except that the left hand side becomes $\mu\psi$.

In the BEC-BCS crossover, a unified description can be found in the Bogoliubov de Gennes (BdG) equation [44]

$$\begin{pmatrix} H_0 & \Delta \\ \Delta^* & -H_0 \end{pmatrix} \begin{pmatrix} u_\eta(\mathbf{r},t) \\ v_\eta(\mathbf{r},t) \end{pmatrix} = i\hbar\frac{\partial}{\partial t} \begin{pmatrix} u_\eta(\mathbf{r},t) \\ v_\eta(\mathbf{r},t) \end{pmatrix}, \tag{2.71}$$

where $H_0 = -\hbar^2\nabla^2/(2m) + V - \mu$ is the single-particle grand canonical Hamiltonian, and $u_\eta(\mathbf{r},t)$ and $v_\eta(\mathbf{r},t)$ are the time-dependent amplitudes describing the particle and hole character of quasiparticles with energy E_η. The order parameter and the density are given by

$$\Delta = -g\sum_\eta u_\eta v_\eta^* \tag{2.72}$$

$$n = 2\sum_\eta |v_\eta|^2 . \tag{2.73}$$

The above equations reduce to the stationary GP equation for the order parameter ψ of a condensate of molecules in the BEC limit [174], the interaction between dimers however being given by the mean-field value $2a$ instead of the exact value $0.6a$. Although approximate, this mean-field theory is expected to give a qualitatively accurate picture of the BEC-BCS crossover. In the following, I will give an introduction of solitonic excitations, making use of the results from the BdG Hamiltonian to provide insight into the crossover.

2.6 Solitonic excitations in atomic superfluids

Solitonic excitations - also known as solitary waves - are excitations that involve a twist in the phase of the superfluid order parameter. These excitations are localized in

one or two directions - typically within the healing length ξ - due to a balance of dispersion and focusing arising from the non-linearity in the wave equation that governs the medium. These excitations are similar to the solitary waves occuring in classical mechanics and fiber optics. Having a well-defined energy E and mass[4], they can be thought of as localized quasiparticles emerging out of the background of the condensate's matter wave. These objects lend themselves as versatile probes of the medium they reside in. For example, a soliton can be thought of as a Josephson junction, and its current-phase relation provides insight into the superfluid wavefunction.

A variety of solitonic excitations exists in trapped atomic superfluid. In this section, I give a review of the solitonic excitations in the context of an atomic superfluid.

2.6.1 Soliton

A soliton is a planar defect in the order parameter of the superfluid. I will first consider a soliton in a weakly-interacting BEC to set the stage and then discuss a soliton in a fermionic superfluid.

Soliton in a weakly-interacting BEC

In the absence of a trap, a dark soliton[5] moving with velocity v_S is the following solution to the GPE[6]:

$$\psi = \sqrt{n_0}\left[i\frac{v_S}{c} + \sqrt{1-\frac{v_S^2}{c^2}}\tanh\left(\frac{(z-v_S t)\sqrt{1-v_S^2/c^2}}{\xi\sqrt{2}}\right)\right]e^{-i\mu t/\hbar}. \tag{2.74}$$

Here, c is the speed of sound given by $\mu = m_B c^2$, and the healing length ξ is given by $\mu = \hbar^2/(2m_B\xi^2)$. The background density is $n_0 = \mu/g$. The coordinate is chosen such that the soliton is at $z = 0$ at $t = 0$. For a derivation of Eq. 2.74, see for

[4]Soon we shall see that in fact, solitonic excitations have two kinds of masses - the inertial and bare (gravitational) mass.

[5]In some works, the term "dark soliton" refers to a soliton with complete density depletion and a soliton with reduced contrast is called a "gray soliton". This thesis adopts the convention that uses the term "dark soliton" to refer to any soliton characterized by a density depletion, in contrast to a "bright soliton" as observed in BECs with attractive interactions.

[6]Here we are either considering a soliton in 1D, or a soliton whose nodal plane is in the $x-y$ plane.

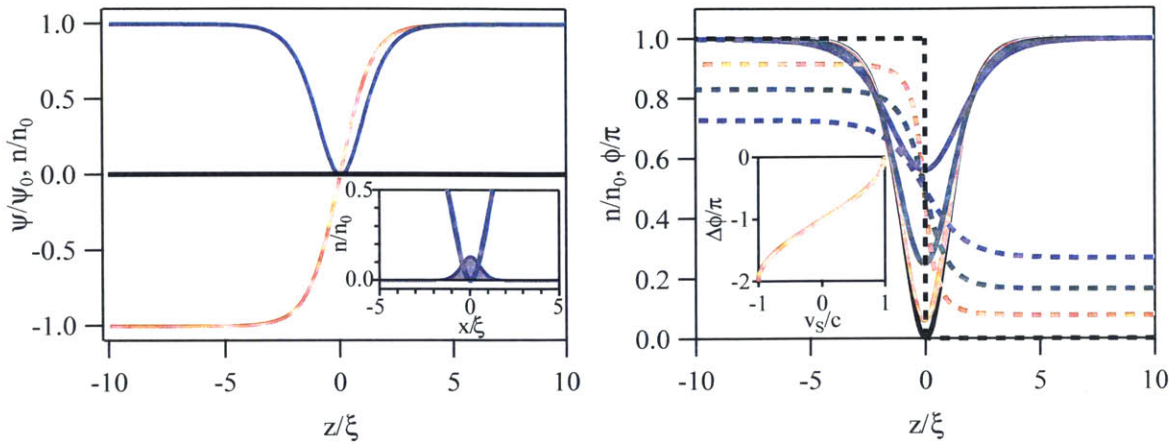

Figure 2-5: Soliton in a weakly-interacting BEC. (a) Wave function ψ (red) and density n (blue) of a stationary soliton. The two quantities are normalized by their asymptotic values. Inset: anomolous mode due to quantum depletion in a BEC with large interaction. (b) Density n (solid curves) and phase ϕ (dashed curves) of soliton for $v_S/c = 0$ (black), 0.25 (red), 0.5 (green), and 0.75 (blue). Inset: the phase difference $\Delta\phi$ as a function of the velocity v_S/c is given by $\Delta\phi = -2\arccos(v_S/c)$.

example Ref. [171]. Fig. 2-5 shows the wave function, density, and phase profile of a soliton, while Fig. 2-9 (a) shows the profile of a planar soliton in a trapped condensate. A stationary soliton in a weakly-interacting BEC is devoid of particles. At finite velocities, the soliton is no longer fully depleted. As $v_S \to c$, the soliton disappears.

The energy of the soliton scales as the number of missing particles times the chemical potential, $E_S \sim n_{1D}\xi\mu$, where $n_{1D} = \mathcal{A}n_0$ is the 1D density and $\mathcal{A}$ is the cross-sectional area of the system. Since $\mu = gn_0$ and $\xi = \hbar/\sqrt{m_B\mu}$, the energy per area scales as $E_S/\mathcal{A} \sim \hbar\mu^{3/2}/(g\sqrt{m_B})$. The exact expression for the energy per unit area $E_S/\mathcal{A}$ of a soliton moving at a velocity v_S is [171]

$$\frac{E_S}{\mathcal{A}} = \frac{4\hbar}{3g\sqrt{m_B}}(\mu - m_B v_S^2)^{3/2} = \frac{4}{3}n_0\hbar c\left(1 - \frac{v_S^2}{c^2}\right)^{3/2}. \tag{2.75}$$

Soliton in BEC-BCS crossover

In fermionic superfluids, solitons are phase twists in the wavefunction of fermion pairs [64, 7]. For s-wave superfluids, the pair wavefunction is the pairing gap $\Delta(\mathbf{r})$. In the BEC-limit, the system is a condensate of weakly-interacting molecules and is well-described by the GPE. As one tunes the interaction towards unitarity, strong interactions increase the importance of quantum fluctuations, leading to a depletion of the condensate and the presence of uncondensed bosons even at zero temperature. In order to minimize their repulsive interaction with the condensate, the uncondensed bosons are expected to fill in the soliton notch [62, 63, 133, 148, 78]. This gives rise to the so-called anomalous mode, which reduces the contrast of the soliton [62, 63, 133]. The inset of Fig. 2-5 (a) shows the density profile of such an anomalous mode. Similar soliton filling has been predicted for BECs in optical lattices, where the effect of interactions and thus the role of quantum fluctuations is enhanced by reducing the particles' kinetic energy [152].

As one moves along the BEC-BCS crossover towards the BCS regime, the composite nature of the pairs is revealed. Near unity, the fermion pair size becomes comparable to the interparticle spacing, and much larger in the BCS limit. A unified description for solitons in fermionic superfluids throughout the BEC-BCS crossover has been found within mean-field theory via the Bogoliubov-de Gennes (BdG) equation for a spatially varying gap $\Delta(z)$ [7, 203, 213, 204], given in Eq. 2.71.

For $\mu > 0$, a gap exists in the single-particle spectrum at finite k. Near the soliton, the gap opens and closes. It is known from the study of superconductivity that such a structure houses fermionic bound states - the Andreev bound states. In the BCS limit of weak attractive interactions, the size of the Andreev bound state becomes much larger than the interparticle spacing, and its energy much smaller than the pairing gap. In this limit, following Andreev [6], one may separate out the fast oscillations at $k_\mu = \sqrt{\frac{2m\mu}{\hbar^2}}$ by writing $u_n(z) = u_{n0}(z)e^{\pm ik_\mu z}$, $v_n(z) = v_{n0}(z)e^{\pm ik_\mu z}$ ($\pm$ for fermions moving to the right or left). The envelope functions $u_{n0}(z)$ and $v_{n0}(z)$ is slowly-varying compared to the fast oscillations. Then, the Bogoliubov-de Gennes equation

simplifies to the Andreev equation [6], which for vanishing transverse momentum is given by [182]:

$$\left(\mp i\hbar v_F \sigma_z \frac{\partial}{\partial z} + \Delta(z)\sigma_x\right)\begin{pmatrix} u_{n0} \\ v_{n0} \end{pmatrix} = E_n \begin{pmatrix} u_{n0} \\ v_{n0} \end{pmatrix} \tag{2.76}$$

This is a Dirac equation - a relativistic wave equation - where the pair wavefunction $\Delta(z)$ serves as a spatially varying mass coupling particles and holes [107]. We thus see that there exists a direct connection between solitons in fermionic superfluids to solitons studied in relativistic quantum field theory [107, 82]. The same equation describes solitons in conducting polymers, described by the Su-Schrieffer-Heeger model [95]. When $\Delta(z)$ changes sign (i.e. near where the gap closes), this equation allows for one normalizable zero-energy mode for each of the Fermi points at $\pm k_\mu$, localized at the zero crossing of the gap [107]. This limiting case of an Andreev bound state, a superposition of half a particle and half a hole, carries half-integer particle number [107] and gives rise to the conductivity of polymers [95]. A self-consistent solution for $\Delta(z)$ is known [95, 13] to be $\Delta(z) = \Delta_0 \tanh(z/\xi_{\rm BCS})$, as in the BEC limit. Therefore, a soliton in the BCS limit is again represented by Fig. 2-5 (a) but with $\sqrt{2}\xi = \xi_{\rm BCS} = \frac{\hbar v_F}{\pi \Delta_0}$ the BCS coherence length, and Δ_0 is the bulk pairing gap. In this case, the density profile of the localized state also looks like the one shown in the inset of Fig. 2-5 (a) (but with a different amplitude), except that here it represents the fermionic Andreev bound state, as opposed to the density of uncondensed bosons in the BEC regime. One can show that the following

$$u_0,\, v_0 = \text{const} \times \text{sech}(z/\xi_{\rm BCS}) \tag{2.77}$$

is a solution to the Andreev equation with $E = 0$. Because the Andreev equation removes the fast oscillations, the actual bound state contains oscillations with wavelength $\sim k_F^{-1}$. Fig. 2-6 shows examples of bound states in dark solitons in the BEC-BCS crossover. The short-wavelength ($\sim k_F^{-1}$) oscillations correspond to Friedel oscillations, and are removed in the derivation of the Andreev equation.

In a BCS superfluid, the Andreev bound state energy is never strictly zero owing

to the non-vanishing kinetic energy cost $\hbar^2/m\xi_{\rm BCS}^2 \sim \Delta_0^2/E_F$ of forming the bound state [40, 244], where $E_F = \frac{\hbar^2 k_F^2}{2m}$ is the Fermi energy. For a vortex in a BCS superfluid described by BdG, this result was proved in Ref. [40], but the result is general and can be derived when $\Delta(z)$ is a step function [244]. The energy of this bound state is also called the minigap $\Delta_{\rm mg}$ in the context of superconductivity. In particular, there are two such bound states in 1D, $\Delta_{\rm mg} \sim \pm\Delta^2/E_F$, i.e. the one with $\Delta_{\rm mg} < 0$ is occupied, and the other one is not. Other than these two bound states, the rest of the eigenstates of the BdG equation are not bound but rather delocalized.

If one considers a system inside a box and takes the soliton to be oriented along the z-direction, the x and y directions are quantized with $\mathbf{k}_\perp = 2\pi/L_\perp(n_x, n_y)$. Bound states may exist for more than one value of $k_\perp$. Therefore, in 3D, one can obtain more than two bound states. The energy of the lowest bound state, the minigap, is still expected to be on the order of Δ^2/E_F.

The Andreev states play an important role in the dynamics of the soliton (and by extension, any kind of defect that can house the Andreev states). Their energetics determine the critical velocity a moving soliton can attain (see Fig. 2-6 and Refs. [204, 66]). Where soliton collisions in a GP condensate are elastic (energy conserving), collisions of solitons in the crossover are not, as found by BdG simulations reported in Ref. [204]. The authors found that in the event of a collision of two moving solitons, the transition between the localized Andreev states and the states in the continuum enable the transfer of particles between different eigenstates. These transitions are associated with density and phase oscillations, and lead to emission of sound and loss of energy from the soliton. The same collision is found to be elastic when a purely bosonic density functional theory is used in simulations [236], which confirms the role Andreev states play in the dynamics.

Solitons in the BCS regime are expected to be essentially completely filled in. Indeed, in this limit of long-range Cooper pairs, only a minute fraction of particles near the Fermi surface takes part in pairing, and the reduction of the pairing gap at the soliton affects the density only very weakly. This is the main mechanism that reduces the soliton contrast. The Andreev states also contribute to the filling, but

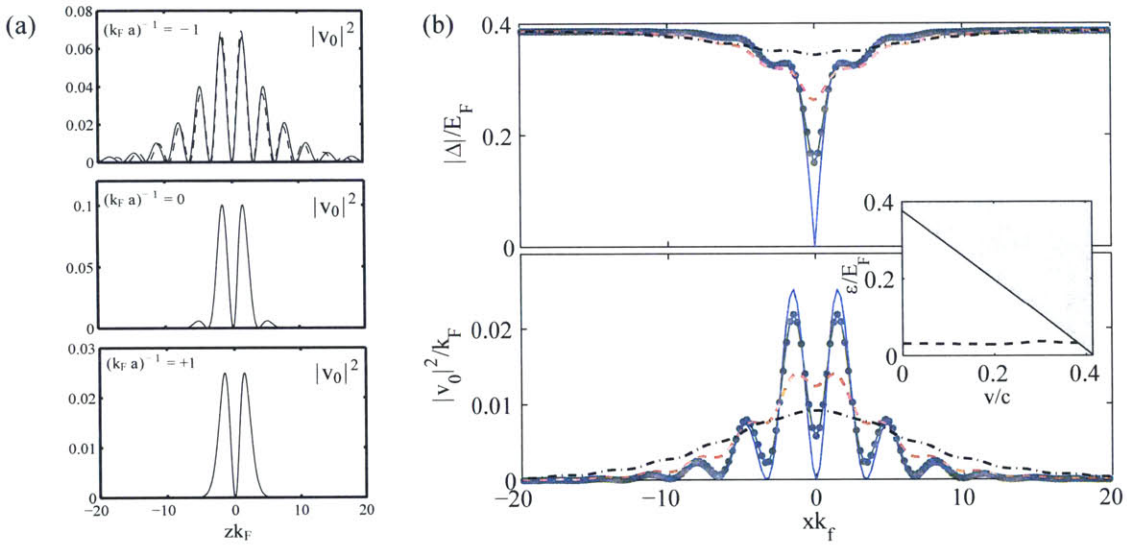

Figure 2-6: Andreev bound states in solitons. (a) Density of the Andreev states, $|v_0|^2$ (solid curves), of a dark (stationary) soliton for $(k_F a)^{-1} = -1$ (top), 0 (middle), and +1 (bottom). Dashed curves in the top panel correspond to ansatz $v_0(z) \sim \sin(k_F z) e^{z/\xi_{\rm BCS}}$, where the BCS coherence length has value $\xi_{\rm BCS} = 10 k_F^{-1}$ at $(k_F a)^{-1} = -1$. The panels are taken from Ref. [7]. (b) Profile of $|\Delta(z)|$ (top panel) and of Andreev states $|v_0(z)|^2$ (bottom panel) of moving solitons. Profiles shown are for $(k_F a)^{-1} = -0.5$ and $v = 0$ (solid blue curve), $0.2c$ (solid green curve with circles), $0.3c$ (dashed red curve), and $0.38c$ (dot-dashed black curve). The figure is taken from Ref. [204]. Inset: the spectrum of energy levels in a homogeneous system containing a soliton for $(k_F a)^{-1} = -0.5$. The solid line shows the gap . The shaded area represents the continuum spectrum for the homogeneous system. The dashed line shows the energy of the Andreev state. When the energy of the Andreev state coincides with the continuum, the Andreev state is no longer bound, and the soliton disappears.

to a smaller degree. As the interactions are tuned from the BCS to the BEC regime, the BdG equations predict a decreasing filling in the density of the soliton [7]. At unitarity, the gas density in the vicinity of the soliton is predicted to be suppressed by 80% of the bulk density, as opposed to 100% for solitons in Bose-Einstein condensates. Here, a substantial part of the soliton filling is due to Andreev bound states.

The BdG equations have been shown to reduce to the Gross-Pitaevskii equation for bosonic molecules in the BEC-limit [214], where stationary solitons are devoid of particles. In the BEC limit, the solution should approach that obtained from solving the GP equation for a gas of bosons with mass $m_B = 2m$ with boson-boson interaction $g_{\mathrm{BB}} = 4\pi\hbar^2 a_{\mathrm{BB}}/m_B$, where a_{BB} is the boson-boson scattering length. The density of the bosonic condensate, $n_B = n/2 = k_F^3/(6\pi^2)$, is once again given by $n_B = n_{B,0}\tanh^2(z/(\sqrt{2}\xi_{\mathrm{BEC}}))$, where the BEC healing length is $\xi_{\mathrm{BEC}} = \hbar/\sqrt{2m_B g_{\mathrm{BB}} n_{B,0}}$. Where $\mu \leq 0$, the single-particle spectrum no longer exhibits a gap at finite k, and hence Andreev states are no longer present to fill the soliton. However, if the interaction is still large, $1/(k_F a) \approx 1$, the uncondensed bosons due to quantum depletion fill the soliton and lead to a decrease in the contrast, as discussed previously.

In the theory of conducting polymers [95], $\Delta(z)$ describes the ion displacement and is a real quantity. This leads to topologically protected solitons. In a superfluid, the superfluid wave function or pairing gap can be complex. The state with a soliton can thus be continuously deformed into the uniform state without a soliton; the soliton is thus not topologically protected. In dimensions higher than 1D, a dark soliton is dynamically unstable, and the soliton can decay via the snake instability [156], the undulation of the soliton plane. A quasi-1D geometry suppresses the dynamical instability. In the absence of the dynamical instability, a soliton can decay via the thermal instability: The scattering of thermal excitations from the soliton reduces its energy, leading the soliton to accelerate towards the speed of sound, eventually losing its contrast and disappearing.

2.6.2 Solitonic vortex

A vortex exists in 2D or 3D, and has a phase winding $\phi = \arctan\left(\frac{y-y_0}{x-x_0}\right)$, where (x_0, y_0) is the location of the vortex. The circulation is quantized,

$$\oint \mathbf{v} \cdot \mathrm{d}\mathbf{l} = l\frac{h}{m_B}, \tag{2.78}$$

where l is an integer. Since the energy of a vortex with multiple quanta of circulation scales as $\sim l^2$, it is energetically favorable to have multiple singly-quantized vortices than to have a single vortex containing multiple quanta.

Writing the condensate wave function as $\psi = \sqrt{n(\rho, z)}e^{i\theta}$, where θ is the polar angle, the GPE leads to an equation for the normalized density $f \equiv \sqrt{n/n_0}$ where n_0 is the asymptotic value for the density:

$$-\frac{1}{x}\frac{d}{dx}\left(x\frac{df}{dx}\right) + \frac{f}{x^2} + f^3 - f = 0, \tag{2.79}$$

where $x = \rho/\xi$. This equation does not have an analytic solution, but it can be solved numerically. An analytic approximation is given by $x/\sqrt{2+x^2}$.

A vortex placed inside a cylindrically shaped superfluid is modified due to the geometry. Such a vortex will align orthogonal to the long axis in order to minimize its energy. In the case where the transverse Thomas-Fermi cloud radius $R_\perp$ is much smaller than the axial radius R_z, a vortex deforms the superfluid phase only in a restricted region of axial extent $\sim R_\perp$ (see Fig. 2-9 (b)). The vortex together with the surrounding flow field thus constitutes an effective particle localized to within $R_\perp \ll R_z$. Its far-field phase profile resembles that of a dark soliton. Significant density depletion exists across the radial direction in the vicinity of the vortex (see Fig. 2-8), reminiscent of the planar depletion of a soliton. Such a vortex is called a solitonic vortex, in reference to its soliton-like properties. In particular, the phase difference across a stationary solitonic vortex in the axial direction is π (modulo 2π), the same as for a stationary dark soliton. A solitonic vortex moving in the axial direction at a critical speed converts into a moving soliton [122]. In the tightly

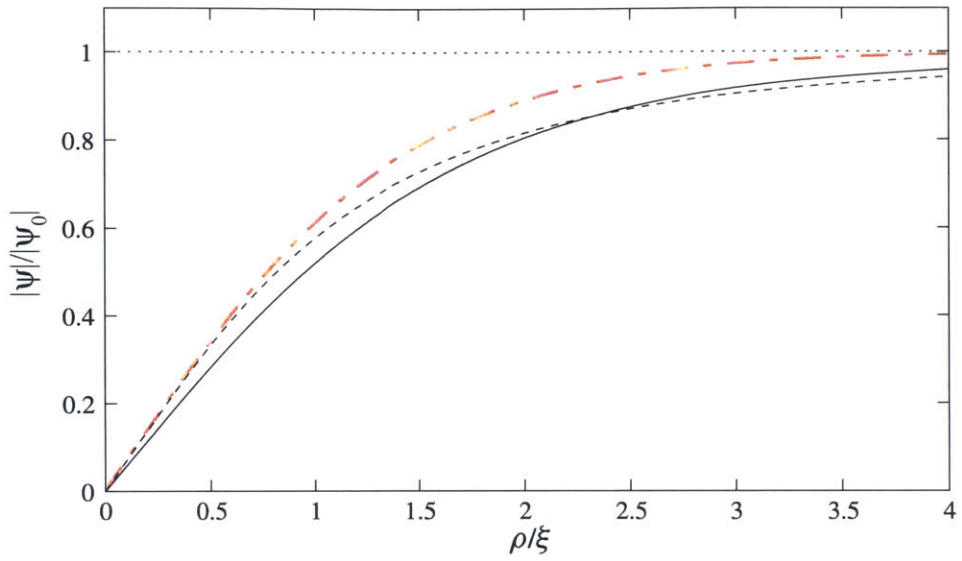

Figure 2-7: The profile of a vortex in a GP condensate. Solid curve: full solution. Black dashed curve: the ansatz $\frac{x}{\sqrt{2+x^2}}$. Red dot-dashed curve: the ansatz $\tanh(x/\sqrt{2})$.

confining limit where $R_\perp$ approaches ξ, the vortex core size, a stationary solitonic vortex becomes energetically degenerate with a dark soliton [25, 122]. In the limit of an isotropic system where $R_\perp \sim R_z$, one recovers a conventional vortex. A solitonic vortex thus represents the link between a planar soliton in 1D and a vortex in 3D.

For a moving solitonic vortex, the far-field phase differs by a value other than π: $\phi(z \to \infty) - \phi(z \to -\infty) = \pi + \Delta\phi$ where $\Delta\phi \neq 0$, just as for a moving soliton. Since the phase necessarily changes by 2π along any contour around the vortex (here we assume the vortex is aligned along the x-axis), the phase has to vary more quickly (or more slowly) on the positive y side of the vortex compared to the negative y side. In other words, the superfluid flow is larger on one side of the vortex. This asymmetry in the flow field leads to an asymmetry in the density distribution, and the vortex itself will be located off-center (see Fig. 2-8). For such a vortex in a trapped superfluid, the vortex experiences a restoring force towards the center of the cloud due to the trapping potential. At the same time, a moving vortex experiences the Magnus force due to its gyroscopic nature. A stable orbit is realized when the Magnus force balances the restoring force. Therefore, an off-center vortex will precess along an equipotential

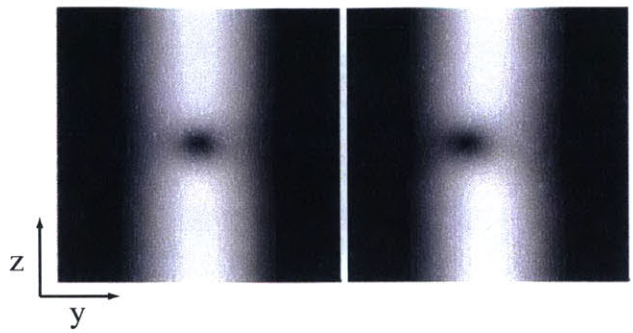

Figure 2-8: The density profile of a solitonic vortex in an infinite cylinder as computed from GPE. Left: a stationary vortex. Right: a vortex moving in the positive z direction. The figures are taken from Ref. [122].

contour [142, 75].

Similar to a soliton, a vortex is also expected to be filled as one moves from the weakly-interacting BEC regime along the BEC-BCS crossover. The filling in the BEC regime is due to uncondensed particles coming from quantum depletion, while at unitarity and on the BCS side, the filling is mostly due to uncondensed fermions and partially due to the Andreev bound states [40].

2.6.3 Vortex ring

Simply speaking, a vortex ring is a vortex line wrapped in a toroidal shape. It is found prominently in turbulent flow of classical fluids [130, 195]. In the context of quantum fluids, it has been observed in liquid Helium [185] and in BECs [4, 19]. If one considers a vortex to be a line current whose magnetic field is analogous to the flow field of the vortex, then a vortex ring can be compared to a magnetic dipole, and its flow field is a dipole field. Therefore, unlike the soliton and the solitonic vortex, a stationary vortex ring has no phase difference across it - the far-field superfluid flow points in the same direction on either side of the vortex ring. Similar to a solitonic vortex, the flow field of a vortex ring in an elongated superfluid has the variation of its phase profile localized within a volume defined by $R_\perp$.

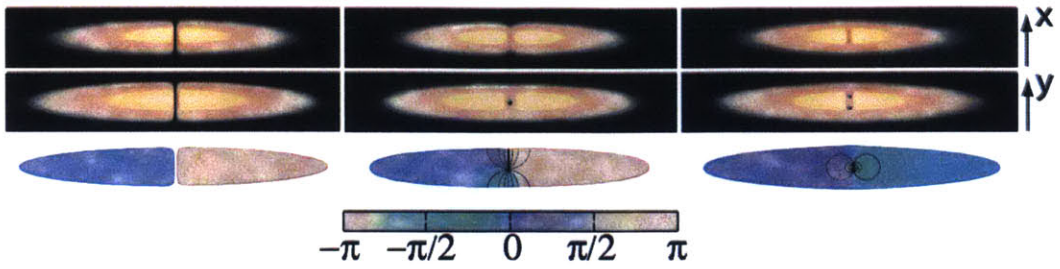

Figure 2-9: Examples of solitary waves in 3D Bose-Einstein condensates. Shown are simulated column density profiles in the $(z-x)$ plane (upper row), the local density of the cloud in a central layer in the $(z-y)$ plane (middle row) and the phase (lower row) for a soliton (left), a solitonic vortex (center) and a vortex ring (right). The images correspond to $\mu/\hbar\omega_\perp$ =7.31, 7.14, and 10.66. This figure is taken from [127].

2.6.4 Chladni solitons

Besides planar solitons, solitonic vortices, and vortex rings, excitations that are composed of intersecting rings and lines are generally possible within an elongated superfluid, as found in Ref. [155]. These objects trace the nodal lines of unstable vibrational modes of a planar soliton, in analogy to Chladni's figures of membrane vibrations.

2.7 Motion of solitonic excitations along a harmonic trap

The form of Eq. 2.75 suggests that for a weakly-interacting BEC placed inside a harmonic trap where the potential on individual bosons is given by $V(z) = \frac{1}{2}m_B\omega_z^2 z^2$, a soliton would undergo oscillations: if the potential varies slowly enough, the local density approximation (LDA) allows one to replace μ with $\mu - \frac{1}{2}m_B\omega_z^2 z^2$, and one obtains $E_S/\mathcal{A} = \frac{4}{3\sqrt{m_B g}}(\mu - \frac{1}{2}m_B\omega_z^2 z_S^2 - m_B v_S^2)^{3/2}$. Since energy is conserved, the quanity $\frac{1}{2}m_B\omega_z^2 z_S^2 - m_B v_S^2$ is conserved. This means that the motion of a soliton is the same as that of a particle of kinetic (or inertial) mass of $2m_B$, experiencing a trapping frequency of $\omega_z/\sqrt{2}$.

In general, the motion of a solitonic excitation will manifest in the difference between its bare mass - the mass of the missing particles, also called the gravitational

mass - and the inertial mass - the mass responsible for the kinetic energy, also called the effective mass.

The force on a solitonic excitation is provided by the trapping force experienced by the atoms missing in the defect, $N_s m\omega_z^2 z \equiv M\omega_z^2 z$, where $|N_s|$ is the number of missing atoms, and $M = N_s m < 0$ the bare mass of the soliton. It is negative as the soliton is a density depletion. Introducing the inertial mass of the soliton M^*, this force causes an acceleration $\ddot{z} = -\frac{M}{M^*}\omega_z^2 z$. One then obtains a direct relation [203] between the relative effective mass M^*/M and the ratio between the soliton period T and the period of a bare particle T_z:

$$\frac{M^*}{M} = \left(\frac{T}{T_z}\right)^2 \tag{2.80}$$

Therefore, the measurement of a defect's oscillation period would allow one to obtain the ratio between the inertial and the gravitational mass. The sign of the inertial mass M^* is expected to also be negative. This implies that a solitonic excitation is an effective particle that decreases its kinetic energy as it speeds up.

The above analysis is valid for small-amplitude oscillations. In the case where the oscillation explores significantlly different local chemical potentials, the varying of M^* and M means that the oscillation may be no longer harmonic. However, for the most part, the change of M^* and M with the local chemical potential cancels, so M^*/M is nearly constant throughout the superfluid. Indeed, in our experiment, we do not to resolve an anharmonicity in the trajectory of the vortex precession, and hence the change in the masses in an oscillation across the cloud is not relevant.

Chapter 3

The ultracold Fermi gas apparatus

The experiments reported in this thesis were performed in a dual-species ^{23}Na-^{6}Li apparatus. The experimental setup consists of a vacuum chamber in which the quantum degenerate gases are created, the laser systems necessary for the trapping, cooling, and control of the atoms, and the supporting electronics and computer control system. A detailed description of this machine can be found in several previous theses. The theses [215, 47] of D. M. Stamper-Kurn and A. Chikkatur provide a detailed description on the ^{23}Na BEC apparatus. The double-species oven is described in detail in the thesis of C. Stan [216]. The coils are described in the diploma thesis of C. Schunck [202]. The laser system for ^{6}Li is described in M. Zwierlein's diploma thesis [247]. The procedure of generating degenerate Fermi gases is described in the theses of Z. Hadzibabic and M. Zwierlein [88, 248]. Here, I give a brief overview of the production of ultracold Fermi gases of ^{6}Li with tunable interactions in the current experimental setup.

Fig. 3-1 shows a schematic of the vacuum system in which the quantum degenerate gas is created. Two pairs of coils (which can be in either a Helmholtz or an anti-Helmholtz configuration) and one pair of cloverleaf coils oriented along the z-axis provides the magnetic field necessary for the magneto-optical trap (MOT), the magnetic confinement for a Ioffe-Pritchard trap, and the Feshbach field. The source of atoms is a dual-species oven, not shown in the figure. The molten sodium and lithium in the oven generate hot vapors that form the atomic beams which travel

through the Zeeman slower. The atomic beam is slowed by laser light along the Zeeman slower as it travels into the main chamber, which is held under ultra-high vacuum (UHV). Both the sodium and lithium atoms are collected and cooled simultaneously in a two-species MOT for a few seconds. Then, the laser light for the MOT is switched off, and the atoms are optically pumped into the stretched hyperfine states, $|F = \frac{3}{2}, m_F = \frac{3}{2}\rangle$ for ^{6}Li and $|F = 2, m_F = 2\rangle$ for ^{23}Na, which are low-field seeking states and are thus magnetically trappable. A weak bias field is turned on during this step to set the quantization axis for the optical pumping. Once the atoms are in their respective stretched states, a Ioffe-Pritchard magnetic trap is turned on. A spin-polarized Fermi gas is non-interacting and hence direct evaporation is not possible. Therefore, the lithium cloud is sympathetically cooled by a forced evaporation of the sodium atoms using a microwave field to transfer the hot (and hence energetic) sodium atoms to the untrapped $|F = 1, m_F = 1\rangle$ state. Sympathetic cooling is what enables the production of large and cold clouds of fermions. Without the lithium atoms, we are able to generate a ^{23}Na BEC of about 10^7 atoms. To generate a cloud of degenerate fermions, we completely evaporate the sodium atoms, after which we are left with a spin-polarized degenerate Fermi gas of about 20 million lithium atoms in the magnetic trap.

The experiments reported in this thesis are performed with the lithium atoms in the lowest two hyperfine states, which we label as $|1\rangle \equiv |F = \frac{1}{2}, m_F = \frac{1}{2}\rangle$ and $|2\rangle \equiv |F = \frac{1}{2}, m_F = -\frac{1}{2}\rangle$. Since these states are high-field seeking at $500\,\mathrm{G} < B$ where interacting mixtures are prepared and studied, they cannot be trapped by a magnetic field alone. Therefore, before converting the spin-polarized gas into a spin-mixture, we turn on an optical dipole trap (ODT) which provides confinement in the radial ρ-direction, and we simultaneously turn off the cloverleaf coil. At this point, the gas is trapped in the z-direction by a residual magnetic curvature[1] from the pair of Helmholtz coils, and in the radial direction by the ODT.

A microwave sweep transfers the atoms from $|F = \frac{3}{2}, m_F = \frac{3}{2}\rangle$ into the state $|1\rangle$. At this point, the magnetic field profile is anti-trapping in the axial direction for state

[1]The magnetic field curvature is confining in the z-direction, but anti-confining in the ρ-direction.

$|1\rangle$, so the direction of the bias field (which points along the z direction) is quickly reversed in order to give the axial curvature a negative sign, and hence allows high-field seekers to be trapped again. This procedure also reverses the quantization axis - a detail that is important for imaging and optical pumping along the side imaging path (see Fig. 3-1) at high fields. The field is also brought close to the Feshbach resonance near $\sim 830\,\mathrm{G}$. A radio-frequency sweep, with the help of decoherence introduced by the inhomogeneous magnetic field, then generates a mixture of $|1\rangle$ and $|2\rangle$.

The preparatory procedure described here is standard for all the experiments reported in this thesis. After a mixture is generated, we have a variety of tools to tune, perturb, and perform measurements. A magnetic Feshbach resonance allows oen to tune the interaction strength. The temperature and also the atom number of the cloud can be controlled with a forced evaporation of the mixture by lowering the trap depth of the ODT. The aspect ratio of the cloud can be tuned by adjusting the strength of the magnetic curvature. Typically, a cloud with condensed fermions contains between 500 thousands and a million pairs. The coldest temperature we can reach is about $0.05T_F$.

3.1 Confinement of the quantum degenerate lithium gas near a Feshbach resonance

As mentioned above, the lowest two hyperfine states used in an interacting Fermi gas experiment cannot be trapped by the magnetic field alone. Therefore, after we have created a spin mixture and have moved into the high-field regime of the experiment ($B > 600\,\mathrm{G}$), we use a hybrid confinement for the Fermi gas.

Two separated pairs of coils in the Helmholtz configuration allow for the independent tuning of both the bias field which tunes the interaction, and the field curvature which controls the axial confinement. To leading order, the magnitude of the magnetic

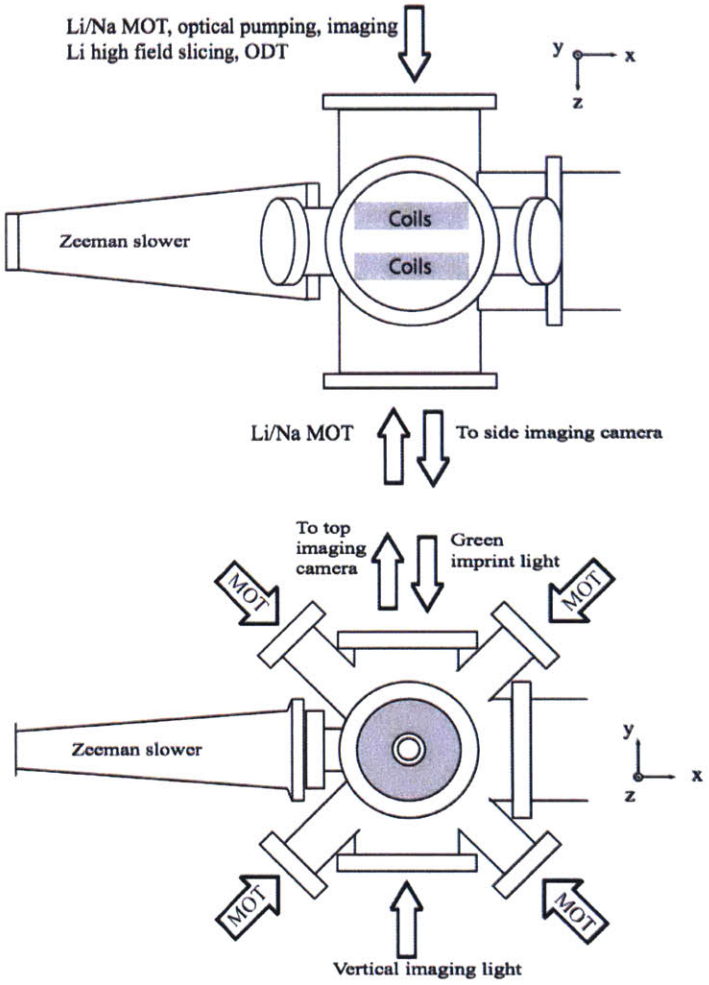

Figure 3-1: Schematics of the vacuum chamber used for the ultracold Fermi gas experiments reported in this thesis.

field has the form

$$B = B_0 + \frac{1}{2}B''\left(z^2 - \frac{1}{2}\rho^2\right) . \tag{3.1}$$

In the adiabatic approxiation, the magnetic moment of the atoms adiabatically follows the magnetic field, so the energy of the atom in the field is given by $g_J\mu_B m_J|B|$, where g_J is the g-factor of the atomic level, μ_B is the Bohr magneton, and m_J is the projection of the electronic angular momentum. Therefore, the potential due to the magnetic field is proportional to the magnitude of the field. Thus, the magnetic coils alone provide confinement in the z-direction and an anti-confinement in the radial direction. We use an ODT pointing along the z-direction to provide radial confinement. The ODT is generated by an infrared Gaussian beam at 1064 nm focused to a waist of $W = 120\,\mu$m. The potential of the ODT has the form

$$V_{\mathrm{ODT}} = -\alpha_{\mathrm{pol}}\frac{\mathcal{P}}{\frac{\pi}{2}W^2}e^{-2\rho^2/W^2} . \tag{3.2}$$

where $\alpha_{\mathrm{pol}} = h \times (0.00127\,\mathrm{s}^2/\mathrm{kg})$ is the polarizability of ^{6}Li at 1064 nm, with h the Planck constant, and $\mathcal{P}$ is the power of the beam. The depth of the ODT is given by $U_0 = \alpha_{\mathrm{pol}}\frac{\mathcal{P}}{\frac{\pi}{2}W^2}$. Due to the large Rayleigh range $\sim 1\,$mm, we can safely neglect the 0.01% contribution to the axial trapping frequency from the variation of the laser power along the z-direction. Therefore, the combined trapping potential has the form

$$V = \frac{1}{2}m\omega_z^2 z^2 - \frac{1}{4}m\omega_z^2\rho^2 - U_0 e^{-2\rho^2/W^2} . \tag{3.3}$$

Forced evaporation on the mixture is performed by lowering the trap depth of the ODT, which allows the energetic atoms to spill out in the radial direction.

Near the center of the trap, one can expand the Gaussian to obtain the harmonic approximation

$$V = \frac{1}{2}m\omega_z^2 z^2 + \frac{1}{2}m\omega_\rho^2\rho^2 , \tag{3.4}$$

where $\omega_\rho = \sqrt{\frac{4U_0}{mW^2} - \frac{1}{2}\omega_z^2}$. This is valid for small filling $\mu \ll U_0$.

To modify the aspect ratio, one can either vary the trap depth or the magnetic cur-

vature (characterized by ω_z). The two pairs of Helmholtz coils allow for independent tuning of the Feshbach field B_0 and the curvature ω_z.

3.2 Imaging paths

Information about the atomic gas is obtained by sending laser light through the gas and recording a 2D image of the transmitted light intensity on a CCD camera. For the experiments reported in this thesis, absorption imaging is used. The scattering rate of an optical transition is given by

$$R = \frac{\Gamma}{2} \frac{I/(\alpha_I I_{\text{sat}})}{1 + (2\delta/\Gamma)^2 + I/(\alpha_I I_{\text{sat}})} . \tag{3.5}$$

The factor of α_I accounts for how much light intensity an atom actually experiences. In the case where the imaging light has the correct circular polarization for the σ_- transition, $\alpha_I = 1$, whereas for linearly polarized light used to image on a σ_- transition along the vertical imaging path, $\alpha_I = 2$.

The absorption cross section is given by

$$\sigma = \frac{\hbar\omega}{I} R = \frac{\sigma_0}{\alpha_I} \frac{1}{1 + (2\delta/\Gamma)^2 + I/(\alpha_I I_{\text{sat}})} , \tag{3.6}$$

where $\sigma_0 = 6\pi(\lambda/(2\pi))^2$ is the resonant absorption cross section, and ω is the frequency of the imaging light. For an imaging light propagating along the x-direction through an atomic cloud with a density distribution n, the attenuation of the intensity is given by the Beer-Lambert law,

$$\frac{dI}{dx} = -\sigma I n = -\frac{\sigma_0}{\alpha_I} \frac{I}{1 + (2\delta/\Gamma)^2 + I/(\alpha_I I)} n . \tag{3.7}$$

The absorption profile I on resonance $\delta = 0$ is obtained by solving this differential equation [189]:

$$\frac{\sigma_0}{\alpha_I} \int \mathrm{d}x\, n = -\ln\left(\frac{I}{I_0}\right) + \frac{I_0}{\alpha_I I_{\text{sat}}} \left(1 - \frac{I}{I_0}\right) , \tag{3.8}$$

where $\int \mathrm{d}x\, n$ is the once-integrated column density. The typical expression for the

absorption profile in the low-intensity limit is given by

$$I = I_0 e^{-\frac{\sigma_0}{\alpha_I}\int \mathrm{d}x\, n}. \tag{3.9}$$

We measure I/I_0 by taking three succsesive images: one frame which probes with atoms (PWA), one frame which probes without atoms (PWOA) taken after the atoms are released, and a frame of dark field (DF) taken with the camera shutter closed. A normalized intensity profile $\tilde{I} \equiv I/I_0 = \frac{\mathrm{PWA-DF}}{\mathrm{PWOA-DF}}$ is then generated from these three frames. Resonant imaging light heats the atoms, so the imaging is destructive. Each frame is separated by ~ 1 s due to the download time required by the camera. Since we are interested in taking low-noise, high-quality images of the cloud for the experiments reported in this thesis, and since imaging multiple spin-states simultaneously is not necessary, we do not make use of the fast kinetic mode available on some cameras.

We choose the duration and the intensity of the pulse to obtain an optimal balance between increasing the signal-to-noise ratio and reducing the non-linearity in the image due to saturation. Reducing the intensity lowers the non-linearity but also increases the photon-shot noise. This shot noise can be alleviated by increasing the imaging pulse duration. However, during a prolonged imaging pulse, the atomic resonance may change due to the Doppler-shift coming from the photon recoil (which is especially pronounced for lithium atoms due to the small atomic mass). Therefore, a compromise must be made. For the equation of state measurement reported in Chapter 4, we use a fast, low-intensity imaging pulse with $I/I_0 = 0.07$ and $4\,\mu$s pulse time. In the same chapter, the effects of the Doppler-shift and the non-linearity are discussed in details. For the other experiments, we use a $10\,\mu$s pulse of $I/I_0 \approx 0.1$ to reduce the intensity noise.

Two imaging systems exist in our experimental setup: a side imaging system in which the imaging light propagates along the z-direction, and a vertical (top) imaging system in which the imaging light propagates along the y-direction. Each imaging system consists of one or more lens pairs that form an image on the plane of the CCD camera. The side imaging system has a resolution of $\sim 10\,\mu$m. The top imaging

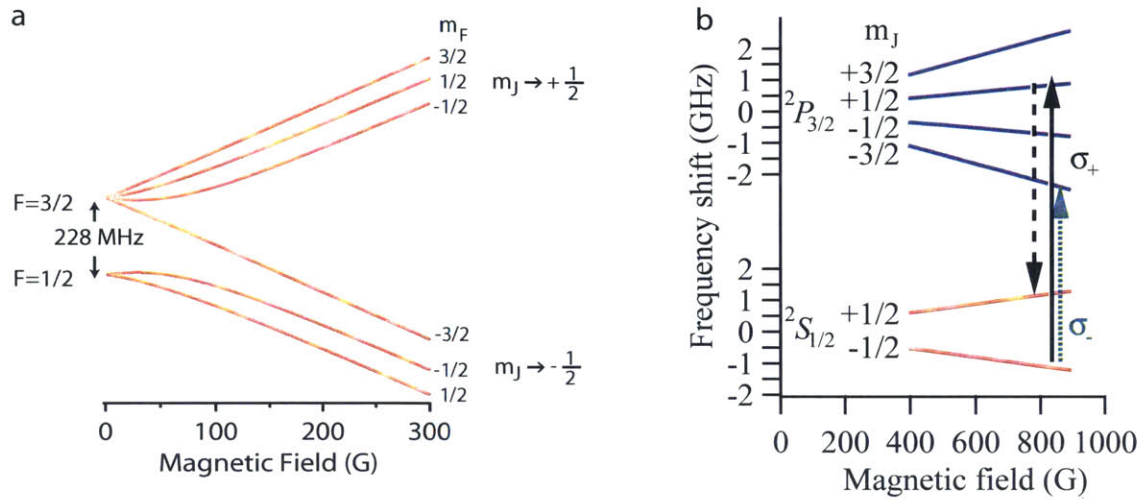

Figure 3-2: Energy levels of ^{6}Li. (a)Energy levels of the ground state manifold at low-fields. (b) Energy levels of the ground state manifold $^2S_{1/2}$ and $^2P_{3/2}$ at high fields, making use of the approximation that at high fields, the levels are dominated by the electronic Zeeman energy $\mu_B g_J m_J B/\hbar$. For $^2S_{1/2}$, $g_J = 2.0023$, and for $^2P_{3/2}$, $g_J = 1.335$. The σ_- cyclic transition for imaging is indicated with the green dashed arrow. The σ_+ pumping transition at high fields, used for tomographic imaging, is indicated by the black solid line (and the decay path to the ground state is indicated by the black dashed arrow).

system has a resolution of $2\,\mu$m. Because of the higher resolution and the smaller optical density (the in-situ atomic image as recorded from the side imaging system is typically too dark to give useful information), the top imaging system is the preferred imaging axis. The majority of the images taken for the experiments reported in this theis are taken along this axis. Since at high fields, the atomic levels are dominated by the electronic spin, both $|1\rangle$ and $|2\rangle$ act as if they were essentially in the $m_J = -1/2$ electronic state. The appropriate transition for imaging is the σ_- cylcing transition to the $|^3P_{3/2},\, m_J = -3/2\rangle$ level.

At low fields, the optical pumping makes uses of σ_+ light, and a $\lambda/4$ waveplate (the same one used for one arm of the MOT) sets the correct polarization. At high fields, the quantization axis is flipped. Luckily, it means that on the side imaging, the high-field imaging light (combined in the path with a polazring beam-splitter)

automatically has σ_- polarization. For the vertical imaging, the imaging beam sent into the chamber has a linear polarization oriented along the x-axis. The projection along the quantization (z) axis effectively leads to half of the light having σ_- polarization which can excite the cycling transition. By placing a $\lambda/2$ waveplate before the chamber, one can tune the detected atom number from zero (corresponding to a complete linear polarization along the z) to the maximal number with a period of 90° on the waveplate, and hence 180° in the polarization.

For the tomographic imaging technique introduced in Chapter 6, the optical pumping at high fields requires σ_+ polarization. As a result, a $\lambda/2$ waveplate is brought into the path of the pumping and side imaging beams via a mechanical flipper mount during the imaging stage. As a result, the cyclic imaging along the z-direction is lost. The pumping light itself provides some imaging capacity, albeit one with much lower quality.

Chapter 4

Thermodynamics of a strongly interacting Fermi gas

4.1 Introduction

A central subject in the study of the strongly interacting Fermi gas is the knowledge of its thermodynamics. A thermodynamic equation of state (EoS) is a relation between thermodynamic variables and encodes all the global information of a system at equilibrium. The information of the phase diagram is contained in the EoS. An experimentally measured EoS thus provides a platform where theories can be compared. The knowledge of the EoS is also immensely useful for experiments because it provides a way to perform thermometry.

Even before the experimental creation of the first degenerate Fermi gases of atoms, the thermodynamics of strongly interacting Fermi gases have been of great interest to nuclear theorists. They have used the unitary Fermi gas - spin-1/2 fermions with short-range interaction characterized by infinite scattering length - as a model of the crust of neutron stars. In this context, G. Bertsch presented the following question [23]: What is the ground state energy of the unitary Fermi gas[1]? As discussed in 2.4.2, scale invariance of the unitary Fermi gas implies that at $T = 0$, the energy

[1]The precise wording is: What are the ground state properties of the many-body system composed of spin-1/2 fermions interacting via a zero-range, infinite scattering length contact interaction?

is proportional to the non-interacting energy at the same density n, up to a universal constant,

$$E = \xi_B \frac{3}{5} N E_F \,. \tag{4.1}$$

Here, $E_F = \frac{\hbar^2 k_F^2}{2m}$ is the Fermi energy, with the Fermi wave vector $k_F = (3\pi^2 n)^{1/3}$. The constant ξ_B has been referred to as the Bertsch paramaeter[2]. The value of ξ_B has been subject to extensive theoretical and experimental investigations.

At high temperatures, where kinetic energy dominates, the equation of state of any gaseous system[3] is described by the ideal gas law $P = nk_BT$. As the temperature is lowered, the strongly interacting Fermi gas is expected to undergo a phase transition into the superfluid phase, whose existence is established by the observation of vortex lattices [249]. Near the phase transition, many systems exhibit critical behaviors, reflected by singularities in thermodynamic quantities. For examples, at a ferromagnetic transition, the magnetic susceptibility diverges, and at the superconducting and superfluid transitions, the specific heat exhibits a jump [223] and a cusp [230] respectively. The latter is experimentally observed in ^{4}He as the famous λ-peak [139]. In the Bardeen-Cooper-Schrieffer (BCS) theory, $T_c/T_F = 0.61e^{-\pi/(2|a|k_F)}$, and hence for weak interactions, the critical temperature is suppressed. In a typical superconductor, $T_c/T_F \approx 10^{-4}$. If one naively takes $1/(k_F|a|) = 0$, one gets $T_c/T_F = 0.61$ according to this model. The expectation is that due to strong interactions, the critical temperature T_c of the unitary Fermi gas is expected to be large, comparable to the Fermi temperature.

Above the critical temperature, the strong interaction is expected to lead to interesting physics in the normal phase. It is possible that even though the interaction is strong, the normal phase can be modeled by the Landau liquid theory, in which the particles, dressed by interactions, act as free particles with a renormalized energy and effective mass. The signature of a Landau Fermi liquid may be observed in the thermodynamics. However, the normal phase above the transition point is not highly

[2]At the time, the sign of ξ_B was not even known. A question contained in Bertsch's challenge is whether the system is stable (i.e. what is the sign of ξ_B). G.A. Baker won the $600 prize for his work, establishing the stability of the system in Phys. Rev. C **60**, 064901 (1999).

[3]Here I assume the system does not form a plasma.

degenerate, and it is questionable whether one can even talk about a Fermi liquid at such temperatures.

Another information of interest is the existence of pre-formed pairs in the normal phase. In the BCS limit, pairing and condensation happens at the same point. In the BEC limit, the spin up and spin down particles form bound molecules at a much higher temperature compared to the condensation temperature. At the crossover, one still expects that there is a window in the phase diagram in which one finds uncondensed pairs. This regime is also called the pseudogap, in analogy to the pseudogap in high-T_c superconductors which is conjectued to be related to uncondensed Cooper pairs. The existence of the pseudogap in a strongly interacting Fermi gas may leave a detectable signature in the thermodynamics.

In this chapter, I discuss the work at MIT to measure the equation of state of a strongly interacting Fermi gas, as reported in Refs. [226] and [129]. I will start with a review of thermodynamics. Then I will describe the details of the experimental measurement. In the subsequent sections, I will discuss the results.

4.2 Review of thermodynamics

4.2.1 General thermodynamics relations and the forms of the EoS

In general, the EoS can be expressed in multiple forms, each describing a relation between different combinations of thermodynamic variables. However, we can use basic thermodynamics to get a sense of the form of the EoS that is easiest to measure experimentally. Our aim is to measure the EoS of a unitary Fermi gas in a homogeneous system. Therefore, we will set $\mathcal{V}$, $N \to \infty$, with $n = N/\mathcal{V}$. We will also consider the EoS in terms of intensive quantities. Therefore, extensive quantities such as the energy will be scaled by either the particle number N or the volume $\mathcal{V}$.

Let us consider the grand potential

$$\Omega = E - TS - \mu N\,, \tag{4.2}$$

$$\mathrm{d}\Omega = -S\mathrm{d}T - P\mathrm{d}\mathcal{V} - N\mathrm{d}\mu\,. \tag{4.3}$$

The natural variables for the grand potential are T, $\mathcal{V}$, and μ, and among them, only $\mathcal{V}$ is extensive. The grand potential itself is extensive. Therefore, in a homogeneous system, if one scales the volume by $\mathcal{V} \to \eta\mathcal{V}$, the grand potential is also scaled by the same factor, $\Omega \to \eta\Omega$. This gives the scaling relation $\Omega(T, \eta\mathcal{V}, \mu) = \eta\Omega(T, \mathcal{V}, \mu)$. Euler's homogeneous function theorem[4] then leads to $\mathcal{V}\left(\frac{\partial\Omega}{\partial\mathcal{V}}\right)_{T,\mu} = \Omega$, and hence we arrive at the following important result for the grand potential:

$$\Omega = -P\mathcal{V}\,, \tag{4.4}$$

and hence $\mathrm{d}\Omega = -P\mathrm{d}\mathcal{V} - \mathcal{V}\mathrm{d}P$. We then have the Gibbs-Duhem relation

$$\mathrm{d}P = \frac{S}{\mathcal{V}}\mathrm{d}T - n\mathrm{d}\mu\,. \tag{4.5}$$

Therefore, a natural form of the EoS is the pressure equation of state

$$P = P(\mu, T)\,. \tag{4.6}$$

Following Eq. 4.5, another natural form of the EoS is the density equation of state

$$n = \left(\frac{\partial}{\partial\mu}P(\mu, T)\right)_T = n(\mu, T)\,. \tag{4.7}$$

From 2.4.2, we know that the EoS of the unitary Fermi gas can be cast in terms of universal functions of dimensionless quantities. To write the pressure and the density equation of state in terms of dimensionless quantities, we normalize P, n, and μ by

[4]Euler's homogeneous function theorem states that $f(\eta x) = \eta^\gamma f(x) \to xf'(x) = \gamma f(x)$.

the temperature to arrive at the following universal form,

$$\beta\lambda^3 P = f_P(\beta\mu)\,, \tag{4.8}$$

$$n\lambda^3 = f_n(\beta\mu) = \frac{df_P(\beta\mu)}{d(\beta\mu)}\,, \tag{4.9}$$

where $\lambda = \sqrt{\frac{2\pi\hbar^2}{mk_BT}}$ is the thermal de Broglie wavelength. We note the quantity $n\lambda^3$ is the phase space density. At high temperatures, these two universal functions admit the virial expansions in terms of the fugacity $e^{\beta\mu}$:

$$f_P(\beta\mu) = 2\left(e^{\beta\mu} + b_2e^{2\beta\mu} + b_3e^{3\beta\mu}...\right)\,, \tag{4.10}$$

$$f_n(\beta\mu) = 2\left(e^{\beta\mu} + 2b_2e^{2\beta\mu} + 3b_3e^{3\beta\mu}...\right)\,. \tag{4.11}$$

At $T = 0$, Eq. 4.1 indicates that the chemical potential $\mu = \left(\frac{\partial E}{\partial N}\right)_{\mathcal{V}}$ is given by $\mu = \xi_B E_F$. Therefore, f_P and f_n have the following limit as $\beta\mu \to \infty$:

$$f_n(\beta\mu) \to \frac{1}{3\pi^2}\left(\frac{4\pi\beta\mu}{\xi_B}\right)^{3/2}\,, \tag{4.12}$$

$$f_P(\beta\mu) \to \frac{1}{30\pi^2}\frac{(4\pi\beta\mu)^{5/2}}{\xi_B^{3/2}}\,. \tag{4.13}$$

We note that for the density equation of state Eq. 4.7, we can also normalize the chemical potential and the temperature by the Fermi energy and the Fermi temperature $T_F = E_F/k_B$ to obtain the temperature-dependence for the chemical potential,

$$\frac{\mu}{E_F} = \tilde{\mu}\left(\frac{T}{T_F}\right)\,, \tag{4.14}$$

where $\tilde{\mu}$ is a universal function that depends on T/T_F.

Let us then consider the Helmholtz free energy

$$F = E - TS = \Omega + \mu N\,, \tag{4.15}$$

$$\mathrm{d}F = -S\mathrm{d}T - P\mathrm{d}\mathcal{V} + \mu\mathrm{d}N\,. \tag{4.16}$$

Since $n = N/\mathcal{V}$, we have $\mathrm{d}N = \mathcal{V}\mathrm{d}n$ while keeping $\mathcal{V}$ fixed, and $\mathrm{d}\mathcal{V} = -(N/n^2)\mathrm{d}n = -(\mathcal{V}/n)\mathrm{d}n$ while keeping N fixed. If we consider keeping N fixed (and hence $\mathcal{V}$ controls the density), then we have $\mathrm{d}\left(\frac{F}{\mathcal{V}}\right) = -\frac{S}{\mathcal{V}}\mathrm{d}T + \frac{P}{n}\mathrm{d}n$. Thus we see the free energy per volume $\mathcal{F} = F/\mathcal{V}$ is a function of n and T,

$$\mathcal{F} = \mathcal{F}(n, T)\,. \tag{4.17}$$

Since $P = -\left(\frac{\partial F}{\partial \mathcal{V}}\right)_{T,N} = n\left(\frac{\partial \mathcal{F}}{\partial n}\right)_T$, we have another form of the pressure equation of state

$$P = n\left(\frac{\partial \mathcal{F}}{\partial n}\right)_T = P(n, T)\,. \tag{4.18}$$

We normalize the free energy and the temperature by the density to obtain the universal form

$$\frac{F}{\frac{3}{5}\mathcal{V}nE_F} = \tilde{F}\left(\frac{T}{T_F}\right) \tag{4.19}$$

$$\frac{P}{\frac{2}{5}nE_F} = \tilde{p}\left(\frac{T}{T_F}\right)\,. \tag{4.20}$$

Further differentiating with respect to the volume gives the compressibility as a function of the density and the temperature,

$$\kappa \equiv -\frac{1}{\mathcal{V}}\left(\frac{\partial \mathcal{V}}{\partial P}\right)_T = -\frac{1}{\mathcal{V}}\left(\frac{\partial P}{\partial \mathcal{V}}\right)_T^{-1} = \frac{1}{n}\left(\frac{\partial P}{\partial n}\right)_T^{-1} = \kappa(n, T)\,. \tag{4.21}$$

Normalizing by the density gives the universal form

$$\frac{\kappa}{\frac{3}{2nE_F}} = \tilde{\kappa}\left(\frac{T}{T_F}\right)\,. \tag{4.22}$$

One can express the compresibility in terms of the density and the pressure to obtain

$$\kappa = \kappa(n, P)\,, \tilde{\kappa} = \tilde{\kappa}(\tilde{p})\,. \tag{4.23}$$

This compressibility equation of state is the starting point for a method to obtain the

equation of state without any fits, which I will discuss in 4.9.

An expression that is convenient for experimentally measuring the compressibility can be obtained as follows: since one can write $P = P(\mu, T)$ and $n = n(\mu, T)$, we can re-express $\partial P/\partial\mu$ in terms of derivatives with respect to μ at fixed T,

$$\kappa = \frac{1}{n}\left(\frac{\partial P/\partial\mu}{\partial n/\partial\mu}\right)^{-1}_{T} = \frac{1}{n^2}\left(\frac{\partial n}{\partial\mu}\right)_{T}. \tag{4.24}$$

Generally, the most common ways to parametrize the temperature dependence is via one of the following two dimensionless quantities formed by normalizing T by an intensive energy scale: T/T_F or $\beta\mu$, where $\beta = 1/(k_B T)$. The latter is also the natural logarithm of fugacity $e^{\beta\mu}$.

Here, I also derive an important relation for scale invariant systems. Recall from Eq. 2.33 that scale invariance implies the following scaling relation for the free energy density: $\mathcal{F}(n/\eta^3, T/\eta^2) = \mathcal{F}(n,T)/\eta^5$. Note that this scaling relation was considered in the case of constant volume. Differentiating with respect to η and setting $\eta = 1$ gives $3n\left(\frac{\partial\mathcal{F}}{\partial n}\right)_{\mathcal{V}} + 2T\left(\frac{\partial\mathcal{F}}{\partial T}\right)_{\mathcal{V}} = 5\mathcal{F}$ and hence $3\mu N - 2TS = 5F$. Making use of $F = E - TS = \Omega + \mu N$ and $\Omega = -PV$, we arrive at the following relation for scale invariant systems:

$$E = \frac{3}{2}P\mathcal{V}. \tag{4.25}$$

4.2.2 Non-interacting Fermi gas

Recall from Section 2.2, the density of the ideal Fermi gas is given by the polylogarithm function (see Eq. 2.4 and 2.5). The density and the pressure equation of state of the ideal Fermi gas is then given by the universal functions

$$f_{n_0}(\beta\mu) = \lambda^3 n_0(T,\mu) = -2\mathrm{Li}_{3/2}(-e^{\beta\mu}) = -2\sum_{k=1}^{\infty}\frac{(-e^{k\beta\mu})}{k^{3/2}} \tag{4.26}$$

and

$$f_{P_0}(\beta\mu) = \beta\lambda^3 P_0(T,\mu) = -2\mathrm{Li}_{5/2}(-e^{\beta\mu}) = -2\sum_{k=1}^{\infty}\frac{(-e^{k\beta\mu})}{k^{5/2}}. \tag{4.27}$$

There is an additional factor of two compared to Eqs. 2.4 and 2.5 because here we are considering a two-component non-interacting gas. In the high temperature limit $\beta\mu \to -\infty$, we recover the Boltzmann gas, whose equation of state is

$$n = 2\lambda^{-3}e^{\beta\mu}, \tag{4.28}$$

$$P = \left(\frac{\partial P}{\partial \mu}\right)_T = 2k_BT\lambda^{-3}e^{\beta\mu}, \tag{4.29}$$

and the ideal gas law

$$P = nk_BT. \tag{4.30}$$

Since the non-interacting gas follows the same universal relation $E = \frac{3}{2}P\mathcal{V}$, we also obtain the familiar form of energy that is usually obtained by the equipartition theorem,

$$E = \frac{3}{2}Nk_BT, \tag{4.31}$$

$$\frac{C_V}{N} = \left(\frac{\partial E}{\partial T}\right)_N = \frac{3}{2}Nk_B. \tag{4.32}$$

4.2.3 Virial expansion of the unitary Fermi gas

The degenerate unitary Fermi gas is theoretically challenging due to the absence of small parameters. However, at high temperatures, there is one such small parameter: the fugacity $e^{\beta\mu}$. Such high-temperature expansion was introduced by Kamerlingh Onnes with the form

$$P = nk_BT\left(1 + B_2(T) + \frac{B_3(T)}{\mathcal{V}} + \frac{B_4(T)}{\mathcal{V}^2} + ...\right). \tag{4.33}$$

A similar expansion in the fugacity is:

$$\beta\lambda^3P = 2\left(e^{\beta\mu} + b_2e^{2\beta\mu} + b_3e^{3\beta\mu} + ...\right). \tag{4.34}$$

For the non-interacting Fermi gas, the virial expansion can be read off from the definition of the polylogarithm function Eq. 4.27. For the unitary Fermi gas, the

second [97] and the third [140] virial coefficients have been determined to be

$$b_2 = \frac{3\sqrt{2}}{8}, \tag{4.35}$$

$$b_3 = -0.29095295.... \tag{4.36}$$

The fourth order virial expansion was also determined in [183] to be $b_4 = -0.016(4)$ after our measurement. This value, however, is contrary to what we obtain (see 4.9).

4.3 Review of past theoretical and experimental studies on the thermodynamics of the unitary Fermi gas

Considerable amount of effort has been put into the study of the thermodynamics of the unitary Fermi gas. On the theoretical front, the difficulty arises from the lack of small parameter. Quantum Monte Carlo (QMC) calculations are plagued by the sign problem. Either one needs to make use of a trial wave function (such as the case of the fixed-node Monte Carlo method), or perform calculations on a lattice, which requires extrapolation. Recently, a diagrammatic Monte Carlo (DMC) method has emerged as another tool for the theoretical study of strongly interacting quantum systems. This approach is ab-initio in nature, same as the lattice calculations, but unlike the lattice calculations which simulate a physical system (in discretized space), the DMC approach "simulates" the mathematical solution coming from the summation of Feynman diagrams.

On the experimental front, initial experimental studies of the thermodynamics of strongly interacting Fermi gases have focused on trap averaged quantities [119, 218, 143] and have obtained measurements of ξ_B. However, the trap averaged quantities wash out critical features, making the superfluid transition difficult to observe.

The most recent experimental studies on the thermodynamics of the unitary Fermi

Table 4.1: Experimental and theoretical works on the thermodyanmics of the unitary Fermi gas.

Year	Work	ξ_B	T_c/T_F	T-dependence
	BCS mean field	0.59		Yes
2004	Fixed-node QMC [37]	0.44(1)		
2004	T-Matrix [170]	0.456		
2004	^{6}Li expansion (Innsbruck) [17]	$0.27^{+0.09}_{-0.12}$		
2005	Fixed-node QMC [10, 39]	0.42(1)		
2005	^{6}Li heat capacity (Duke) [119]	0.51(4)		
2006	^{6}Li imbalanced (Rice) [168]	0.46(5)		
2006	Lattice QMC [35]		0.152(7)	
2006	^{40}K (JILA) [218]	$0.46^{+0.12}_{+0.05}$		Yes
2006	Lattice [27]		0.23(2)	Yes
2007	T-Matrix, first-order diagram [93]	0.36(1)	0.16	Yes
2007	ϵ-expansion [9]	0.367(9)		
2007	^{6}Li expansion (ENS) [221]	0.41(15)		
2009	^{6}Li (Duke) [144]	0.41(2)	≈ 0.2	Yes
2010	ξ_B upper bound [77]	$< 0.383(1)$		
2010	Lattice QMC [84]	0.429(9)	0.171(5)	
2010	^{6}Li (Tokyo) [101]		0.17(1)	Yes
2010	^{6}Li (ENS) [158]	0.415(10)	0.157(15)	Yes
2011	Auxiliary-field QMC [38]	0.372(5)		
2012	DMC [226]			Yes
2012	^{6}Li (MIT) [129]	0.376(4)	0.167(3)	Yes
2012	Lattice [60]			Yes
2012	Lattice [67]	$0.366^{+0.016}_{-0.011}$		

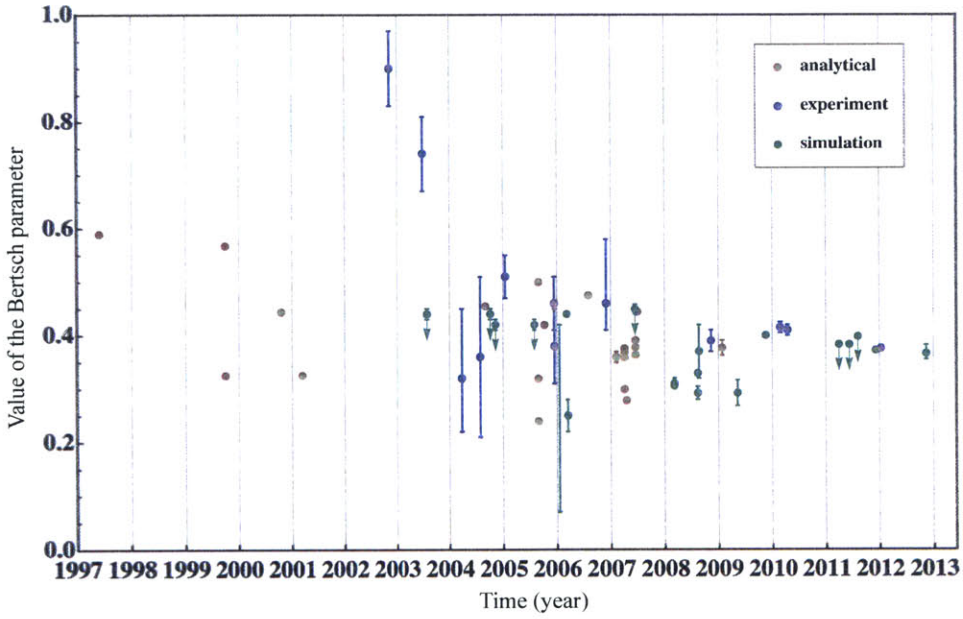

Figure 4-1: Historical results for the Bertsch parameter. The value obtained in the MIT experiment corresponds to the last experimental point in the year of 2012. This figure is taken from [67].

gas were performed by the ENS [158] and the Tokyo [101] groups. Both of these experiments extract the equation of state of a homogeneous gas, in particular, the pressure P as a function of the temperature and the chemical potential. However, since the superfluid phase transition in a spin-balanced Fermi gas is a second order transition and accompanied by only a kink in the density [116], quantities that involve integration of the density over the local potential, such as the pressure P, are only weakly sensitive to the phase transition. In addition, the calibration of the temperature and the chemical potential in these two experiments require either an external thermometer - the bosonic ^{7}Li in the case of the ENS experiment- and/or inputs from a prior theory or experiment - the virial expansion for the ENS experiment, and the Duke entropy vs energy measurement [144] for the Tokyo experiment. Therefore, an experimental measurement that can clearly resolve the critical transition in the thermodynamics and is independent of prior theory or experiment is highly desirable.

Table 4.1 is a non-exhaustive compilation of the experimental and theoretical studies of the thermodynamics of the unitary Fermi gas. Fig. 4-1 shows historical results of the Bertsch parameter as a function of time.

4.4 Outline of the experimental procedure

We prepare an ultracold two-component mixture of fermions described as in the previous chapter. After sympathetic cooling with ^{23}Na, a two-state mixture of the lowest two hyperfine states of ^{6}Li is created. A bias field of $834.15 \pm 1.5\,\mathrm{G}$ [16] brings the mixture to unitarity. At the time of the experiment, this was the best value for the position of the broad Feshbach resonance. The MIT thermodynamic measurement had such a precision that it became clear that the limiting factor was the accuracy of the position of the Feshbach resonance. An updated value of the Feshbach resonance $832.18(8)\,\mathrm{G}$ [245] was obtained after our thermodynamic measurement and was used in our subsequent experiments.

The trapping potential is harmonic in the z-direction, with frequency $\omega_z = 2\pi \times 22.85(5)\,\mathrm{Hz}$. The optical dipole trap (ODT) has a waist $W = 120\,\mu\mathrm{m}$ and an initial

depth $U_0 \sim 100\,\mathrm{kHz}$ when the mixture is created. The mixture is futher cooled through forced evaporation by lowering the trap depth. The final trap depth ranges from $U_0 \sim 9 - 20\,\mathrm{kHz}$, depending on the desired degeneracy of the cloud. A typical cloud contains $N/2 \sim 0.1 - 1$ million particles per spin state and is at a temperature $T \sim 20 - 100\,\mathrm{nK}$.

We obtain high resolution absorption images of a single state of ^{6}Li with the vertical imaging path (see 3.2). The imaging light has a large waist compared to the cloud size. The intensity of the light is $I = 0.07\, I_{\mathrm{sat}}$, where $I_{\mathrm{sat}} = 2.54\,\mathrm{mW/cm^2}$ is the saturation intensity of the ^{6}Li D_2 line. To image the atoms, the light is pulsed for $4\,\mu\mathrm{s}$. The absorption profile contains the once-integrated column density $n_{2\mathrm{D}}(x,z) = \int \mathrm{d}y\, n(\mathbf{r})$. We then convert the column density to the local density $n(\mathbf{r})$ via the inverse Abel transform.

The key to generate the equation of state of a homogeneous system from images of clouds trapped by an inhomogeneous potential is to make use of the local density apprxoimation (LDA). In general, a Fermi gas in a trap is built up by filling the energy levels of the trap. When the particle filling is large, one can consider the neighborhood at each point $\mathbf{r}$ to be a locally homogeneous system, with the energy landscape shifted by the local trapping potential[5] $V(\mathbf{r})$. Then, one can define the local chemical potential $\mu(\mathbf{r}) = \mu - V(\mathbf{r})$, where μ is the chemical potential at the point where the trapping potential is at the minimum (assumed to be $\mathbf{r} = \mathbf{0}$). Since a given atomic cloud is in thermal equilibrium with a uniform T, the density distribution is then given by

$$n(\mathbf{r}) = n\left(V(\mathbf{r})\right) = n(T, \mu - V(\mathbf{r}))\,. \tag{4.37}$$

Therefore, the measurement of the density profile with respect to the trapping potential contains the equation of state. If one has the knowledge of T and μ, then one can convert the local density measurement into an EoS of the form $n\lambda^3 = f_n(\beta\mu)$, or as we shall discuss in 4.9, one can also generate the compressibility EoS.

[5]This is analogous to the WKB approximation, in which one treats the wave function as a plane wave in the vicinity of each neighborhood and assigns a "local momentum" $p(x) = \sqrt{2m(E - V(x))}$.

4.5 Imaging characterization

The key to obtaining a precise measurement of the thermodynamics is to have an accurate measurement of the local density and to be able to characterize the systematic errors. Much of the challenge occurs at the stage of imaging. In this section, I will describe the characterization of our imaging procedure.

4.5.1 Detuning due to recoils

For near-resonant light, the photon scattering rate is

$$R = \frac{\Gamma}{2} \frac{I/(\alpha_I I_{\text{sat}})}{1 + (2\delta/\Gamma)^2 + I/(\alpha_I I_{\text{sat}})}. \tag{4.38}$$

The factor of $\alpha_I = 2$ accounts for using linearly polarized light for imaging on a σ_- transition along the vertical imaging path. On resonance and with $I/I_{\text{sat}} = 0.07$, the rate is $R = 0.60\,\text{photon}/\mu\text{s}$, or $t_{\text{scatter}} = 1.66\,\mu\text{s}$ per scattering event. Therefore, if we do not account for the Doppler shift due to each scattering event, an average number of 3.02 photons are scattered. The recoil velocity of ^{6}Li at the D_2 transition $\lambda_{\text{opt}} = 671\,\text{nm}$ is $v_R = \frac{h}{m\lambda_{\text{opt}}} = 0.099\,\text{m/s}$. Therefore, the mean shift in the resonance frequency corresponding to one recoil is $\Delta\nu = \frac{v_R}{\lambda} = 0.15\,\text{MHz}$. After each scattering, the scattering rate is modified since the atom is slightly off resonance. Taking this into account, the average number of photons scattered is 3.01. The change is less than 0.5%. When there is an intensity attenuation, the effect will only be more negligible, since there will be less scattering and hence less detuning that results. Therefore we can neglect this effect.

4.5.2 Atom movements due to recoils

We want to ensure that movements due to photon recoils are small compared to the spatial imaging resolution. For simplicity, we ignore the Doppler shift due to recoils. We also ignore recoils due to spontaneous emissions, which average to zero. With three photon recoils, an atom will move $1\,\mu\text{m}$ during the imaging pulse, which is less

than the imaging resolution of $2\,\mu$m.

4.5.3 Non-linearity in saturation

The absorption cross section is given by

$$\sigma = \frac{\hbar\omega}{I} R_{\text{eff}} = \frac{\sigma_0}{\alpha_I} \frac{1}{1 + (2\delta/\Gamma)^2 + I/(\alpha_I I_{\text{sat}})}, \tag{4.39}$$

where $\sigma_0 = 6\pi(\lambda_{\text{opt}}/(2\pi))^2$ is the resonant absorption cross section, and $\alpha_I = 2$ as before. From the Beer-Lambert law, $\frac{dI}{dx} = -\sigma I n$, the absorption on resonance is then given by [189]

$$\text{OD} \equiv \frac{\sigma_0}{\alpha_I} \int \mathrm{d}x\, n = -\ln\left(\frac{I}{I_0}\right) + \frac{I_0}{\alpha_I I_{\text{sat}}}\left(1 - \frac{I}{I_0}\right). \tag{4.40}$$

We want to quantify the effect of saturation when we use the formula for the optical density at the low-intensity limit, $\text{OD}_{\text{apparent}} = -\ln(I/I_0)$. In the limit where the attenuation of the intensity is small, Eq. 4.39 indicates that one can simply apply a calibration factor to obtain the correct OD. This is certainly not the case if the attenuation is significant. Nevertheless, we can characterize the error that results from applying a fixed calibration factor. In the experiment, we only use the region with $0 \leq \text{OD}_{\text{apparent}} \leq 1.8$. The upper cutoff ensures that we do not use regions of the image where the absorption is too dark and hence have large noises. In this range of $\text{OD}_{\text{apparent}}$, the ratio $\text{OD}_{\text{apparent}}/\text{OD}$ ranges from 0.966 (corresponding to $1/(1+I/(\alpha_I I_{\text{sat}}))$) at $\text{OD}_{\text{apparent}} = 0$ to 0.984 at $\text{OD}_{\text{apparent}} = 1.8$. Using the midpoint 0.975 as the calibration factor leads to an error of 1%.

4.6 Generating density profiles

Here, I describe the procedure to generate the density profiles $n(V)$ from the absorption images.

4.6.1 Image processing

We first apply a super-sampling procedure to each of the frame taken by the CCD camera: the frame probed with atoms (PWA), the frame probed without atoms (PWOA) taken after the atoms are released, and the frame of dark field (DF) taken with the camera shutter closed. For a frame of the size $L \times L$, where L is the number of pixels in each dimension, we duplicate each pixel into four and generate a $2L \times 2L$ image. The frame is then passed through a nearest-neighbor average filter. This procedure is beneficial to the inverse Abel transform because it reduces the problem of pixelation in a numerical procedure (see 4.6.2) and filters out high spatial frequency components above the imaging resolution that arise from the noise. A normalized intensity profile $\tilde{I} \equiv I/I_0 = \frac{\text{PWA}-\text{DF}}{\text{PWOA}-\text{DF}}$ is then generated from these three frames.

Next, we perform quadrant-averaging $\frac{1}{4}\sum_{i,j=\pm 1} \tilde{I}(ix, jz)$ on the intensity profile to reduce the noise. The noise on the intensity profile leaves a systematic offset in the background when taking the log: $-\ln(1+\Delta\tilde{I}) \simeq \Delta\tilde{I} + \frac{1}{2}(\Delta\tilde{I})^2 + \mathcal{O}(\Delta\tilde{I}^3)$. The linear term averages to zero but the quadratic term does not. This is detrimental for generating the pressure from integrating the density. Therefore, quadrant averaging on the intensity profile has the advantage of suppressing this systematic offset.

We then obtain the 2D column density

$$n_{2\text{D}}(x,z) = -\frac{\alpha_I}{\sigma_0}\ln\left(\frac{I}{I_0}\right) \tag{4.41}$$

4.6.2 Inverse Abel Transform to obtain local density

The 2D column density is the Abel transform of the local density distribution, $n_{2\text{D}} = \int \mathrm{d}y\, n(\mathbf{r})$. With cylindrical symmetry, the local density $n(\rho, z)$ can be obtained from the column density[6] via the inverse Abel transform:

$$n(\rho,z) = -\frac{1}{\pi}\int_{\rho}^{\infty} \mathrm{d}x \frac{1}{\sqrt{x^2-\rho^2}} \frac{\partial n_{2\text{D}}(x,z)}{\partial x}. \tag{4.42}$$

[6]We multiply the column density obtained from absorption images by a factor of two so the extracted density correspond to the total density.

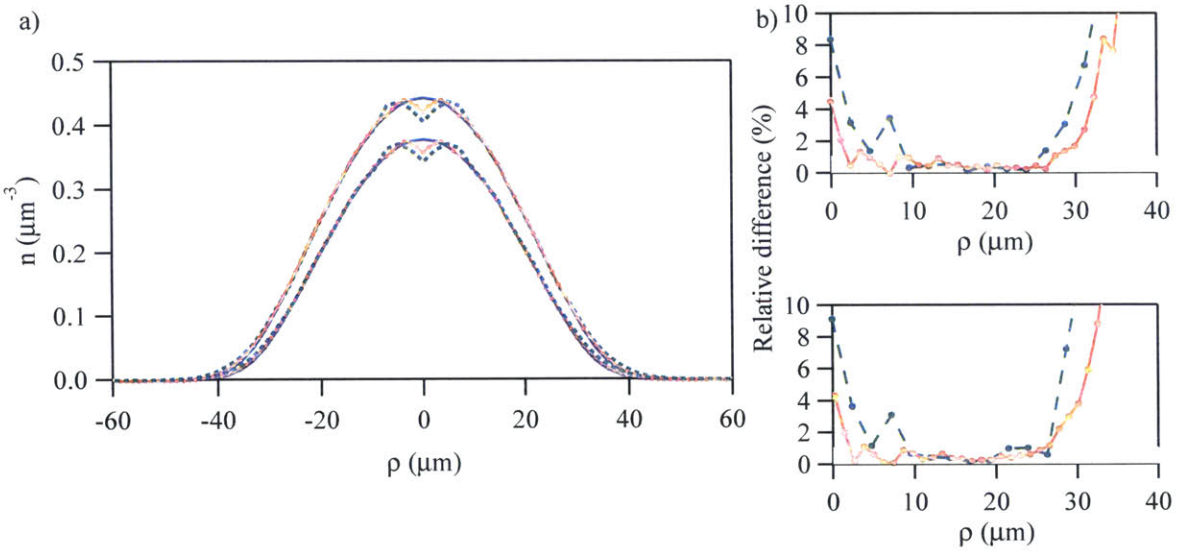

Figure 4-2: Benchmarking the numerical inverse Abel transform with a simulated cloud profile. To check the accuracy of the inverse Abel transform, we generate a simulated profile $n_{2D}(x, z)$ using the non-interacting EoS at $T = 50\,\mathrm{nK}$ and $\mu = 350\,\mathrm{nK}$. The parameters are chosen to match the typical peak density $n \sim 0.5\,\mu\mathrm{m}^{-3}$ and radial size $\sim 30\,\mu\mathrm{m}$. The column density is then fed into the numerical inverse Abel implementation to generate $n(\rho, z)$, and compared to the true local density coming from the non-interacdting EoS. (a) Radial-cut of $n(\rho, z = 0)$ (upper set of curves) and $n(\rho, z = 70\,\mu\mathrm{m})$ (lower set of curve). Blue solid curves: true local density. Green dashed curves: local density from the inverse Abel transform without super-sampling. Red connected circles: local density from the inverse Abel transform with two times super-sampling. (b) Relative difference compared to the true density for $z = 0$ (upper panel) and $z = 70\,\mu\mathrm{m}$ (lower panel). The same convention is used as in (a) to distinguish the result with and without fine-graining.

In practice, one has to numerically implement this carefully due to the singularity at $x = \rho$. The pixelation of n_{2D} means that the integrand diverges near the singularity. Therefore, we use the following form, which is obtained with a change of variable $\tau = \sqrt{x^2 - \rho^2}$:

$$n(\rho, z) = -\frac{1}{\pi} \int_0^\infty \mathrm{d}\tau \, \frac{1}{\sqrt{\tau^2 + \rho^2}} \left. \frac{\partial n_{2D}(x, z)}{\partial x} \right|_{x=\sqrt{\tau^2+\rho^2}} . \tag{4.43}$$

With this form, the integrand is well behaved except near $\rho = 0$. Our numerical procedure accurately reproduces the density of a simulated profile to better than 1% accuracy for $\rho > 3\Delta l = 7.2\,\mu$m (see Fig. 4-2).

The accuracy drops off beyond $\rho \gtrsim 30\,\mu$m due to the decreasing signal available for integration. Nevertheless, the absolute difference is small, and the uncertainty will be dominated by shot noise, so the amount of relative deviation is not of concern here.

4.6.3 Obtaining the trapping potential

The trapping potential (see 3.1) is given by

$$V(\rho, z) = V_\rho(\rho) + V_z(z) \equiv \frac{1}{2} m\omega_z^2 z^2 - \frac{1}{4} m\omega_z^2 \rho^2 - \alpha_{\mathrm{pol}} \frac{\mathcal{P}}{\frac{\pi}{2} W^2} e^{-2\rho^2/W^2} , \tag{4.44}$$

where α_{pol} is the polarizability, $\mathcal{P}$ is the power of the ODT, and $W = 120\,\mu$m is the waist of the ODT. The trap depth of the ODT is given by $U_0 = \alpha_{\mathrm{pol}} \frac{\mathcal{P}}{\frac{\pi}{2} W^2}$. For the thermodynamic experiment, the trapping frequency ω_z is measured to be $\omega_z = 2\pi \times 22.83(5)$ Hz.

We do not rely on the waist and power measurement of the laser beam but in fact measure the trapping potential directly using the atomic distribution. According to the local density approximation, equi-density contours correspond to equipotential contours. Since the potential is excellently known in the axial (z) direction, equi-density contours then calibrate the potential everywhere. For this measurement, one may average many independently measured 3D density profiles as long as they are

taken under the same experimental condition, even if the atom number or temperature vary from shot to shot. At any point (ρ, z), if the averaged density profile is $n_{\text{avg}}(\rho, z)$, the potential at that point $V(\rho, z)$ is then given by $V = V(0, z_0)$, where z_0 is the equi-density point on the z-axis, $n_{\text{avg}}(\rho, z) = n_{\text{avg}}(0, z_0)$. The resulting potential can be fit to the model of Eq. 4.44, which yields a waist that agrees with the measured waist to within 1%, and a power that agrees with the measured power to within 10% (a typical error for standard power meters).

With this method, anharmonicities in the trapping potential have been incorporated into the analysis of the density profiles. The ENS and the Tokyo experiments attempted to model anharmonic traps as harmonic potentials and measured the trapping frequencies [101, 158]. However, anharmonicities cause such frequencies to depend on the trap filling, rendering this method less reliable.

Note that the gravity does not enter into the potential. Gravity modifies the saddle point potential $\frac{1}{2}m\omega_z^2(z^2 - \frac{1}{2}\rho^2)$ only by shifting the saddle point. Therefore, by centering the ODT onto the saddle point - the "sweet spot" - the effect of gravity is not felt.

4.6.4 Density profile n vs. V

Knowing the trapping potential, a single experimental density profile $n(\rho, z)$ can now be averaged over equipotential lines $V(\rho, z)$, yielding a low-noise determination of the density as a function of the local potential V.

Fig. 4-3 presents a sample image processed with the procedure described in this section.

4.7 Calibrating the optical density

The accurate conversion of an image to a density profile is crucial for the measurement of the EoS. Ideally, the optical density $\text{OD} = -\ln(I/I_0)$ should correspond to the column density times the absorption cross section. However, several imperfections in imaging modify this relation: nonlinearity associated with saturation, imaging light

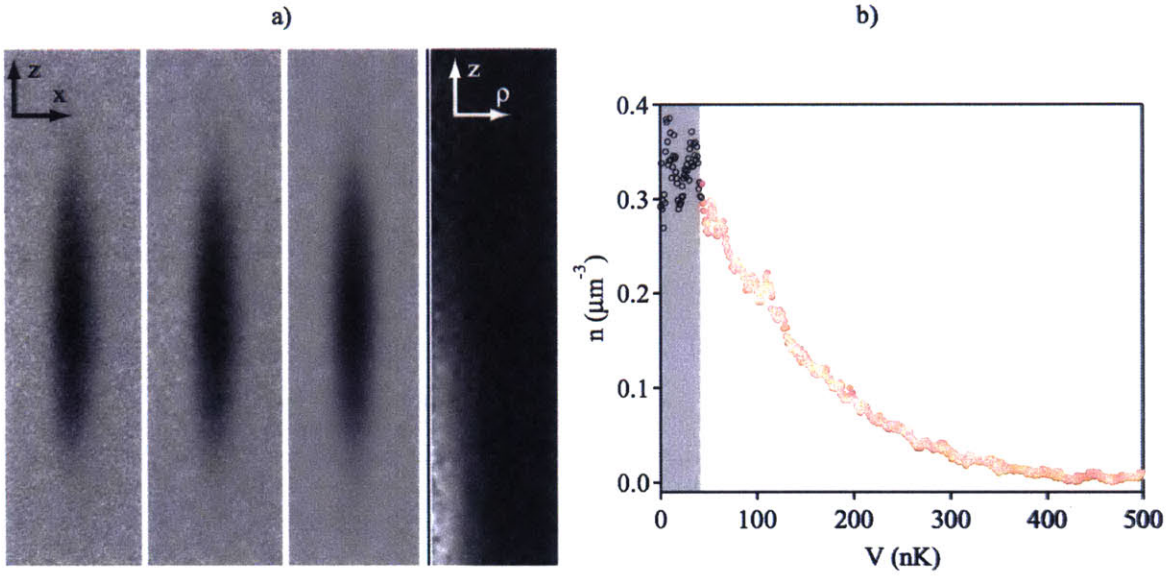

Figure 4-3: Obtaining the density profile from an atomic image. (a) From left to right: (i) Normalized intensity $\tilde{I} = I/I_0$ from the CCD camera without super-sampling nor quadrant-averaging, (ii) $\tilde{I}$ with super-sampling, (iii) $\tilde{I}$ with super-sampling and quadrant-averaging, and (iv) $n(\rho, z)$ obtained via the inverse Abel transform, with the three pixels (indicated by the white space near $\rho = 0$) from the axial center removed. (b) Density profile $n(V)$ obtained from the same image. The black open circles (as well as the gray band) indicate the points removed because they involve OD that is above the cutoff value.

being slightly off resonant, and imperfections in the polarization (which may be either that the polarization is not fully linear, or that it does not fully align with the x-axis, see 3.2). The latter two imperfections simply add a proportionality factor in the conversion from the optical density to the column density. The effect of saturation is nonlinear, but as disussed in 4.5.3, in the regime of intensity we operate at, we can model the effect as a simple scaling factor and still be accurate within 1%.

We use the following method to obtain the overall scaling factor to convert the OD to the column density. We prepare a highly imbalanced mixture at unitarity (see Fig. 4-4). Following the local density approximation, the majority atoms in the region where the minority atoms vanish is described by the non-interacting EoS. By fitting the density profile of the majority atoms to a non-interacting EoS with a variable oveall scaling factor, we can determine the calibration factor. The typical factor is around ~ 0.6.

One might envision that one can accomplish calibration by realizing non-interacting clouds near the zero-crossing of the scattering length[7] $B \sim 550\,\mathrm{G}$ and fitting the density profiles of such clouds to the non-interacting EoS. However, since the calibration images are taken at a different field, there is a possibility that the actual calibration factor is different. Furthermore, the cloud is much hotter, since the interaction is weak and thermalization is inefficient. A highly imbalanced cloud at unitarity offers the advantage of taking calibration image at the same field, and also of a cold cloud. Having a cold cloud is important for the following reason. In the high-temperature regime, the density is predominantly given by the EoS of a Boltzmann gas, $n \sim \lambda^{-3} e^{\beta(\mu - V)}$. The scaling factor can be absorbed into the chemical potential, and hence one is not sensitive to the scaling factor. It is only in the low temperature regime, where $n \propto (\mu - V)^{3/2}$, that a fit to the (non-interacting) EoS can disentangle the scaling factor from the chemical potential.

We take the imbalanced images for calibration after taking every couple images of the balanced gas in order to identify systematic drifts, if any.

[7] One would actually not go to exactly the zero-crossing, but rather nearby where the scattering length is small but finite to allow thermalization.

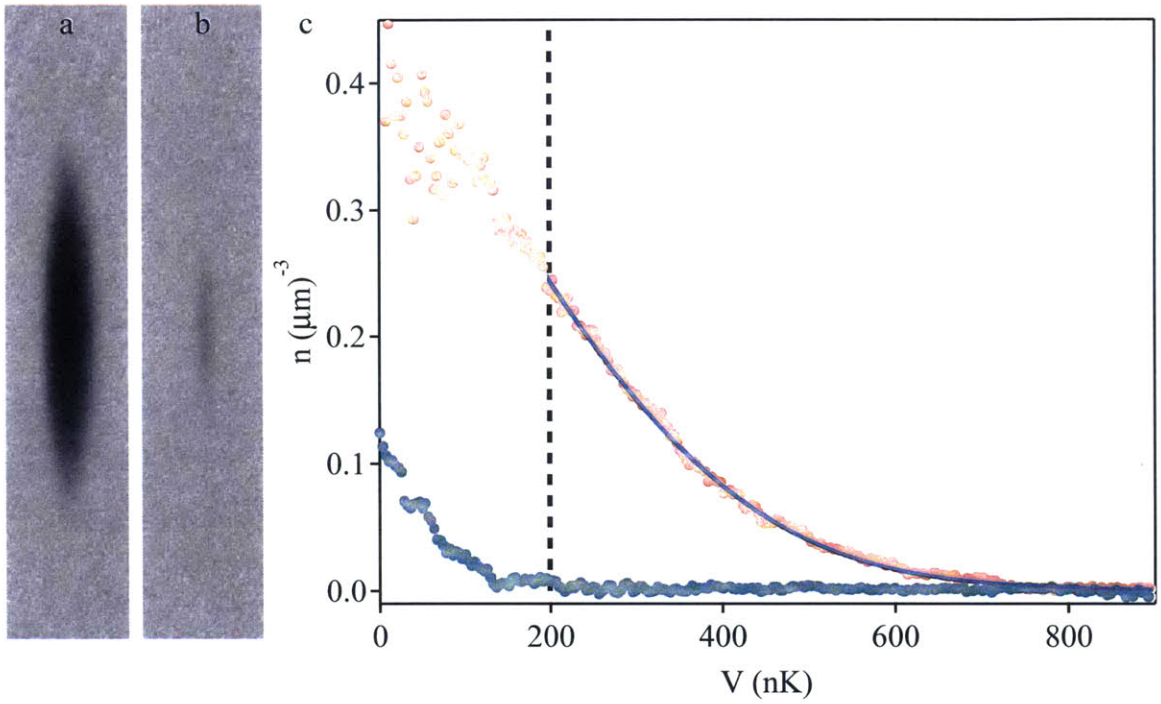

Figure 4-4: Image calibration with a highly imbalanced gas at unitarity. (a) Image of the majority cloud. (b) Image of the minority cloud. (c) Density profile $n(V)$ for the majority (red) and the minority (black) atoms. The vertical black dashed line signals the boundary of the minority atoms, and the region where we fit the majority cloud. The fit is shown in the blue curve.

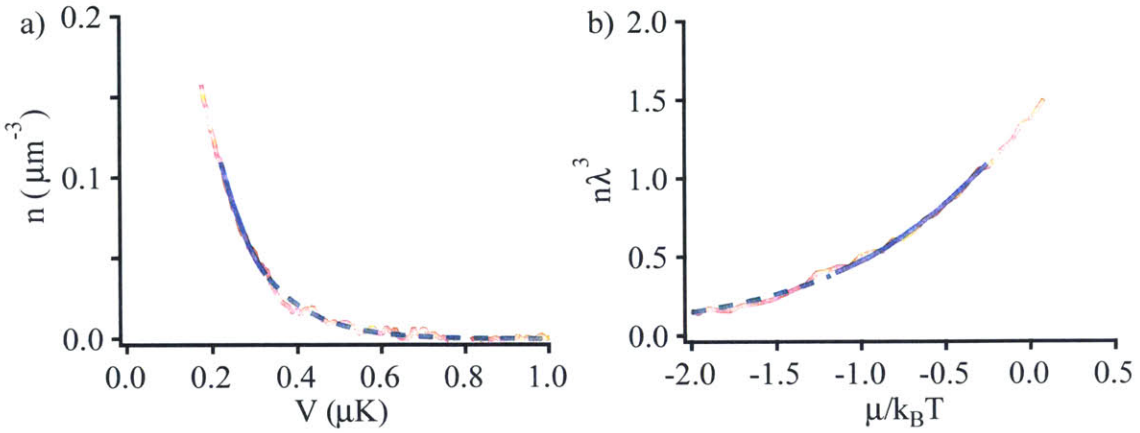

Figure 4-5: (a) Thermometry on a low-noise density profile, $n = n(V)$, is performed by fitting the experimental data (red) to the known portion of the EoS (solid blue line), starting with the virial expansion for $\beta\mu < -1.25$ (green dashed line). In this example, the EoS is known for $\beta\mu \leq -0.25$, and the fit to the density profile yields $T = 113\,\mathrm{nK}$, and $\beta\mu = 1.63$. (b) Given μ and T, the density profile can be rescaled to produce the EoS $n\lambda^3 = f_n(\beta\mu)$. The figure is taken from [226]

4.8 Measurement of the EoS in the normal phase (with iterative fitting)

To convert the density profile $n = n(V)$ into an EoS of the form Eq. 4.7, one needs the input of the chemical potential μ and the temperature T. To obtain these two quantities, one can fit the high-temperature wing of the density profile to a known EoS. Once μ and T are obtained, the density profile is rescaled to obtain $n\lambda^3$ vs $\beta\mu$, and the data closer to the cloud center provides the measurement of the EoS to a colder (namely larger $\beta\mu$) regime (Fig. 4-5). One can then use this updated EoS to fit a colder cloud, and this procedure is iterated to access lower temperatures. The EoS in the normal phase of the unitary Fermi gas was measured with this iterative procedure in [226]. This was used to validate the diagrammatic Monte Carlo calculation described in the same work. A similar procedure was used in [158] to measure the pressure EoS. The first iteration requires a known EoS in the high-temperature regime, for which we use the virial expansion up to the third order. The third-order

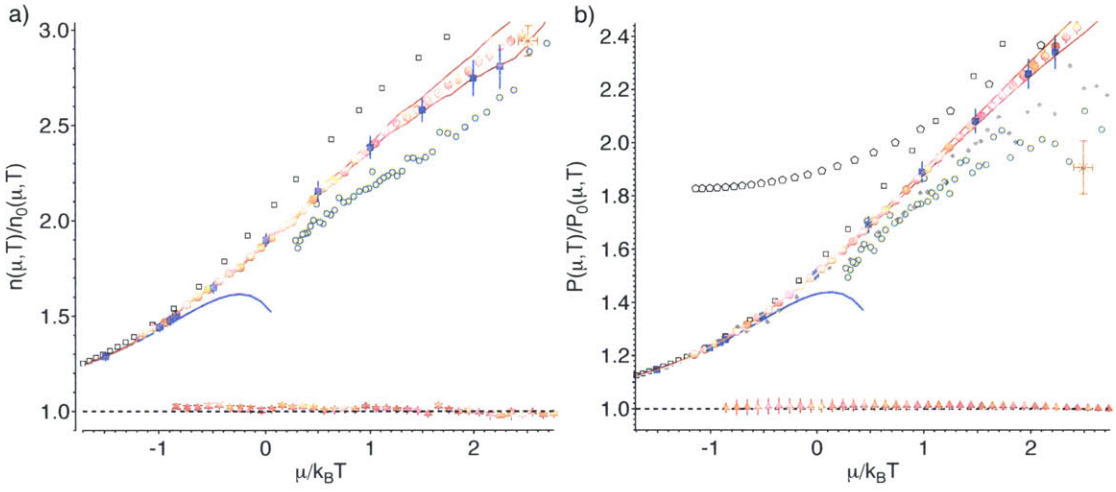

Figure 4-6: EoS measurement obtained with the iterative fit method. The figure is taken from [226]. (a) Density and (b) pressure equation of state of a unitary Fermi gas versus $\mu/(k_BT)$, normalized by the EoS of a non-interacting Fermi gas at the same $\mu/(k_BT)$. Solid squares: diagrammatic Monte Carlo (DMC). Solid circles: MIT experiment, with solid margins giving the error from the uncertainty in the Feshbach resonance position. Triangles and dashed line: MIT experiment and theory for the ideal Fermi gas. Solid line: third order virial expansion. Open squares: first order Feynman diagram [93]. Open circles: Auxiliary Field QMC [27]. Star: Critical point form determinental QMC [84]. Diamonds: ENS experimental pressure EoS [158]. Open pentagons: pressure EoS from Tokyo experiment [101].

virial expansion agrees with the DMC to within 1% for $\beta\mu \leq -0.85$. We use the virial expansion as the known EoS for the regime $\beta\mu \leq -1.25$.

Looking at the form of the density EoS $n = \lambda^{-3} f_n(\beta\mu)$ and the virial expansion $n = 2\lambda^{-3}(e^{-\beta(\mu-V)} + 2b_2 e^{-2\beta(\mu-V)} + ...)$, it is clear that the temperature is determined mainly from the curvature of the density profile, while the chemical potential is determined mainly from the height of the central points. Uncertainty in the EoS due to the use of fitting procedure mainly comes from the uncertainty in the chemical potential, while the temperature can be determined much more accurately.

Care was taken to contain and assess the errors of the EoS measurement. A typical experimental run gives a hundred images with signal-to-noise ratio of 3-to-10. Each image produces an EoS curve, and about 30-40 curves are averaged to construct a low-noise EoS measurement. About 4 such independent measurements are averaged

to produce the final EoS curve with an average statistical errors below 1% in $n\lambda^3$. To truly assess the systematic errors, we applied our protocol to measure the EoS of a non-interacting Fermi gas. The resulting EoS agrees with the theoretical EoS to 1% on average, which we assign as the systematic uncertainties of our measurement at unitarity. The statistical error is $< 0.5\%$. Therefore, we assess that the measured unitary EoS is accurate to better than 1.5% in $n\lambda^3$. The error in $n\lambda^3$ that comes from the uncertainty of the position of the Feshbach resonance is estimated to be 3% (see 4.15).

Uncertainty in thermometry gives an error of $\delta(\beta\mu) = \pm 0.04$ in the $\beta\mu$ axis. A binning of the EoS in the $\beta\mu$ direction to reduce noises acts as a filter and gives the EoS a resolution of 0.1 in the $\beta\mu$ direction. Due to the noise in $\beta\mu$, the iterative procedure is expected to wash out the sharp feature at the critical point and obscure the signal of superfluid transition in the thermodynamics.

4.9 Compressibility EoS

To clearly observe the signature of the superfluid transition in the thermodynamics, we developed a technique to obtain the EoS that requires no fitting, as described in [129]. Starting with the density profile $n(V)$, we note that it contains not just the measurement of n, but also the measurement of the trapping potential V. In the LDA, the variation of the chemical potential is given by the variation in the trapping potential, $\mathrm{d}\mu = -\mathrm{d}V$. In a system with a uniform temperature, the Gibbs-Duhem relation gives $\mathrm{d}P = n\mathrm{d}\mu$. Therefore, one can generate the local pressure

$$P(V) = \int_{\infty}^{V} \mathrm{d}V' \, n(V') \,. \tag{4.45}$$

The other thermodynamic quanity one can generate is the compressibility via Eq. 4.24,

$$\kappa = \frac{1}{n^2}\left(\frac{\partial n}{\partial \mu}\right)_T = -\frac{1}{n^2}\frac{dn}{dV} \,. \tag{4.46}$$

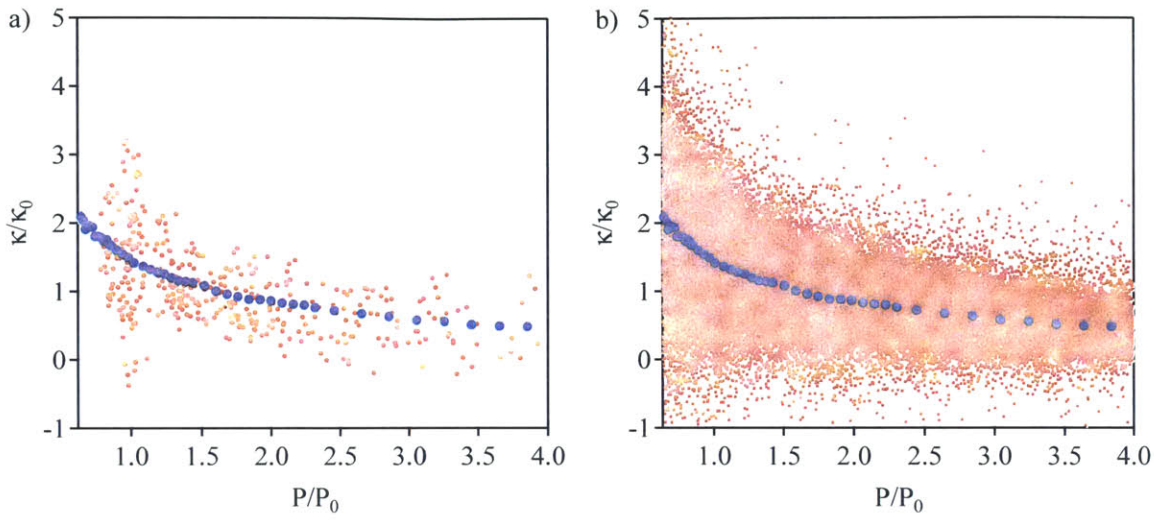

Figure 4-7: Construction of the $\tilde{\kappa}(\tilde{p})$ curve in the normal phase. (a) Normalized compressibility vs normalized pressure for a single profile (red) in the normal phase, compared to the final data (blue). (b) Shown in red is all the data points used from all the profiles used to generate the data (blue).

The relation between these three variables form an EoS. The compressibility EoS $\kappa(n, P)$ can be obtained directly from the density profile without fitting or an external thermometer. Furthermore, the compressibility, a quantity related to the second derivative of the energy, is expected to display singular behavior at the critical point.

With κ, n, and P, we form dimensionless quantities according to Eqs. 4.20 and 4.22. We define the normalized compressibility $\tilde{\kappa} \equiv \kappa/\kappa_0$ and the normalized pressure $\tilde{p} \equiv P/P_0$, where $\kappa_0 = \frac{3}{2}(nE_F)^{-1}$ and $P_0 = \frac{2}{5}nE_F$. Due to scale invariance, any measurement on an atomic cloud at any temperature, atom number, and trapping potential must produce the same universal curve $\tilde{\kappa}(\tilde{p})$. By averaging over many profiles, we obtain a low noise measurement of the compressibility equation of state $\tilde{\kappa}(\tilde{p})$.

For each density profile $n(V)$, we generate $P(V)$ via Eq. 4.45, and obtain the normalized pressure $\tilde{p} = P/P_0$. We obtain the normalized compressibility with the following relation

$$\tilde{\kappa} = \left(\frac{\partial E_F}{\partial \mu}\right)_T = -\frac{dE_F}{dV}\,. \tag{4.47}$$

In Fig. 4-7, we show $\tilde{\kappa}$ vs. $\tilde{p}$ for (a) a single profile and (b) all the profiles used to generate the experimental measurement. The normalized pressure can be thought

of as a thermometer, with the higher $\tilde{p}$ corresponding to larger T/T_F. The points are binned with respect to $\tilde{p}$ to generate the data. The binning $\Delta\tilde{p} = 0.015 - 0.4$ is chosen such that the $\beta\mu$ (see 4.10) has a spacing of around 0.1. Though the normalized compressibility of a single profile is noisy, after averaging over many profiles, a low-noise measurement can be obtained. This procedure is used to generate the EoS in the normal phase up to up to $0.64 < \tilde{p}$, in which the EoS contains no singularity and is smooth. However, near the phase transition, averaging many $\tilde{\kappa}(\tilde{p})$ is expected to wash out the singular feature.

To clearly reveal the feature in the compressibility associated with the superfluid transition, we adopt a different strategy to obtain the $\tilde{\kappa}(\tilde{p})$ for $\tilde{p} < 0.63$. We first average a few $n(V)$ (between 4 to 20 profiles, depending on the set), obtained under the same experimental condition. This produces an averaged profile $n_{\mathrm{avg},1}(V)$ for a given set of profiles, which has much less noise. Fig. 4-8 (a) shows one such averaged profile, and the kink in the density at the critical point is visible. From the averaged profile, we then generate $\tilde{\kappa}_{\mathrm{avg},1}(\tilde{p}_{\mathrm{avg},1})$ as described above (Fig. 4-8 (b)). We do the same for the other sets of profiles, with each set taken at the same experimental condition, to generate $n_{\mathrm{avg},2}, ..., n_{\mathrm{avg},6}$ and the corresponding $\tilde{\kappa}_{\mathrm{avg},2}(\tilde{p}_{\mathrm{avg},2}), ..., \tilde{\kappa}_{\mathrm{avg},6}(\tilde{p}_{\mathrm{avg},6})$. Finally, with $\tilde{\kappa}_{\mathrm{avg},i}(\tilde{p}_{\mathrm{avg},i})$ from six averaged profiles, we bin the points, weighted by the number of profiles in each set, to obtain the measurement (Fig. 4-8 (c)). In Fig. 4-9, we plot the measured $\tilde{\kappa}(\tilde{p})$ from the superfluid phase to the high-temperature regime where the virial expansion becomes valid.

A data point typically contains between 30 to 150 profiles. Error bars for the data shown contain both the statistical error (the standard error) and the systematic error from imaging calibration. The error in the absorption cross section is assessed to be 4% for a single calibration. The corresponding uncertainty for $\tilde{\kappa}$ and $\tilde{p}$ is suppressed by a factor of 2/3. Using several independently measured absorption cross sections for a given data point $\tilde{\kappa}(\tilde{p})$ provides an additional suppression of this error. The typical error for $\tilde{\kappa}$ and $\tilde{p}$ from imaging calibration is thus about 2%.

The method described here has been tested on the non-interacting Fermi gas that can be studied in two independent ways: In spin-balanced gases near the zero-crossing

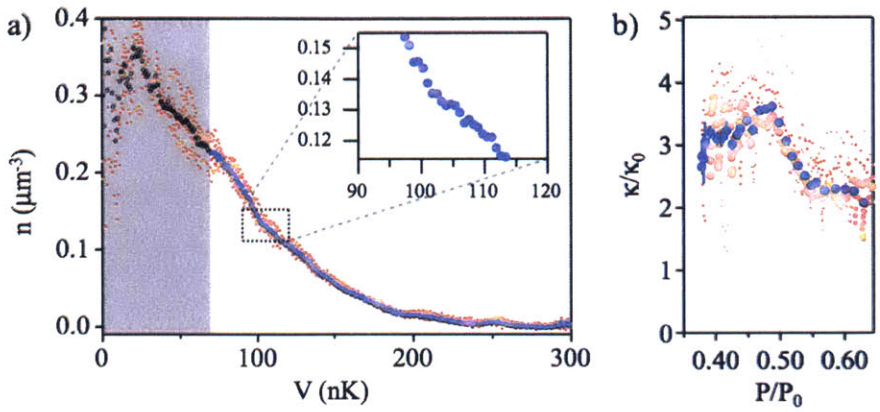

Figure 4-8: Obtaining the compressibility EoS in the regime near and below the superfluid transition point. (a) A set of four $n(V)$ taken under the same experimental condition (red) is averaged to generate a low-noise profile (blue). The black points in the gray region involve OD that is above the cutoff (OD ≤ 1.8) and hence not used for the data. Inset: the kink in the density associated with the second order phase transition is visible in the averaged profile. (b) Red: $\tilde{\kappa}$ vs. $\tilde{p}$ from six sets of averaged profiles such as the one in (a). The size of the points are weighted by the number of individual profiles in each set. Binning the points weighted by the number of profiles in each set leads to the measurement in the low-temperature regime $\tilde{p} < 0.63$.

of the scattering length and in the wings of highly imbalanced clouds at unitarity. Both determinations yield the same non-interacting compressibility EoS (Fig. 4-9). This provides a check for the effective absorption cross section: If the cross section had been determined too large by a factor of γ, $\tilde{\kappa} \propto \gamma^{-2/3}$ would be too small, and $\tilde{p} \propto \gamma^{2/3}$ too large.

In the high-temperature ($\tilde{p} \gg 1$) regime, our data shows good agreement with the third order virial expansion. Fixing b_2 and b_3, our measurement yields a prediction for the fourth-order virial coefficient $b_4 = +0.065(10)$, in agreement with [158], but contradicting a four-body calculation that gives a negative sign [183].

At degenerate temperatures ($\tilde{p} \lesssim 1$), the normalized compressibility rises beyond that of a non-interacting Fermi gas, as expected for an attractively interacting gas. At around $\tilde{p} = 0.55$, the compressibility rises suddenly and then decreases at lower temperatures. This marks the superfluid transition. The expected singularity of the compressibility at the transition is rounded off by the finite resolution of our imaging

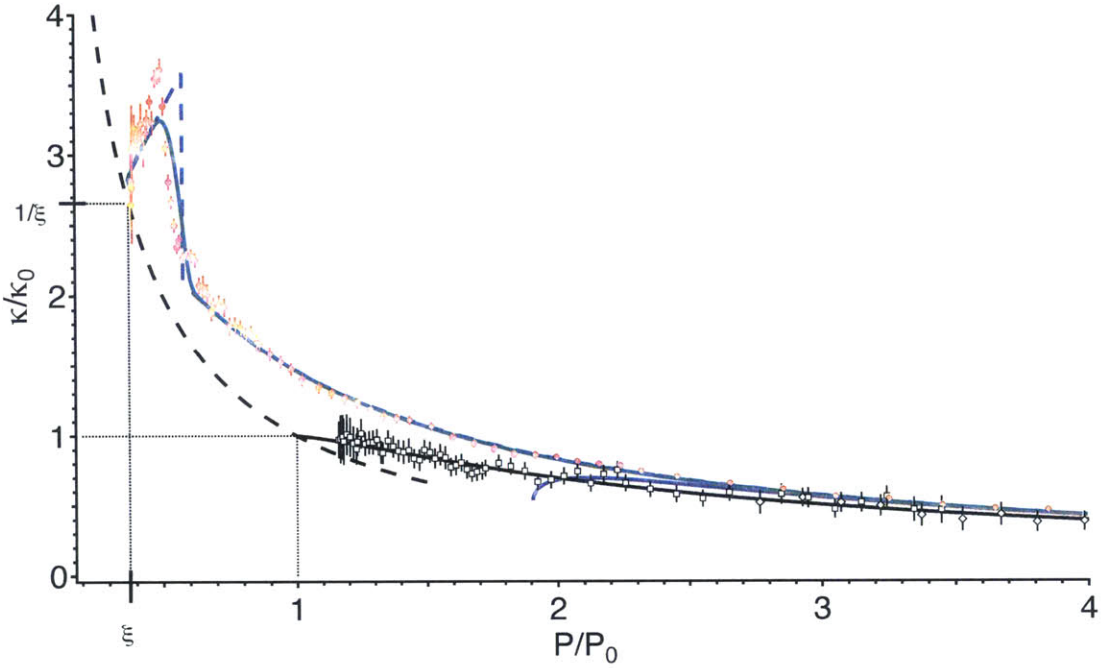

Figure 4-9: Normalized compressibility κ/κ_0 versus normalized pressure P/P_0 of the unitary Fermi gas (red solid circles). Each data point is the average of between 30 and 150 profiles. The error bars show one standard deviation, including systematic errors from image calibration. Blue solid line: 3rd order virial expansion. Black open squares (black open diamonds): data for a non-interacting Fermi gas obtained with a highly spin-imbalanced mixture at the unitarity (spin-balanced gas near zero-crossing of the scattering length). Black solid curve: the $T = 0$ limit of $\tilde{\kappa} = 1/\tilde{p}$. The dotted lines indicate $\tilde{\kappa} = 1/\tilde{p} = 1$ for the non-interacting gas, and $\tilde{\kappa} = 1/\tilde{p} = 1/\xi_B$ for the unitary Fermi gas. Gray band: the uncertainty region for the $T = 0$ value of $\tilde{\kappa} = 1/\xi_B$ and $\tilde{p} = \xi_B$. Blue dashed curve: model for the EoS of the unitary Fermi gas (above T_c: interpolation from the Monte-Carlo calculation [226], below T_c: BCS theory including phonon and pair-breaking excitations). Green solid curve: Effect of $2\,\mu$m optical resolution on the model EoS. This figure is taken from [129]

system. Below the transition point, the decrease of the compressibility is consistent with the expectation from the BCS theory where single-particle excitations freeze out and pairs form (see the model in Fig. 4-9).

At zero temperature, $\mu = \xi_B E_F$, and hence $\tilde{\kappa} = \frac{\partial E_F}{\partial \mu} = 1/\xi_B$, while $P = \int n \, \mathrm{d}(\xi_B E_F) = \xi_B P_0$. As a result, $\tilde{\kappa}(\tilde{p})$ terminates on the curve $\tilde{\kappa} = 1/\tilde{p}$ at $T = 0$. We see that this constraint is satisfied by both the non-interacting EoS, which can be thought to have a "ξ_B" of 1, and the unitary EoS. Extrapolation of the experimental data for $\tilde{\kappa}(\tilde{p})$ towards the $T = 0$ limit gives 0.37(1) for the Bertsch parameter, consistent with the value that we extract from the normalized chemical potential, energy, and free energy, which I will describe later.

4.10 Generating thermodynamic quantities from the compressibility EoS

All the thermodynamic information is encoded in the EoS, regardless of the state variables involved. Therefore, with the compressibility equation of state $\kappa(n, P)$, one can obtain all the other thermodynamic quantities. To start, we look at the temperature dependence of n, P, and κ. For each of these quantities, we define the following universal functions of $X \equiv \beta\mu$:

$$P = \frac{1}{\beta\lambda^3} f_P(X) , \tag{4.48}$$

$$n = \frac{1}{\lambda^3} f_P'(X) \equiv \frac{1}{\lambda^3} f_n(X) , \tag{4.49}$$

$$\kappa n^2 = \frac{\beta}{\lambda^3} f_P''(X) . \tag{4.50}$$

The phase space density $n\lambda^3 = f_n$ is related to T/T_F by

$$\frac{T}{T_F} = \frac{4\pi}{(3\pi^2)^{2/3}} \frac{1}{f_n^{2/3}} . \tag{4.51}$$

In terms of the functions f_P and f_n, the normalized compressibility and the nor-

malized pressure are given by the following

$$\tilde{\kappa} = \frac{2}{3}\frac{T_F}{T}\frac{f_n}{f_n}, \tag{4.52}$$

$$\tilde{p} = \frac{5}{2}\frac{T}{T_F}\frac{f_P}{f_n}. \tag{4.53}$$

Differentiating $\tilde{p}$ and T/T_F with respect to $X = \beta\mu$ then gives us the following relations on how the different thermometers, $\tilde{p}$, $X = \beta\mu$ and T/T_F are related:

$$\frac{\mathrm{d}\tilde{p}}{\mathrm{d}X} = \frac{5}{2}\frac{T}{T_F}(1 - \tilde{\kappa}\tilde{p}) \tag{4.54}$$

$$\frac{\mathrm{d}(T/T_F)}{\mathrm{d}X} = -\tilde{\kappa}\left(\frac{T}{T_F}\right)^2 \tag{4.55}$$

$$\frac{\mathrm{d}\tilde{p}}{\mathrm{d}(T/T_F)} = \frac{5}{2}\frac{T_F}{T}\left(\tilde{p} - \frac{1}{\tilde{\kappa}}\right). \tag{4.56}$$

Note that apart from a prefactor, the last equation is just the heat capacity per particle (using $E = \frac{3}{2}P\mathcal{V}$ valid at unitarity):

$$\frac{C_V}{k_B N} = \frac{1}{k_B N}\frac{\partial E}{\partial T}\Big|_{N,\mathcal{V}} = \frac{3}{5}\frac{\mathrm{d}\tilde{p}}{\mathrm{d}\,(T/T_F)} = \frac{3}{2}\frac{T_F}{T}\left(\tilde{p} - \frac{1}{\tilde{\kappa}}\right). \tag{4.57}$$

Eq. 4.56 is also equivalent to $\frac{\mathrm{d}\tilde{p}}{\mathrm{d}\ln(T/T_F)} = \frac{5}{2}\left(\tilde{p} - \frac{1}{\tilde{\kappa}}\right)$. This then gives

$$\frac{T}{T_F} = \left(\frac{T}{T_F}\right)_i \exp\left\{\frac{2}{5}\int_{\tilde{p}_i}^{\tilde{p}} \mathrm{d}\tilde{p}\frac{1}{\tilde{p} - \frac{1}{\tilde{\kappa}}}\right\}, \tag{4.58}$$

where $\tilde{\kappa}$ is known as a function of $\tilde{p}$, and $(T/T_F)_i$ is the reduced temperature at the initial normalized pressure $\tilde{p}_i$. This "anchor" point can be taken to be in the Boltzmann regime of the classical gas. Since the compressibility EoS has already validated the third order virial expansion, we may take this initial point to be in the virial regime, where the experimental data is less noisy.

Eq. 4.58 relates the reduced temperature T/T_F to the reduced pressure $\tilde{p}$, and at unitarity this relation is unique. Away from resonance, the relation would still hold, provided one fixes all other parameters specifying the system, for example the scattering length a or the imbalance $\delta n = n_\uparrow - n_\downarrow$.

There are two ways to obtain $\beta\mu$ vs T/T_F. One can consider $\tilde{\kappa}$ as a function of T/T_F and obtain

$$\beta\mu = (\beta\mu)_i - \int_{T_i/T_F}^{T/T_F} \mathrm{d}(\tfrac{T}{T_F})\frac{1}{\tilde{\kappa}}\left(\frac{T_F}{T}\right)^2, \tag{4.59}$$

or one can consider T/T_F as a function of $\tilde{p}$ and obtain

$$\beta\mu = (\beta\mu)_i + \frac{2}{5}\int_{\tilde{p}_i}^{\tilde{p}} \mathrm{d}\tilde{p}\,\frac{T_F}{T}\frac{1}{1-\tilde{\kappa}\tilde{p}}. \tag{4.60}$$

For the entropy per particle, we have

$$S/Nk_B = \frac{T_F}{T}(\tilde{p} - \frac{\mu}{E_F}). \tag{4.61}$$

Finally, since T/T_F is known, we can obtain f_n from Eq. 4.51 and f_P from Eq. 4.53.

Note that the determination of T/T_F from $\tilde{\kappa}(\tilde{p})$ is insensitive to errors in the absorption cross section. Even if the absorption cross section has been determined by too large a factor of γ, all factors of γ cancel in Eq. 4.58. This means that one can determine T/T_F of a cloud of unitary Fermi gas from the density profile without requiring a calibration. This is in fact also true for the non-interacting Fermi gas.

4.11 Signature of the λ-transition in the compressibility and the heat capacity

Armed with the relations in 4.10, from $\tilde{\kappa}(\tilde{p})$ we obtain T/T_F via Eq. 4.58 and $C_V/(k_BN)$ via Eq. 4.57. In Fig. 4-10, we plot $\tilde{\kappa}$ and $C_V/(k_BN)$ vs T/T_F. At high temperatures, the specific heat approaches that of a non-interacting Fermi gas and eventually $C_V = \frac{3}{2}Nk_B$, the value for a Boltzmann gas. As T/T_F is lowered, a dramatic rise is observed for T/T_F at around 0.16, followed by a steep drop. Jumps in the specific heat are well-known from superconductors [223] and ^{3}He [230]. In particular, the λ-shaped feature observed in the specific heat here is characteristic of second-order phase transitions, as in the famous λ-transition in ^{4}He [139]. In experiments on atomic gases, such jumps had only been inferred from derivatives to fit functions

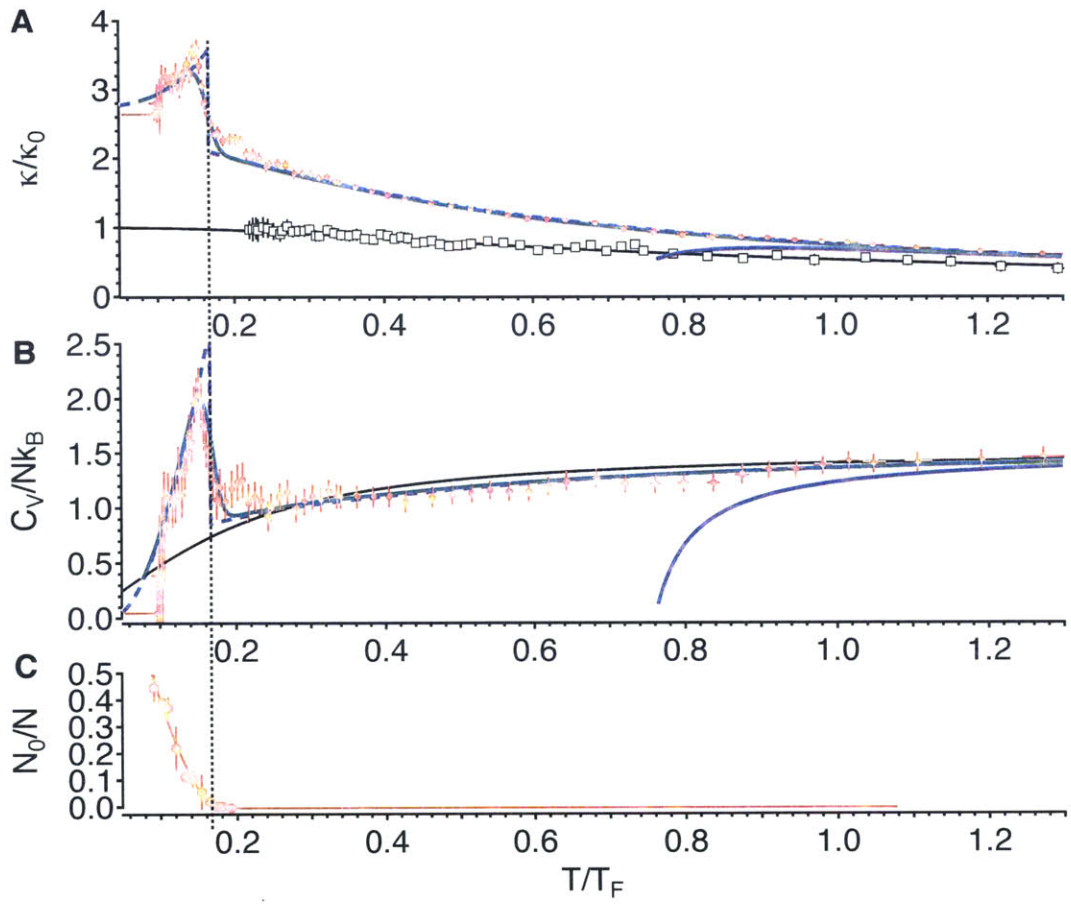

Figure 4-10: (a) Normalized compressibility $\tilde{\kappa}$ and (b) specific heat per particle $C_V/(Nk_B)$ of a unitary Fermi gas as a function of T/T_F (solid red circles). Black solid curve: theory for a non-interacting Fermi gas. Blue solid curve: 3rd order virial expansion for the unitary gas. Black open squares: data for the normalized compressibility as a function of T/T_F of a non-interacting Fermi gas (combining data from both highly imbalanced gases at unitarity and balanced gases near zero-crossing). Blue dashed (green solid) curve: model from Fig. 4-9, excluding (including) the effect of finite imaging resolution. (c) Global condensate fraction at unitarity as determined from a rapid ramp to the molecular side of the Feshbach resonance, plotted as a function of local T/T_F at the trap center. All error bars show one standard deviation. This figure is taken from [129]

that implied a jump [69, 144].

Near the phase transition, the specific heat scales as $C_V \propto |1 - T/T_c|^{-\alpha_c}$, where α_c is the critical exponent. The superfluid phase transition of the unitary Fermi gas corresponds to the 3D XY universality class, and the critical exponent α_c is known to be slightly negative, $\alpha_c \approx -0.01$ (see for example [139]). This corresponds to a cusp, rather than a divergence, in the heatp capacity at the critical point. We do not expect to resolve the critical behavior very close to T_c due to the finite resolution of the imaging system, (2 μm or about 5% of the cloud size in the radial direction). In our trapped sample, the critical region is confined to a narrow shell. Based on the estimate in [177], the thickness of the critical shell is 1% of the cloud size. The finite optical resolution suffices to explain the rounding of the singularity expected from criticality. The rounding also reduces the observed jump in the heat capacity at the transition, giving us a lower bound on the jump to be $\Delta C/C_n \equiv (C_s - C_n)/C_n \geq 1.0^{+4}_{-1}$, where C_s/N and C_n/N is the specific heat per particle at the peak and at the onset of the sudden rise respectively. This is close to the BCS value of 1.43 [223], which is surprising given the strong interactions.

Below T_c, the specific heat is expected to decrease as $\sim e^{-\Delta_0/k_B T}$ due to the pairing gap Δ_0. At low temperatures $T \ll T_c$, the heat capacity is dominated by contributions from phonons $\propto T^3$ [93]. Our data is consistent with the expected temperature-dependence, but we do not resolve the phonon regime.

We obtained the critical temperature $T_c/T_F = 0.167(13)$ from the jump in the specific heat. This value is determined as the midpoint of the sudden rise, and the error is assessed as the shift due to the uncertainty of the Feshbach resonance (discussed in 4.15). To validate the the measurement from the specific heat, we have employed the rapid ramp method to detect fermion pair condensation [186, 251] (also discussed in 6.2.3). We prepare a Fermi gas at various temperatures by tuning the final trap depth U_0. For each U_0, we obtain both the in-situ images and the rapid-ramp expansion images, which reveals the bimodal profile associated with the condensation of fermion pairs. From the rapid-ramp images, we obtain the global condensate fractions. From the in-situ images, we obtain T/T_F by fitting the images to the

EoS. The reproducibility of the experiment ensures that the temperature obtained from the in-situ profile corresopnds to that of the rapid-ramp image taken under the same experimental condition. The results (Fig. 4-10 (c)) show that the onset of condensation and the sudden rise in the specific heat and the compressibility all occur at the same critical temperature, within the error bars.

The measured critical temperature is in very good agreement with theoretical determinations, such as the self-consistent T-matrix approach that gives a T/T_c of 0.16 [93], and Monte-Carlo calculations which give 0.171(5) [84] and 0.152(7) [35].

The existence of a pseudogap is expected to affect the the temperature dependence of the specific heat. A pairing gap for single-particle excitations above the transition should cause a downturn in the specific heat in the degenerate regime above T_c. We do not observe such a downturn in our measurements. If the decrease in the specific heat due to pairing above T_c is small, or if the pseudogap occupies a narrow window in the phase diagram, the signal will be obscured by the noise in the measurement as well as the rounding due to the finite imaging resolution.

4.12 Temperature-dependence of the thermodynamic poetntials

Eq. 4.59 or 4.60 enables us to obtain the reduced chemical potential μ/E_F as a function of the T/T_F (Fig. 4-11). In the interval of $0.25 \lesssim T/T_F \lesssim 1$, the reduced chemical potential is close to that of a non-interacting Fermi gas, shifted vertically by an offset of $(\xi_n - 1)$, with $\xi_n = 0.45(2)$. If we model the normal state by the Landau liquid theory, the chemical potential follows a quadratic behavior as a function of T in the low temperature regime, with the curvature given by the effective mass $m^*/m = 1.2(2)$ of the quasiparticle (see 4.16 for a discussion on the validity of the Fermi liquid model).

Unlike a normal Fermi gas, the chemical potential attains a maximum of $\mu/E_F = 0.42(1)$ at $T/T_F = 0.171(10)$, and then decreases at lower temperatures. This decrease

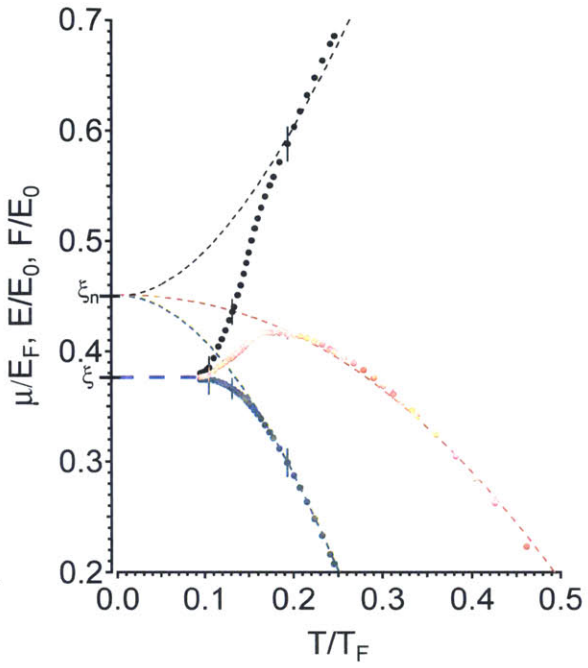

Figure 4-11: Chemical potential μ, energy E and free energy F of the unitary Fermi gas versus T/T_F. μ (red solid circles) is normalized by the Fermi energy E_F, E (black solid circle) and F (green solid circle) are normalized by $E_0 = \frac{3}{5}NE_F$. At high temperatures, all quantities approximately track those for a non-interacting Fermi gas, shifted by $\xi_n - 1$ (dashed curves). The peak in the chemical potential signals the onset of superfluidity. In the deeply superfluid regime at low temperatures, μ/E_F, E/E_0 and F/F_0 all approach ξ_B. A few representative error bars are shown, representing one standard deviation. This figure is taken from [129]

is expected for a superfluid of paired fermions [93]. In a superfluid, as the temperature is increased from zero, the increase in the chemical potential is first due to phonons at temperatures close to zero, and at larger temperatures, dominated by the contribution from the breaking of fermion pairs. At T_c, the singular compressibility implies a sharp change in slope for μ/E_F, in agreement with our observation and theory [93]. At the critical point, we obtain $k_BT_c/\mu_c = 0.40(3)$, in excellent agreement with the most accurate theoretical determination $k_BT_c/\mu_c = 0.400(14)$ from [84] as well as the T-matrix calculation $k_BT_c/\mu_c = 0.406$ from [93].

At low temperatures, the reduced chemical potential μ/E_F saturates to ξ_B. Since the energy E and the free energy F satisfy the inequality $E > \frac{3}{5}N\xi_BE_F > F$ for all

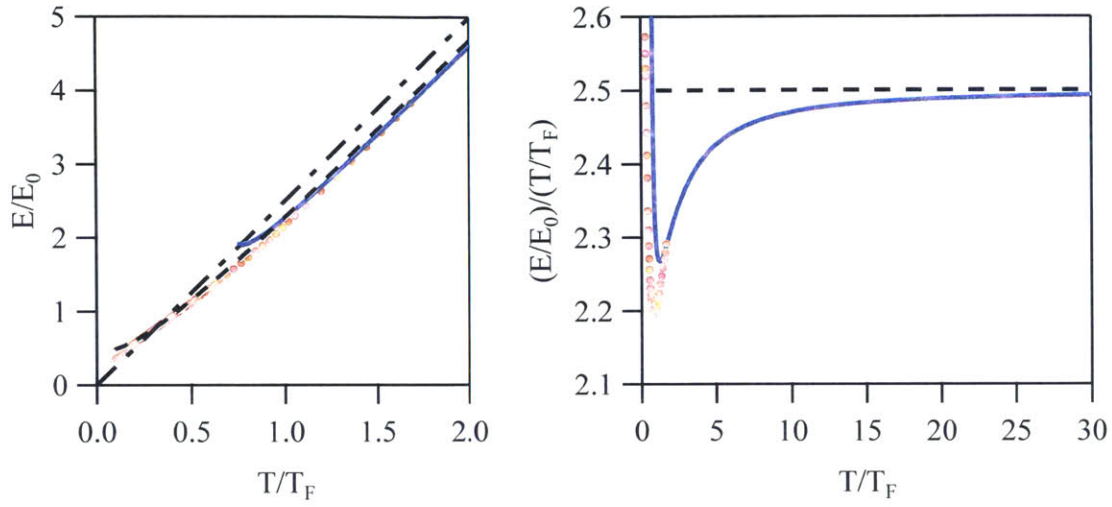

Figure 4-12: Energy as a function of temperature in the high temperature limit. (a) E/E_0 vs T/T_F up to $T/T_F = 2$. Red points: experimental data. Blue curve: third order virial expansion. Black dashed curve: ideal gas. We see that the third order virial expansion is accurate (in the case of energy) up to $T/T_F \simeq 1.2$. (b) $(E/E_0)/(T/T_F)$ vs T/T_F. The same convention is used as in (a) for the labels. The classical limit is 5/2. We see that the third order virial expansion starts to approach the classical limit around $T/T_F = 30$. This is where kinetic energy starts to dominate and the effect of quantum mechanics starts to disappear.

T [42], the reduced quantities $\tilde{E} \equiv \frac{5}{3}\frac{E}{NE_F} = \tilde{p}$ and $\tilde{F} \equiv \frac{5}{3}\frac{F}{NE_F} = \frac{5}{3}\frac{\mu}{E_F} - \frac{2}{3}\tilde{p}$ (Fig. 4-11) provide upper and lower bounds for ξ_B. Taking the coldest points of these three curves and including the systematic error due to the effective interaction range, we find $\xi_B = 0.376(4)$. The uncertainty in the Feshbach resonance is expected to shift ξ_B by at most 2% (see 4.15).

The measured value of ξ_B is consistent with the upper bound $\xi_B < 0.383(1)$ from [77], is close to the value of 0.36(1) from a self-consistent T-matrix calculation [93], and agrees with the result of an ϵ-expansion 0.367(9) [9]. Estimates from fixed-node quantum Monte-Carlo give 0.44(2) [37] and 0.42(1) [10] that provide upper bounds on ξ_B, and our measurement lies below these. The value of ξ_B we obtained agrees with several less accurate experimental determinations [81], but disagrees with the most recent experimental value 0.415(10) that was used to calibrate the pressure in [158].

Note that the EoS $\tilde{p}(T/T_F)$ gives the pressure equation of state $P(n,T) = \tilde{p}(T/T_F)P_0$. In the high-temperature limit, it reduces to the ideal gas relation $P = \frac{2}{3}E/\mathcal{V} = nk_BT$, in other words, $\tilde{p} = \frac{5}{2}T/T_F$ for large T/T_F. In Fig. 4-12, I show $\frac{E/E_0}{T/T_F}$, which in the classical limit should approach to 5/2. The system reaches the classical limit at $T/T_F \simeq 30$.

In the absence of condensation, the normalized energy and free energy would attain a value that is above ξ_B. Condensation lowers the energy and hence is the preferred phase. From the BCS theory, we have at $T = 0$ [131]

$$E - E_n = -N\frac{3}{8}\frac{\Delta_0^2}{E_F}, \tag{4.62}$$

where Δ_0 is the gap at zero temperature, and E_n is what the energy would be in the absence of condensation. If we model the energy of the normal phase as that of the non-interacting gas shifted vertically by ξ_n, then $(E - E_n)/E_0 = \xi_B - \xi_n$. This gives an estimate for the pairng gap $\Delta_0/E_F = 0.34$. This value has fortuitous agreement with the universal relation given by the BCS theory [223] $\Delta_0 = 1.764k_BT_c$, which with our measured T_c gives $\Delta_0/E_F = 0.29$, but deviates from the radio-frequency measurement that gives $\Delta/E_F = 0.44(3)$ [199],

4.13 Entropy of the unitary Fermi gas

We can obtain the entropy per particle $S/(Nk_B)$ with Eq. 4.61. In Fig. 4-13, I show $S/(Nk_B)$ as a function of T/T_F. At high temperatures, S is close to the entropy of an ideal Fermi gas at the same T/T_F. Above T_c, the entropy per particle is not small compared to k_B. Also, the specific heat C_V is not linear in T in the normal phase. Both of these observations show that the normal regime above T_c cannot be described in terms of a Landau Fermi liquid picture, although some thermodynamic quantities agree well with the expectation for a Fermi liquid (see [158] and a discussion on the validity of the Fermi liquid picture in 4.16). At the critical point we obtain $S_c = 0.73(13)Nk_B$, in agreement with [93]. Below about $T/T_F = 0.17$, the entropy

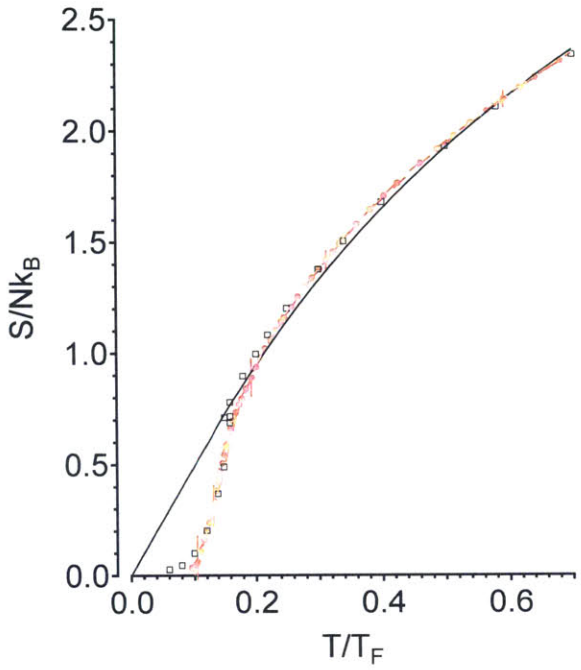

Figure 4-13: Entropy per particle of the unitary Fermi gas. At high temperatures, the entropy closely tracks that of a non-interacting Fermi gas (black solid curve). The open squares are from the self-consistent T-matrix calculation [93]. A few representative error bars are shown, representing one standard deviation. This figure is taken from [129]

quickly falls off compared to that of a non-interacting Fermi gas, which we again interpret as the freezing out of single-particle excitations due to formation of fermion pairs. At $T \simeq 0$, phonons dominate. They only have a minute contribution to the entropy [93], less than 0.02 k_B at $T/T_F = 0.1$, consistent with our measurements. At the lowest temperature, we obtain entropies less than $0.04\,Nk_B$, far below critical entropies required to reach magnetically ordered phases.

4.14 Realization of a Feynman quantum simulator

From $\tilde{p}$, μ/E_F, and T/T_F, we can obtain the universal functions $n\lambda^3 = f_n(\beta\mu)$ and $f_P = \beta\lambda^3 P$ (see Eqs. 4.51 and 4.53).

Fig. 4-14 shows the density and pressure normalized by their non-interacting counterparts at the same chemical potential and temperature, $\frac{n(\mu,T)}{n_0(\mu,T)} = \frac{f_n(\beta\mu)}{f_{n_0}(\beta\mu)}$ and

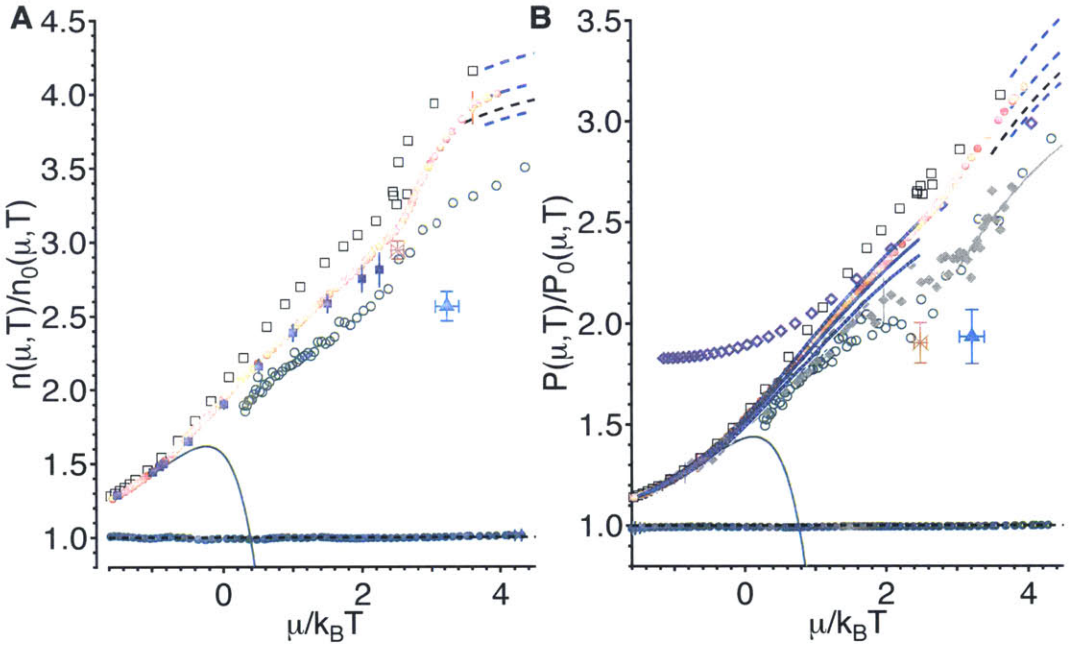

Figure 4-14: (a) Density and (b) pressure of a unitary Fermi gas versus μ/k_BT, normalized by the density and pressure of a non-interacting Fermi gas at the same chemical potential μ and temperature T. Red solid circles: experimental EoS. Blue dashed curves: low-temperature behavior with $\xi = 0.364$ (upper), 0.376 (middle), and 0.388 (lower). Black dashed curve: low-temperature behavior with ξ at upper bound of 0.383 from [77]. Green solid circles (black fine dashed line): MIT experimental data (theory) for the ideal Fermi gas. Blue solid squares (blue curve): Diagrammatic Monte Carlo [226] for density (pressure, with blue dashed curves denoting the uncertainty bands). Solid green line: 3rd order virial expansion. Open black squares: self-consistent T-matrix calculation [93]. Open green circles: lattice calculation [27]. Orange star and blue triangle: critical point from the Monte Carlo calculations [84] and [35], respectively. Solid diamonds: ENS experiment [158]. Purple open diamonds: Tokyo experiment [101].. This figure is taken from [129]

$\frac{P(\mu,T)}{P_0(\mu,T)} = \frac{f_P(\beta\mu)}{f_{P_0}(\beta\mu)}$. With the precision achieved here, we can compare the same quantities obtained by many-body theories and benchmark the validity of the theories.

For the normal phase, the DMC calculation agrees excellently with the data, as in [226]. Interestingly, the calculation of Ref. [93] which includes the first-order Feynman diagram already has decent agreement with the experimental measurement. Our data for pressure deviates from the ENS experiment [158] that was calibrated with an independently measured value of $\xi_B = 0.415(10)$ [157], and disagrees with the Tokyo experiment [101] that used a thermometry inconsistent with the virial expansion [143]. Around the critical point the density shows a strong variation, while the pressure, being the integral of the density over μ at constant T, is naturally less sensitive to the superfluid transition.

4.15 Systematic uncertainty due to non-universality

In a real experiment, we do not expect to completely satisfy the conditions for unitarity (discussed in 2.4.1). Here, I discuss systematic errors in our experiment from possible non-universal behavior. Recall that the s-wave scattering amplitude $f(k)$ for atom-atom collisions is

$$f(k) = \frac{1}{-\frac{1}{a} + \frac{1}{2}r_e k^2 + \mathcal{O}(k^4) - ik}, \tag{4.63}$$

where a is the scattering length, and r_e is the effective range. To be in the universal regime at unitarity, where one can write $n\lambda^3 = (\beta\mu)$, we require that the scattering length has to be large compared to the interparticle spacing $\sim 1/k_F$, while all other interaction-dependent length scales need to be small: $k_F r_e$, $k_F b ... \ll 1 \ll k_F a$. Otherwise, the additional length scales a, r_e and b will feature in the more complex equation of state that would be written as $n\lambda^3 = f(\beta\mu, \lambda/a, \lambda/r_e, \lambda/b)$. We discuss the possible influence of the various terms separately in the following.

4.15.1 Effect of the uncertainty in the Feshbach resonance position

The position of the wide Feshbach resonance used in this experiment was measured by Ref. [16] to be (834.15 ± 1.5) G. The systematic error from the uncertainty of $\delta B = 1.5$ G can be estimated using the contact [220], which quantifies the change in the energy of the system as the scattering length varies:

$$\left(\frac{\partial E}{\partial a^{-1}}\right)_{S,N,\mathcal{V}} = -\frac{\hbar^2}{4\pi m}\mathcal{C}\mathcal{V}. \tag{4.64}$$

Here, $\mathcal{C}$ is the contact density. From this relation, the change in the pressure and the density $n = \frac{\partial P}{\partial \mu}|_T$ with a can be estimated, provided the information of $\mathcal{C}$ is available. Diagrammatic Monte-Carlo calculations yield the temperature dependence of the contact [104]. We can therefore predict the true density profiles. We pick a typical temperature $T = 50$ nK and typical chemical potential $\mu = 225$ nK, generate the density profile with experimentally measured EoS, and then generate what the true density would be if the actual Feshbach resonance is different from 834.15 G by ± 1.5 G. The generated density profile can then be used to generate the compressibility EoS $\tilde{\kappa}(\tilde{p})$ in the manner described previously. The result is shown as the triangles pointing up and down in Fig. 4-15.

From these upper and lower bounds on the true compressibility EoS, we can deduce the upper and lower bounds for the various thermodynamic quantities. All errors grow as the temperature is lowered, as the contact increases. At the lowest temperatures, the error in the density is 3%, in the pressure 1%, in the chemical potential (and therefore ξ_B) 2%, in the normalized energy (free energy) 4% (1%). As it turns out, the entropy per particle S/N is only very weakly sensitive to the uncertainty in the resonance position, as the systematic error in the pressure and density cancel to a high degree. At the lowest temperatures, the error has grown to only $\pm 0.08 k_B$. At higher temperatures, the systematic error in S/N from the error in B_0 is much smaller than the statistical error bars. Note that δB is much larger than the variation of the magnetic field along the axial direction of the cloud of about

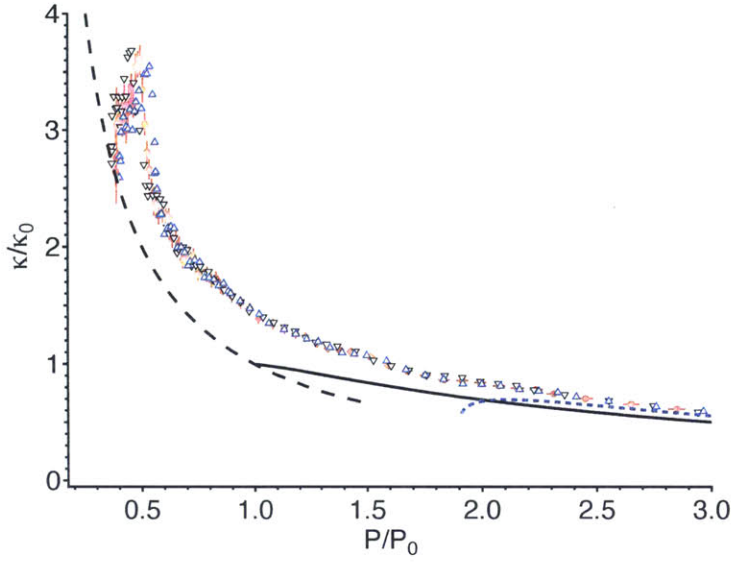

Figure 4-15: The effect of the uncertainty in the Feshbach resonance position on $\tilde{\kappa}(\tilde{p})$. The experimental result at 834.15 G is shown in red solid circles. The estimated curve is shown as triangles pointing up (down) if the true resonance position is at 832.65 G (835.65 G). Also shown are the third order virial expansion (blue solid curve), the non-interacting EoS (black solid curve), and the curve $\tilde{\kappa} = 1/\tilde{p}$ of the $T = 0$ limit.

15 mG due to the magnetic confinement, which contributes only a 0.01% error in ξ_B.

After our thermodynamic measurement, the Heidelberg group obtained an updated measurement that provides the position of the resonance with a better precision: $B_0 = 832.18(8)$ G [245]. The value of ξ_B corrected by this updated measurement of the resonance position is $\xi_B = 0.37(1)$, which is used in the subsequent experiments reported in this thesis.

4.15.2 Effective range correction

Recall from 2.4.1, the effective range near a Feshbach resonance can be modeled as [239]:

$$r_e = -2R_* \left(1 - \frac{a_{\rm bg}}{a}\right)^2 + \frac{4b}{\sqrt{\pi}} - \frac{2b^2}{a}, \tag{4.65}$$

where $R_* = 0.0269\,\text{nm}$ and $b = 2.1\,\text{nm}$ for ^{6}Li [239]. Therefore, near resonance, the main contribution to the effective range is b. At our typical densities, $1/k_F \approx 400\,\text{nm}$ and thus $k_F r_e = 0.012$. All thermodynamic potentials and thus also the ground state

energy $E = \frac{3}{5}\xi_B N E_F$ are expected to depend linearly on this parameter [238]. From the Quantum Monte-Carlo values of ξ_B versus effective range given in [80, 38] one can deduce a linear behavior of the upper bound on ξ_B:

$$\xi_B(k_F r_e) = \xi_B(r_e = 0) + 0.12(3) \cdot k_F r_e + \ldots . \tag{4.66}$$

With this dependence of ξ_B on the effective range, the error on ξ_B in our experiment is at most $+0.002$ or $+0.5\%$. This is small compared to the error due to the uncertainty in the Feshbach resonance position.

4.16 Fermi liquid behavior

In Fig. 4-16 we plot the density and pressure, normalized by that of a non-interacting Fermi gas at zero temperature, versus $(k_B T/\mu)^2$. The superfluid transition leads to a dramatic upturn at low T in the normalized density. Since we have already seen the downturn in the chemical potential (Fig. 4-11), this behavior in the normalized density is expected, as $n(\mu, T)/n_0(\mu, 0) \propto (\mu/E_F)^{-3/2}$. The minimum value of the normalized density occurs at $k_B T/\mu = 0.41(5)$, close to $k_B T_c/\mu_c = 0.40(3)$. At low temperatures, the normalized density reaches the zero-temperature value $1/\xi_B^{3/2}$. The normalized pressure is monotonic and saturates to a limiting value. The smooth behavior is expected for a second-order transition. The intercept of a straight line at the $T = 0$ limit $P(\mu, 0)/P_0(\mu, 0) = 1/\xi_B^{3/2}$ with the linear fit at high temperatures underestimates $k_B T_c/\mu_c$ by 22%. This method resulted in $k_B T_c/\mu_c = 0.32(3)$ in [158], inconsistent with our determination.

In a Fermi liquid, one has [158]

$$P(\mu, T) = P_0(\mu, 0)\left(\xi_n^{-3/2} + \frac{5\pi^2}{8}\xi_n^{-1/2}\frac{m^*}{m}\left(\frac{k_B T}{\mu}\right)^2\right) . \tag{4.67}$$

The linear behavior of the normalized density and pressure at high temperatures therefore resembles the expectation of a Fermi liquid. If one attempts to model

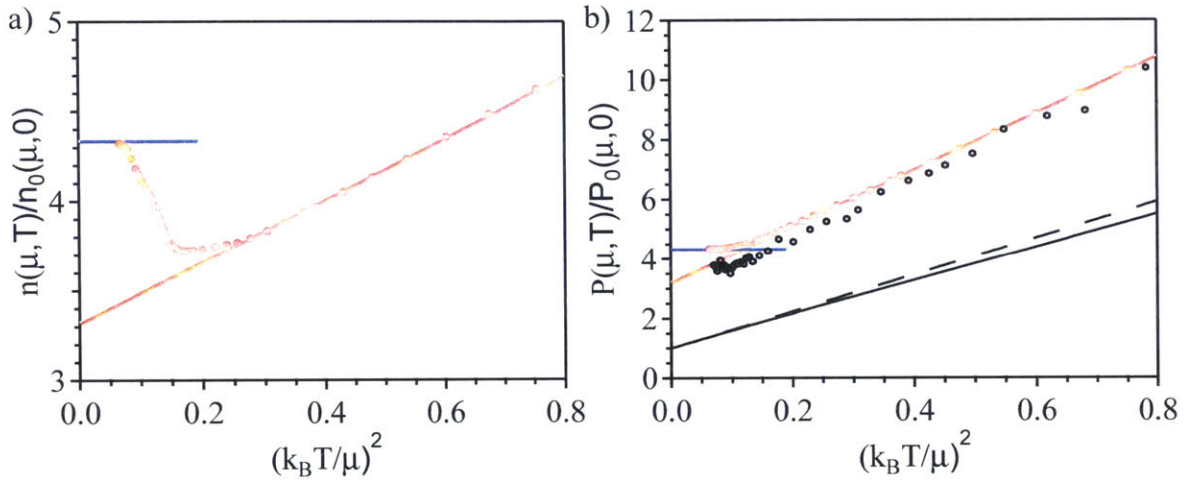

Figure 4-16: Modelling the thermodynamics in the normal phase as Landau Fermi liquid. (a) Density $n(\mu, T)$, normalized by the density $n_0(\mu, 0)$ of the non-interacting Fermi gas at zero temperature and same chemical potential μ, versus $(k_B T/\mu)^2$. The solid blue line denotes the zero-temperature limit, $n(\mu, 0)/n_0(\mu, 0) = 1/\xi_B^{3/2}$. The solid red line is a linear fit, resembling Fermi liquid behavior of the density above T_c. (b) Pressure $P(\mu, T)$, normalized by the pressure $P_0(\mu, 0)$ of the non-interacting Fermi gas at zero temperature and same chemical potential μ, versus $(k_B T/\mu)^2$. Red solid circles are the experimental data from this work. Black open circles are from [158]. The solid blue line denotes the zero-temperature limit, $P(\mu, 0)/P_0(\mu, 0) = 1/\xi_B^{3/2}$, the red solid line is a linear fit, resembling Fermi liquid behavior for the pressure above T_c. The black solid line shows the pressure of a non-interacting Fermi gas, the dashed solid line the linear approximation, valid if $T \ll T_F$.

the data with the Fermi liquid behavior, a linear fit versus $(k_BT/\mu)^2$ gives the fit parameters $\xi_n = 0.46(1)$, in agreement with the determination of the same parameter from the chemical potential (see 4.12), and $\frac{m^*}{m} = 1.04(2)$. Note that at $T \simeq 0$, the non-interacting Fermi gas also has the limiting behavior given by Eq. 4.67, with $\xi_n = 1$ and $m^* = m$. In the same temperature regime where we perform a linear fit to the normalized pressure, the same fit for a non-interacting Fermi gas (solid line in Fig. 4-16) gives $\frac{m_0^*}{m} = 0.91$, differing from the value of unity for a non-interacting Fermi gas. The reason for this discrepancy is that the pressure of the non-interacting Fermi gas in the temperature range $0.2 \lesssim (k_BT/\mu)^2 \lesssim 1$ is not yet in the linear regime valid at low temperatures (shown as the dashed line in Fig. 4-16). In the case of the unitary Fermig gas, the regime expected of Fermi liquid $(k_BT/\mu)^2 \lesssim 0.15$ is already below the critical point. Equivalently, the entropy per particle (see 4.13) above the critical point is not much smaller than k_B. In addition, the specific heat is not linear above T_c (see 4.11). In lieu of these observations, we conclude that the usual Landau Fermi liquid picture, valid when the temperature is much smaller than the Fermi energy, cannot properly describe all thermodynamic properties of the normal unitary Fermi gas. Therefore, one does not expect to truly observe a Fermi liquid in the normal phase.

Although the agreement with the Landau Fermi liquid is fortuitous, we may nevertheless use it to model the data. The fit-parameter m^* should not be taken literally as the effective mass of particles in the normal state. However, the general observation that the thermodynamic properties of the normal phase at unitarity resembles the expectation of a weakly renormalized normal state [158] remains true. Compared to the non-interacting Fermi gas in the same regime of k_BT/μ, the unitary Fermi gas has an apparent effective mass enhancement of only about 12%.

Note that our determination of fit parameters differs from the previous result [158] $\frac{m*}{m} = 1.13(3)$ and $\xi_n = 0.51(2)$, possibly due to the mentioned differences in calibration between the experiments.

4.17 Conclusion

In conclusion, we have performed thermodynamic measurements of the unitary Fermi gas across the superfluid phase transition at the level of uncertainty of a few percent, without any fits or input from theory, enabling validation of theories for strongly interacting matters. Similar unbiased methods can be applied to other systems, for example, two-dimensional Bose and Fermi gases or fermions in optical lattices. In particular, a fitless measurement of the 2D Bose gas based on the method described here has been performed [56].

The measurement presented in this chapter represents a fruit of the quantum simulation program envisioned in the past two decades: realize a model system with cold atoms in a well-controlled environment, and ask the nature itself with experiments to obtain properties of the model. The answers to the questions of what is the ground state energy and the critical temperature are now on a firm footing. The precise quantitative knowledge of the thermodynamics enables the study of other topics of the unitary Fermi gas. For example, the measured EoS enables the prediction of the temperature dependence of collective modes [222] and provides an input necessary for theories on dynamics [31]. The precision thermometry enabled by this study will also be useful in the experimental studies on the unitary Fermi gas in general.

Chapter 5

Thermodynamics of a trapped gas and temperature dependence of collective modes

5.1 Introduction

Precision measurement of the homogeneous equation of state (EoS) provides an important resource for the further study of the unitary Fermi gas. On one hand, knowledge of the EoS enables a more precise characterization of the cloud, such as its temperature. On the other hand, the EoS provides a necessary input for the theory of non-equilibrium dynamics. In this chapter, I will describe two studies that take advantage of the EoS measurement reported in the previous chapter.

Note that in this chapter, a number of thermodynamic quantities are defined in terms of the global properties of a harmonically trapped gas. The Fermi energy is defined by the atom number as $E_{F,\mathrm{trap}} = \hbar\bar{\omega}(3N)^{1/3}$, where $\bar{\omega} = (\omega_x\omega_y\omega_z)^{1/3}$ is the geometric mean of the trapping frequencies. The Fermi temperature is defined by this Fermi energy, $k_B T_{F,\mathrm{trap}} = E_{F,\mathrm{trap}}$. Extensive quantities, such as energy E, grand potential Ω, free energy F, heat capacity C_V, and entropy S, are defined in terms of the entire cloud. The chemical potential μ refers to the chemical potential at the

center of the cloud.

5.2 Thermodynamics and thermometry of trapped gases from the column density

Perhaps the most obvious method to apply the homogeneous equation of state for thermometry is to fit the density profile of the cloud to the EoS. In this approach, one would take a cloud with cylindrical symmetry, apply the inverse Abel transform to obtain the density distribution $n(\mathbf{r})$, and fit the density distribution to the density equation of state $n = \lambda^{-3} f_n(\beta(\mu - V(\mathbf{r})))$, where $\lambda = \sqrt{2\pi\hbar^2/(mk_BT)}$ and $\beta = 1/(k_BT)$. However, this technique is not suitable for experiments with large aspect ratios or small atom numbers, as the inverse Abel transform requires a large radial size in order to generate a good signal. An alternative, in the case of harmonic confinement, is to generate the twice-integrated column density $n_{1D}(z) = \int \mathrm{d}x\mathrm{d}y\, n$, which is proportional to the local pressure according to the relation $P(T, \mu - V(z)) = \frac{m\omega_x\omega_y}{2\pi} n_{1D}(z)$ [98, 158]. The local pressure can then be fitted to the pressure equation of state $P = k_BT\lambda^{-3} f_P(\beta(\mu - V))$.

In this section, I describe a technique for obtaining the thermodynamics of harmonically trapped gases from the column density. In this method, the entire EoS is determined from the column density and its moments with respect to the trapping potential. The EoS measured this way is a relation between global thermodynamic quantities of the entire cloud, e.g. the total energy and atom number. Similarly to the no-fit method for the homogeneous EoS described in the previous chapter, this method does not require the input of thermodynamic quantities, such as the temperature T and the chemical potential μ, whose determination requires the use of a fitting procedure or an external thermometer. This procedure is suitable both for determing the EoS and also for thermometry and calibration, if the EoS is already known. In particular, since the inverse Abel transformation is not needed, this procedure is suitable for all experiments where a harmonic trapping potential can be safely assumed,

regardless of the aspect ratio. This is of practical importance in many experimental setups which have large aspect ratios. We demonstrate the procedure on Fermi gases at unitarity, and present the EoS of trapped unitary Fermi gases. We also describe the inverse procedure to obtain the homogeneous EoS from the EoS of a trapped gas. This work is reported in Ref. [126].

In a given trapped gas, the total atom number N is determined by the temperature T and the chemical potential μ. The relation $N(T,\mu)$ is a parametrization of the EoS. In the local density approximation (LDA), the spatial density n at any given location $\mathbf{r}$ is given by $n(T,\mu,\mathbf{r}) = n(T,\mu - V(\mathbf{r}))$, where $n(T,\mu)$ is the density of the homogeneous system at temperature T and chemical potential μ, and $V(\mathbf{r})$ is the trapping potential. We shall work with a harmonic trap $V(\mathbf{r}) = m(\omega_x^2 x^2 + \omega_y^2 y^2 + \omega_z^2 z^2)/2$, where ω_i is the trapping frequency in the i^{th} direction. Imaging of the atomic cloud measures the column density $n_{2\text{D}}(T,\mu,V(y,z)) = 2\int_0^\infty \mathrm{d}x\, n(T,\mu - V(\mathbf{r}))$, where $V(y,z) = V(x = 0,y,z)$. With integration by parts, one obtains the following relation

$$\begin{aligned} & n_{2\text{D}}(T,\mu,V(y,z)) \\ & = xn(T,\mu - V(y,z) - m\omega_x^2 x^2/2)\big|_{x=0}^{x=\infty} \\ & \quad + m\omega_x^2 \int_0^\infty \mathrm{d}x\, x^2 \frac{\partial}{\partial\mu} n(T,\mu - V(y,z) - m\omega_x^2 x^2/2)\,. \end{aligned} \tag{5.1}$$

For large x, $n \sim e^{-\beta m\omega_x^2 x^2/2}$ and therefore the first term vanishes. The integral of the second term is equivalent to an integral over all volume $\int \mathrm{d}^3 r$ with a change of variable $r = x$. Therefore, we have shown that the column density $n_{2\text{D}}(y,z)$ of a gas with chemical potential μ at temperature T is related to the rate of change of the atom number with respect to the chemical potential at temperature T and chemical potential $\mu - V(y,z)$:

$$\frac{\partial}{\partial\mu} N(T,\mu - V) = \frac{2\pi}{m\omega_y\omega_z} n_{2\text{D}}(T,\mu,V). \tag{5.2}$$

Then, the total atom number at temperature T and chemical potential $\mu - V$ is

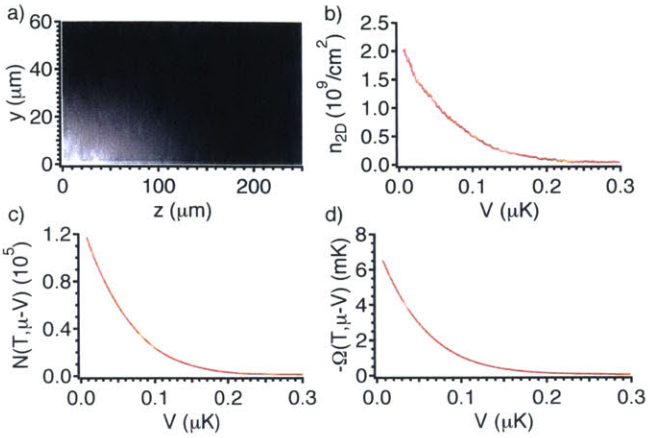

Figure 5-1: a) Imaging of an atomic cloud measures the once-integrated column density $n_{2D}(y, z)$. b) The column density can be equipotential-averaged. Shown is the curve n_{2D} vs. V. The column density at potential V, taken at temperature T and with a chemical potential μ, is directly proportional to the rate of change $\frac{\partial N}{\partial \mu}$ at the same temperature T and at the chemical potential $\mu - V$. Its integral with respect to V leads to c) atom number of a trapped gas at the same T with chemical potential $\mu - V$. Integrating once more with respect to V leads to d) the grand potential Ω at T and chemical potential $\mu - V$.

given by

$$N(T, \mu - V) = \frac{2\pi}{m\omega_y\omega_z} \int_V^\infty \mathrm{d}V'\, n_{2D}(T, \mu, V'). \tag{5.3}$$

In the grand canonical ensemble, the atom number is related to the grand potential $\Omega = -\int \mathrm{d}\mathcal{V}\, P$ by $N = -\frac{\partial \Omega}{\partial \mu}|_{T,\mathcal{V}}$. Therefore, one can construct one more quantity by an additional integration

$$\Omega(T, \mu - V) = -\int_V^\infty \mathrm{d}V'\, N(T, \mu - V'). \tag{5.4}$$

Since any three state variables determine the EoS, we can replace T and μ in favor of the directly measurable quantities. To relate $\partial N/\partial \mu$ to a thermodynamic quantity, we note that in the homogeneous case, the derivative $\partial n/\partial \mu$ is related to compressibility $\kappa = \frac{1}{n^2}\frac{\partial n}{\partial \mu}$. Therefore, in the trapped gas, we can define a generalized compressibility $\kappa \equiv \frac{1}{N^2}\frac{\partial N}{\partial \mu}$. Hence, the column density and its integrals with respect to trapping potential yields the EoS $\kappa(N, \Omega)$.

We demonstrate this method for trapped Fermi gases at unitarity. In Fig. 5-1,

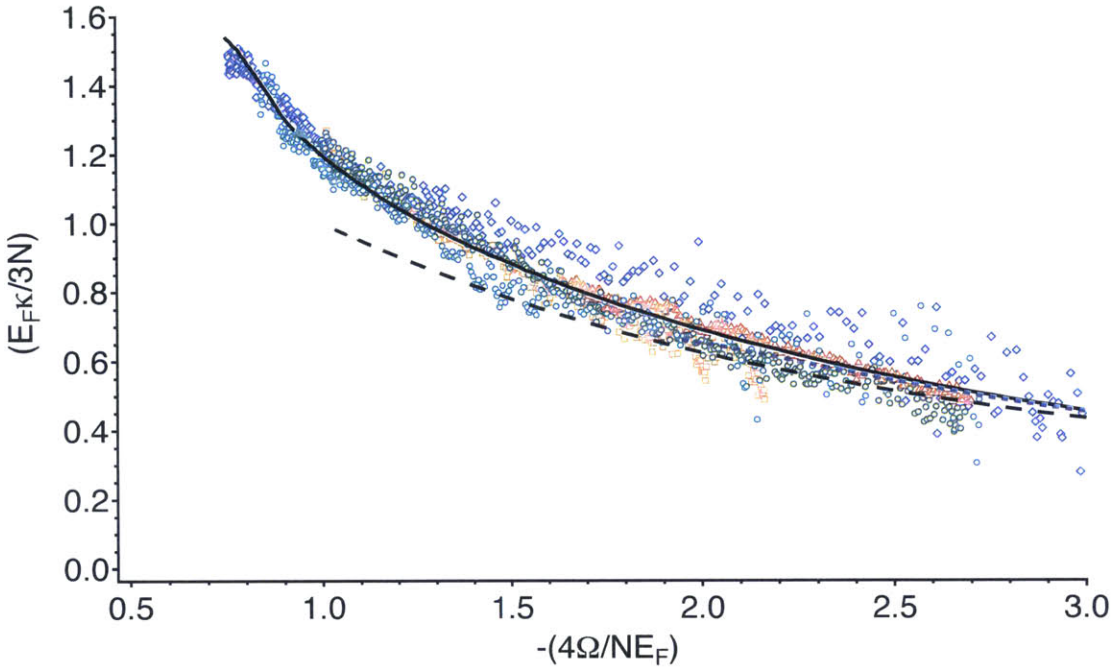

Figure 5-2: Trap compressibility $\kappa \equiv \frac{1}{N^2}\frac{\partial N}{\partial \mu}$ versus grand potential Ω of the trapped unitary Fermi gas. The compressibility and grand potential are normalized by their respective values $\kappa_0 = 3/(NE_{F,\mathrm{trap}})$ and $\Omega_0 = -NE_{F,\mathrm{trap}}/4$ for a non-interacting Fermi gas at the same density. The black solid curve shows the EoS of a trapped unitary Fermi gas obtained from the EoS of a homogeneous gas. The blue dashed curve is the third order virial expansion. Colored open circles are the universal curves obtained from different atomic images, ranging from hot (red) to intermediate temperatures (orange and green) and cold (light blue and blue). The atomic image from Fig. 5-1 corresponds to light blue. The EoS of a non-interacting gas is shown as the black dashed curve.

we show (a) the two-dimensional column density $n_{2\mathrm{D}}(y,z)$, (b) the equipotential-averaged column density $n_{2\mathrm{D}}$ vs. V (or, alternatively, one can plot $\bar{n}_{2\mathrm{D}}$ vs z where $\bar{n}_{2\mathrm{D}}(z)$ is averaged over the contour $z^2 + (\omega_y/\omega_z)^2 y^2 = \text{const.}$), (c) the atom number $N(T, \mu - V)$, where $N(T, \mu - V)$ can be constructed either by Eq. (5.4) or by the following:

$$N(T, \mu - \frac{m}{2}\omega_z^2 z^2) = 2\pi \frac{\omega_z^2}{\omega_x \omega_y} \int_{z=\frac{1}{\omega_z}\sqrt{\frac{2V}{m}}}^{\infty} \mathrm{d}z'\, z' \bar{n}_{2D}(T, \mu, z') \tag{5.5}$$

and (d), the grand potential $-\Omega(T, \mu - V)$, which can be constructed by either

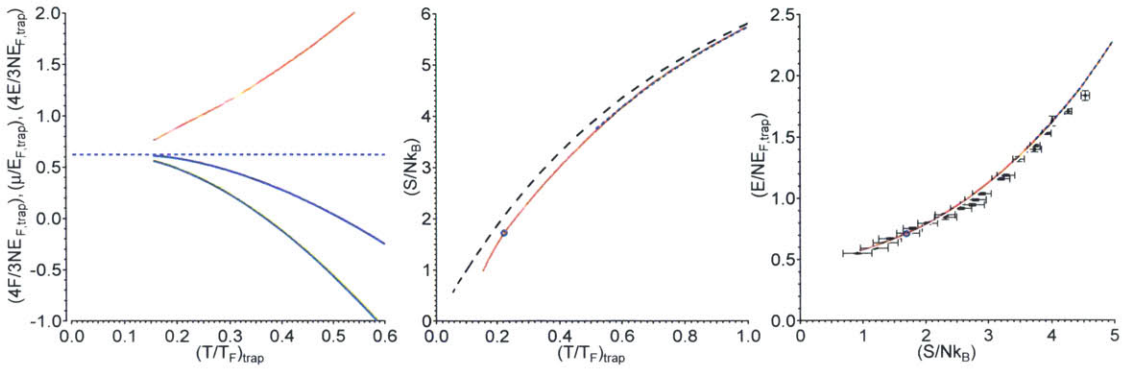

Figure 5-3: a) Total energy (red solid curve), total free energy (green solid curve), and chemical potential (blue solid curve) of a trapped Fermi gas as a function of temperature, obtained from the homogeneous EoS. Energy and free energy are normalized by the corresponding quantities for a non-interacting Fermi gas with the same atom number at $T = 0$, $3NE_{F,\mathrm{trap}}/4$. Chemical potential is normalized by the Fermi energy $E_{F,\mathrm{trap}}$. Temperature is normalized by $T_{F,\mathrm{trap}}$. The blue dashed line is the $T = 0$ limit $\sqrt{\xi_B}$, where $\xi_B = 0.376$ [129]. b) Entropy per particle S/Nk_B as a function of reduced temperature $T/T_{F,\mathrm{trap}}$. The red curve comes from the homogeneous EoS. The blue dashed curve is from the third virial expansion. The black dashed curve is for the non-interacting gas. c) Entropy vs. energy. The red curve comes from the homogeneous EoS. Black solid circles are from the measurement of Ref. [144]. The critical point is marked by an open blue circle in both b) and c).

Eq. (5.3) or one of the following:

$$\begin{aligned} & \Omega(T, \mu - V) \\ = & -\frac{2\pi}{m\omega_y\omega_z}\int_V^\infty \mathrm{d}V'\,(V' - V) n_{2\mathrm{D}}(T, \mu, V') \\ = & -\frac{\pi m\omega_z^4}{\omega_y\omega_z}\int_{z=\frac{1}{\omega_z}\sqrt{\frac{2V}{m}}}^\infty \mathrm{d}z'\,(z'^2 - z^2) z' \bar{n}_{2\mathrm{D}}(T, \mu, z')\,. \end{aligned} \tag{5.6}$$

We define the normalized compressibility $\tilde{\kappa} \equiv \kappa/\kappa_0$, where $\kappa_0 = 3/(NE_{F,\mathrm{trap}})$ is the compressibility of a zero-temperature non-interacting gas at the same atom number N. Likewise, we define the normalized grand potential $\tilde{\Omega} \equiv \Omega/\Omega_0$, where $\Omega_0 = -NE_{F,\mathrm{trap}}/4$ is the zero-temperature non-interacting energy at the same atom number N. Due to universality, $\tilde{\kappa}$ vs. $\tilde{\Omega}$ produced by any image of a trapped Fermi gas at unitarity must lie on the same curve. In Fig. 5-2, we show the curve $\tilde{\kappa}(\tilde{\Omega})$ from the atomic image shown in Fig. 5-1 as well as from other atomic images. We compare this

to the EoS of a trapped Fermi gas at unitarity obtained from the homogeneous EoS measured in Ref. [129]. Homogeneous and trapped EoS are related to one another through a class of universal function $f_i(\beta\mu)$, where i takes on integer or half-integer values. We define $f_{3/2}(x)$ as the universal function that gives the phase density, $n(\mu, T) = \lambda^{-3} f_{3/2}(\beta\mu)$. One can then generate various moments of the EoS with operator $\mathcal{M}_j$ defined as follow:

$$f_{i+j}(\beta\mu) = \mathcal{M}_j[f_i(\beta\mu)] \equiv \frac{1}{\Gamma(j)} \int_{-\infty}^{\beta\mu} dx (\beta\mu - x)^{j-1} f_i(x)\,, \tag{5.7}$$

for $j > 0$. For $f_i(x \to -\infty) \to e^x$, one can show that $f_{i+j+k} \equiv \mathcal{M}_{i+j}[f_k] = \mathcal{M}_i[\mathcal{M}_j[f_k]]$. In addition, since $\mathcal{M}_1[f(x)] = \int_{-\infty}^{x} \mathrm{d}x'\, f(x')$, one can define $\mathcal{M}_{-1}[f(x)] \equiv df/dx$. The various moments of the homogeneous EoS relate to the thermodynamic quantities of a trapped gas as follows:

$$\frac{\partial}{\partial\mu} N(T,\mu) = \frac{1}{k_B T} \left(\frac{k_B T}{\bar{\omega}\hbar}\right)^3 f_2(\beta\mu)\,, \tag{5.8}$$

$$N(T,\mu) = \left(\frac{k_B T}{\bar{\omega}\hbar}\right)^3 f_3(\beta\mu)\,, \tag{5.9}$$

$$\Omega(T,\mu) = -k_B T \left(\frac{k_B T}{\bar{\omega}\hbar}\right)^3 f_4(\beta\mu)\,. \tag{5.10}$$

We see that the trapped EoS for the unitary Fermi gas obtained with the prescribed procedure agrees excellently with that obtained from the homogeneous EOS.

From $\tilde{\kappa}$ vs. $\tilde{\Omega}$ one can obtain all other thermodynamic quantities. One can obtain the reduced temperature $(T/T_F)_{\mathrm{trap}}$ by the following transformation

$$\left(\frac{T}{T_F}\right)_{\mathrm{trap}} = \left(\frac{T}{T_F}\right)_{i,\mathrm{trap}} \exp\left(\frac{1}{4}\int_{\tilde{\Omega}_i}^{\tilde{\Omega}} \mathrm{d}\tilde{\Omega}\, \frac{1}{\tilde{\Omega} - \frac{1}{\tilde{\kappa}}}\right)\,. \tag{5.11}$$

where $(\tilde{\Omega}_i, (T/T_F)_{i,\mathrm{trap}})$ is some initial point from which to integrate. We note that this relation can be applied on a single profile regardless of whether the gas is at unitarity, as long as one has a starting point $(\tilde{\Omega}_i, (T/T_F)_{i,\mathrm{trap}})$ from which to perform the integration. This relation, coupled with the prescribed technique to obtain $\tilde{\Omega}$ vs.

$\tilde{\kappa}$, provides a powerful way to perform thermometry. One can simply obtain $\tilde{\Omega}$ vs. $\tilde{\kappa}$ from the various moments of the column density, perform the above integration, and obtain the temperature of the cloud. The calibration curve $-\tilde{\Omega}$ vs. $(T/T_F)_{\text{trap}}$ in the special case of the unitary Fermi gas is Ω/Ω_0 vs. $(T/T_F)_{\text{trap}}$, and is shown as the red curve in Fig. 5-3 (a). For the atomic cloud in Fig. 5-1, we have $T/T_F = 0.175$, with absolute temperature $T = 47$ nK and Fermi energy $E_F = 266$ nK.

The reduced chemical potential μ/k_BT can be obtained by

$$\frac{\mu}{k_BT} = \left(\frac{\mu}{k_BT}\right)_i - \int_{\left(\frac{T}{T_F}\right)_{i,\text{trap}}}^{\left(\frac{T}{T_F}\right)_{\text{trap}}} \mathrm{d}\left(\frac{T}{T_F}\right) \frac{1}{\tilde{\kappa}} \left(\frac{T_F}{T}\right)^2 . \tag{5.12}$$

The entropy is then given by

$$\frac{S}{k_BN} = \tilde{\Omega}\left(\frac{T}{T_F}\right)^{-1}_{\text{trap}} - \frac{\mu}{k_BT} . \tag{5.13}$$

We display normalized energy, chemical potential, free energy (Fig. 5-3 a)), and entropy (Fig. 5-3 b)) as a function of reduced temperature $(T/T_F)_{\text{trap}}$. The critical temperature in the trap is $(T_c/T_F)_{\text{trap}} = 0.223(15)$. At unitarity, the energy of the trapped Fermi gas is directly proportional to the grand potential, $E = -3\Omega$. The trapped energy, chemical potential, free energy, and entropy are featureless and do not display a clear thermodynamic signature for superfluid transition. In Fig. 5-3 c), we display the energy vs entropy curve obtained from the homogeneous EoS, and compare with Ref. [144]. We see that the two results have good agreement.

The average heat capacity of a trapped unitary Fermi gas is given by

$$\frac{C_V}{Nk_B} = 12\frac{f_4(\beta\mu)}{f_3(\beta\mu)} - 9\frac{f_3(\beta\mu)}{f_2(\beta\mu)} = 4\left(\frac{T_{F,\text{trap}}}{T}\right)\left(\tilde{\Omega} - \frac{1}{\tilde{\kappa}}\right) . \tag{5.14}$$

We display the average heat capacity as a function of reduced temperature in Fig. 5-4. We see the thermodynamic signature of the superfluid transition in the average heat capacity. The average heat capacity decreases steadily as temperature is lowered, reaches a minimum and begins to increase sharply at the critical point, reaches a

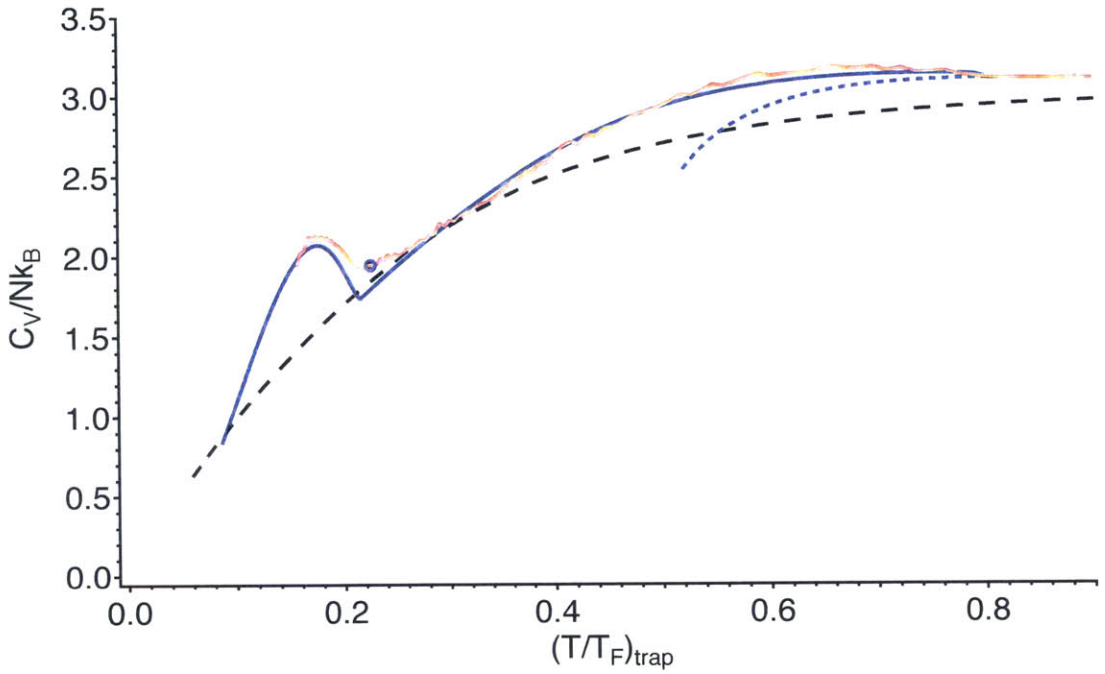

Figure 5-4: Average heat capacity C_V/Nk_B as a function of reduced temperature $(T/T_F)_{\text{trap}}$. Red curve is obtained from homogeneous EoS. The blue solid curve is obtained from a theoretical model that incorporates the Monte Carlo calculation of Ref. [226] in the normal phase, and Bardeen-Cooper-Schrieffer (BCS) theory with phonons in the superfluid phase. The blue dashed curve is from the third virial expansion. The black dashed curve is for the non-interacting gas. The critical point $(T_c/T_F)_{\text{trap}} = 0.223$ is marked by the open blue circle.

maximum, and then decreases once again torwards zero. This is the expected behavior of the heat capacity in a trapped gas, as the homogeneous heat capacity displays a jump at the critical point.

In Fig. 5-5 we show the energy versus entropy for a harmonically trapped Fermi gas at unitarity, obtained from our experimental determination of the homogeneous density EoS and temperature. The data are compared with the earlier measurement of the same quantities by the Duke group [143] that have been corrected in [144] to take into account the finite interaction strength present in the entropy measurement. The agreement is excellent. Note that the energy vs entropy curve is smooth and on its own does not allow for a determination of the critical energy or entropy, in contrast to earlier interpretations of the Duke data [143, 144]. From the bulk thermometry, we obtain $E_{c,\text{trap}} = 0.698(23)NE_{F,\text{trap}}$ and $S_{c,\text{trap}} = 1.70(10)Nk_B$. This result is in

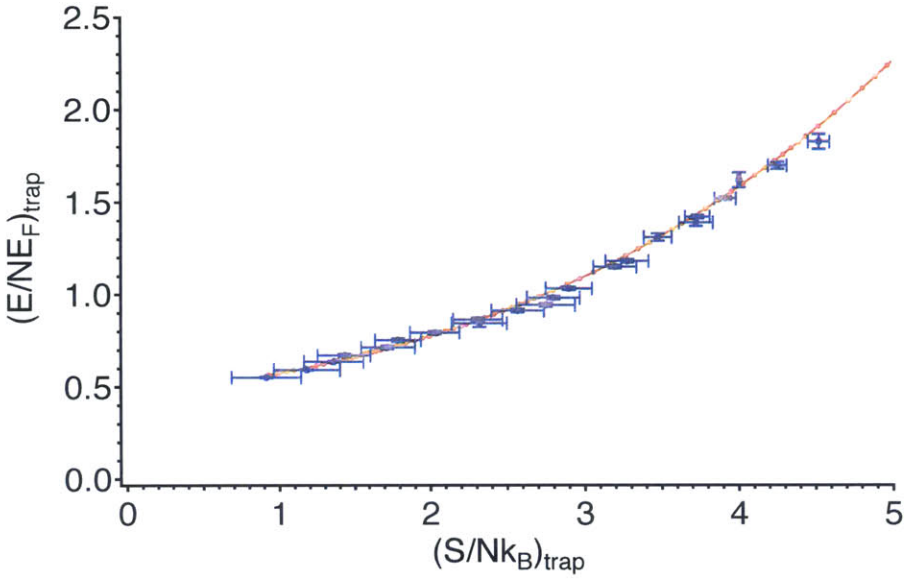

Figure 5-5: Energy vs entropy of a harmonically trapped gas at unitarity, deduced from our measured bulk equation of state (red solid dots). The curve is smooth, as required by thermodynamics. Blue diamonds: Duke experiment [143, 144], for which an interaction correction has been applied to the entropy.

reasonable agreement with the calculation of [94], which gives $0.656 < \frac{E_{\mathrm{c,trap}}}{NE_{F,\mathrm{trap}}} < 0.677$ and $1.56 < \frac{S_{\mathrm{c,trap}}}{Nk_B} < 1.66$.

The trap-averaged quantities do not show a pronounced signature around the phase transition which was claimed by the Duke measurement [144]. In the Duke experiment, a fit was applied to $E_{\mathrm{trap}}(S_{\mathrm{trap}})$ to parameterize the data, and the parametrization was then used to generate the other thermodynamic quanitites. The fit assumed a model containing a sharp feature, which was taken to be either a discontinuity or a cusp in the temperature dependence of the trap-averaged heat capacity. In Fig. 5-6, we compare the trap-averaged quantities from the homogeneous EoS with the Duke group's result. The temperature-dependence of the energy, entropy, and the heat capacity from the Duke experiment all manifest a pronounced feature of the phase transition, because the signature of the transition is built into the model used to fit the heat capacity. In contrast, the trap-averaged energy and entropy obtained from the homogeneous EoS are smooth. The trap-averaged heat capacity shows a more pronounced signature. However, the feature is rather smooth, contrary to what was

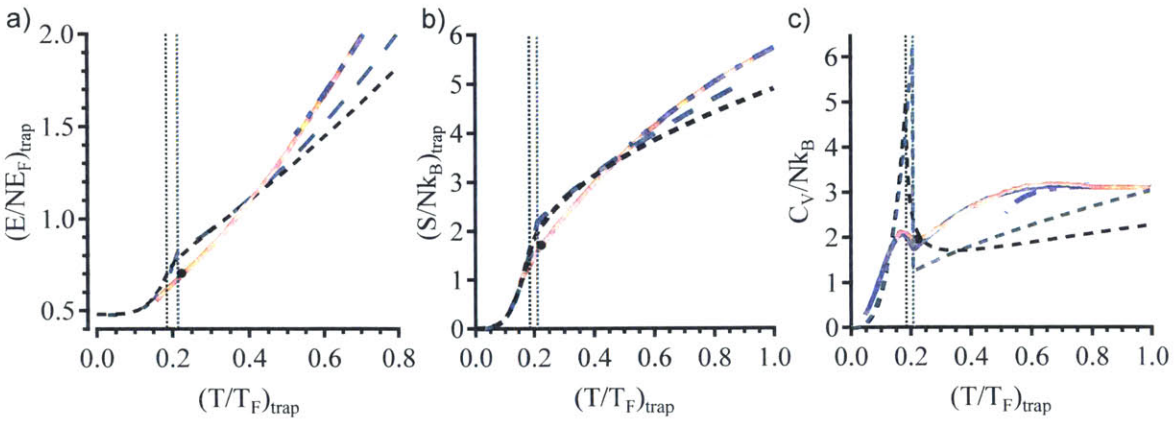

Figure 5-6: (a) Averaged energy $(E/NE_F)_{\text{trap}}$, (b) average entropy $(S/Nk_B)_{\text{trap}}$, and average heat capacity C_V/Nk_B as a function of reduced temperature T/T_F. Red curve is obtained from homogeneous EoS. The black (green) dashed curves correspond to the Duke model that assumes discontinuity (cusp) in the heat capacity at the phase transition, and the dashed vertical lines with the same color indicate the critical point obtained by the corresponding model. The blue dashed curve is from third virial expansion. The black dashed curve is for the non-interacting gas. The critical point $(T_c/T_F)_{\text{trap}} = 0.223$ is marked by the black circle.

assumed in the Duke model.

Once one has obtained the EoS of the trapped gas, one can transform it back into the EoS of the homogeneous gas, provided that one has enough precision and that the local density approximation is valid. The procedure is analogous to applying an inverse Abel transformation, and the problem is formally equivalent to the following: given the function

$$f_3(x) \equiv \sqrt{\frac{2}{\pi}} \int_{-\infty}^{x} \sqrt{x - x'} f(x') \,, \tag{5.15}$$

one wants to extract $f(x)$ from $f_3(x)$.

First, we show the following identity, assuming $f(x) \to e^x$ as $x \to -\infty$:

$$\begin{aligned} \int_0^\infty \mathrm{d}x \, f(x_0 - x^2/2) &= x f(x_0 - x^2/2)\big|_0^\infty - \int_0^\infty \mathrm{d}x \, x^2 f'(x_0 - x^2/2) \\ &= \frac{1}{4\pi} \int \mathrm{d}^3 r \, f'(x_0 - r^2/2) \end{aligned} \tag{5.16}$$

This is essentially the same statement as Eq. 5.1: column density coming from integration along one axis is proportional to derivative of the atom number with respect

to the chemical potential. Now, the inverse Abel transformation says if

$$F(y) = 2\int_0^\infty \mathrm{d}x\, f(\sqrt{x^2+y^2}), \tag{5.17}$$

then

$$f(\rho) = -\frac{1}{\pi}\int_\rho^\infty \frac{\partial F}{\partial y}\frac{\mathrm{d}y}{\sqrt{y^2-\rho^2}}. \tag{5.18}$$

Now, let us define $g(\rho) \equiv f(x_0 - \rho^2/2)$, and let $G(y) \equiv 2\int_0^\infty \mathrm{d}x\, g(\sqrt{x^2+y^2})$ be its forward Abel transform. Then, using Eq. 5.16, we obtain the followign expression for $G(y)$:

$$\begin{aligned} G(y) &= 2\int_0^\infty \mathrm{d}x\, f(x_0 - (x^2+y^2)/2) \\ &= \frac{1}{2\pi}\int_0^\infty \mathrm{d}^3 r\, f'(x_0 - (y^2+r^2)/2). \end{aligned} \tag{5.19}$$

Then, the inverse Abel transform gives us

$$\begin{aligned} g(\rho) &= -\frac{1}{\pi}\int_\rho^\infty \frac{\partial G}{\partial y}\frac{\mathrm{d}y}{\sqrt{y^2-\rho^2}} \\ &= -\frac{1}{\pi}\int_\rho^\infty \frac{\mathrm{d}y}{\sqrt{y^2-\rho^2}}\frac{1}{2\pi}\int_0^\infty \mathrm{d}^3 r\, f''(x_0 - (y^2-y^2)/2)(-y) \end{aligned} \tag{5.20}$$

or, in other words,

$$f(x_0 - \rho^2/2) = \frac{1}{2\pi^2}\int_\rho^\infty \mathrm{d}y\, \frac{y}{\sqrt{y^2-\rho^2}}\int_0^\infty \mathrm{d}r^3\, f''(x_0 - (y^2-r^2)/2). \tag{5.21}$$

Setting $\rho = 0$, then we have

$$f(x_0) = \frac{1}{2\pi^2}\int_0^\infty \partial y\, \frac{\partial^2}{dx^2}\int \mathrm{d}^3 r\, f(x_0 - (y^2+r^2)/2). \tag{5.22}$$

We note that, with a change of variables $x \equiv x_0 - r^2/2$, the following identity holds:

$$\begin{aligned}\int \mathrm{d}^3 r\, f(x_0 - r^2/2) &= 4\pi \int_0^\infty \mathrm{d}r\, r^2 f(x_0 - r^2/2) \\ &= 4\pi\sqrt{2} \int_{-\infty}^{x_0} \mathrm{d}x\, \sqrt{x_0 - x} f(x) \qquad (5.23) \\ &= (2\pi)^{3/2} f_3(x_0). \qquad (5.24)\end{aligned}$$

Therefore, with the reduced temperature $(T/T_F)_{\mathrm{trap}} = (3f_3)^{-1/3}$ and reduced chemical potential $\beta\mu$, the inverse transformation for $f_3(\beta\mu)$ is given by

$$\begin{aligned}f_{3/2}(\beta\mu) &= \frac{1}{\sqrt{\pi}} \int_{-\infty}^{\beta\mu} \mathrm{d}x\, (\beta\mu - x)^{-1/2} f_3''(x) = \mathcal{M}_{1/2}[f_2'(\beta\mu)] \\ &= \frac{2}{\sqrt{\pi}} \int_{-\infty}^{\beta\mu} \mathrm{d}x\, (\beta\mu - x)^{1/2} f_3'''(x) = \mathcal{M}_{3/2}[f_2''(\beta\mu)]\,.\end{aligned} \qquad (5.25)$$

We can test this procedure it out on $f_{3/2}(x) = e^{kx}$. The corresponding f_3 is $f_3(x) = \frac{e^{kx}}{k^{3/2}}$. Then, $f_3''(x) = \sqrt{k} e^{kx}$, and Eq. 5.25 gives $\frac{1}{\sqrt{\pi}} \int_{-\infty}^{x} \mathrm{d}z\, (x - z)^{-1/2} f_3''(z) = e^{kx}$.

In conclusion, we have provided a procedure to obtain the equation of state of a harmonically trapped gas from the once-integrated column density and its moments. This procedure allows for obtaining trap-averaged thermodynamic potentials, entropy, and heat capacity requiring neither an inverse Abel transformation nor taking derivatives of data. We have demonstrated this procedure on the unitary Fermi gas, and have found that it produces excellent agreement with the EoS of a trapped gas obtained from that of homogeneous gas. We have also described the procedure to obtain the EoS of a homogeneous gas from that of a trapped gas, and vice versa. Our procedure provides a powerful tool for thermometry of trapped atomic gases and for obtaining the EoS of a wide range of systems.

5.3 Collective modes across the superfluid phase transition

The study of collective oscillations provides an important platform for probing quantum many-body physics and for testing many-body theories. They can reveal different dynamical regimes, such as the superfluid, collisional, or collisioness regimes. The sensitivity of the modes to temperature variations can be used to probe the equation of state. On the other hand, it also means that the equation of state is a necessary input to understand the collective modes. For a unitary Fermi gas, the strong interactions lead to a large window of a collisional hydrodynamic regime even in the normal phase, in contrast to the common situation in weakly-interacting BECs. The temperature-dependence of low frequency modes (for example, radial breathing modes and scissor modes) in the unitary Fermi gas have been studied in [118, 241, 191]. These modes turn out to be insensitive to whether the gas is superfluid or normal, and their frequencies do not demonstrate a visible temperature dependence in the degenerate regime.

In Ref. [222], we participated in a joint experimental-theoretical study on the higher-nodal collective modes. The experiment was conducted by the Innsbruck group. We participated in the theoretical effort led by the Trento group to use the homogeneous EoS of the unitary Fermi gas to yield a predicdtion for the temperature-dependence of the mode frequencies. We also provided experimental consultation to the Innsbruck team. In this section, I will outline the theoretical calculation.

The starting point of the description of the collective modes is the Landau two-fluid hydrodynamic equations. The inputs for these equations are the equation of state and the superfluid density. In the case of the collective oscillations of the density (first sound), the search for the solutions can be simplified by requiring that the velocity fields of the normal and the superfluid components are equal - as opposed to oscillating with an opposite phase in the case of the second sound, in which the superfluid density enters. Under this approximation, the equations of motion involve only the EoS.

In the case of a trapped cloud with inhomogeneous density, the solution of Landau's equations is highly nontrivial. However, for a very elongated trap, it was shown that under certain conditions, one can derive simplified 1D hydrodynamic equations starting from Landau's equations in 3D [22]. In fact, such a geometry is also more suitable to experimentally excite and observe the collective modes. It was not clear that the experimental condition justified the required conditions, and the applicability of the 1D hydrodynamic formulation was demonstrated *a posteriori* [222].

The derivation of the 1D hydrodynamic formulation and the variational solution for predicting the modes is given systematically in Ref. [102]. Here, I give a summary of the result. For the oscillations in time proportional to $e^{-i\omega t}$, in the 1D hydrodynamic formulation, the equation for the velocity field $v_z = \dot{u}$ characterizing the density oscillations, with u being the displacement field that gives $\delta n_{1\mathrm{D}} = -\partial_z(nu)$, can be obtained by the variational procedure $\delta\omega^2/\delta u = 0$ and is given by

$$m(\omega^2 - \omega_z^2)v_z - \frac{7}{2}m\omega_z^2 z\partial_z v_z + \frac{7}{5}\frac{P_1}{n_1}\partial_z^2 v_z = 0\,. \tag{5.26}$$

Here, $P_1 = \int P\mathrm{d}x\mathrm{d}y$ is the "1D pressure" and $n_{1\mathrm{D}} = \int n\mathrm{d}x\mathrm{d}y$ is the twice-integrated column density. The 1D pressure can also be thought of as the integral of pressure with respect to the chemical potential $\int P\mathrm{d}\mu$, up to factors of mass and trapping frequencies.

Analytic solutions of the polynomial form $u = a_k z^k + a_{k-2}z^{k-2}$ exist for the zero-temperature and classical regimes, where k is an integer value. At $T = 0$, the frequency of the kth mode is given by

$$\omega_{k,T=0}^2 = \frac{1}{5}(k+1)(k+5)\omega_z^2\,, \tag{5.27}$$

while in the classical limit, it is given by

$$\omega_{k,T=\infty}^2 = \frac{1}{5}(7k+5)\omega_z^2\,. \tag{5.28}$$

One can see that these two frequencies are the same for $k = 0$ (center of mass

oscillation) and $k = 1$ (lowest axial breathing mode) modes. One naturally expects that the center of mass oscillation is temperature-independent. It turns out that one can prove the frequency of the $k = 1$ mode does not depend on temperature either [103] due to the exact scaling solutions exhibited by the two fluid hydrodynamic equations at unitarity. Consequently, the higher modes $k \geq 2$ are the ones that will display temperature dependence.

For the $k = 2$ and $k = 3$ modes, Hou and co-workers developed a variational approach using the ansatzes $u = a_2 z^2 + a_0$ and $u = a_3 z^3 + a_1 z$ respectively. These ansatzes reproduce exactly the frequencies in both the $T = 0$ and classical limits. The variation is done with respect to the parameters a_0, a_1, and a_2. One then finds

$$\omega_{k=2}^2 = \frac{129t_2 - 25}{45t_2 - 25}\omega_z^2 \tag{5.29}$$

$$\omega_{k=3}^2 = \frac{440t_3 - 252}{5(25t_3 - 21)}\omega_z^2 . \tag{5.30}$$

Here, $t_2 = M_0 M_4 / M_2^2$ and $t_3 = M_2 M_6 / M_4^2$, and the dimensionless moments M_l are given by

$$M_l(\beta\mu) \equiv \int_{-\infty}^{\beta\mu} \mathrm{d}x (\beta\mu - x)^{\frac{l+1}{2}} f_n(x) = \Gamma\left(\frac{l+3}{2}\right) f_{\frac{l}{2}+3}(\beta\mu) , \tag{5.31}$$

related to the moments of the EoS f_i introduced in Eq. 5.7.

We evaluate the temperature dependence of these moments using the homogeneous EoS. In the high-temperature regime, for $\beta\mu \lesssim -1.5$, the virial expansion of the EoS allows us to integrate from $\beta\mu = -\infty$ to a finite value below -1.5. At low temperatures corresponding to $\beta\mu \gtrsim 4$, where there is no experimentally measured EoS, we do know that the EoS is dominated by phonons, and the contribution is solely determined by the Bertsch paramter ξ_B. Therefore, we can extend the calculation into arbitrarily cold regimes. The error of the quantities t_2 and t_3 resulting from the error in the density EoS is less than 1%.

The quantity $(T/T_F)_{\mathrm{trap}} = (3M_0/\sqrt{\pi})^{-1/3}$ provides a convenient temperature scale. The temperature of the experimental cloud is obtained in two ways: by ob-

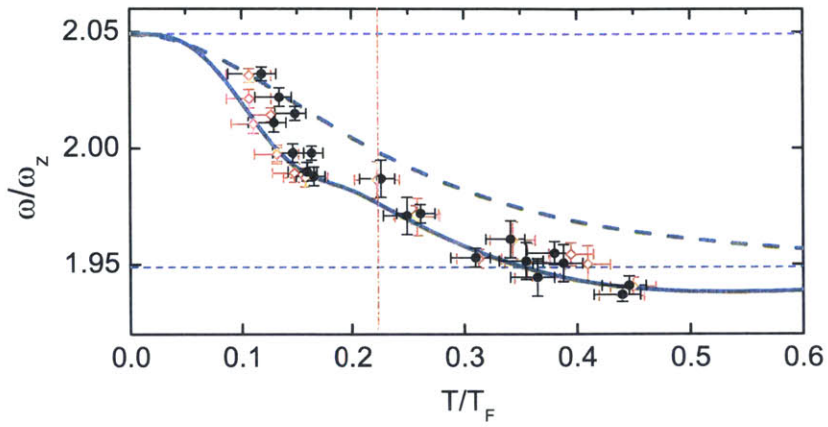

Figure 5-7: Comparison between experimental (circles) and theoretical frequencies (solid curve) of the $k = 2$ mode. The temperature of the experimental data is obtained in two different ways: either by generating $(E/E_0)_{\text{trap}}$ from the density profile and converting it to $(T/T_F)_{\text{trap}}$ (black filled circles), or by fitting the density profile to the homogeneous EoS (red open circles). Dashed curve: the mode frequencies that would result from the EoS of the ideal Fermi gas. Horizontal dashed lines: the $T = 0$ superfluid limit ($\omega/\omega_z = \sqrt{21/5}$) and the classical hydrodynamic limit ($\omega/\omega_z = \sqrt{19/5}$) according to Eqs. 5.29 and 5.30, respectively. Vertical line: the critical temperature $(T_c/T_F)_{\text{trap}} = 0.223(15)$. This figure is taken from Ref. [222].

taining the trap-averaged energy $(E/E_0)_{\text{trap}}$ and converting to $(T/T_F)_{\text{trap}}$ as outlined in 5.2, or by fitting to the homogeneous EoS.

Fig. 5-7 presents the comparison between the experimental measurement and the theoretical prediction for the frequencies of the $k = 2$ mode. The frequencies are normalized by ω_z. The $k = 2$ mode demonstrates a significant variation as a function of $(T/T_F)_{\text{trap}}$. In comparison, the $k = 2$ mode of the unitary Fermi gas is markedly different from what one would obtain if the EoS of the ideal Fermi gas is used. At the lowest temperatures ($(T/T_F)_{\text{trap}} \approx 0.1$) the frequency lies close to the $T = 0$ superfluid limit, but already a deviation of $\sim 1\%$ from this limit due to the finite temperature is observed. At the highest temperatures ($(T/T_F)_{\text{trap}} \approx 0.45$), the data go below the high-temperature, classical limit. One thus expects that ω/ω_z to turn upward again, which is indeed demonstrated by the prediction. The nonmonotonic temperature dependence can be understood based on looking at the first-order correction to the EoS from the ideal gas law.

In the subsequent experimental studies, the Innsbruck group observed the $k = 3$ mode [196] and second sound [208]. The $k = 3$ mode demonstrated moderate agreement with the 1D hydrodynamic result but the deviation is significant compared to the $k = 2$ mode. In the $k = 3$ mode, severe damping is observed, indicating that the applicability of the 1D hydrodynamic model breaks down for this case. For second sound, the superfluid density n_s plays a role. Therefore, with the measurement of the second sound and knowledge of the EoS, the superfluid density can be measured [208].

5.4 Conclusion

In this chapter, I have described two works that build on the measurement of the homogeneous equation of state of a strongly interacting Fermi gas. The method of measuring the thermodynamics of trapped gases allows for convenient thermometry without fitting and is widely applicable. A joint theoretical-experimental collaboration led to a prediction of the $k = 2$ collective modes of the unitary Fermi gas, obtained with the homogeneous EoS as an input. The prediction is in good agreement with the experimental measurement. The successful prediction of the $k = 2$ mode from the EoS sets the stage for the Innsbruck-Trento collaboration to measure the superfluid density. This is one example of how the knowledge of the equation of state is crucial in enabling further quantitative understanding of the system.

Chapter 6

Precession of a long-lived solitonic vortex in a strongly-interacting fermionic superfluid

6.1 Introduction

While the knowledge of the thermodynamics provides tremendous information on the strongly-interacting Fermi gas, it is only the starting point of obtaining a comprehensive understanding of the system. Below the critical temperature, the system enters the superfluid phase in which all the particles behave as a coherent matter wave, described by a macroscopic wave function, also known as the superfluid order parameter. In a weakly-interacting BEC, the order parameter is given by $\psi = \sqrt{n}e^{i\phi}$, where n is the density and ϕ is the phase of the wave function. In a fermionic superfluid, the wave function is also complex, $\Delta = \Delta_0 e^{i\phi}$, where Δ_0 is the pairing gap. Unlike the case of the weakly-interacting BECs, whose wave function is described by the Gross-Pitaevskii equation (GPE), there is not yet a quantitative knowledge of the wave function of the strongly-interacting fermionic superfluid.

The ground state of a corresponds to an uniform order parameter. Similar to the normal phase, small perturbations from the ground state lead to elementary

excitations, such as the Bogoliubov modes in a BEC. What is unique to the superfluid phase is that the coherence of the mater wave supports excitations charactierzied by phase-defect in the superfluid wave function which varies on the scale of the healing length (in the case of a BEC) or the coherence length (in the case of a BCS superfluid) - the length scale over which the superfluid wave function can vary while minimizing the free energy. An example of such a phase excitation is a planar soliton, consisting of a jump in the phase ϕ of the superfluid wave function across a nodal plane. Another example is the well known vortex in 2D or 3D, which consists of the phase ϕ varying between 0 and 2π along a closed contour around a nodal point or a nodal line of density depletion. We will refer to these excitations in superfluids as solitary waves or solitonic excitations.

Because of the short length scale in which the wave function varies, these excitations are localized objects with defined energy and mass, and as such they can be described as an effective single particle emerging from a medium of matter waves. They are involved generally in the dynamics of the superfluid and observed in shock waves [61, 111], rotating gases [1, 249], and evolution of microscopic defects [61]. In the case of a strongly-interacting superfluid, there have been various theoretical formulations that have been developed to study its dynamics in the context of the evolution of solitonic excitations. These theories include the time-dependent superfluid local density approximation (TSLDA) [31] and the time-dependent Ginzburg-Landau model [198]. The theoretical study of such dynamics is highly non-trivial, and experimental studies are needed to serve as benchmarks or to provide inputs for theory. The dynamics of these excitations and their interactions are central to the study of quantum turbulence [229, 225, 165, 228, 227]. One particular scenario in which quantum turbulence manifests is found in vortex recombination, considered to be responsible for neutron star glitching [240]. Solitons have a structure similar to that of a Josephson junction and allow for the study of coherence across a weak link. In particular, the study of the phase-velocity relation of a soliton in a strongly-interacting fermionic superfluid will provide insight into the descriptions of the superfluid dynamics. In the presence of spin imbalance, a soliton represents a limiting case of the long-sought

Fulde-Ferrell-Larkin-Ovchinnikov state of moving Cooper pairs [145, 244, 28, 182]. Therefore, solitonic excitations such as solitons and vortices serve as excellent dynamical probes of a fermionic superfluid.

In atomic superfluids, solitonic excitations have been generated and studied extensively in weakly-interacting BECs. Solitons in BECs have been studied both theoretically and experimentally [78]. In a series of pioneering experiments, dark solitons have been created via phase-imprinting [34, 54, 4, 20] or in the wake of shock waves [61, 68, 235]. Collisions of two dark solitons [235] and soliton oscillations [20, 235] have been observed. Solitons in 3D are known to be unstable, and in BEC experiments, they have been observed to decay into vortex rings [4, 61]. The latter further decay into a vortex-anti-vortex pair that eventually breaks up, leaving behind a single remnant solitonic vortex, a process which was elucidated in a discussion of apparent soliton oscillations observed in weakly interacting BECs [20, 19]. Experiments with BECs have demonstrated the generation of a single vortex [150], multiple vortices [99, 146], and even a lattice of $\sim$ 100 vortices [1]. Planar solitons, votex rings, solitonic vortices, and more exotic excitations whose structures resemble the Chladni figures have been studied via the GPE [25, 122, 155]. In fermionic superfluids, a vortex lattice was observed as the smoking gun of superfluidicty [249]. However, prior to our work, there was no experimental study of the dynamics of a single vortex or soliton in fermionic superfluids.

While they serve as a probe of the background superfluid in which they reside, solitonic excitations are interesting in their own right and are ubiquitous in nature. Therefore, atomic superfluids provide an excellent platform to study the physics of these excitations. In fermionic systems, solitons and vortices may provide bound states for fermions that often play a crucial role in the system's transport properties. Famous examples are the Andreev bound states inside vortex cores [40], fractionally charged solitons in relativistic quantum field theory [107, 82], and the spinless charged solitons responsible for the high conductivity of polymers [95]. However, the free motion of such defects in electronic systems is hindered by pinning at impurities [95, 154]. Fermionic superfluids of ultracold atomic gases provide a platform that

is free of impurities, where one can directly study the real-time dynamics of solitonic excitations.

In this chapter, I discuss our work on the generation of a single solitonic vortex and the study of its motion in a fermionic superfluid, reported in Refs. [243] and [127]. I will begin with a description of the first observation of a long-lived solitonic excitation with large inertial mass [243]. Then, I will describe our work to identify this object with tomographic imaging [127]. We confirm that the excitation is a solitonic vortex, and observe the vortex' precession motion. The period of the precession is measured in the BEC-BCS crossover, and is found to agree well with a hydrodynamic model.

6.2 Generation and detection of a long-lived solitonic excitation in a fermionic superfluid

The creation of solitonic excitations in a strongly interacting fermionic superfluid poses several challenges. Solitonic excitations are not the ground state of the superfluid, so the temperature of the gas has to be low enough for dissipation to be negligible. Dissipation can happen via collisions of the excitation with sound waves, leading to its acceleration. Acceleration can result in either the excitation leaving the system, or it reaching its critical velocity, at which point it decays into phonons (for BECs) or pair excitations (for fermionic superfluids) [71, 213, 204].

Being highly energetic excitations, care need to be taken to ensure that the solitonic excitation generated is stable. Planar solitons can generally decay into vortices via the so-called snake instability [156, 70, 4, 61] unless the healing length is on the order of the transverse cloud size $R_\perp$ (or alternatively, that the chemical potential μ is comparable to a quantum of the radial confinement $\hbar\omega_\perp$). We do not expect to reach this 1D regime with our experiments, but at the same time, it is not a priori clear how strict this condition needs to be achieved in order to stabilize a planar soliton. Regardless, reducing the transverse size is beneficial because it ensures that the excitation - whether soliton, vortex, or vortex ring - cannot become too energetic,

since the energy depends on the size of the nodal structure.

In this section, I discuss our initial experiment [243] to create and observe a long-lived solitonic excitation - which we will later confirm to be a solitonic vortex - in a strongly interacting fermionic superfluid of ^{6}Li atoms near a Feshbach resonance. The excitations are created via phase imprinting (see Fig. 1b), a technique successfully employed to generate solitons in weakly-interacting BECs [34, 54, 20]. A rapid ramp technique is used to image the solitonic excitation. We measured large inertial-to-bare mass ratio in the BEC-BCS crossover, which does not correspond to the expectation for a planar soliton.

6.2.1 Preparation

The atomic gas is composed of a balanced mixture of the two lowest hyperfine states of ^{6}Li initially prepared at 760 G. The superfluid containing typically $\sim 2 \times 10^5$ atom pairs is prepared in an elongated trap with a cylindrical symmetry and a tunable aspect ratio $\alpha = \omega_\perp/\omega_z$. The axial periods are $T_z \approx 210$ ms, 95 ms and 45 ms, respectively (corresponding to $\omega_z/(2\pi) \approx 5\,\mathrm{Hz}$, 11 Hz, and 22 Hz), for the three aspect ratios considered here. The radial trapping frequency is $\omega_\perp \approx 70\,\mathrm{Hz}$. The axial trapping frequency is controlled by tuning the currents in two pairs of Helmholtz coil, which allows for an independent adjustment of the magnetic field and the field curvature. This is also the primary means to adjust the aspect ratio in our solitonic excitations experiments, as we have to keep the trap depth of the ODT low in order to avoid heating. After evaporation, the ODT trap depth is increased to tighten the confinement in the radial direction. Gravity slightly weakens the trapping potential along the vertical y-direction (except for the $\omega_z/(2\pi) \approx 23\,\mathrm{Hz}$ configuration), causing a residual anharmonicity and an anisotropy $\omega_y/\omega_x - 1 \approx -5\%$ (see Appendix A).

Because the profile of the magnetic saddle potential of the $\omega_z/(2\pi) \approx 11\,\mathrm{Hz}$ configuration is not well mode-matched to the low-field magnetic trap, a large sloshing along the z-direction occurs once the atoms are transferred to the high-field. We turn on a separate ODT pointing along the vertical direction to damp out the sloshing motion. In the mean while, the trap depth of the primary ODT is lowered to further

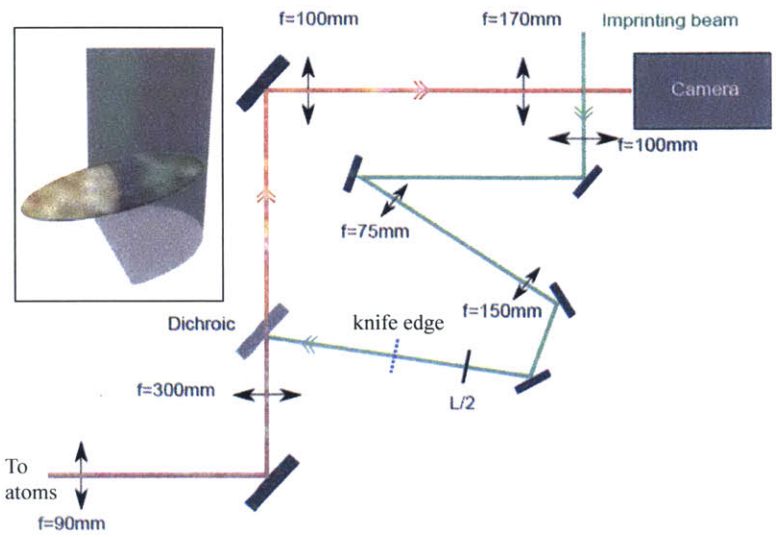

Figure 6-1: Schematic of the phase imprint setup. An blue-detuned laser beam (532 nm) twists the phase of one half of the trapped superfluid by approximately π. The knife edge, whose image is projected onto the atom cloud, masks half of the superfluid from the imprinting light. The knife edge is on a translational stage and can be moved in three dimensions.

evaporate the atoms. After this damping-evaporation stage, one can either proceed to imprint, or further enlarge the aspect ratio by slowly turning the axial frequency to $\omega_z/(2\pi) \approx 5\,\mathrm{Hz}$.

6.2.2 Imprinting a phase defect

A green laser beam (wavelength 532 nm, power ~200 mW) far detuned from the atomic resonance is masked to shine on one-half of the superfluid. We use a knife edge as the mask. A 2 μm resolution imaging system projects the intensity distribution at the mask location onto the atoms. The light is pulsed on for a time Δt, during when the applied potential U, as experienced by a single fermion pair, advances the phase of the superfluid order parameter in the exposed region by $\Delta\phi = 2Ut/\hbar$ relative to the unexposed region. The time $t \approx 35\,\mu\mathrm{s}$ is experimentally adjusted in order to create one high-contrast defect in the long-time regime $500\,\mathrm{ms} < t$.

The setup is shown in details in Fig. 6-1. The green beam from the laser source has a diameter of about 1.0(5) mm. It goes through a telescope which magnifies the

beam size to about 2.0(5) mm. The beam goes through a knife edge, is combined with the vertical imaging path by a dichroic, and travels through a telescope with a magnification (a de-magnification in the case of the green beam) of 3.3, which forms part of the top imaging system. Via this telescope, the knife edge is imaged onto the atoms. The measured beam diameter on the atoms is 380 μm. Shown in Fig. 6-2 is the green beam (with knife edge) on a 832 G cloud, compared to a typical cloud at 760 G where the imprinting is done. The size of the 760 G cloud is about 210 μm in radius. With $\omega_z/(2\pi) = 10.4$ Hz, the cloud has $\mu = 1400$ Hz, and hence $h/\mu = 730\,\mu$s.

An optimized imprint requires that the width of the edge of the phase-step to be on the order of the healing length ξ. We perform the imprinting in the BEC side at $B = 760 - 780$ G, where the healing length $\xi = \hbar/\sqrt{2m_B\mu} \sim \mu$m is relatively large. Near unitarity, the healing length is on the scale of the interparticle spacing, $\xi \sim 1/k_F = \hbar/\sqrt{2m\mu}$ and therefore has the same scaling with the chemical potential, but with a larger μ. In the BCS side, $\xi_{\mathrm{BCS}} \sim 1/k_F e^{\pi/(2k_F|a|)}$ and can be large; however, the reduced density means a larger T/T_F and the cloud is not as cold. In addition, the chemical potential μ is smaller in the BEC side, and hence the time scale h/μ, which determines whether the density of the cloud is perturbed by the imprinting potential U, is not as stringent [1]. The cloud in the BEC regime is also smaller, and hence its size is better matched to the size of the beam. As I will discuss later, the necessary sharpness may actually come from sub-resolution fringes rather than from the phase step provided by the knife edge.

The imprinting light enters the experiment via the top imaging path. For the initial alignment, the knife edge is not in the path of the imprinting light, and the imprinting light is first overlapped with the imaging light. Then, we use the image of the atoms to align the imprinting light. We first prepare an atomic cloud, and then gradually ramp up the imprinting light (about 1.5 s to avoid causing dynamics in the cloud) until the atomic cloud is visibly deformed by the potential due to the green light. One can move the green light until it is centered on the atom cloud, as

[1] The system will still experience a perturbation as long as the mode of the phase imprint is not matched to the solitonic excitation generated. At any rate, such dynamics will occur in the time scale larger than h/μ

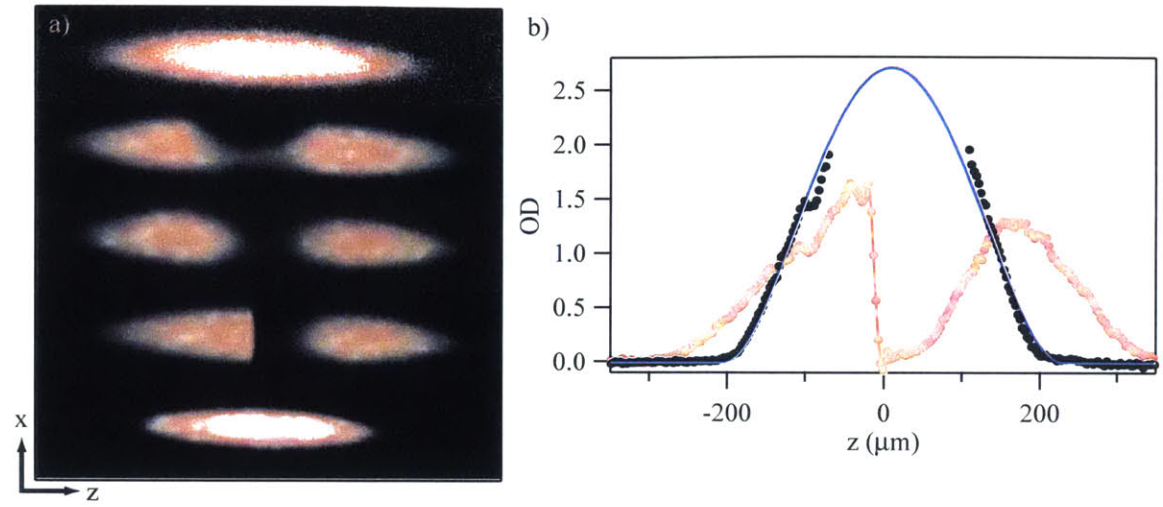

Figure 6-2: Aligning the green light and the knife edge. (a) Top to bottom: a cloud at 832 G without the green light, with the green light off-center, with the green light centered, with the knife edge in the beam path, and a cloud at 760 G. (b) A cut along the z-axis of the optical density. Red: a cloud at 832 G with the green light and the knife edge aligned. Black: a cloud at 760 G without the green light. Blue: a fit to the BEC profile for the cloud at 760 G.

judged by the image of the atoms. If the green light is well aligned, only a small power ($\sim$ 10 mW) suffices to cause the deformation. Then, the knife edge is finally brought in to the beam path to cover one side of the superfluid. The position of the knife edge along the axis of the optical path is tuned to optimize the generation of a long-lived excitation [2].

Since we imprint only a phase step but not a density depletion, sound waves must be generated in addition to the defect [34, 54]. The sound waves are found to die out in a quarter axial trapping period when they have reached the edge of the atom cloud. Besides the sound waves, we also observe that the cloud is filled with excitations immediately after the imprint. I will discuss the study on the time-evolution of the superfluid after imprint in Chapter 7. The study of a single long-lived defect is done by imaging the superfluid tyipcally at least 300 ms after the imprint. For the data above 760 G the solitonic excitation is created at 760 G, and after typically 50 ms wait

[2] As I will discuss in Chapter 7, the best position to generate a long-lived excitation (which turns out to be a solitonic vortex) is not at where the knife edge is focused on the cloud, but rather away from the focus.

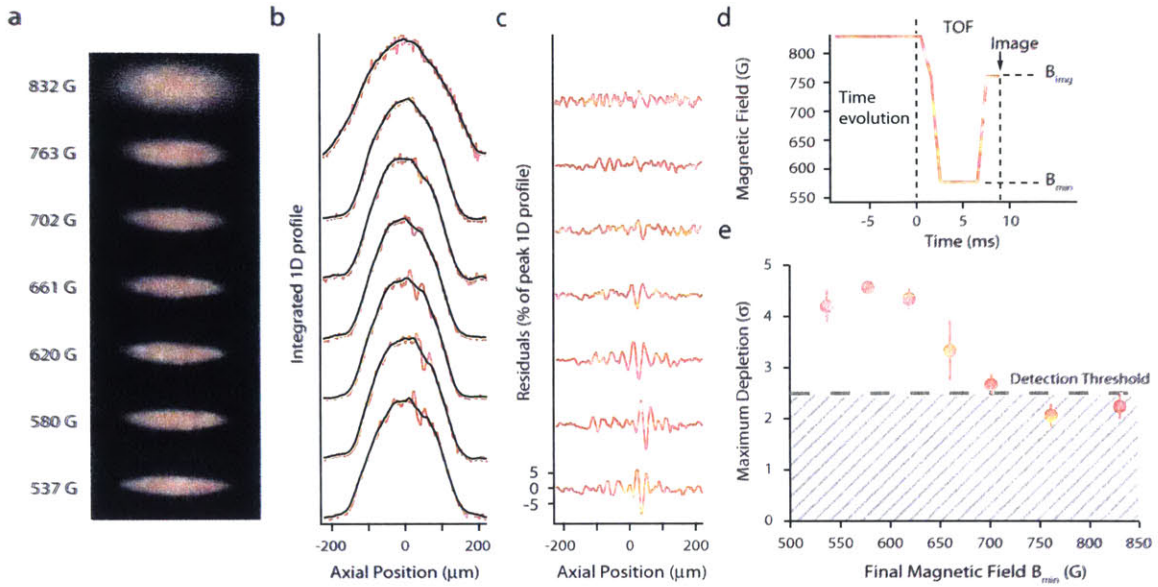

Figure 6-3: Imaging solitonic excitations. (a) Optical density, (b) integrated 1D profiles and (c) corresponding residuals of a fermionic superfluid, prepared at 832 G, after expansion and rapid ramp to various final magnetic fields B_{min}. Without any ramp, the superfluid at 832 G, observed after 9 ms time of flight, does not show a clear signature of the defect. For $B_{\mathrm{min}} < 700\,\mathrm{G}$ the defect is clearly revealed. (d) Sequence of a typical magnetic field ramp used in our experiment, indicating time of flight (TOF), the low-field B_{min} and the imaging field B_{img}, at which the image is taken. The initial field during the time evolution depends on the experiment. The actual ramp may differ slighly in terms of the speed, the value of B_{min}, and the value of B_{img}. (e) The maximum depletion detected in the optical density, in units of the standard deviation σ found outside the defect. The detection threshold of 2.5 σ is indicated.

time for the extra energy to dissipate, the magnetic field is subsequently ramped (in about $200\,\mathrm{ms} \approx 2T_z$) to the final magnetic field where the defect's motion is studied. For final magnetic fields below 760 G, the defect is created at that field, and the motion of the defect is studied starting at around 250 ms after the imprint. We found that the solitonic excitation can be created directly at the Feshbach resonance as well.

6.2.3 Imaging the solitonic excitation

Excitations such as vortices and solitons are known to gradually fill in as the interaction strength is tuned from the BEC-regime to the BCS-regime of the crossover.

Indeed, in the BCS regime only a minute fraction Δ_0/E_F of the gas is Cooper paired, and only this fraction is missing at the center of the defect. The contrast in the particle density thus vanishes in the BCS limit. Indeed, absorption images of atom clouds at the Feshbach resonance, whether in-situ or after an expansion (Fig. 6-3 (a)), do not show any observable ($\gtrsim 3\%$) contrast. In addition, the size of the defect in-situ is on the order of $\xi \sim 1/k_F \lesssim 1\,\mu$m, below the imaging resolution $\sim 2\,\mu$m.

While the defect is not visible in situ, the amplitude of the pair wavefunction can be imaged by a rapid ramp technique similar to what was used for the observation of vortex lattices in the BEC-BCS crossover [249, 116]. A magnetic field ramp to the weakly-interacting BEC-regime $B_{\min} \sim 580\,$G turns the large fermion pairs into molecules. Weak interaction serves to empty the defect from fillings. In addition, the ramp reduces the interaction strength and thus increases the healing length $\propto 1/\sqrt{na}$ of the superfluid to an observable value, $\sim 20\,\mu$m. The ODT is released to allow for free expansion of the molecular cloud in the radial direction, which is needed to get rid of the uncondensed filling and serves to enlarge the cloud. Therefore, a rapid ramp accompanied by a time of flight expansion can serve as a magnifying glass that enhances the contrast. Since the molecule cannot be directly imaged, the magnetic field is ramped back to a field near the resonance, where the absorption cross section of the atoms is maximal. An absorption image is taken, which corresponds to an image of the molecules and thus qualitatively reflects the magnitude of the fermion pair wavefunction before the ramp.

We have found the rapid ramp technique necessary to reveal the defect in the strongly interacting regime. To show the importance of the rapid ramp, we have varied the final field of the rapid ramp $B_{\min}$ between 500 and 832 G. The depth of the maximum depletion, normalized by the standard deviation σ outside of the defect, is shown in Fig 6-3. For ramp fields $B_{\min} < 650\,$G, the defect is clearly revealed as a stripe of depletion in the optical density.

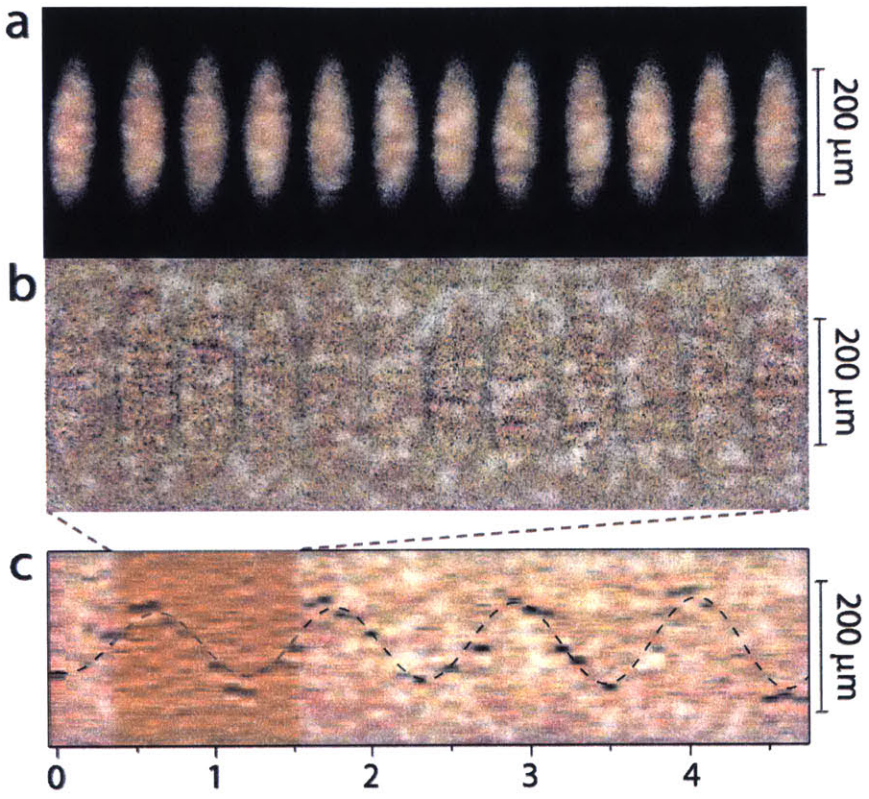

Figure 6-4: (a) Optical density and (b) residuals of atom clouds at 815 G, imaged via the rapid ramp method [249], showing a defect at various hold times after creation. One period of defect's oscillation is shown. The in-trap aspect ratio was $\alpha = 6.5(1)$. (c) Radially integrated residuals as a function of time revealing long-lived defect oscillations. The defect's period is $T = 12(2)\,T_z$, much longer than the trapping period of $T_z = 93.76(5)$ ms, revealing an extreme enhancement of the solitonic excitation's relative effective mass M^*/M.

6.3 Observation of long-lived solitonic excitation with large inertial mass

Fig. 6-4 (a)-(c) reports the observation of a single solitonic excitation in a fermionic superfluid prepared at 815 G, close to the 832 G Feshbach resonance, for various hold times following the phase imprint. Here, the interaction parameter at the cloud center is $1/k_F a = 0.30(2)$. The defect can be identified easily in the absorption images by eye. However, to automize defect detection, we implemented the following

method. For each absorption image, we first generate a residual profile by subtracting a smoothened version of the optical density profile from the actual optical density profile. We determine the standard deviation of fluctuations σ and identify a depletion in the residual profile as a a defect if its depth is greater than 2.5 σ.

Fig. 6-4 (a) shows the optical density in absorption images taken after time of flight and the rapid ramp to $\sim 580\,\mathrm{G}$, while Fig. 6-4 (b) displays residuals obtained by subtracting a smoothened copy of the same absorption image. The optical density contrast is about 10%. A sequence of radially integrated residuals as a function of time (the time label shown in the figure starts at about 250 ms after the imprint) is displayed in Fig. 6-4 (c), demonstrating the defect to be stable for more than 4 s or 100 000 times the microscopic time scale $\hbar/E_F$. This establishes that we have generated a solitonic excitation in fermionic superfluids that can exist as a stable and long-lived excitation.

The defect is observed to undergo oscillations in the harmonically trapped superfluid, demonstrating its emergent particle nature. The motion is to a high degree deterministic, as the defect positions for different realizations of the experiment at varying wait times lie on the same classical sinusoidal trajectory. The observed period of oscillation T is about one order of magnitude longer than the trapping period T_z for single atoms. This directly indicates an extreme enhancement of the relative effective mass.

In Fig. 6-5 (a), we find that the period of the defect, and hence the relative effective mass $M^*/M = (T/T_z)^2$, increases dramatically as the interactions are tuned from the BEC limit (Fig. 6-5 (a.i)) towards the BCS limit. At 700 G, where $1/k_F a = 2.6(2)$, the system represents a strongly interacting Bose gas of molecules [116]. The defect period is $T = 4.4(5)T_z$, already three times longer than the expectation of a planar soliton in a weakly-interacting BEC, which is $T_s = \sqrt{2}T_z$. At the Feshbach resonance (Fig. 6-5 (d)), we measure a period of $T = 14(2)\,T_z$, corresponding to a relative effective mass of $M^*/M = 200(50)$.

Note that the superfluid is fully three-dimensional: on resonance, the chemical potential is $\mu \approx 35\hbar\omega_\perp$. One expects that the geometry can affect the dynamics of

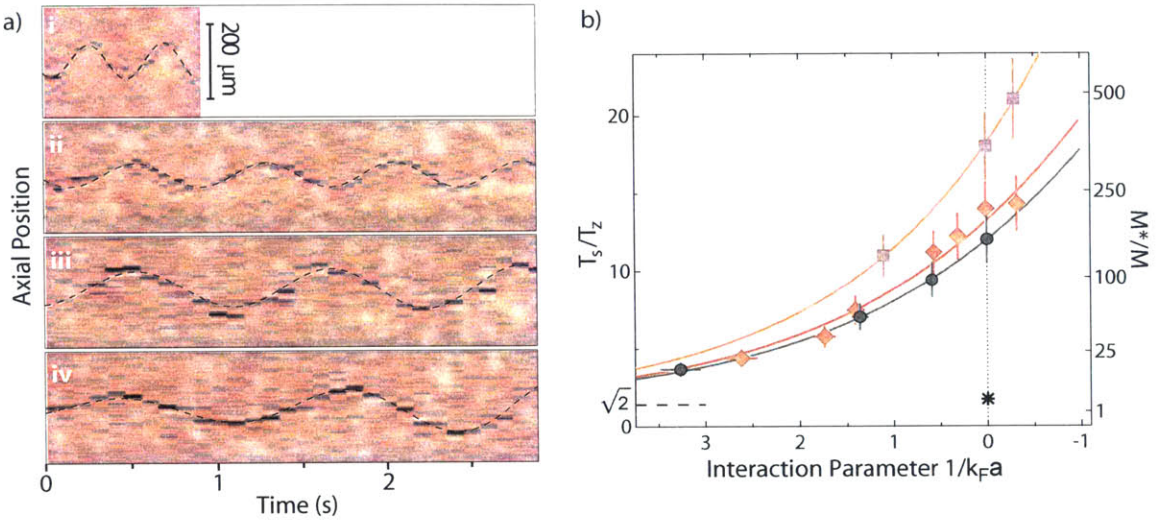

Figure 6-5: Measurement of the oscillations of the long-lived solitonic excitation in the BEC-BCS crossover. (a) Shown are oscillatory motion of the defect in a trapped fermionic superfluid for various magnetic fields B and the interaction parameter $1/(k_F a)$ at the cloud center: (i) 700 G, 2.6(2) (ii) 760 G, 1.4(1) (iii) 815 G, 0.30(2) and (iv) 832 G, 0. The aspect ratio is $\alpha = 6.2(7)$. Note that at $B = 700$ G, the superfluid is short lived due to enhanced three-body loss. (b) The period and effective mass of the defect versus interaction strength $1/(k_F a)$ (in the cloud center). The data are taken for three different aspect ratios: $\alpha = 15(1)$ (black circles), 6.2(7) (red diamonds) and 3.3(1) (orange squares). The error bars correspond to the typical spread over five measurements and the solid lines are guides to the eye. Dashed line is for the result of a planar soliton in a weakly-interacting BEC, $T_s/T_z = \sqrt{2}$. The star marks the mean-field prediction [203] $M^*/M = (T_s/T_z)^2 = 3$ for a planar soliton at unitarity.

the solitonic excitation in question. This prompted us to study the dependence of the defect's period on the aspect ratio of our trap.

Fig. 6-5 (b) summarizes our measurements for the defect period and the relative effective mass as a function of the interaction parameter $1/(k_F a)$ throughout the BEC-BCS crossover, for aspect ratios $\alpha = 3.3$, 6.2 and 15. The strong increase of M^*/M towards the BCS regime is observed for all trap geometries. At each $1/(k_F a)$, the normalized period T/T_z appears to converge to a limiting value for the most elongated trap: the normalized period changes by only 15% as the aspect ratio is increased by more than a factor of two from 6.2 to 15. However, as we shall discuss later, it is not an indication that one has reached the quasi-1D limit; rather, the object in question is a solitonic vortex, whose motion can be well-described by a hydrodynamic formalism.

6.3.1 Discussion

The first experiment on the generation and observation of a solitonic excitation in a fermionic superfluid brought up several questions regarding the identity of this object. Given the profile of the imprinted phase, one naturally expects a soliton to arise from the phase-imprint. This, plus the excellent contrast in the profile, led us to interpret the object as a planar soliton in the first experiment. However, because we record the once-integrated column density $n_{2D}(x,z) = \int \mathrm{d}y\, n(\mathbf{r})$, we are not able to decisively distinguish a soliton, a vortex ring, a vortex, or even other Chladni solitons from each other, so long as the object is aligned transverse to the long-axis. The findings in this study are surprising for a planar soliton, but cannot provide conclusive evidence for the identity of this object.

The energy of a solitonic excitation is concentrated in its nodal region. As a result, solitonic excitations follow an energy hierarchy given by their nodal structures [122]. For example, the nodal plane of a soliton is energetically more costly than the nodal line of a vortex. If there is a path for decay, the system will thus tend to reduce the size of the nodal regions. Such a pathway for planar solitons to decay into lower energy excitations is the so-called snake instability, the undulation of the soliton plane [156, 70, 4, 61]. In the case of weakly-interacting BECs in elongated traps,

stability requires the chemical potential μ of the condensate to be not much larger than the transverse confinement energy [156]. For a Fermi gas, this would require a quasi-1D geometry where the transverse cloud width is one interparticle spacing. For strongly interacting superfluids, it is a priori not obvious that solitons are stable against quantum fluctuations [62, 63, 133, 152, 148, 78, 232]. We have found the defect to live up to $\sim 7\,\mathrm{s}$, an exceedingly long lifetime. This observation here is therefore not expected if the defect is a planar soliton.

For weakly-interacting BECs, a soliton has been observed to decay into a vortex rings [4], which further decay into a vortex-anti-vortex pair that eventually breaks up, leaving behind a single remnant vortex [19]. In the case of strongly interacting fermionic superfluids, the understanding of such non-trivial dynamics presents a challenging non-equilibrium many-body problem. The interest in understanding such dynamical process has led to several theoretical works following our first solitonic excitation experiment, suggesting that these solitary waves are vortex rings [30, 188, 237].

The large inertial mass of the defect is also a surprise given the interpretation of the object as a soliton. In general, the difference between the effective mass M^* and the bare mass M of a solitonic excitation arises from the phase slip $\Delta\phi$ across the excitation, which implies a superfluid counterflow [203]. For the defect to move, an entire sheet of atoms thus has to flow past it. The inertial mass thus is related to the volume occupied by the superfluid flow. In contrast, the soliton's bare mass M is only due to the mass deficit associated with the number of the missing atoms number $|N_s|$. For a planar soliton, the volume in which the phase varies is $\xi R_\perp^2$, and hence $M^* \sim m\xi R_\perp^2 n$. In the absence of filling (e.g. in a weakly-interacting BEC), this is the same volume in which the density depletes, and hence M also follows the same scaling, and as a result, $M^*/M \sim 1$ is on the order of unity. For weakly-interacting BECs, $M^*/M = 2$, and hence $T = \sqrt{2}T_z$ [36, 123], as has been observed in experiments [20, 235]. In the BCS limit, where only a minute fraction Δ_0/E_F of the gas contributes to Cooper pairing, $|N_s| \propto \Delta_0/E_F \propto e^{-\frac{\pi}{2k_F|a|}}$ and thus the soliton's relative effective mass can be expected to become exponentially large. On the other hand, in the case of a solitonic vortex or a vortex ring, the region in which the phase

varies is $\sim R_\perp^3$, and hence $M^* \sim mnR_\perp^3$, while $M \sim mn\xi^2 R_\perp$ (here I am neglecting a logarithmic factor). Therefore, for these two objects, $M^*/M \sim R_\perp^2/\xi^2$, and if we take $\xi \sim 1\,\mu$m and $R_\perp \sim 30\mu$m, M^*/M can easily be large.

Note that on resonance, the fastest defects we have observed move at the exceedingly slow speed of 0.50 mm/s or 5% of the (independently measured) speed of sound on resonance. Their observed sudden disappearance (e.g. in Fig. 6-11 (c)) can thus not be related to a motion close to the Landau critical speed, an upper bound on the velocity of a soliton [136, 204]. If the defects were vortices, then it is reasonable that an accelerating vortex eventually acquires enough energy to eject itself from the system.

6.4 Tomographic imaging of the solitonic vortex

In order to lift the ambiguity on the nature of the observed excitation, we employ a tomographic technique whereby only a chosen slice of the full atom cloud is imaged after time of flight. This method gives direct access to the local density of the 3D cloud. Tomography is realized by optically pumping within 10 μs all atoms outside the desired slice into hyperfine states that are off-resonant with the imaging transition for state $|1\rangle$, predominantly state $|6\rangle$. In this section, I will discuss the details of the tomographic imaging method, and report our finding that establishes the identity of the long-lived excitation to be a solitonic vortex.

At high fields $\sim 670 - 850\,$G, the atomic levels are dominated by the electronic Zeeman energy, and $|1\rangle$ and $|2\rangle$ are almost $|S_{\frac{1}{2}}, m_J = -\frac{1}{2}\rangle$. We pump atoms in $|1\rangle$ to $|6\rangle \sim |S_{\frac{1}{2}}, m_J = \frac{1}{2}\rangle$ by a σ_+ transition to $|P_{\frac{3}{2}}, m_J = \frac{1}{2}\rangle$ (see Fig. 6-6 (a)). To estimate the detuning from the zero-field transition, we approximate the energy change from the zero-field value with $\Delta E \approx \mu_B g_J m_J B$, where $\mu_B = 1.4\,$MHz/G is the Bohr magneton, and the g-factors are $g_J = 2$ for $|S_{\frac{1}{2}}, m_J\rangle$ and $g_J = 1.335$ for $|P_{\frac{3}{2}}, m_J\rangle$. The detuning from the zero-field transition is then given by $\delta \approx 1.6675\frac{\mu_B}{\hbar}B$, which yields 1.94 GHz for 832 G, and 1.63 GHz for 700 G. The pumping laser is provided by a single Toptica DL Pro diode laser. With this large detuning, one cannot directly

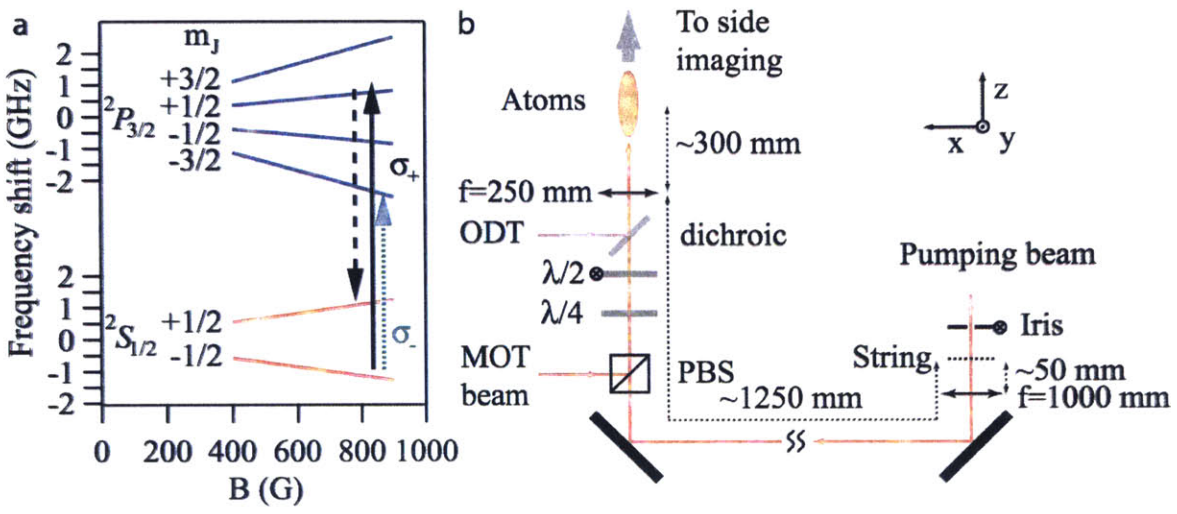

Figure 6-6: (a) Energy levels of the states of interest for optical pumping at high fields. The target state for the cyclic (σ_-) transition for imaging is $|P_{\frac{3}{2}}, m_J = -\frac{3}{2}\rangle$. The pumping ($\sigma_+$) transition excites the atoms to $|P_{\frac{3}{2}}, m_J = \frac{1}{2}\rangle$. (b) Schematic of the setup for the tomographic imaging.

lock the laser to the atomic transition. Instead, the beat between the pumping and the master laser is stabilized via a phase lock.

The slice is selected by masking part of the optical pumping light with a thin string, and projecting the string's shadow onto the atom cloud. The schematics of the setup is shown in Fig. 6-6 (b). The high-field pumping beam shares the same path as the low-field pumping beam that is used immediately after the magneto-optical trap (MOT) stage. The string is imaged onto the atom cloud by a single f=250 mm lens. A f=1000 mm lens forms a telescope with the aforementioned lens to shrink the beam. Since the distance of the string to the f=1000 mm lens is much less compared to the focal length, the f=1000 mm lens can be essentially ignored in terms of forming an image of the string. The de-magnification of the string is $\approx 1300/300 = 4.3$. The size of the string is $90\,\mu$m, and when projected onto the cloud is $\approx 21\,\mu$m. The aperture of the system is limited by a 2-inch polarizing beam splitter cube located at about 300 mm prior to the imaging lens. This leads to a resolution of about $15\,\mu$m and an estimated thickness of the slice to be $\approx 24\,\mu$m on the atoms, in agreement with the measurement from the vertical-slicing of the atom cloud (see Fig. 6-7). An iris

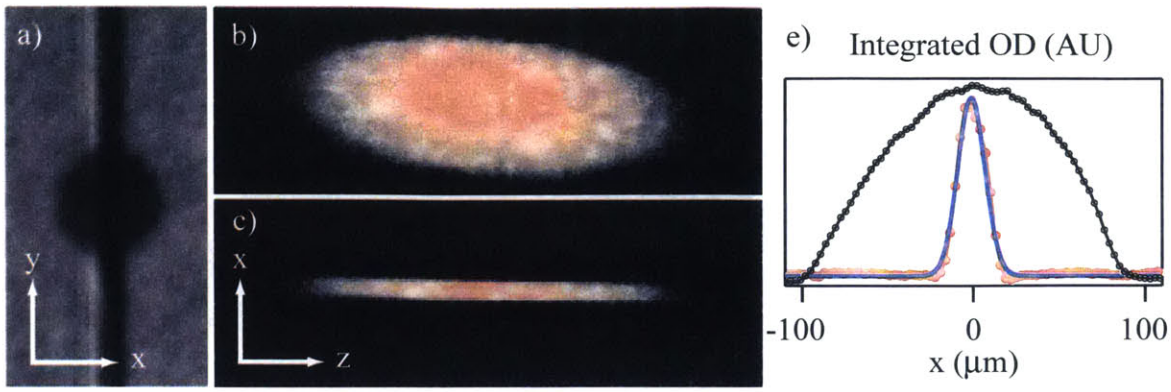

Figure 6-7: Vertical slicing of an expanded superfluid. (a) An (unnormalized) image of the superfluid with the string oriented vertically in the background, as seen from the side imaging camera. (b) Top: the superfluid as seen from the top. Bottom: a slice of the same superfluid with the string orientied vertically. (c) Twice-integrate optical density $\mathrm{OD}_{1\mathrm{D}}(x) = \sigma_0 \int \mathrm{d}y\mathrm{d}z\, n(\mathbf{r})$ of (b). Black: unsliced superfluid. Red: sliced superfluid. Blue: a Gaussian fit to the slice yields a thickness of 23(1) μm. This is about 1/5 to 1/6 of the radial size of the superfluid.

on a motorized flipper mount is placed close to the string. It restricts the pumping light to reduce undesired fringes that could imprint features on the atoms, and is removed from the optical path during the preparation of the degenerate Fermi gas in order to not block the optical pumping light. The quantization axis is $+\hat{z}$ prior to the preparation of an interacting mixture, and $-\hat{z}$ afterward. Since the MOT beam, the low-field pumping beam, and the high-field pumping beam all operate at a σ_+ transition, a $\lambda/2$ wave plate on a motorized flipper mount is placed into the optical path to reverse the circular polarization for the high-field pumping light. As a result, when the tomographic imaging is being used, the side-imaging beam, which normally excites atoms via the cyclic transition, will also have a σ_+ polarization and will not be scattered by the atoms. Nevertheless, absorption of the high-field pumping light can serve to image the atoms, though the quality is much worse because it is not a cyclic transition.

The string is on a rotatable mount and a translational stage. By rotating the string so it is vertical, we can create a vertical slice of the atom cloud, which we can image through the high-resolution vertical imaging path and use that to characterize

the slicing. Shown in Fig. 6-7 (c) is the optical density (OD) of a vertical slice of an atom cloud, and a cut across the central part of the cloud is shown in Fig. 6-7 (d). The vertical slicing position is also useful for putting the string to the right focus. The translational stage can be moved in all three dimensions, allowing for both focusing and adjusting the position of the slice along the $x-y$ plane (as seen from the atoms).

With the vertical slicing, a Gaussian fit of the twice-integrated optical density $\mathrm{OD}_{1\mathrm{D}} = \sigma_0 \int \mathrm{d}y\mathrm{d}z\, n(\mathbf{r})$ to the ansatz Ae^{-x^2/w^2} gives the width of the slice to be $2w = 23(1)\,\mu$m. The thickness is comparable to the width of the observed solitary wave after time of flight, and about one fifth to one sixth of the transverse cloud diameter after expansion. Since the imaging procedure is destructive, each run of the experiment provides a single slice at a given time of the defect's motion. Thanks to the high degree of stability of our experiment, reliable tomography can be built up from many repetitions of the experiment.

Representative tomographic images for the unitary fermionic superfluid are shown in Fig. 6-8, taken 1.6 s after the phase imprint. A line of depletion with about 40% contrast cuts across the entire cloud in one particular slice. This immediately demonstrates that the solitary wave is not a vortex ring. On average, only a specific one of the six slices imaged features the depletion. Therefore, the strong depletion is not a planar soliton either, as we interpreted in our previous paper [243] . Instead, our observation confirms the defect has the structure of a nodal line, consistent with the structure of a single quantized vortex line. As discussed in 2.6.2, a vortex in an elongated superfluid, such as the one in our experiments, has properties similar to those of a planar soliton, and hence is called a solitonic vortex. For the present experimental conditions we observe the vortex to be horizontal in every single repetition of the experiment. Due to the slight anisotropy of the trap, the vortex can minimize its energy by aligning along the short axis, while orientation along the longer, intermediate axis is unstable [219, 19]. Slight tilts of the vortex into the vertical direction cause partial vortex lines to be detected in a given slice, as seen for slice position $y = -39\,\mu$m in Fig. 6-8 (c).

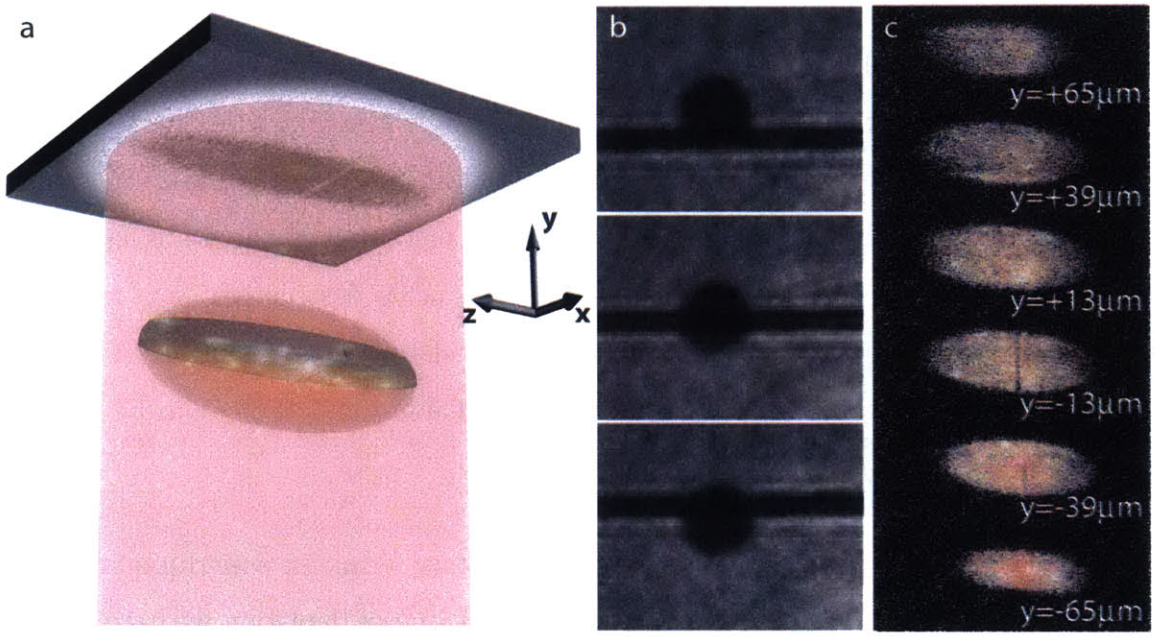

Figure 6-8: Tomography of superfluid revealing the presence of a solitonic vortex. (a) The string is oriented such that the slice it produces is normal to the vertical imaging beam, allowing for accessing the local density. (b) Examples of (unnormalized) images of the superfluid with the string oriented horizontally, as seen from the side imaging camera. Shown is the string in a few different positions. When the high-field pumping light is applied, this allows for accessing the local density $n(x, y_0, z)$ in different $y = y_0$ slices. (c) Tomography of a unitary fermionic superfluid of ^{6}Li atoms containing a solitary wave. Shown are density distributions of horizontal slices selected at different y positions. Tomography reveals a single solitonic vortex. The image is taken at $t = 1.6\,\mathrm{s}$ after the phase imprint. The imprint is performed at 760 G. The superfluid is brought to unitarity over 600 ms, and then evolves for another 1s.

6.5 Vortex precession in a unitary Fermi superfluid

In a 3D geometry where the radial cloud size $R_\perp$ is much larger than the vortex core size ξ, an off-center transverse vortex will undergo precessional motion along an equipotential contour [142, 75]. An observation of the precession will confirm the gyroscopic nature of the vortex. Tomographic imaging enables a measurement of the vortex position in the z-y plane as a function of time (see Fig. 6-8 (b) and (c)). The vortex' z coordinate is readily obtained from the images. The y coordinate is given by the position of the slice that contains the vortex (e.g: in Fig. 6-8 (c), the vortex is observed at $y = -13\,\mu$m). In order to refine the determination of the y position of the vortex, a histogram of occurrence as a function of the slice position is built up from several ($\sim$7 runs per slice position) repetitions of the experiment at each given time of the vortex' motion. Representative images and density profiles of slices containing the vortex are shown in Fig. 6-9, along with histograms of the occurrence of vortex observations in each slice. The z-y coordinates of the vortex are found to lie on an ellipse with the same aspect ratio (after expansion) as the atom cloud, as expected for vortex precession along equipotential lines.

The period of the vortex motion can be estimated from superfluid hydrodynamics and the equation of state in the BEC-BCS crossover [159]. We have developed a Hamiltonian approach analogous to that used to describe the motion of vortex rings in [176], which I will describe here. Let us consider a vortex aligned in the transverse x-direction, and located at $\mathbf{r}_0 = (y_0, z_0)$ in the y-z plane. The energy E_V of the vortex is dominated by the kinetic energy of its flow field $\mathbf{v} = \hbar\nabla\phi/m_B$, where $\phi = \arctan\frac{y-y_0}{z-z_0}$ is the phase profile near the vortex, and $m_B = 2m$ the boson mass. One finds $E_V \approx \int \mathrm{d}^3r \frac{1}{2}mnv^2 = \frac{\pi\hbar^2 m}{m_B^2} n_{2\mathrm{D}}(y_0, z_0)\ln(R_\perp/\xi)$ in the limit of $\ln(R_\perp/\xi) \gg 1$. Here, $n_{2\mathrm{D}}$ is the column density along the vortex line, and ξ is the characteristic size of the vortex core. In the crossover, we may take $\xi = \frac{1}{\sqrt{2}}\hbar/m_B c$, with c the speed of sound. This definition recovers the healing length in the BEC-regime. At unitarity, this gives $\xi \approx 1/k_F$, which is a reasonable estimate [32].

The canonical momentum of the vortex along the axial z-direction is given by

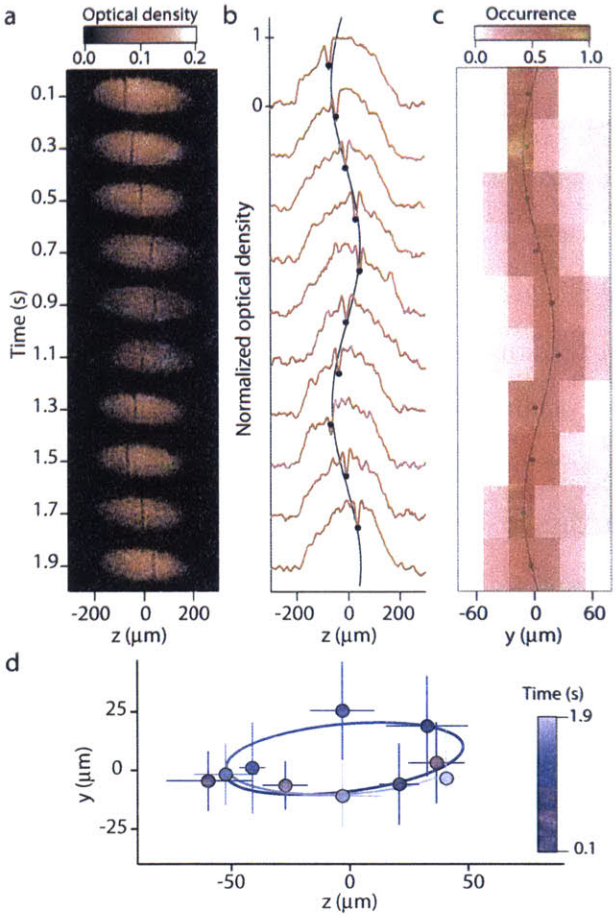

Figure 6-9: Observation of vortex precession in a unitary fermionic superfluid via tomographic imaging. (a) Representative horizontal slices showing the oscillation of the vortex along the z-axis. Time $t = 0\,\mathrm{s}$ marks 600 ms after the phase imprint. The y position of each slice can be inferred from c). (b) Density profiles normalized by the peak density, showing a depletion of typically 30% contrast. The solid line is a sine fit to the vortex positions (black dots). (c) Average occurrence of the vortex at a given y position of the slice as function of time, showing the vortex oscillation along the y-axis. Red dots: Average y position of the vortex from gaussian fit at the given time; solid red line: sine fit. (d) Reconstructed precessional motion in the z-y plane.

$P_z = \int \mathrm{d}^3r\, mnv_z = \frac{m}{m_B}\int \mathrm{d}^3r\, \hbar n \partial_z \phi$. Since we consider a geometry where $R_\perp \ll R_z$, the phase gradient is concentrated in the neighborhood of the vortex in a range of size $\sim R_\perp$ along the z-direction. This allows us to set $n(x,y,z) \approx n(x,y,z_0)$. The integral of $\partial_z\phi$ over the z-direction thus equals π or $-\pi$, depending on whether the path runs along $y < y_0$ or $y > y_0$. One thus has $P_z \simeq \frac{m}{m_B}\hbar\pi(\int_{-R_\perp}^{y_0}\mathrm{d}y - \int_{y_0}^{R_\perp}\mathrm{d}y)\, n_{2\mathrm{D}}(y,z_0) = \frac{m}{m_B}\hbar\pi\int_{-y_0}^{y_0}\mathrm{d}y\, n_{2\mathrm{D}}(y,z_0)$. Assuming harmonic trapping and the local density approximation, we obtain the axial velocity of the vortex from Hamilton's equation

$$\dot{z}_0 = \frac{\partial E_V}{\partial P_z} = \frac{\partial E_V/\partial y_0}{\partial P_z/\partial y_0} = -\frac{\omega_\perp}{\omega_z}\Omega\, y_0\,, \tag{6.1}$$

and similarly $\dot{y}_0 = \frac{\omega_z}{\omega_\perp}\,\Omega\, z_0$, with the angular frequency

$$\frac{\Omega}{\omega_z} = \frac{2\gamma+1}{8}\frac{\hbar\omega_\perp}{\mu}\ln\left(\frac{R_\perp}{\xi}\right). \tag{6.2}$$

Here, $\gamma \equiv \frac{\mu}{n}\frac{\partial n}{\partial \mu}$ is the polytropic index determined by the $T=0$ equation of state in the BEC-BCS crossover, and μ is evaluated at the vortex position. $\gamma = 1$ in the BEC regime, while $\gamma = 3/2$ at unitarity and in the BCS regime. Eqs. 6.1 and 6.2 describe the precessional motion of the vortex with angular frequency Ω along an equipotential contour of the trap where $\mu =$ const. i.e. $y_0^2/R_\perp^2 + z_0^2/R_z^2 =$ const. The result can also be obtained by equating the Magnus force [8] $hn_{2\mathrm{D}}\hat{x}\times\dot{\vec{r}}_0$ to the force $-\nabla E_V$ acting on the vortex. This model generalizes the known result for the vortex motion in the weakly-interactingBECs [142, 75] to superfluids with arbitrary equation of state. The inertial mass of the vortex [203] is

$$M^* = \frac{\partial P_z}{\partial \dot{z}_0} = \frac{\partial P_z/\partial y_0}{\partial \dot{z}_0/\partial y_0} = -\frac{4\pi}{2\gamma+1}\frac{n_{2\mathrm{D}}R_\perp^2}{\ln(R_\perp/\xi)}m\,, \tag{6.3}$$

which is proportional to the total mass of atoms contained in the volume $R_\perp^3$, while the bare mass

$$M = -\frac{\partial E_V}{\partial \mu}m = -\pi\frac{2\gamma+1}{4\gamma}\, n_{2\mathrm{D}}\xi^2\ln\left(\frac{R_\perp}{\xi}\right)m \tag{6.4}$$

is only proportional to the mass of "missing" atoms contained in the vortex core.

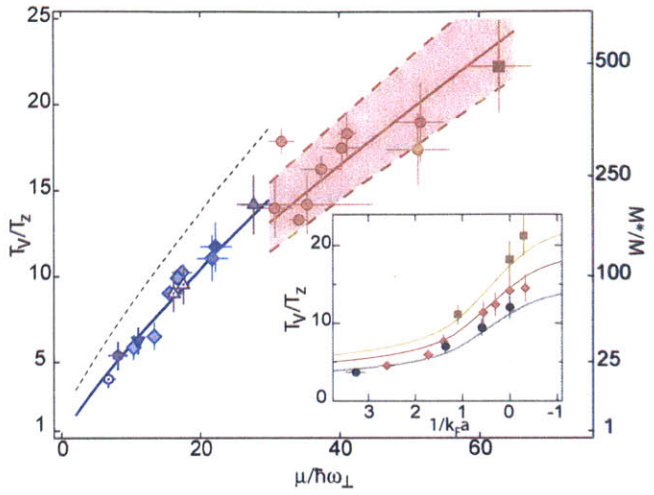

Figure 6-10: Normalized period of the solitonic vortex T_V/T_z, as a function of the normalized chemical potential $\mu/\hbar\omega_\perp$. Experimental data are for magnetic fields $B = 850\,\mathrm{G}$ (BCS side, square), 832 G (unitarity, circle), and for the BEC-side at 800 G (triangle), 760 G (diamond), 740 G (inverted triangle), and 700 G (hexagon). $\omega_z/2\pi$ was 23 Hz (solid symbols), 10 Hz (framed), 5 Hz (dotted). Predictions in the BEC regime: Solid blue line from [142], dashed black line from [75]. Red solid curve: hydrodynamic prediction on resonance, assuming $\xi = 1/k_F$. The error band is bounded by the choice $\xi = 1/2k_F$ (lower bound) and $\xi = 2/k_F$ (upper bound). Inset: T_V/T_z as a function of the interaction parameter $1/k_F a$, data from [243]. Square, diamond, and circle are for $\omega_z/2\pi = 23$, 10, and 5 Hz, respectively. Atom numbers range from $N/2 = 1 \times 10^5$ per spin state in the BEC regime to 3×10^5 around resonance. Solid curves: hydrodynamic prediction fixing $N/2 = 3 \times 10^5$, and $\omega_z/2\pi = 23\,\mathrm{Hz}$ (gold), 10 Hz (red), and 5 Hz (black).

This is in agreement with the physical picture given in 6.3.1. Here we have used $\mu = \gamma mc^2 = \gamma\hbar^2/2m\xi^2$. The ratio $M^*/M \propto R_\perp^2/\xi^2/(\ln(R_\perp/\xi))^2$ thus depends on the transverse size of the system and can become large.

The inset in Fig. 6-10 shows the data from [243] along with the theoretical prediction for a fixed, characteristic atom number of $N/2 = 3 \times 10^5$ per spin state, using the known equation of state in the BEC-BCS crossover [159]. Using the experimental parameters of $\mu/\hbar\omega_\perp \approx 25 - 35$ [243], the hydrodynamical model yields $T_V/T_z \approx 11 - 15$ and $M^*/M = 130 - 220$, in close agreement with the measured values in [243].

We have taken data for the vortex period in the BEC-BCS crossover exploring a wide range of chemical potentials. Fig. 6-10 shows the normalized period T_V/T_z

versus $\mu/\hbar\omega_\perp$ including data for several aspect ratios, interaction strengths and atom numbers. Chemical potentials were extracted from the measured axial Thomas-Fermi radius of the cloud. For a molecular BEC, the prediction from the GP equation is [142, 75]

$$\frac{\Omega}{\omega_z} = \frac{3}{8}\frac{\hbar\omega_\perp}{\mu}\left(\ln\left(\frac{R_\perp}{\xi}\right) + \frac{3}{4}\right) \tag{6.5}$$

and is shown in Fig. 6-10 to agree well with the data in the BEC regime. On resonance, we do not know the precise value of ξ, but we do know that it is on the order of $1/k_F$. Therefore, we take $\xi = 0.5/k_F$, $1/k_F$, and $2/k_F$ to construct an error band with the hydrodnamic model. The data on resonance and in the BCS regime is in good agreement with the hydrodynamic theory within this error band.

Corrections to this model beyond logarithmic accuracy could be important as $\ln(R_\perp/\xi)$ is only $3-5$, but they are not known in the crossover beyond the weakly interacting BEC regime, and are subject of debate [212]. The superfluid backflow will contribute to the vortex' inertial mass, known as the Baym-Chandler mass [18]. For a strongly-interacting Bose gas, quantum depletions localized inside vortex cores will modify the inertial and bare mass [73, 74]. In the BCS regime, one expects a contribution due to fermions trapped in Andreev bound states inside the vortex core [40], the Kopnin mass [124].

6.6 Temperature-dependence of the solitonic excitation

In Ref. [243], we investigated the motion of the solitonic vortex as a function of temperatures for the unitary Fermi gas (see Fig. 6-11). Thermometry from fits of the density profiles to the equation of state measured in [129] yielded an upper limit of $T = 0.05T_F = 10\,\mathrm{nK} \approx 3\hbar\omega_\perp$ for our lowest temperatures. At such low temperatures, thermometry via fitting is less sensitive to small changes in temperature [116]. We therefore use the thermal fraction of molecules after a rapid ramp to the BEC-side of the Feshbach resonance as a robust thermometer [116]. To control the temperature

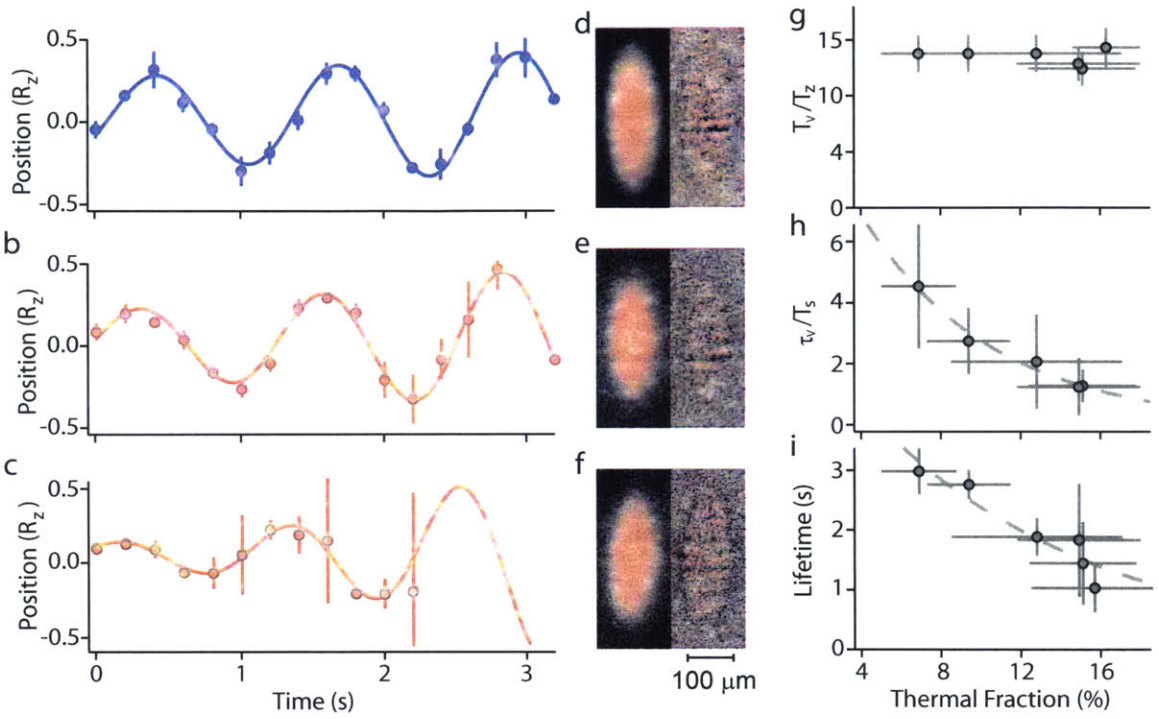

Figure 6-11: Effects of finite temperature. (a-c) are trajectories of the defect for increasing temperature, with thermal fractions (a) 7(2)%, (b) 9(2)%, and (c) 15(3)%. The error bars indicate the standard deviation of typically five repetitions and the solid lines are fits to the data to the anti-damped sinusoidal function $f(t) \propto \exp(t/\tau_s)\sin(2\pi t/T_s + \phi)$. While the period is found to be independent of temperature within our uncertainty, the anti-damping time decreases from $\tau_s/T_s = 5(2)$ for the coldest clouds (a) to $\tau_s/T_s = 1.3(5)$ for the hottest ones (c). (d-f) are representative optical densities and residuals of the superfluid after the rapid ramp. While at low temperatures, the defect generated by phase imprint is the only significant density variation, at higher temperatures transverse stripes appear that we tentatively interpret as thermal defects. (g) The defect period is found to be insensitive to temperature. (h) The $1/e$ anti-damping time and (i) the defect lifetime are found to be strongly dependent on the thermal fraction. The lifetime is defined as the time when the probability of observing a defect decreased to 50%. Solid lines are guides to the eye. The horizontal error bars indicate the standard deviation of the thermal fraction within a data set. The vertical error bars in (g) represent the typical spread over five measurements, those in (h) result from the contribution of the fitting error on τ_s and the error on T_s, and those in (i) reflect the time difference between having 90% and 10% survival probability.

without changing the evaporation (in order to maintain the same atom number), we make use of the residual heating coming from the noise of the ODT. Therefore, the temperature can be controlled by adjusting the final trap depth of the ODT.

The vortex period is found to be insensitive to changes in the temperature within uncertainty (Fig. 6-11 (g)). The stability of the vortex is however strongly affected. At low temperatures, the vortex oscillates essentially without energy loss, demonstrating dissipationless flow (Fig. 6-11 (a)). For increasing temperatures, we observe anti-damping of oscillations (Fig. 6-11 (b)). This is characteristic for a particle with negative mass that can lower its energy by acceleration. To our knowledge, such anti-damping of a solitonic excitation - whether a soliton or a vortex - had not been directly observed previously in a quantum gas experiment. The energy loss is likely due to collisions with thermally induced phonons [78], and we indeed observe a strong decrease in the anti-damping time constant (Fig. 6-11 (h)). As the temperature rises, the vortex's position becomes less reproducible (Fig. 6-11 (c)) and its lifetime is strongly reduced (Fig. 6-11 (i)). At higher temperatures, we observe increased fluctuations in the form of stripes (see insets in Fig. 6-11 (d-f)), some of which appear to have comparable contrast to the imprinted vortex. These additional stripes might be "thermal defects", such as "thermal solitons" predicted to occur even in equilibrium in weakly-interacting BECs [113], or thermal vortices as in a 2D BEC [49]. These soliton-anti-soliton or vortex-anti-vortex pairs can be expected to spontaneously break and proliferate, similarly to the vortex-anti-vortex pairs in a 2D gas [21, 125, 49]. Since the production of these defects are not deterministic, it is not possible to perform tomographic imaging to ascertain their identity as solitons/domain walls or vortices. However, the expectation is that it is less likely to generate spontaneous domain wall in the order parameter than to have thermally activated circulating current, so the thermal defects observed here are probably thermal vortcies.

6.7 Conclusion

To conclude this chapter, we have generated a long-lived solitonic vortex and have studied its motion in a fermionic superfluid. Such solitonic excitations have not been studied experimentally prior to our works. In the initial study, we created the excitation using the well-established phase imprint technique [34, 54, 20]. The resulting excitation is long-lived and has large inertial-to-bare-mass. As the standard integrated imaging does not provide enough information to definitively identify the object, we followed up with a second study in which we implemented a tomographic imaging technique that allows us to probe the 3D structure of the defect. Tomography of the defect conclusively demonstrates that the long-lived solitary wave observed in our fermionic superfluid is a solitonic vortex. The vortex is topologically protected, explaining its long lifetime, and its theoretical inertial to bare mass ratio agrees with that found experimentally. Solitonic vortices can be expected to occur as persistent defects created via a Kibble-Zurek mechanism [234, 58], via phase-imprinting [20, 19] or even via thermal excitations, as hinted at by the observation of thermally induced defects in [243]. They also correspond to the "N"-shaped vortices created via rotation in [193], in the limit of zero rotation frequency (called "S"-shaped in [121]). With the ability to create a solitonic vortex on demand, there are a number of interesting physics that can be studied with this topological excitation: a study of the interaction of multiple solitonic vortices in fermionic superfluids, a measurement of the current-phase relation of a solitonic vortex [122], the investigation of its contribution to the flow resistance of the superfluid [92], and the observation of the Andreev states bound to vortex cores [40], to name a few.

Chapter 7

Cascade of solitonic excitations

7.1 Introduction

The study of the dynamics of a single vortex [243, 127] in a strongly interactin fermionic superfluid, reported in the previous chapter, opens a new arena of experimental investigation. As discussed in the last chapter, the large ratio of the inertial mass to the gravitational mass of the vortex can, to a large degree, be quantitatively explained by a hydrodynamic formalism, which describes the dynamics over the length scale larger than the healing length ξ. In this description, the mass ratio of the vortex is controlled by the compressibility of the medium in which the vortex resides. It is already interesting to know that the vortex mass is mostly explained by hydrodynamics, compared to other contributions, such as the superfluid backflow and fillings due to quantum depletions or Andreev states. However, the hydrodynamic formalism lacks the description of the dynamics at the length scale of ξ - the length scale over which the defects are localized. A microscopic description is required to completely capture the behaviors of phase defects. While weakly-interacting Bose-Einstein condensates (BECs) are well understood in terms of the Gross-Pitaevskii equation (GPE), there is no miscroscopic wave equation available for the strongly-interacting Fermi superfluid, where the dynamics occuring at the core of these phase-defects is highly nontrivial [29]. At the mean-field level, a unified description is found in the Bogoliubov-de Gennes (BdG) formalism [7, 236, 203, 66]. It provides a crossover theory that con-

nects the regime of weakly-interacting BECs of molecules and superfluidity of Cooper pairs described by the Bardeen-Cooper-Schrieffer (BCS) theory. However, as a mean-field theory, the BdG approach is not expected to accurately capture the behavior of solitonic excitations in the strongly-interacting regime. Formalisms that are beyond the BdG theory have been developed to study the dynamics of phase defects in the unitary Fermi gas, such as the time-dependent superfluid local density approximation (TSLDA) [31] and the time-dependent Ginzburg-Landau (TDGL) theory [198]. Experiments with the unitary Fermi gases provide the necessary input for such dynamical theories.

An experiment which studies the microscopic dynamics of solitonic excitations requires creating these excitations in a controlled way and setting the conditions for the core dynamics to be revealed and analyzed. One way in which microscopic dynamics can be observed is through the interaction of these phase-defects, for instance in vortex recombination where two initially separated vortices come close to each other and combine their cores [31]. Another approach is to observe the relaxation of a highly energetic defect [61, 30, 188, 198, 240]. Solitonic excitations follow a well-defined hierarchy in terms of stability and energy cost in 3D. The planar soliton, with a large nodal volume, is the most energetic [25] and is dynamically unstable towards decay. It can decay via the snake-instability [156], the undulation of the soliton plane, towards the formation of other solitary waves of lower energies. Recently, a family of these solitary waves has been identified as solutions of the GPE [155]. These objects resemble the Chladni figures and trace the nodal lines of the unstable vibration modes of a planar soliton. They include the vortex ring and the vortex line, as well as more exotic excitations whose nodal structures are composed of intersecting rings and lines.

In weakly-interacting BECs, solitons have been observed to decay into a vortex ring [4] that subsequently break into a vortex-antivortex pair before leaving a single vortex line [19]. In the case of strongly interacting fermionic superfluids, similar scenarios have been predicted numerically by the BdG approach [240, 188, 198], but an experimental investigation on such microscopic dynamics is still lacking.

In this chapter, I describe the study of a cascade of solitonic excitations in a

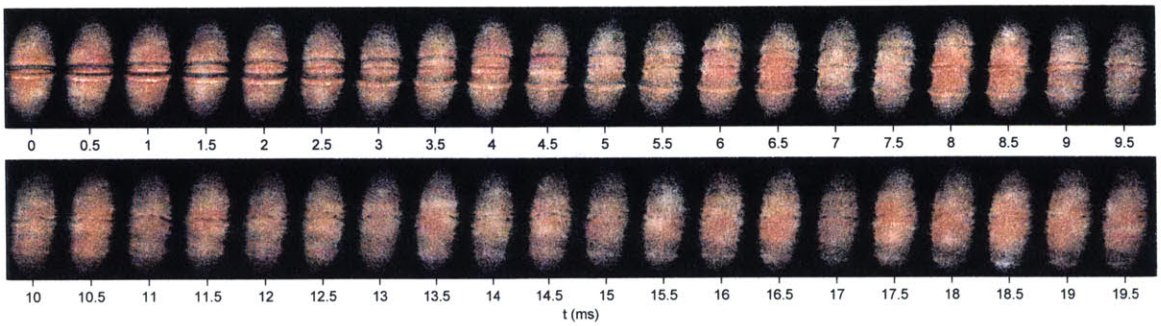

Figure 7-1: Time-evolution of the central slice ($y = -13\,\mu$m) for $0\,\text{ms} \leq t \leq 19.5\,\text{ms}$, with 0.5 ms time-steps.

unitary Fermi superfluid [128]. The cascade is initiated by a one-sided phase imprint. Via tomographic imaging, we observe a planar dark soliton as the initial product of the imprint and trace its subsequent evolution. We are able to follow the the nodal plane's surface dynamics which occurs at the level of interparticle spacing, as the soliton snakes, punctures, and breaks. The decay of the soliton leads to a ring defect, which continuously disintegrates, finally leaving behind a single, remnant vortex line. In intermediate stages we find evidence for more exotic structures resembling Φ-solitons. We also measure the growth rate of the modes in the snaking dynamics. The observed evolution of the nodal surface represents dynamics beyond superfluid hydrodynamics, and provides a benchmark in the quest for an adequate wave equation describing the unitary fermionic superfluid far out-of-equilibirum.

7.2 Dynamics of a unitary Fermi gas after a phase imprint

Similar to the experiments on solitonic vortex, we create a strongly interacting fermionic superfluid using a balanced mixture of the two lowest hyperfine states of ^{6}Li, $|1\rangle$ and $|2\rangle$ at a Feshbach resonance 832 G. The atomic clouds contain $\sim 7 \times 10^5$ atoms per spin state. The trapping frequencies for the axial and the radial (in the harmonic approximation) directions are $\omega_z/2\pi = 10.87(1)$ Hz and $\omega_\perp/2\pi = 69(6)$ Hz, respectively. Gravity slightly weakens and distorts the trapping potential along the vertical

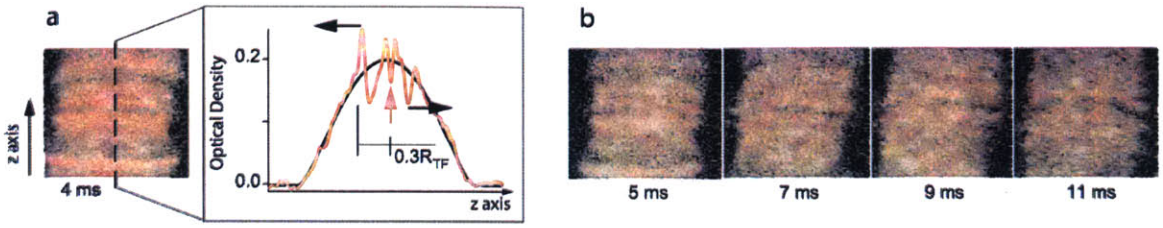

Figure 7-2: Magnified view of the central slice. (a) Central slice at 4 ms after the imprint, showing the structure of the generated objects. Square box: a cut of the density distribution (red) is compared to the corresponding Thomas-Fermi profile (black) without density perturbation. Both sound waves display a valley-hill structure, with a markedly higher amplitude for the hill of wavefront on the negative-z side. (b) Magnified images of the density at $t = 5$, 7, 9, and 11 ms showing the bending of the defect resulting from the snake instability.

y-direction (see Appendix A). The axial and radial Thomas-Fermi radii of the cloud are $R_z = 326(2)\,\mu$m and $R_\perp = 54(2)\,\mu$m, and correspond to a chemical potential at the center of the cloud of $\mu = h \times 3.7(1)$ kHz. The techniques for phase imprinting, rapid-ramp expansion for revealing the superfluid order parameter, and tomographic imaging are the same as used in the works reported in the previous chapter and described in details in 6.2.2, 6.2.3, and 6.4 respectively.

In Fig. 7-1, we show the time sequence of images recorded in the first 20 ms (with 0.5 ms time step) following the phase imprint, which corresponds to the density distribution at the central slice of our superfluid samples. Immediately after the imprint, we observe a strong disturbance near the central axial position ($z = 0$) of the cloud, as expected from the symmetry of our imprinting setup, where the imprinting laser light is exposed on one half ($z > 0$) of the cloud. The initial perturbation then decomposes into: (i) two wavefronts quickly propagating in opposite directions to the edge of the cloud, and (ii) a sharp density defect, with a very small velocity, that remains straight for about 5 ms and then undergoes a complex dynamics. This object we shall identify as a planar dark soliton via tomographic imaging. The velocities of the upper and lower wavefronts are found to be 13.1(4) mm/s and 13.1(8) mm/s respectively, which coincide with the speed of sound of 12.9(1) mm/s estimated from the peak density using the relation $c_s = \sqrt{\xi_B/3}v_F$, where $\xi_B = 0.37$ is the Bertsch

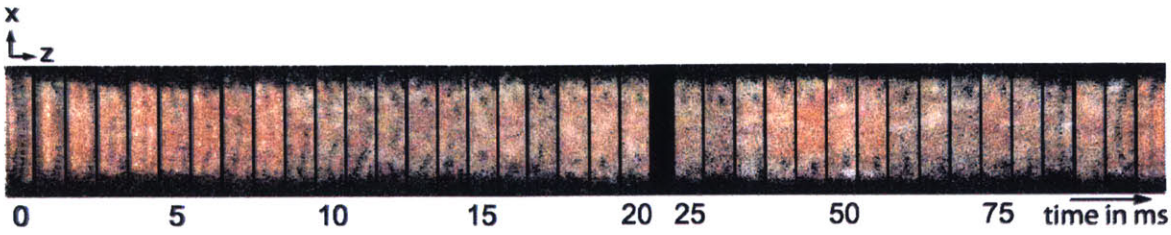

Figure 7-3: Time-series of the central slice up to $t = 100\,\mathrm{ms}$, focusing on the region around $z = 0$.

parameter [129] and v_F the Fermi velocity[1] (see 7.2.1 for more details). Therefore, we identify these two wavefronts as sound waves. Note that the apparent large amplitudes of these sound waves is a consequence of the rapid-ramp, which will be discussed shortly in 7.2.3.

In contrast to the fast sound wave, the slow defect displays a much richer dynamics, which is shown in greater detail in Fig. 7-3. We first observe that the defect core undergoes an undulation during the interval $5\,\mathrm{ms} \lesssim t \lesssim 15\,\mathrm{ms}$, after which it breaks into a pair of dots located at opposite edges of the cloud, which suggests a ring structure. This structure survives up to $t = 80\,\mathrm{ms}$, after which the return of a stripe of depletion indicates the presence of a horizontal vortex line.

Before discussing further this complex dynamics, I will first describe in more detail the speed of sound measurement, the dynamics during the rapid-ramp expansion, and effects of the rapid-ramp on the sound wavefronts. In 7.3, I will return the focus to the dynamics of the defect and discuss its evolution as observed via tomographic imaging.

7.2.1 Sound measurement

The two wavefronts that rapidly propagate towards the edges of the cloud feature a valley-hill combination characteristic of sound waves [110]. We focus on the central part of these wavefronts (i.e. around $x = 0$) and extract, for each wavefront, the

[1]The observations made here are reminiscent of the first phase-imprinting experiment realized in Bose-Einstein condensates [20], where two waves rapidly propagating in opposite directions were created, one of which has been interpreted as a fast dark soliton. Here however, we observe that both wavefronts propagate at the speed of sound.

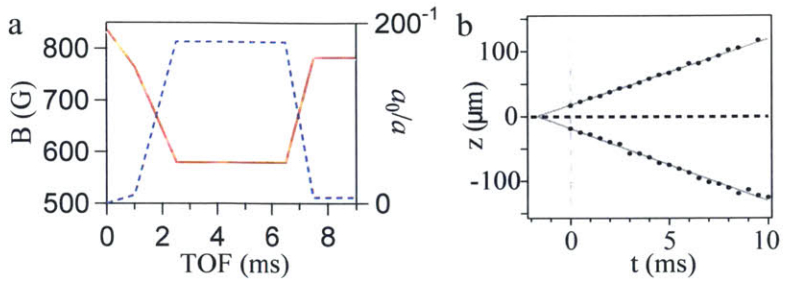

Figure 7-4: a) Schematics of the rapid ramp. The solid line shows the ramp of the Feshbach field. At wait time t after the imprint, the field is ramped from 832 G to 760 G in 1 ms, and then ramped down to 576 G over 1.5 ms. The field is held at that value for 4 ms, and then ramped back to 780 G over 1 ms. The field is held at 780 G for 1.5 ms before the spatially selective optical pumping light is applied and the cloud is imaged. The dashed line shows the corresponding a_0/a, where a is the scattering length and a_0 is the Bohr radius: 0 at 832 G, 4300^{-1} at 760 G, 225^{-1} at 576 G, and 6500^{-1} at 780 G. b) Extraction of the effective time delay after the rapid ramp, from the extrapolation of the sound wave trajectories. Solid black circles: upper and lower sound wave positions as function of time t. The linear fit (solid gray lines) yields an effective lag of $\Delta t \approx 1.7$ ms.

position of both the valley and the hill as a function of time. For the upper wavefront, we find that the valley (density minimum) propagates at 12.1(2) mm/s and the hill (density maximum) at 14.2(8) mm/s, which gives an average speed of the wavefront of 13.1(8) mm/s. For the lower wavefront, we find that the valley propagates at 13.1(3) mm/s and the hill at 13.1(1) mm/s, giving an average velocity of 13.1(4) mm/s. These measurements can be directly compared to the prediction of the speed of sound in a unitary Fermi gas, which only depends on the density and the Bertsch parameter $\xi_B = 0.37$ through the relation $c_s = \sqrt{\xi_B/3}\hbar k_{\mathrm{F}}/m$, where $k_F = (3\pi^2 n)^{2/3}$ is the Fermi wave vector. With the chemical potential at the center $\mu(0) = h \times 3.7(1)$ kHz, we obtain the peak value of the Fermi wave vector $k_F = 3.47(2)\,\mu\mathrm{m}^{-1}$. The local speed of sound at the center of the cloud is therefore found to be 12.9(1) mm/s, in very good agreement with the measured local speed of the two wavefronts, which we therefore identify as sound waves.

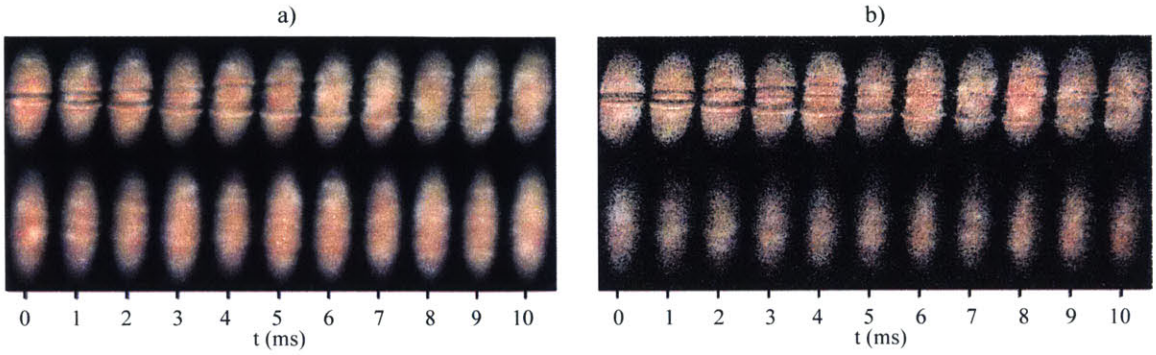

Figure 7-5: Comparison of images with and withou at rapid ramp of the Feshbach field. Top: images after 9 ms expansion with rapid ramp described previously. Bottom: images after 4 ms expansion without changing the Feshbach field. The expansion time is chosen so the radial size of the cloud roughly matches those obtained with rapid ramp. In each case we show (a) the integrated density (no slicing) and (b) the density of the central layer. Without rapid ramp, the amplitude of the initial wave fronts is strongly reduced.

7.2.2 Dynamics during the rapid ramp

The detection procedure requires a 9 ms interval between the time t of the dynamics that we want to observe and the time when the image is actually taken. During this stage, the cloud spends ~ 2 ms in the strongly-interacting regime $(k_F a)^{-1} \lesssim 1$ where the expansion is hydrodynamic. For the rest of the rapid ramp, the cloud is so weakly-interacting that the expansion can be essentially considered ballistic. Therefore, we estimate that the 9 ms of the combined rapid ramp and expansion can be accounted for as an effective lag of ~ 2 ms in the dynamics of the observed images. One can notice this lag in Fig. 7-4 (b), where we show the early stage of the sound trajectories. By extrapolating the sound trajectories, we find an effective lag of 1.7 ms, consistent with our estimate.

7.2.3 Rapid-ramp versus time-of-flight imaging

The images obtained after rapid-ramp show strong modulations of the density distribution. Based on these images, one may conclude that the phase-imprinting leads to an intense disturbance in the density accompanied by shock waves. This is however

not the case. In order to clarify this point, we repeated the time sequence of the dynamics following the imprint by probing the density distribution after a time-of-flight expansion of 4 ms (chosen so the radial size matches that of the rapid-ramp profiles), without any change in the scattering length. The corresponding images are shown in Fig. 7-5 (a), where we observe weak perturbations in the density profile. In particular, we observe two density wavefronts of small amplitudes propagating in opposite direction to the edges of the cloud, which we identify as the previously observed fast wavefronts in the rapid-ramp images. We also show the same time-sequence recorded after time-of-flight combined with the slicing stage (Fig. 7-5 b)). The images without rapid-ramp obviously suffer from a lower signal-to-noise, and the fast wavefronts are barely visible. This comparison shows that the phase-imprint performed in our experiment is indeed a gentle process, which affects predominantly the phase of the superfluid order parameter rather than the density. This also demonstrates another powerful aspect of the rapid-ramp, which not only magnifies the short-ranged variations of the order parameter $\Delta(\mathbf{r})$, but also seems to enhance the contrast of simple and perturbative density variations.

7.3 Evolution of the solitonic excitations revealed by tomographic imaging

In order to understand further the dynamics of the central defect, we employ tomographic imaging. In Fig. 7-6, we show a set of representative tomographic images at various times of the dynamics. From these images, we are able to reconstruct the shape of the defects and follow their formation within the superfluid. The right panel of Fig. 7-6 shows the reconstructed nodal structure as seen from the long axis (the z-axis) of the cloud. At $t = 3$ ms, the tomography indicates a density depletion across the whole atom cloud, demonstrating that the initial defect is a planar dark soliton. This is supported by its extremely slow velocity, relative to the speed of sound, and also by the undulation dynamics seen after ~ 5 ms. The condition for dynamic stabil-

ity in an axisymmetric cloud is $R_\perp \lesssim \xi$, where ξ is the size of the defect. At unitarity, $\xi \sim 1/k_F$ [31]. In the present experiment we have $R_\perp \sim 50/k_F$, so the system is well in the 3D regime. The snaking of the nodal plane is clearly observed at $t = 7\,\text{ms}$. There, the depleted area of the soliton features high-order snaking modes, and in fact has already developed a small puncture, as seen in the slice located at $y = +65\,\mu\text{m}$ and reflected in the reconstructed nodal structure.

Remarkably, the subsequent dynamics is not a random tearing of the soliton plane. For the next $\sim$ 10 ms, the hole in the punctured soliton plane observed at 7 ms continuously grows in size in the upper half of the plane. This transforms the planar soliton into an asymmetric vortex ring, combining the bottom part of the soliton plane and a vortex line in the form of a semicircle on the upper part. This unconventional structure is observed at 16 ms and also at 20 ms where the area of planar depletion seems to be further reduced. We thus see that the soliton tears in its upper half and subsequently undergoes successive transformations into well-defined structures of smaller and smaller nodal volumes.

At this stage, one might anticipate that this structure will seed the formation of a vortex ring, with the hole in the nodal plane continuously increasing in size until the nodal volume is constricted to a loop with a core of size ξ. However, the tomographic images obtained at later times suggest a more complicated scenario[2], where a second puncture occurs in the lower nodal plane, resulting in the formation of a nodal structure consisting of a line intersecting a ring. This structure is seen in the tomographic images at $t = 85\,\text{ms}$ and resembles the Φ-soliton recently proposed in Ref. [155]. Further in time, the ring part of this exotic defect continuously disintegrates (as seen at $t = 95\,\text{ms}$ and 400 ms), and leaves behind a single vortex ($t = 1\,\text{s}$), which precesses in the superfluid, as reported in the previous chapter.

The full collection of tomographic images is included in Appendix B.

[2]This may be inferred from the statistical analysis of multiple images of each slice taken at each t. The collection of these images between 50 ms and 100 ms is shown in Fig. B-2 of Appendix B.

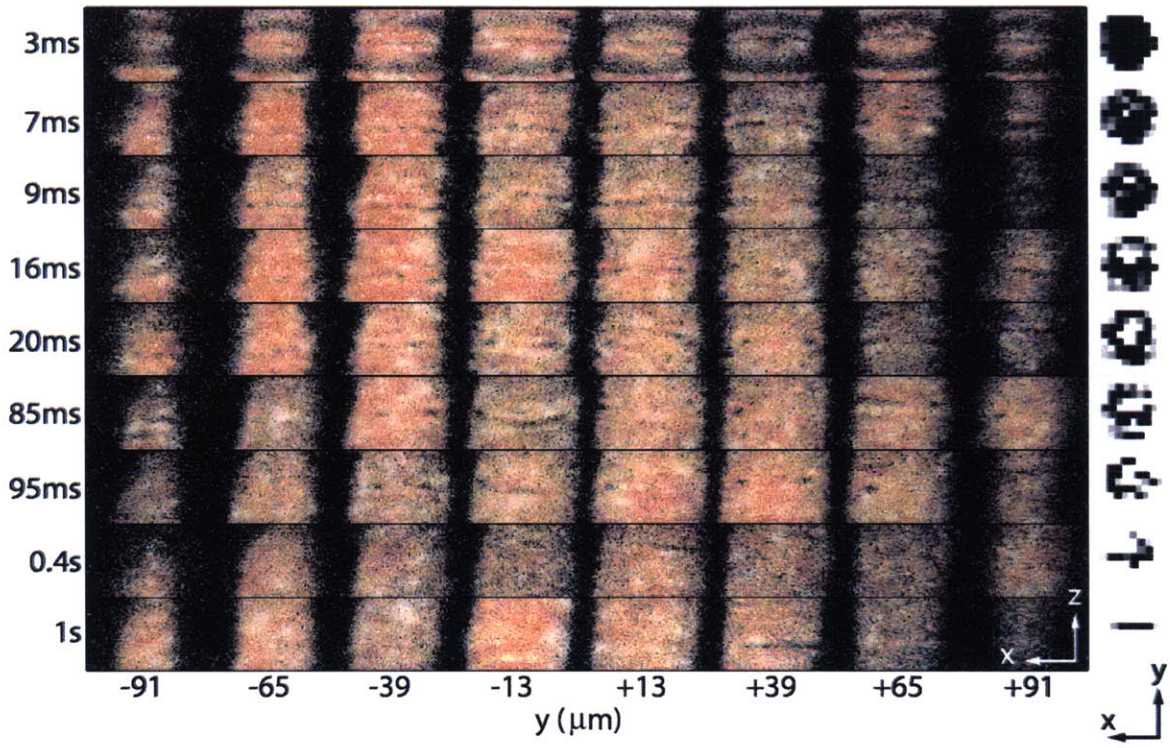

Figure 7-6: Tomography of the cascade. Main panel (left): representative tomographic images at different stages of the cascade. Right column: shows the structure of the depletion due to the defect, as seen along the z-axis, reconstructed with the tomographic images. $t = 3$ ms: sharp density depletion across the whole cloud signaling a planar dark soliton. $t = 7$ ms: snaking of the soliton plane and first signature of a puncture. $t = 9$, 16 and 20 ms: the puncture in the upper half of the soliton plane grows and yields the formation of an asymmetric vortex ring, combining half of the soliton plane and vortex line in semicircle. $t = 85$ ms: the lower plane is punctured and a vortex line forms across a ring. $t = 95$ ms and $t = 400$ ms: the ring part of the defect progressively disintegrates. $t = 1000$ ms: a solitonic vortex has been formed and precesses in the superfluid.

7.4 Snaking dynamics of the soliton

I will now discuss the analysis of the soliton's snaking, which is responsible for initiating the cascade. Qualitatively, the snake instability observed here is not surprising given the 3D character of our superfluid [156] where $R_\perp \sim 50/k_\mathrm{F}$, far from the condition for the dynamic stability of a soliton in an axisymmetric cloud $R_\perp \lesssim \xi \sim 1/k_\mathrm{F}$. However, at the quantitative level, little is known of the soliton's snaking dynamics at unitarity [43, 237] where the available microscopic descriptions rely on the mean-field BdG formalism and extensions of it [81].

For perturbations on the soliton surface $z_\mathrm{s}(x)$ in the form of $z_\mathrm{s} \propto \cos(qx - \omega_q t)$, instability is associated with imaginary component in the mode ω_q, which corresponds to the rate of growth. At long wavelengths (corresponding to small wave numbers q), a hydrodynamic argument shows that the mode is purely imaginary, and the growth rate has a linear dispersion [112],

$$\omega_q = \pm iq\sqrt{\frac{E_s}{|M^*|}}, \tag{7.1}$$

where M^* is the inertial mass of the soliton, and E_s is the energy of the soliton. This growth rate of the snake instability therefore provides information on the microscopic properties of the soliton. BdG simulations have confirmed this linear dispersion in the BEC-BCS crossover [43]. In addition, in the same work, the growth rate is observed to have a downturn at shorter wavelengths (larger q).

In order to quantify the undulation dynamics, we perform a Fourier analysis on the soliton's shape $z_\mathrm{s}(x)$ in terms of the transverse modes $\lambda_n = 2R_\perp/n$, with $n = 1, 2, ...$ being the mode number. More precisely, we search for an expansion of the form $z_\mathrm{s}(x) \approx A_0 + \Sigma_{n=1}^{N_\mathrm{max}} A_n \cos\left(2\pi n \frac{x}{2R_\perp} + \phi_n\right)$, where the Fourier amplitudes A_n (and phases ϕ_n) are determined numerically. In Fig. 7-7 (a), we display snapshots of the superfluid containing the soliton for $2\,\mathrm{ms} \leq t \leq 11\,\mathrm{ms}$ and, in Fig. 7-7 (b), the corresponding soliton shapes $z_\mathrm{s}(x)$ that we extracted by tracking the density minima. For each of these snaking curves, the result of the Fourier expansion up to the 5^{th} order

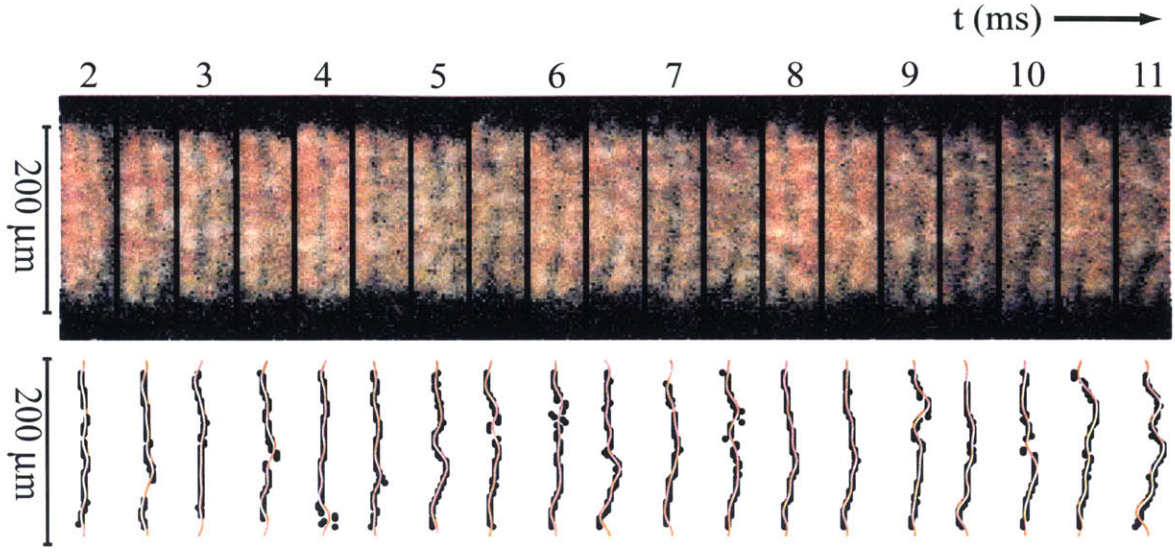

Figure 7-7: Extraction of the soliton shape for Fourier analysis. Top: snapshots of the superfluid containing the soliton. Bottom: extracted soliton profiles $z_s(x)$ (black dots) along with the corresponding profiles of the Fourier expansions to the 5^{th} order (solid gold line).

(gold solid line) is superimposed and shows a good overlap, demonstrating that the soliton's undulation observed here is well characterized in terms of transverse mode excitations. We computed the Fourier spectra of the soliton's undulation between $t = 2\,\text{ms}$ and $11\,\text{ms}$ (see Fig. 7-8 (a)), and obtained the evolution of the Fourier amplitudes A_n shown in Fig. 7-8 (b). Here we see that the fundamental mode $\lambda_1 = 2R_\perp$ dominates the undulation dynamics, with a consistently large weight and a significantlly higher growth rate $\dot{A}_1$ compared to the higher harmonics. We observe that the rates $\dot{A}_n$ monotonically decrease as the mode number n increases (see Fig. 7-8 (e)). The contribution of the modes $n > 5$ was found to be within the noise.

The trend observed in Fig. 7-8 for the growth rates $\dot{A}_n$ stands in contrast[3] to the expectation of a linear growth at small mode numbers. Physically, the large contribution of the fundamental mode and its large growth rate found observed here are not surprising given the inhomogeneity of our superfluids. The velocity of the soliton

[3]Note that the growth rate that we report here is in the units of a speed, and not a frequency as considered in [112, 43], because the data for $\lambda_n \neq \lambda_1$ does not allow for an exponential fit. The trend comparison is however still relevant.

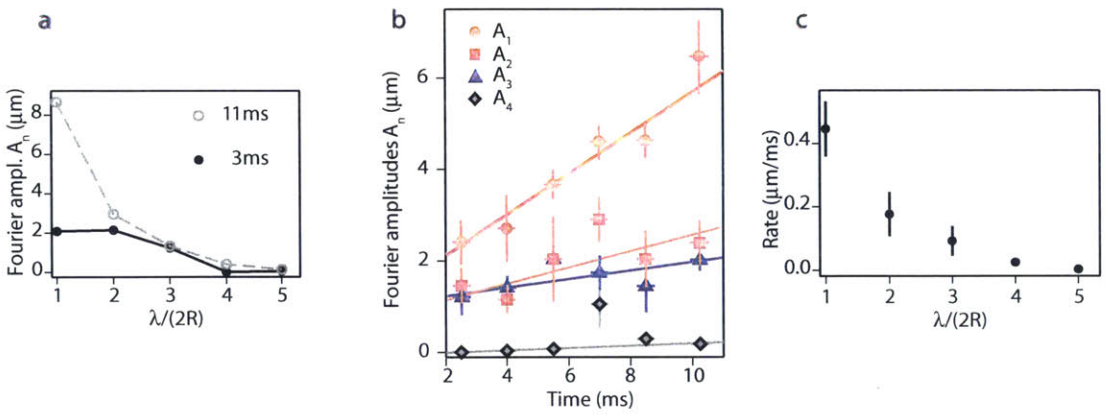

Figure 7-8: Spectral analysis of the snaking dynamics. (a) Fourier spectra at $t = 3$ and 11 ms. (b) Fourier amplitudes A_n as a function of time, for $n = 1$ (circle), 2 (square), 3 (triangle) and 4 (diamond) and their fits to a line (solid lines). The error bars indicate the statistical spread due to a 3-points binning of the data. (c) Growth rates $\dot{A}_n$ for $n = 1$ to 5, obtained from the linear fits in (b), with the error bars being the fit error.

is given by the phase-velocity relation $v/v_c = f(\Delta\phi)$, where $\Delta\phi$ is the phase difference across the soliton and v_c is the superfluid critical velocity. While the functional form of f is not known for the unitary Fermi gas, it is believed to be monotonic at small relative velocities [204]. Therefore, in an inhomogeneous cloud as ours, $v_c \propto k_F$ depends on the x coordinate, and is the largest at the center of the cloud. As a result, the velocity of the soliton is the highest at the center ($x = 0$) and gradually decreases towards the edges ($x \to \pm R_\perp$). Consequently, a travelling soliton (in the z-direction) develops to a drum-like profile that continuously stretches along the propagation direction. This explains (at least partially) the growth of A_1. In order to have a quantitative understanding of our measurements, it would require the use of the correct current-phase relation of a dark soliton in a unitary Fermi gas. Alternatively, one may perform the same experiment in a homogeneous potential (discussed in Chapter 8), which would allow for obtaining the dispersion of the snaking rate in a homogeneous system that can be compared to available theories.

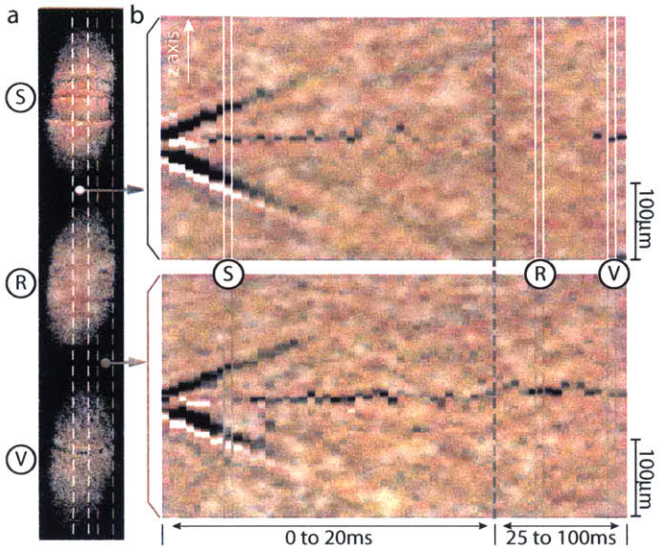

Figure 7-9: Summary of dynamics following the phase imprint. (a) Representative images of the central slice at t =4, 50, and 95 ms showing a planar soliton (S), vortex ring (R), and vortex line (V). The vertical lines mark the region of interest used to generate the residuals in (b). (b) Upper panel: Residuals of the central slice along the central axial cut $x = 0$. Lower panel: Residuals in the central slice along the outer axial cut. Bright (dark) shading indicates density excess (depletion).

7.5 Evolution of solitonic excitations towards a single vortex

In Fig. 7-9, we summarize the time evolution following the phase imprint by tracking the motion of the waves generated in the superfluid. The upper panel of Fig. 7-9 shows the residuals in the central slice along the central axial cut at $x = 0$, while the lower panel shows the residuals along its outer edge. The two panels therefore allow us to distinguish between a depleted stripe across the cloud, a short depleted segment, and a pair of nodal points. In Fig. 7-10, we record the position of the density minima detected in each residual plot as a function of time. In these two diagrams, we recognize the initially created sound waves which follow two linear trajectories with opposite slopes, while the central defect slowly moves towards the $z > 0$ direction. We also notice shallower sound waves emitted at$\sim$ 5 ms. These sound waves form a pattern of hydrodynamic wakes.

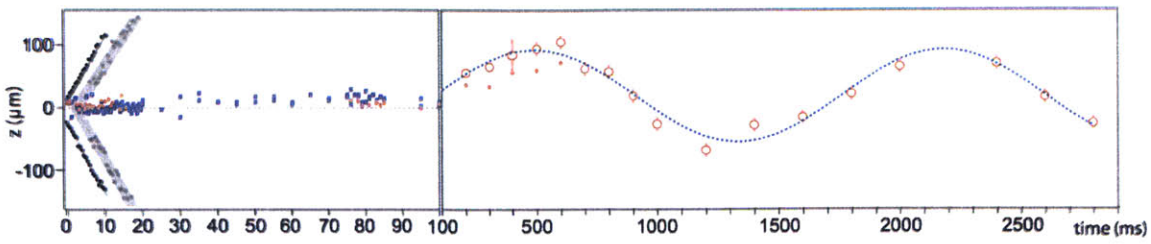

Figure 7-10: Displacement as a function of time for sound waves and defects. In the left panels are: initial sound waves (black solid circles), the second set of sound waves (gray solid circles and band), the defect in the central axial cut (red circles), and the defect in the outer axial cuts (blue squares). Right: precession motion (projected on the z-axis) of the solitonic vortex resulting from the cascade.

The insight of the tomographic images (discussed in 7.3) allow us to identify the course of evolution shown in Figs. 7-9 and 7-10. The presence of depletions along both the central and the outer axial cuts up to $t \sim 15\,\text{ms}$ is associated with the initially created planar soliton. Between about 15 ms and 80 ms, the disappearance of the depletions in the central axial cut indicates that we have an object with at least a partial ring structure. The return of a line of depletion at $t \sim 80\,\text{ms}$ marks the eventual transition of the object into its final form. We note that all along the decay cascade, from the puncture of the soliton plane to the return of a horizontal vortex line, we do not observe any significant displacement of the defects along the z direction. This fact is probably an important factor in favor of the repeatability of the vortex trajectory which is shown in Fig. 7-10. Here we plot the oscillation along the z direction, which is the projection of the precessional motion of the vortex on the long axis. It is remarkable that the observed cascade, despite involving multiple (*a priori*) stochastic decays, leads to the formation of a solitonic vortex with a reproducible trajectory.

7.5.1 Comparison to simulations

In recent simulations, several cascade scenarios, starting from a phase imprinted planar soliton, have been proposed in the context of the unitary Fermi gas. In some of these works, it has been found that in a cylindrically symmetric potential with

negligible dissipation, a planar soliton decays into a long-lived vortex ring which then undergoes oscillatory motion along the z-axis [30, 237, 188]. Later works introduced dissipations and observed the consistent formation of a single vortex with a precessional motion [198, 240]. Closely related to our case is the recent work of [240], based on the TSLDA, in which the authors take into account the trap distortion due to gravity. Among the various scenarios considered in [240], none is in our regime of parameters (see Appendix A), hence a direct comparison is not possible. For the simulations that include intermediate anisotropy and anharmonicity, it is observed that the soliton's decay is followed by the formation of a vortex ring which propagates over a significant distance before breaking into a vortex-antivortex pair [240]. Eventually, one vortex is ejected while the other precesses in the superfluid. This scenario is therefore qualitatively distinct from our observation, which calls for further simulations with the use of our experimental parameters.

In Appendix C, I discuss what we have found to be ingredients in generating a long-lived vortex as a remnant of the imprint.

7.6 Conclusion

In conclusion, we have observed a cascade of solitonic excitations in a strongly-interacting fermionic superfluid. Using tomographic imaging, we observe the decay pathway of a planar soliton into a single long-lived vortex. We also analyzed the snaking dynamics of the soliton and characterized it in terms of transverse mode excitations. Our work investigates the dynamics of the unitary Fermi gas which occurs at the length scale of the interparticle spacing and provides a novel experimental input for microscopic theories of strongly interacting fermions.

The ability to create a planar soliton on demand in the unitary Fermi gas opens the door to study a number of rich physical phenomena not yet explored experimentally. One may envision to stabilize a soliton in the tightly-confining regime and study the soliton's current-phase relation. Due to its large nodal region (compared to, for example, a vortex), solitons serve as a resource for the observation and manipulation

of Andreev states. In particular, solitons in the presence of spin imbalance provide a possible venue for the detection of the Fulde-Ferrell-Larkin-Ovchinnikov phase.

Chapter 8

Conclusion

When I came to MIT in 2009, I was inspired by the potential of experiments with ultracold atoms to address long-standing questions in many-body physics. I believe I can say with confidence that during my time at MIT, the field has lived up to its potential and continues to show great promise, especially in the program of quantum simulation. For example, experiments with 2D Bose gases have demonstrated scale invariance [105], obtained the equation of state [242], and measured the superfluid critical velocity [55]. Advances in quantum gas microscopy for Bose gases [12, 205] and Fermi gases [91, 45, 167] create the opportunity to directly probe the Hubbard model and to study quantum magnetism with single lattice site resolution. The realization of the Harper Hamiltonian [2, 153] enables the study of systems with high magnetic fields. The creation of ground-state dipolar molecules makes it possible to study many-body systems with dipolar interactions [160, 166].

My colleagues and I have had the privilege to contribute to the growing knowledge of the unitary Fermi gas. The precision measurement of its thermodynamics serves as a benchmark for theories, and our measurement of the Bertsch parameter and the critical temperature have become a standard reference for other theoretical and experimental studies. Additionally, our experiments on solitonic excitations have observed for the first time the dynamics of solitary waves such as planar solitons and vortices in the unitary Fermi superfluid. The realization of these objects has paved the way for the study of the phase-velocity relation, Andreev states, and vortex

interactions in the strongly interacting Fermi superfluid.

Throughout these investigations, it has become increasingly clear that the inhomogeneous trapping potential, which has served cold atom experiments fantastically over the past two decades, is now a limiting factor that hinders us from obtaining further insights into the unitary Fermi gas. Take, for example, the experiment reported in the last chapter. In the spectral analysis of the snake instability, it was found that the fundamental transverse mode had the highest growth rate. As I have argued previously, this phenomenon is very likely due to the transverse density inhomogeneity of our atomic samples. While our measurments bring in the velocity-phase relation of the soliton as a new interesting ingredient in its snaking dynamics, with respect to the uniform case, they also raise even higher the challenge of a theoretical understanding. In particular, they cannot be directly compared to the available calculations, such as in Ref. [43] where a homogenous system is considered, and already constitute a tour-de-force.

This is just one demonstration of the need for tailored trapping potentials in cold atom experiments. While inhomogeneous trapping potentials can offer advantages in specific cases, such as for scanning through the phase diagram in the measurement of the equation of state (in fact, it is necessary if one is to make use of the no-fit procedure described in Chapter 4), in most other instances, it hinders one's ability to obtain a measurement that can be conveniently compared to a theory. This is especially true for transport measurements, such as the spin-transport experiments [209, 210] that I participated in my early days at MIT.

Confining Fermi gases with tailored potentials offers crucial advantages in many areas of investigation, including the precision measurement of the thermodynamics, the observation of phases confined to narrow parameter regimes, the study of critical phenomena, and the accurate determination of transport coefficients. This is the route that my team is currently taking. In a nutshell, we are implementing a tailored potential that is homogeneous along the x and y directions, while along the z direction the potential may be either uniform or harmonic. To construct such a potential, we forego the traditional red-detuned optical dipole trap. Instead, we let the atoms sit in

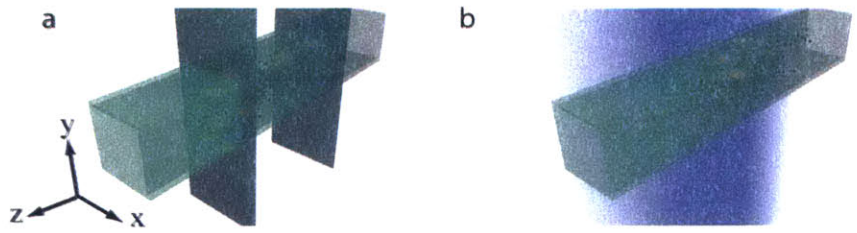

Figure 8-1: Tailored potentials for Fermi gas experiments. The Fermi gas is confined by walls of light formed from blue-detuned lasers at 532 nm. The potential is uniform in the x-y directions. This may be realized in one of the following ways: two pairs of orthogonal sheets for a rectangular potential (as shown in this figure), or a circular sheet for a cylindrical potential. Along the z-direction, the potential may be uniform (shown in (a)), with the system sealed off by two end caps formed by sheets of green light, or harmonic (shown in (b)) with the use of a magnetic curvature.

the dark and make use of blue-detuned light to construct repulsive walls through the use of opaque intensity masks whose shapes can be custom designed. The masks are illuminated by green (532 nm) laser beams and imaged onto the atoms. Specifically, we form a sharp wall of either rectangular or circular shape in the x-y plane (see Fig. 8-1). The confinement in the z-direction can be accomplished with either a pair of end caps formed by two sheets of light (in the case of a uniform potential) or with a harmonic potential provided by a magnetic curvature. To make effective use of laser power, the green beams will be shaped appropriately. For example, for the circular wall in the x-y plane, a single green beam is shaped into a ring with the use of an axicon combined with a microscope objective, while for the rectangular walls, the beam is shaped into two separate pairs of orthogonal sheets using a set of prisms.

Naturally, our first scientific goal using such tailored potentials is to directly observe the Fermi surface of a non-interacting Fermi gas. Surprisingly, this paradigmatic phenomenon has not been observed experimentally: electrons in condensed-matter systems always have interactions, while in cold atom experiments, density inhomogeneity hinders the detection of a sharp Fermi surface with a large signal-to-noise ratio. For example, in Ref. [59], a measurement of the Fermi surface is accomplished in an inhomogeneous gas by probing only the central region of the gas. This leads to a smaller available signal, and the residual inhomogeneity in the probed region can

still blur out the sharpness of the fermi surface. With a uniform potential, one can circumvent these issues, as the entire gas contributes to the measurement. Following a successful observation of the Fermi surface, it is natural to ask how interactions modify the Fermi surface. In particular, the limiting case of a single fermionic impurity interacting with a Fermi sea of majority fermions - the Fermi polaron - offers a platform to study the Landau Fermi liquid theory. With a homogeneous Fermi gas, one should be able to observe a relatively sharp Fermi surface with a Fermi polaron, and measure the quasiparticle weight.

A tailored potential which is homogenous in the $x-y$ directions and harmonic in the z direction is highly advantageous for precision measurement of the thermodynamics. In the case of a box potential of size $L \times L$ in the $x-y$ directions, the column density (measured using an imaging beam along either the x or y direction) is directly related to the local density, $n(x,z) = Ln(x,y,z)$. Therefore, one does not need to perform the inverse Abel transform to obtain the local density. The inhomogeneity along the z direction provides a scan through the phase diagram. One can then apply the same procedure as in the equation of state measurement for a balanced unitary Fermi gas to perform thermodynamic measurements of Fermi gases with spin-imbalance or away from unitarity (or both). Such measurements will address two important outstanding questions. First, is there a pseudogap phase of preformed Cooper pairs above T_c? Second, is there a magnetic superfluid phase, in which superfulidity occurs with a spin imbalance? A measurement of the phase diagram of the spin-balanced gas in the BEC-BCS crossover and of the unitary Fermi gas with spin imbalance will address the first and the second questions respectively. With a tailored trapping potential, one will be able to perform such measurement with high precision.

Lastly, with a homogeneous potential, one may finally be able to observe the elusive Fulde-Ferrell-Larkin-Ovchinnikov (FFLO) state. There has been a long debate about the ground state of spin-imbalanced fermionic superfluids. Fulde and Ferrell (FF) [79], and independently Larkin and Ovchinnikov (LO) [132] proposed that the Cooper pairs condense into one (FF) or two (LO) opposing non-zero momentum states. For smaller imbalance, it can be proven in 1D [149, 244] that the LO phase is

a soliton train with the excess fermions occupying the Andreev bound states located at the nodes of the order parameter. Therefore, in a finite system, a single soliton in the presence of spin imbalance realizes one limit of the long-sought LO phase [244, 145]. In the BCS limit, the existence of the LO phase is guaranteed by the fact that the energy cost for having a single excess fermion localized in a soliton, $E_{\text{soliton}} = \frac{2}{\pi}\Delta_0 = 0.64\Delta_0$ is smaller than the Clogston limit $h_{\text{Clogston}} = \frac{\sqrt{2}}{2}\Delta_0 = 0.71\Delta_0$, which provides the difference in chemical potentials $h = \mu_\uparrow - \mu_\downarrow$ needed to break the Cooper pairs. With an inhomogeneous potential, only a small shell of the cloud has the correct local chemical potential $\mu(\mathbf{r})$ and local order parameter $\Delta(\mathbf{r})$ within the parameter regime (e.g. $0.64 < h(\mathbf{r})/\Delta(\mathbf{r}) < 0.71$ in the BCS limit), and hence the signal of the LO phase will be greatly reduced. For Fermi gases in a homogeneous box potential, however, the density imbalance, and hence the chemical potential imbalance, can be set globally. Therefore, one can realize a bulk Fermi gas in the region of the phase diagram occupied by the LO phase, which will significantly improve the available signal. With a homogeneous Fermi gas, one can thus study whether or not a soliton can be stabilized by being filled with excess fermions, which is suggested by the LO scenario. This can be realized by creating a soliton train and studing the stability of the system as a function of spin imbalance.

With the study of degenerate Fermi gases continuing for over a decade and a half, we are now beginning to be able to address open questions in strongly interacting fermionic systems and provide insight into new phenomena in many-body physics. Despite the progress made so far, I can safely say that the works presented in this thesis are just a starting point for a bright future of fruitful research, with no lack of intriguing new discoveries to come.

Appendix A

Characterization of the trapping potential used in the solitonic excitations experiments

Because the geometry affects the outcome of the dynamics, if an experiment studying solitonic excitations is to be compared to simulation, it is necessary for the two to be in the similar parameter regime. In particular, simulations have found that the outcome of the dynamics is sensitive to deviation from a cylindrically symmetric harmonic trap. Therefore, it is important to provide a characterization of the trapping potential in our experiment. To characterize our trap, we will make use of the anisotropy factor δ and anharmonicity factor C as defined in [240]. First, we start with a complete model of our trapping potential

$$\begin{aligned} V(x,y,z) &= \frac{1}{2}m\omega_z^2\left[z^2 - \frac{1}{2}(x-x_{\mathrm{mc}})^2 + \frac{1}{2}(y-y_{\mathrm{mc}})^2\right] \\ &\quad + V_0\left[1 - e^{-\left(\frac{x^2+y^2}{W^2}\right)}\right] + mgy\,. \end{aligned} \tag{A.1}$$

The first term is a saddle point potential that comes from the magnetic curvature of the Feshbach field. The second term describes the potential resulting from the optical dipole trap (ODT), with a trap depth V_0 and a gaussian waist W. The ODT

counters the anti-confinement in the radial x and y directions due to the magnetic saddle point. The effective confinement in the x and y directions, in the absence of gravity, can then be modeled with a single parameter ω_x, the radial trapping frequency, which can be experimentally measured. The offset betweeen the center of the two potentials is $(x_{\rm mc}, y_{\rm mc})$. In principle, it is possible to fully compensate the effect of gravity by setting $y_{\rm mc} = 2g/\omega_z^2$ and hence the minimum of the saddle potential plus gravity coincides with the one of the ODT. However, the experimental parameters of the present work are set up such that $x_{\rm mc} = 0$ and $y_{\rm mc}$ has a nonzero value. The atom cloud therefore experiences a potential with a displaced saddle point along the vertical direction, due to an effective vertical gradient. We shall denote the acceleration due to this gradient as a. By releasing the cloud for variable amount of time and measuring its displacement, we have obtained $a = 1.9(3)\, m/s^2$. Then, we can model our potential by neglecting the anti-confining term of the saddle potential, and incorporating ω_x and a:

$$V(x,y,z) = \frac{1}{2}m\omega_z^2 z^2 + V_0\left[1 - e^{-\frac{m\omega_x^2(x^2+y^2)}{2V_0}}\right] + may\,. \tag{A.2}$$

This is the same model potential as in Ref. [240].

To find the location of the potential minimum y_0, we expand the potential for small x and y:

$$\begin{aligned} V(x,y,z) \;&\approx\; \frac{1}{2}m\omega_z^2 z^2 + \frac{1}{2}m\omega_x^2(x^2+y^2) \\ &-\; \frac{m^2\omega_x^4}{8V_0}(x^4+y^4) + may\,. \end{aligned} \tag{A.3}$$

To the leading order, the value of y_0 corresponds to the minimum of the parabola $\frac{1}{2}m\omega_x^2 y^2 + may$. This then gives $y_0 = a/\omega_x^2$. In our experiment, $y_0 = 16\,\mu$m, and is small compared to the other length scales such as the waist W and radial Thomas–Fermi radius $R_\perp = 54(2)\,\mu$m. By making the shift of coordinate $y + y_0 \to y$, we

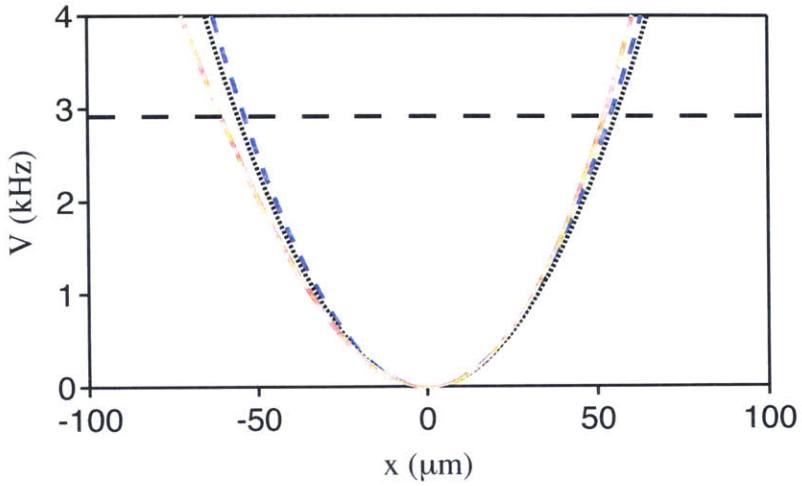

Figure A-1:]
Trapping potential in the x-y plane. The dashed curve is the potential in the x-direction. The thinly dashed curve is the potential in the y-direction, given by Eq. A.5, taking into account only the quadratic correction. The solid curve includes the cubic correction. The horizontal line indicates the chemical potential μ.

obtain

$$\begin{aligned} V(x,y,z) &= \frac{1}{2}m\omega_z^2 z^2 + \frac{1}{2}m\omega_x^2 x^2 + O(x^4) \\ &+ \frac{1}{2}m\omega_x^2 y^2 - \frac{3a^2m^2}{4V_0}y^2 + \frac{am^2}{2V_0}y^3 \\ &+ O(y_0^3) + O(y^4) + \text{const}\,. \end{aligned} \tag{A.4}$$

We note that the $O(y_0^3)$ term is $-\frac{m^2 y_0^3 \omega_x^4}{V_0}y$, which corresponds to less than $1\,\mu$m correction to the potential minimum, confirming that y_0 is primarily set by the quadratic and the gradient term, and that y_0 is a suitable small expansion parameter.

Combining the like terms, we get

$$\begin{aligned} V(x,y,z) &= \frac{1}{2}m\omega_z^2 z^2 + \frac{1}{2}m\omega_x^2 x^2 + \frac{1}{2}m\omega_y^2 y^2 + Cy^3 \\ &+ O(y_0^3) + O(x^4) + O(y^4)\,, \end{aligned} \tag{A.5}$$

where $\omega_y \equiv \omega_x \left(1 - \frac{3}{2}\frac{ma^2}{\omega_x^2}\right)^{1/2}$, and $C \equiv \frac{am^2\omega_x^2}{2V_0}$.

We can rewrite these quantities in terms ω_x, which we can extract from the image

of the atomic cloud directly:

$$\omega_y = \omega_x\sqrt{1-2\delta} \approx \omega_x(1-\delta)\,, \quad \delta \equiv \frac{3ma^2}{4\omega_x^2 V_0}\,, \tag{A.6}$$

and

$$C \approx \frac{2m\omega_x^4}{3a}\delta\,. \tag{A.7}$$

C is to be compared to $C_0 \equiv \frac{m\omega_y^2}{2R_\perp}$ [240]. With our parameter, we have $\delta = 0.03(1)$ and $C/C_0 = 0.16(6)$.

A plot of the potential of Eq. A.5 is in Fig. A-1

Appendix B

Collection of tomographic images

Fig. B-1 contains the representative tomographic images recorded at several instances of the dynamics from $t = 3.5\,\text{ms}$ to $t = 1000\,\text{ms}$, taken for the experimental study of the cascade of solitonic excitations.

Fig. B-2 contains all the tomographic images taken between 50 ms and 100 ms. The images in each row are not sorted in any particular order. At each slice, there is at least one image for each wait time.

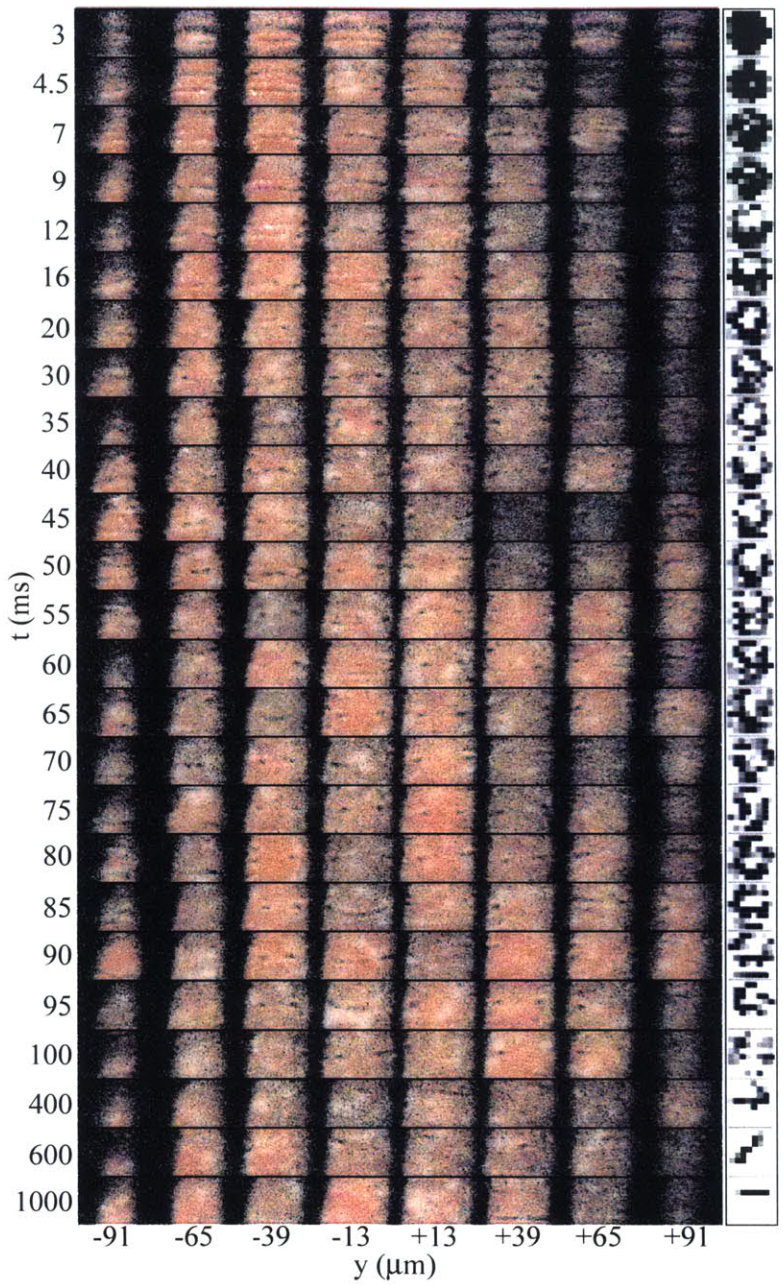

Figure B-1: Tomographic images at various times t after the phase-imprint. The right column shows the structure of the solitary waves as seen along the z-axis, reconstructed with the residuals of the tomographic images.

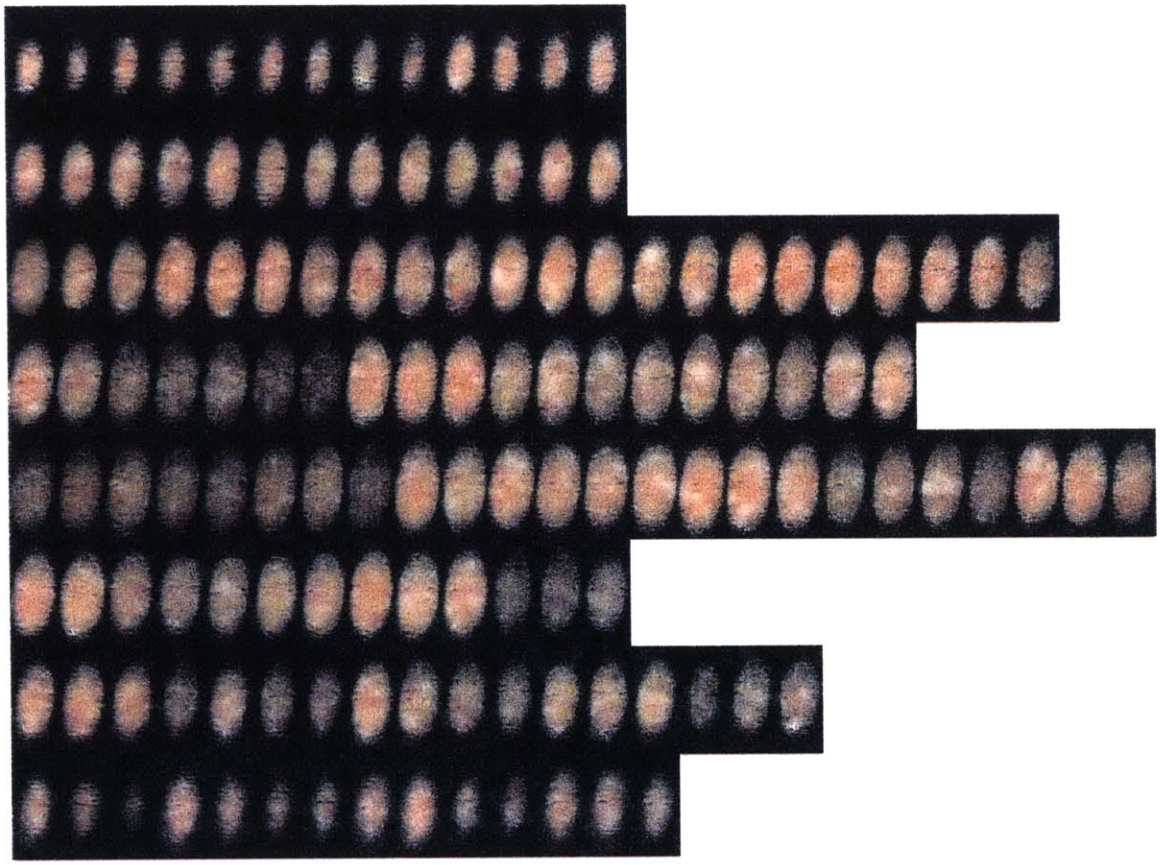

Figure B-2: Full set of tomographic images between 50 ms and 100 ms. The images in each row are not sorted in any particular order. At each slice, there is at least one image for each wait time. The rows from top to bottom correspond y =-91, -65, -39, -13, +13, +39, +65, and +91 μm.

Appendix C

Deterministic generation of a long-lived solitonic vortex

In the experiment reported in Chapter 6 and 7, the phase imprint leads to a long-lived solitonic vortex following a deterministic (instead of erratic) trajectory. However, this needs not to be the case. Experimentally, we have observed a long-lived (lifetime on the order of seconds) vortex only in certain parameter regime. As long as the vortex makes it past 1 s, it will remain persist until it speeds up due spontaneous heating of the cloud and eventually exits the system.

Simulations [237, 197, 240] have shown that in many cases, the evolution of the defect is highly sensitive to the parameters of the system. If an experiment is performed in the neighborhood of such a parameter regime, then even a small deviation of experimental conditions from shot to shot can lead to very different dynamics in each experimental run, and hence the evolution of the defect will appear to be stochastic.

In this section, I describe the measurement we have performed to delineate the factors that contribute to the formation of a long-lived solitonic vortex.

C.1 Out-of-focus phase-imprinting

In addition to the phase difference $\Delta\phi$ applied between the two sides of the superfluid, an important parameter of the phase-imprinting procedure is the sharpness of the

phase-step. In our setup, the length scale over which the phase changes from ϕ_1 on one side of the superfluid to $\phi_2 = \phi_1 + \Delta\phi$ on the other side is tied to the optical resolution with which we produce the image of the mask onto the atomic plane. For an optical wavelength of 532 nm, our optical resolution defined by the Rayleigh criterion is $\delta_o \approx 2.5\,\mu$m, which is much larger than the interparticle spacing $\sim 0.1\mu$m. Therefore, even an imprinted phase difference $\Delta\phi = \pi$, which we can control via the laser intensity and the pulse duration, does not guarantee the creation of a stationary dark soliton, as the phase profile is not "mode-matched" to an ideal $0 - \pi$ phase step. In fact, we have found that for a phase difference ranging from $\Delta\phi \approx \pi$ to $\Delta\phi \approx 2\pi$ we were never able to produce a single stand still dark soliton. Instead, the system healed into deterministic combinations of one (or several) dark soliton(s) accompanied by sound waves.

In order to create the almost stationary solitons presented in this work, we have utilized an artifact of the "out-of-focus" projection of the mask onto the atoms. When the mask is moved away from its focus position, *i.e* the position of the object plane which is the optical conjugate of the atom cloud, the intensity profile of imprinting light projected onto the atoms displays fringes as expected from diffraction. In Fig. C-1, we show a few examples of intensity profiles as a function of the mask position ζ, where $\zeta = 0$ stands for the best focus position. For $\zeta = +1$ mm and $\zeta = -1$ mm, a sharp dark fringe appears as a prominent feature in the out-of-focus images. As a result of diffraction, the intensity variation at the fringe is sharper than the one at the actual edge and allows us to imprint a single slow soliton. Furthermore, we notice that the observed fringe bends with a positive or negative curvature depending on the sign of ζ. We found that this bending shapes the soliton with the same curvature, as we can see from Fig. C-1, and controls its direction of propagation. Therefore, by tuning the focus, we can adjust the velocity and the direction of the soliton, while the focus position $\zeta = 0$ leads to a rather fast soliton propagating towards the $z > 0$ direction.

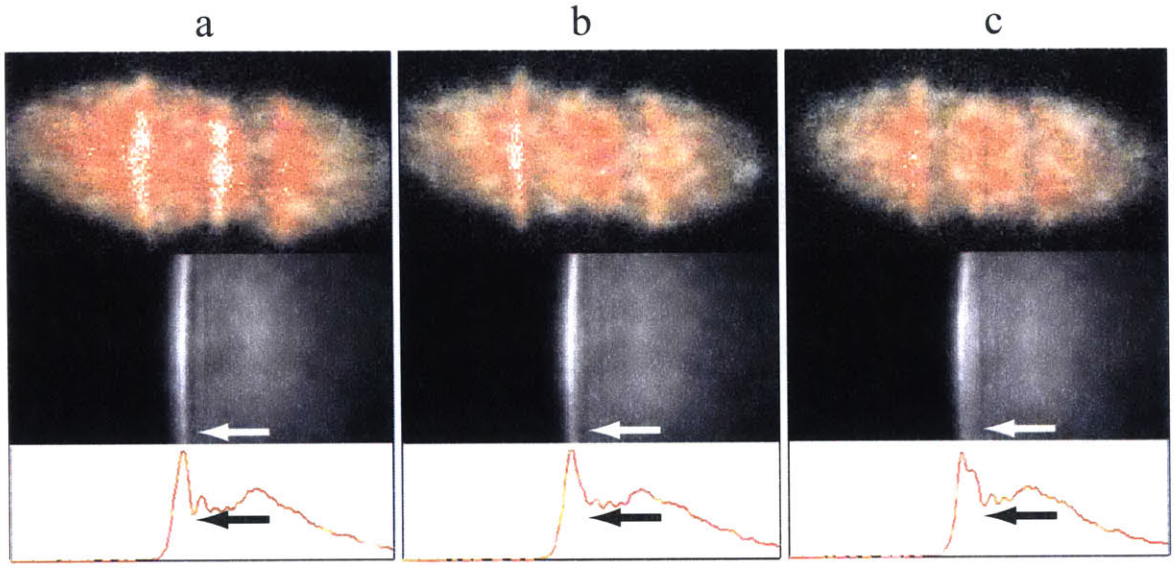

Figure C-1: Controlling the curvature and direction of the soliton. Shown are images with knife position a) $\zeta = +1\,\mathrm{mm}$, b) $\zeta = 0\,\mathrm{mm}$, and $\zeta = -1\,\mathrm{mm}$, respectively. The top row shows the soliton produced at $t = 4\,\mathrm{ms}$. The middle row shows the intensity profile of the imprinting beam on the atom. The bottom row shows a cut of the intensity profile. The edge of the masked is not sharp. Rather, the sharp feature is the first small-wavelength fringe, as indicated by arrows. At $\zeta = +1\,\mathrm{mm}$, the fringe is straight, and the soliton is observed to move to the $-z$-direction, as expected from phase imprinting with the indicated fringe. At $\zeta = 0\,\mathrm{mm}$, the fringe is no longer sharp, and the generated soliton is faint and fast. At $\zeta = -1\,\mathrm{mm}$, the fringe becomes sharp again, even more so compared to $\zeta = +1\,\mathrm{mm}$. This allows for a more deterministic generation of soliton and long-lived vortex (see Fig. C-2). The fringe is curved to the right, and it forces the soliton to moves in the $+z$-direction.

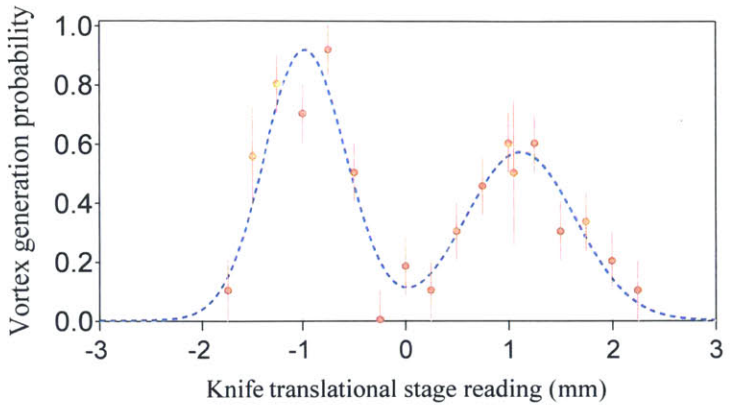

Figure C-2: Generation probability of long-lived vortex at $t = 1\,\mathrm{s}$. The dashed curve is a guide to the eye.

C.2 Slow-soliton decaying into long-lived vortex

From a momentum conservation argument, one would expect that the soliton velocity directly controls the velocity of its decay products. This assumption is however difficult to test as it requires long-lived excitations. In this work, we have seen that the soliton decays before any motion is observed and the only long-lived excitation, from which we can infer a velocity, is the vortex. However, we only observe a long-lived vortex in the specific situation where the initially imprinted planar soliton is slow. For fast solitons, which appear as shallow and strongly bent in the first milliseconds following the imprint, the decay products survive less than 0.5 s on average. In Fig. C-2 we show the survival probability of the vortex as a function of the focus position, which controls the velocity and the direction of the soliton. We notice a bimodal distribution with two peaks at $\zeta = -1\,\mathrm{mm}$ and $\zeta = +1\,\mathrm{mm}$, which correspond to the configurations producing slow dark solitons, propagating towards $z < 0$ and $z > 0$ respectively. This observation is consistent with the fact that the velocity of the vortex increases with the soliton's velocity.

A single long-lived vortex with a well-defined trajectory is produced for the two optimal focus positions $\zeta \simeq \pm 1\,\mathrm{mm}$. In Fig. C-3 (a), we show the trajectory $z(t)$ of the vortex generated at each of the optimal focus positions. The two trajectories $z(t)$ are out of phase by roughly 180°, which is reasonable given that the initial solitons

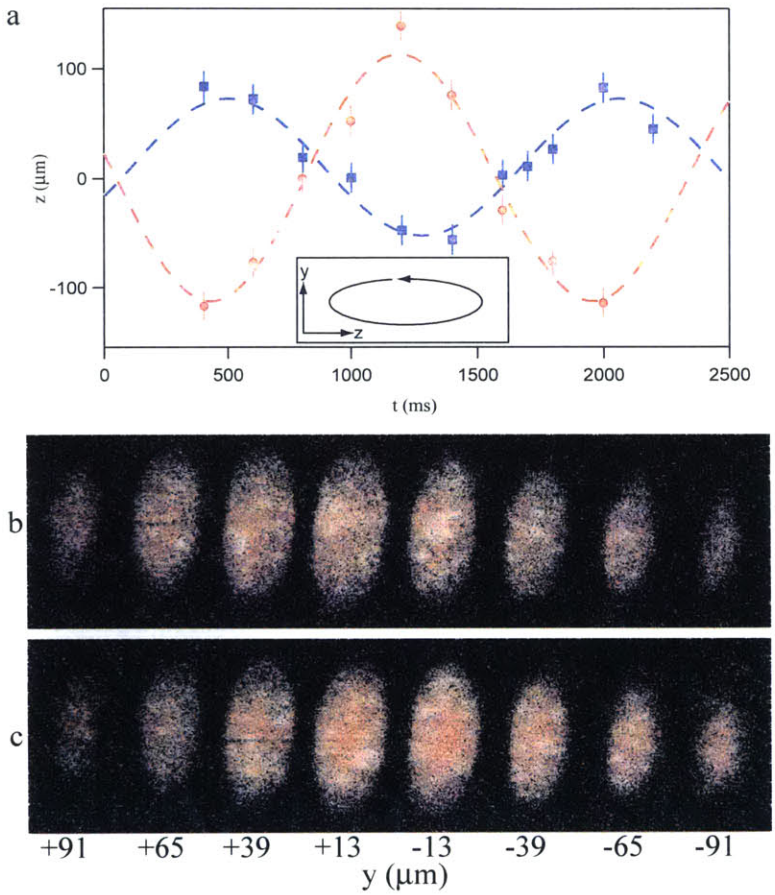

Figure C-3: (a) Trajectory of the vortex generated at the focus position $\zeta = -1\,\mathrm{mm}$ (red circle) and $\zeta = +1\,\mathrm{mm}$ (blue square). (b) Tomographic images taken at $t = 700\,\mathrm{ms}$ for the vortex generated at the knife position $\zeta = +1\,\mathrm{mm}$, showing the vortex at $y > 0$. (c) Tomographic images taken at $t = 1700\,\mathrm{ms}$ for the vortex generated at the knife position $\zeta = -1\,\mathrm{mm}$, showing the vortex at $y > 0$. Inset: the orientation of the vortex precession in both cases.

move in the opposite directions. However, we note that the charge of the vortex - the orientation of the quantized flow around the vortex line - is the same in both cases. The charge of the vortex can be established by observing the orientation of the vortex precession in the superfluid. In Fig. C-3 (b) and (c), we show the tomographic images at the instance when the vortex is crossing $z = 0$ towards the negative z-direction. For the vortex generated at $\zeta = +1\,\mathrm{mm}$ $(-1\,\mathrm{mm})$, this corresponds to $t = 700\,\mathrm{ms}$ $(1700\,\mathrm{ms})$. The fact that the vortex is found at $0 < y$ in both cases demonstrates that the orientation of the vortex precession is the same, and hence the charge of the vortex is the same.

Appendix D

Revealing the Superfluid Lambda Transition in the UniversalThermodynamics of a Unitary Fermi Gas

This appendix contains a reprint of Ref. [129]: Mark J.H. Ku, Ariel T. Sommer, Lawrence W. Cheuk, and Martin W. Zwierlein, *Revealing the superfluid lambda transition in the universal thermodynamics of a unitary Fermi gas*, Science, **335**, 563-567, (2012).

will slow down their spin rates with time after the RLDP. However, they cannot explain the apparent difference in spin distributions between AXMSPs and radio MSPs, because radio MSPs, which have weak surface magnetic field strengths, could not spin down by the required amount even in a Hubble time. The true age of a pulsar (*23*) is given by $t = P/((n-1)\dot{P})[1-(P_0/P)^{n-1}]$. Assuming an evolution with a braking index $n = 3$ and $B = 1.0\times 10^8$ G, the time scale t is larger than 10 Gy, using $P_0 = \langle P\rangle_{AXMSP} = 3.3$ ms and $P(t) = \langle P\rangle_{MSP} = 5.5$ ms. To make things worse, one has to add the main-sequence lifetime of the LMXB donor star, which is typically 3 to 12 Gy, thereby reaching unrealistic large total ages. Although the statistics of AXMSPs still has its basis in small numbers and care must be taken for both detection biases (such as eclipsing effects of radio MSPs) and comparison between various subpopulations (*8*), it is evident from both observations and theoretical work that the RLDP effect presented here plays an important role for the spin distribution of MSPs.

The RLDP effect may also help explain a few other puzzles, for example, why characteristic (or spin-down) ages of radio MSPs often largely exceed cooling age determinations of their white dwarf companions (*24*). It has been suggested that standard cooling models of white dwarfs may not be correct (*25*–*27*), particularly for low-mass helium white dwarfs. These white dwarfs avoid hydrogen shell flashes at early stages and retain thick hydrogen envelopes, at the bottom of which residual hydrogen burning can continue for several billion years after their formation, keeping the white dwarfs relatively hot (~10^4 K) and thereby appearing much younger than they actually are. However, it is well known that the characteristic age is not a trustworthy measure of true age (*28*), and the RLDP effect exacerbates this discrepancy even further. In the model calculation presented in Fig. 1, it was assumed that $B = 1.0\times 10^8$ G and $\varphi = 1.0$. However, P_0 and τ_0 depend strongly on both B and φ. This is shown in Fig. 2, where I have calculated the RLDP effect for different choices of B and φ by using the same stellar donor model [i.e., same $\dot{M}(t)$ profile] as before. The use of other LMXB donor star masses, metallicities, and initial orbital periods would lead to other $\dot{M}(t)$ profiles (*16*, *17*) and hence different evolutionary tracks. The conclusion is that recycled MSPs can basically be born with any characteristic age. Thus, we are left with the cooling age of the white dwarf companion as the sole reliable, although still not accurate, measure as an age indicator.

A final puzzle is why no sub-millisecond pulsars have been found among the 216 radio MSPs detected in total so far. Although modern observational techniques are sensitive enough to pick up sub-millisecond radio pulsations, the fastest spinning known radio MSP, J1748−2446ad (*29*), has a spin frequency of only 716 Hz, corresponding to a spin period of 1.4 ms. This spin rate is far from the expected minimum equilibrium spin period (*8*) and the physical mass shedding limit of about 1500 Hz. It has been suggested that gravitational wave radiation during the accretion phase halts the spin period above a certain level (*30*, *31*). The RLDP effect presented here is a promising candidate for an alternative mechanism, in case a sub-millisecond AXMSP is detected (*8*).

References and Notes

1. M. A. Alpar, A. F. Cheng, M. A. Ruderman, J. Shaham, *Nature* **300**, 728 (1982).
2. D. Bhattacharya, E. P. J. van den Heuvel, *Phys. Rep.* **203**, 1 (1991).
3. L. Bildsten *et al.*, *Astrophys. J. Suppl. Ser.* **113**, 367 (1997).
4. R. Wijnands, M. van der Klis, *Nature* **394**, 344 (1998).
5. J. W. T. Hessels *et al.*, *AIP Conf. Proc.* **1068**, 130 (2008).
6. The Roche lobe of a binary star is the innermost equipotential surface passing through the first Lagrangian point, L1. If a star fills its Roche lobe, the unbalanced pressure at L1 will cause mass transfer to the other star (*2*).
7. A. M. Archibald *et al.*, *Science* **324**, 1411 (2009); 10.1126/science.1172740.
8. Materials and methods are available as supporting material on *Science* Online.
9. F. K. Lamb, C. J. Pethick, D. A. Pines, *Astrophys. J.* **184**, 271 (1973).
10. P. Ghosh, F. K. Lamb, *NATO Sci. Ser.* **377**, 487 (1992).
11. J. Frank, A. King, D. J. Raine, *Accretion Power in Astrophysics* (Cambridge Univ. Press, Cambridge, 2002).
12. A. F. Illarionov, R. A. Sunyaev, *Astron. Astrophys.* **39**, 185 (1975).
13. M. Ruderman, J. Shaham, M. Tavani, *Astrophys. J.* **336**, 507 (1989).
14. R. F. Webbink, S. Rappaport, G. J. Savonije, *Astrophys. J.* **270**, 678 (1983).
15. S. Rappaport, Ph. Podsiadlowski, P. C. Joss, R. Di Stefano, Z. Han, *Mon. Not. R. Astron. Soc.* **273**, 731 (1995).
16. T. M. Tauris, G. J. Savonije, *Astron. Astrophys.* **350**, 928 (1999).
17. Ph. Podsiadlowski, S. Rappaport, E. D. Pfahl, *Astrophys. J.* **565**, 1107 (2002).
18. The magnetospheric coupling parameter, $0.5 < \varphi < 1.4$ is a numerical factor of order unity depending on the accretion flow, the disk model, and the magnetic inclination angle of the pulsar (*10*, *11*, *32*–*34*).
19. S. L. Shapiro, S. A. Teukolsky, *Black Holes, White Dwarfs, and Neutron Stars: The Physics of Compact Objects* (Wiley-Interscience, New York, 1983).
20. S. A. Rappaport, J. M. Fregeau, H. C. Spruit, *Astrophys. J.* **606**, 436 (2004).
21. L. Burderi *et al.*, *Astrophys. J.* **560**, L71 (2001).
22. This "turn-off problem" has previously been debated elsewhere (*13*, *33*, *35*).
23. R. N. Manchester, J. H. Taylor, *Pulsars* (Freeman, San Francisco, CA, 1977).
24. D. R. Lorimer, A. G. Lyne, L. Festin, L. Nicastro, *Nature* **376**, 393 (1995).
25. F. Alberts, G. J. Savonije, E. P. J. van den Heuvel, O. R. Pols, *Nature* **380**, 676 (1996).
26. L. A. Nelson, E. Dubeau, K. A. MacCannell, *Astrophys. J.* **616**, 1124 (2004).
27. M. H. van Kerkwijk, C. G. Bassa, B. A. Jacoby, P. G. Jonker, in *Binary Radio Pulsars*, F. A. Rasio, I. H. Stairs, Eds. [Astronomical Society of the Pacific (ASP) Conference Series, San Francisco, CA, 2005], vol. 328, pp. 357–370.
28. This is the case if the pulsar spin period, P, is close to its initial spin period, P_0.
29. J. W. T. Hessels *et al.*, *Science* **311**, 1901 (2006).
30. L. Bildsten, *Astrophys. J.* **501**, L89 (1998).
31. D. Chakrabarty *et al.*, *Nature* **424**, 42 (2003).
32. Y.-M. Wang, *Astrophys. J.* **475**, L135 (1997).
33. F. Lamb, W. Yu, in *Binary Radio Pulsars*, F. A. Rasio, I. H. Stairs, Eds. (ASP Conference Series, San Francisco, CA, 2005), vol. 328, pp. 299–310.
34. C. R. D'Angelo, H. C. Spruit, *Mon. Not. R. Astron. Soc.* **406**, 1208 (2010).
35. M. Ruderman, J. Shaham, M. Tavani, D. Eichler, *Astrophys. J.* **343**, 292 (1989).
36. A. Patruno, *Astrophys. J.* **722**, 909 (2010).
37. I. S. Shklovskii, *Sov. Astron.* **13**, 562 (1970).

Acknowledgments: I gratefully thank N. Langer and M. Kramer for discussions and funding and without whom these results would not be possible and R. Eatough for helpful comments on the SOM. This work was partly supported by the Cluster of Excellence proposal EXC 1076, "The nature of forces and matter," at the University of Bonn. Radio pulsar data has been obtained from the *ATNF Pulsar Catalogue* (www.atnf.csiro.au/research/pulsar/psrcat/).

Supporting Online Material

www.sciencemag.org/cgi/content/full/335/6068/561/DC1
Materials and Methods
SOM Text
Figs. S1 and S2
References (*38*–*54*)

8 November 2011; accepted 6 January 2012
10.1126/science.1216355

Revealing the Superfluid Lambda Transition in the Universal Thermodynamics of a Unitary Fermi Gas

Mark J. H. Ku, Ariel T. Sommer, Lawrence W. Cheuk, Martin W. Zwierlein*

Fermi gases, collections of fermions such as neutrons and electrons, are found throughout nature, from solids to neutron stars. Interacting Fermi gases can form a superfluid or, for charged fermions, a superconductor. We have observed the superfluid phase transition in a strongly interacting Fermi gas by high-precision measurements of the local compressibility, density, and pressure. Our data completely determine the universal thermodynamics of these gases without any fit or external thermometer. The onset of superfluidity is observed in the compressibility, the chemical potential, the entropy, and the heat capacity, which displays a characteristic lambda-like feature at the critical temperature $T_c/T_F = 0.167(13)$. The ground-state energy is $\frac{3}{5}\xi N E_F$ with $\xi = 0.376(4)$. Our measurements provide a benchmark for many-body theories of strongly interacting fermions.

Phase transitions are ubiquitous in nature: Water freezes into ice, electron spins suddenly align as materials turn into magnets, and metals become superconducting. Near the transitions, many systems exhibit critical behavior, reflected by singularities in thermodynamic quantities: The magnetic susceptibility diverges at a ferromagnetic transition, and the specific heat

shows a jump at superconducting and superfluid transitions (*1*, *2*), resolved as the famous lambda peak in ^{4}He (*3*). A novel form of superfluidity has been realized in trapped, ultracold atomic gases of strongly interacting fermions, particles with half-integer spin (*4*–*7*). Thanks to an exquisite control over relevant system parameters, these gases have recently emerged as a versatile system well suited to solve open problems in many-body physics (*7*).

Initial measurements on the thermodynamics of strongly interacting Fermi gases have focused on trap-averaged quantities (*8*–*10*) in which the superfluid transition is inherently difficult to observe. The emergence of the condensate of fermion pairs in a spin-balanced Fermi gas is accompanied by only minute changes in the gas density (*5*). Quantities that involve integration of the density over the local potential, such as the energy E (*11*) and the pressure P (*12*), are only weakly sensitive to the sudden variations in the thermodynamics of the gas expected near the superfluid phase transition (*13*).

For a neutral gas, thermodynamic quantities involving the second derivative of the pressure P are expected to become singular at the second-order phase transition into the superfluid state. An example is the isothermal compressibility $\kappa = \frac{1}{n}\frac{\partial n}{\partial P}|_T$, the relative change of the gas density n due to a change in the pressure P. Because the change in pressure is related to the change in chemical potential μ of the gas via $dP = n\,d\mu$ at constant temperature, $\kappa = \frac{1}{n^2}\frac{\partial^2 P}{\partial \mu^2}|_T$ is a second derivative of the pressure, and thus should reveal a clear signature of the transition.

The general strategy to determine the thermodynamic properties of a given substance is to measure an equation of state (EoS), such as the pressure $P(\mu,T)$ as a function of the chemical potential μ and the temperature T. Equivalently, replacing the pressure by the density $n = \frac{\partial P}{\partial \mu}|_T$, one can determine the density EoS $n(\mu,T)$. We directly measure the local gas density $n(V)$ as a function of the local potential V from in situ absorption images of a trapped, strongly interacting Fermi gas of ^{6}Li atoms at a Feshbach resonance (*5*). The trapping potential is cylindrically symmetric, with harmonic confinement along the axial direction; this symmetry allows us to find the three-dimensional (3D) density through the inverse Abel transform of the measured column density (*14*, *15*). The local potential is directly determined from the atomic density distribution and the accurately known harmonic potential along the axial direction.

The compressibility κ follows as the change of the density n with respect to the local potential V experienced by the trapped gas. The change in the local chemical potential is given by the negative change in the local potential, $d\mu = -dV$, and hence the local compressibility is $\kappa = -\frac{1}{n^2}\frac{dn}{dV}|_T$. We can then replace the unknown chemical potential μ in the density EoS $n(\mu,T)$ by the known variation of n with μ in the atom trap, given by κ. Instead of the a priori unknown temperature T, we determine the pressure $P(V) = \int_{-\infty}^{\mu} d\mu' n(\mu') = \int_{V}^{\infty} dV' n(V')$ given by the integral of the density over the potential (*16*). The resulting equation of state $n(\kappa,P)$ contains only quantities that can be directly obtained from the density distribution. This represents a crucial advance over previous methods that require the input of additional thermodynamic quantities, such as the temperature T and the chemical potential μ, whose determination requires the use of a fitting procedure or an external thermometer, as in (*11*, *12*).

We normalize the compressibility and the pressure by the respective quantities at the same local density for a noninteracting Fermi gas at $T = 0$, $\kappa_0 = \frac{3}{2}\frac{1}{nE_F}$, and $P_0 = \frac{2}{5}nE_F$, where $E_F = \frac{\hbar^2(3\pi^2 n)^{2/3}}{2m}$ is the local Fermi energy and m is the particle mass, yielding $\tilde{\kappa} \equiv \kappa/\kappa_0$ and $\tilde{p} \equiv P/P_0$. For dilute gases at the Feshbach resonance, the scattering length diverges and is no longer a relevant length scale. In the absence of an interaction-dependent length scale, the thermodynamics of such resonant gases are universal (*17*), and $\tilde{\kappa}$ is a universal function of $\tilde{p}$ only. Every experimental profile $n(V)$, irrespective of the trapping potential, the total number of atoms, or the temperature, must produce the same universal curve $\tilde{\kappa}$ versus $\tilde{p}$. By averaging many profiles, one obtains a low-noise determination of $\tilde{\kappa}(\tilde{p})$.

Our method has been tested on the noninteracting Fermi gas that can be studied in two independent ways: in spin-balanced gases near the zero-crossing of the scattering length and in the wings of highly imbalanced clouds at unitarity, where only one spin state is present locally. Both determinations yield the same noninteracting compressibility EoS (Fig. 1).

Figure 1 also shows the compressibility equation of state $\tilde{\kappa}(\tilde{p})$ for the unitary Fermi gas. In the high-temperature ($\tilde{p} >> 1$) regime, the pressure, and hence all other thermodynamic quantities, allow for a Virial expansion in terms of the fugacity $e^{\beta\mu}$ (*18*): $P\,\beta\lambda^3 = 2\sum_j b_j e^{j\beta\mu}$, with the nth-order Virial coefficients b_n. It is known that $b_1 = 1$, $b_2 = 3\sqrt{2}/8$, and $b_3 = -0.29095295$ (*18*); our data show good agreement with the third-order Virial expansion. Fixing b_2 and b_3, our measurement yields a prediction for $b_4 = +0.065(10)$, in agreement with (*12*), but contradicting a recent four-body calculation that gives a negative sign (*19*).

At degenerate temperatures ($\tilde{p} \lesssim 1$), the normalized compressibility rises beyond that of a noninteracting Fermi gas, as expected for an attractively interacting gas. A sudden rise of the compressibility at around $\tilde{p} = 0.55$, followed by a decrease at lower temperatures marks the superfluid transition. The expected singularity of the compressibility at the transition is rounded off by the finite resolution of our imaging system. Below the transition point, the decrease of the compressibility is consistent with the expectation from Bardeen-Cooper-Schrieffer (BCS) theory, in which

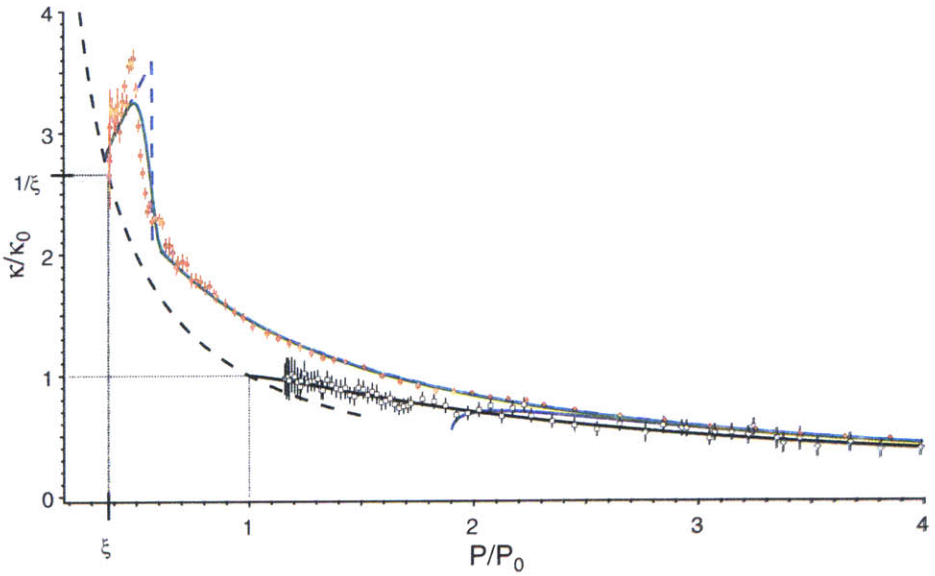

Fig. 1. Normalized compressibility κ/κ_0 versus normalized pressure P/P_0 of the unitary Fermi gas (red solid circles). Each data point is the average of between 30 and 150 profiles. The error bars show mean ± SD, including systematic errors from image calibration (*13*). Blue solid line: third-order Virial expansion. Black open squares (black open diamonds): data for a noninteracting Fermi gas obtained with a highly spin-imbalanced mixture at the Feshbach resonance (spin-balanced gas near zero-crossing of the scattering length). Black solid curve: theory for a noninteracting Fermi gas. Black dashed curve: the relation $\tilde{\kappa} = 1/\tilde{p}$ that must be obeyed at zero temperature both for the noninteracting gas ($\tilde{\kappa} = 1/\tilde{p} = 1$) and the unitary gas ($\tilde{\kappa} = 1/\tilde{p} = 1/\xi$) (dotted lines). Gray band: the uncertainty region for the $T = 0$ value of $\tilde{\kappa} = 1/\xi$ and $\tilde{p} = \xi$. Blue dashed curve: model for the EoS of the unitary Fermi gas [above T_c: interpolation from the Monte Carlo calculation (*34*); below T_c: BCS theory, including phonon and pair-breaking excitations]. Green solid curve: effect of 2 μm optical resolution on the model EoS.

Department of Physics, Massachusetts Institute of Technology (MIT), MIT Harvard Center for Ultracold Atoms, and Research Laboratory of Electronics, MIT, Cambridge, MA 02139, USA.

*To whom correspondence should be addressed. E-mail: zwierlein@mit.edu

single-particle excitations freeze out and pairs form (see model in Fig. 1).

As $T \to 0$, the Fermi energy E_F is the only intensive energy scale, so the chemical potential must be related to E_F by a universal number, $\mu = \xi E_F$, where ξ is known as the Bertsch parameter (*6*, *7*). It follows that at $T = 0$, $\tilde{\kappa} = 1/\tilde{p} = 1/\xi$ (*13*). The extrapolation of the low-temperature experimental data for $\tilde{\kappa}(\tilde{p})$ toward the curve $\tilde{\kappa} = 1/\tilde{p}$ gives $\xi = 0.37(1)$, a value that we find consistently for the normalized chemical potential, energy, and free energy at our lowest temperatures.

From the universal function $\tilde{\kappa}(\tilde{p})$, we obtain all other thermodynamic quantities of the unitary gas. First, to find the normalized temperature T/T_F (where $k_B T_F = E_F$), note that the change in pressure with T/T_F at constant temperature is related to the compressibility. One finds $\frac{d\tilde{p}}{d(T/T_F)} = \frac{5}{2}\frac{T_F}{T}\left(\tilde{p} - \frac{1}{\tilde{\kappa}}\right)$, so by integration (*13*)

$$\frac{T}{T_F} = \left(\frac{T}{T_F}\right)_i \exp\left\{\frac{2}{5}\int_{\tilde{p}_i}^{\tilde{p}} d\tilde{p}\,\frac{1}{\tilde{p} - \frac{1}{\tilde{\kappa}}}\right\} \qquad (1)$$

where $(T/T_F)_i$ is the normalized temperature at an initial normalized pressure $\tilde{p}_i$ that can be chosen to lie in the Virial regime validated above.

Thanks to the relation $E = \frac{3}{2}PV$, valid at unitarity (*17*), we can also directly obtain the heat capacity per particle at constant volume V (*13*),

$$\frac{C_V}{k_B N} \equiv \frac{1}{k_B N}\frac{\partial E}{\partial T}\Big|_{N,V} = \frac{3}{5}\frac{d\tilde{p}}{d(T/T_F)} = \frac{3}{2}\frac{T_F}{T}\left(\tilde{p} - \frac{1}{\tilde{\kappa}}\right) \qquad (2)$$

Figure 2 shows the normalized compressibility and the specific heat as a function of T/T_F. At high temperatures, the specific heat approaches that of a noninteracting Fermi gas and eventually $C_V = \frac{3}{2} N k_B$, the value for a Boltzmann gas. A dramatic rise is observed for T/T_F at around 0.16, followed by a steep drop at lower temperatures. Such a λ-shaped feature in the specific heat is characteristic of second-order phase transitions, as in the famous λ transition in ^{4}He (*3*). Jumps in the specific heat are well known from superconductors (*1*) and ^{3}He (*2*). In experiments on atomic gases, such jumps had only been inferred from derivatives to fit functions that implied a jump (*20*, *21*). We do not expect to resolve the critical behavior very close to T_c. Because of the spatially varying chemical potential in our trapped sample, the critical region is confined to a narrow shell.

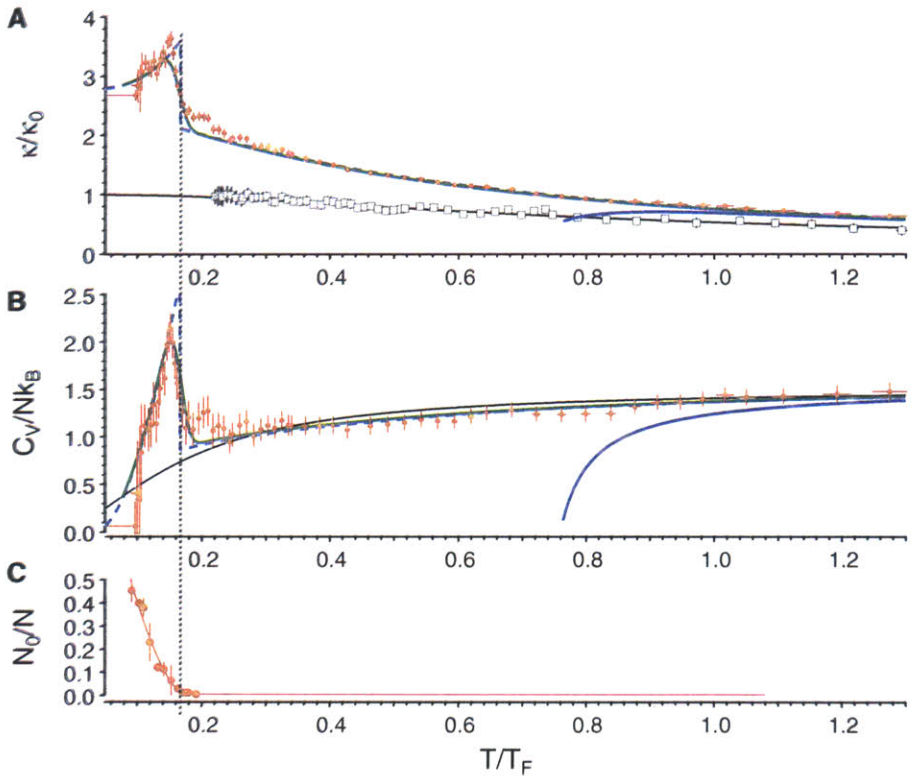

Fig. 2. (A) Normalized compressibility $\tilde{\kappa} = [2/3]\kappa\, n\, E_F$ and **(B)** specific heat per particle C_V/Nk_B of a unitary Fermi gas as a function of reduced temperature T/T_F (solid red circles). Black solid curve: theory for a noninteracting Fermi gas. Blue solid curve: third-order Virial expansion for the unitary gas. Black open squares: data for the normalized compressibility as a function of T/T_F of a noninteracting Fermi gas (combining data from both highly imbalanced gases at unitarity and balanced gases near zero-crossing). Blue dashed (green solid) curve: model from Fig. 1, excluding (including) the effect of finite imaging resolution. **(C)** Global condensate fraction at unitarity as determined from a rapid ramp to the molecular side of the Feshbach resonance, plotted as a function of local T/T_F at the trap center. The onset of condensation coincides with the sudden rise of the specific heat. Error bars, mean ± SD.

Based on the estimate in (*22*), the thickness of the critical shell is 1% of the cloud size. The finite resolution of our imaging system (2 μm or about 5% of the cloud size in the radial direction) suffices to explain the rounding of the singularity expected from criticality. The rounding also reduces the observed jump in the heat capacity at the transition. We obtain a lower bound $\Delta C/C_n \equiv (C_s - C_n)/C_n \geq 1.0^{+4}_{-1}$, where C_s/N (C_n/N) is the specific heat per particle at the peak (the onset of the sudden rise). Considering the strong interactions, this is surprisingly close to the BCS value of 1.43 (*1*). Below T_c, the specific heat is expected to decrease as $\sim \exp(-\Delta_0/k_B T)$ due to the pairing gap Δ_0. At low temperatures, $T \ll T_c$, the phonon contribution $\propto T^3$ dominates (*23*). This behavior is consistent with our data, but the phonon regime is not resolved.

To validate our in situ measurements of the superfluid phase transition, we have employed the rapid ramp method to detect fermion pair condensation (*24*, *25*). The results (Fig. 2C) show that the onset of condensation and the sudden rise in specific heat and compressibility all occur at the same critical temperature, within the error bars. Unlike previous experimental determinations of T_c/T_F for the homogeneous unitary Fermi gas (*11*, *12*), we determine T_c/T_F directly from the density profiles, finding a sudden rise in the specific heat and the onset of condensation at $T_c/T_F = 0.167(13)$. This value is determined as the midpoint of the sudden rise, and the error is assessed as the shift due to the uncertainty of the Feshbach resonance (*13*). This is in very good agreement with theoretical determinations, such as the self-consistent T-matrix approach that gives $T_c/T_F \approx 0.16$ (*23*), and Monte Carlo calculations that give $T_c/T_F = 0.171(5)$ (*26*) and $0.152(7)$ (*27*). There is a current debate on the possibility of a pseudogap phase of preformed pairs above T_c (*12*, *28*). A pairing gap for single-particle excitations above the transition should be signaled by a downturn of the specific heat above T_c, which is not observed in our measurements.

From the definition of the compressibility $\kappa = \frac{1}{n^2}\frac{\partial n}{\partial \mu}\big|_T$, we can obtain the reduced chemical potential μ/E_F as a function of the T/T_F (Fig. 3A) (*13*). This function is here obtained from measured quantities, rather than from numerical derivatives of data that involved uncontrolled thermometry (*11*). In the interval of T/T_F from around 0.25 to 1, the chemical potential is close to that of a noninteracting Fermi gas, shifted by $(\xi_n - 1)E_F$ because of interactions present in the normal state, with $\xi_n \approx 0.45$. Unlike a normal Fermi gas, the chemical potential attains a maximum of $\mu/E_F = 0.42(1)$ at $T/T_F = 0.171(10)$, and then decreases at lower temperatures, as expected for a superfluid of paired fermions (*23*). As the temperature is increased from zero in a superfluid, first the emergence of phonons (sound excitations) and then the breaking of fermion pairs contribute to increasing the chemical potential. At T_c, the singular compressibility implies a sharp change in slope for μ/E_F, in agreement with our observa-

tion and theory (*23*). At low temperatures, the reduced chemical potential μ/E_F saturates to the universal value ξ. As the internal energy E and the free energy F satisfy $E(T) > E(0) = \frac{3}{5}N\xi E_F = F(0) > F(T)$ for all T, the reduced quantities $f_E \equiv \frac{5}{3}\frac{E}{NE_F} = \tilde{p}$ and $f_F \equiv \frac{5}{3}\frac{F}{NE_F} = \frac{5}{3}\frac{\mu}{E_F} - \frac{2}{3}\tilde{p}$ (Fig. 3A) provide upper and lower bounds for ξ (*29*). Taking the coldest points of these three curves and including the systematic error due to the effective interaction range, we find $\xi = 0.376(4)$. The uncertainty in the Feshbach resonance is expected to shift ξ by at most 2% (*13*). This value is consistent with a recent upper bound $\xi < 0.383(1)$ from (*30*), is close to $\xi = 0.36(1)$ from a self-consistent T-matrix calculation (*23*), and agrees with $\xi = 0.367(9)$ from an epsilon expansion (*31*). It lies below earlier estimates $\xi = 0.44(2)$ (*32*) and $\xi = 0.42(1)$ (*33*) from fixed-node quantum Monte Carlo calculation that provides upper bounds on ξ. Our measurement agrees with several less accurate experimental determinations (*6*) but disagrees with the most recent experimental value 0.415(10) that was used to calibrate the pressure in (*12*).

From the energy, pressure, and chemical potential, we can obtain the entropy $S = \frac{1}{T}(E + PV - \mu N)$, and hence the entropy per particle $S/Nk_B = \frac{T_F}{T}\left(\tilde{p} - \frac{\mu}{E_F}\right)$ as a function of T/T_F (Fig. 3B). At high temperatures, S is close to the entropy of an ideal Fermi gas at the same T/T_F. Above T_c, the entropy per particle is nowhere small compared with k_B. Also, the specific heat C_V is not linear in T in the normal phase. This shows that the normal regime above T_c cannot be described in terms of a Landau Fermi Liquid picture, although some thermodynamic quantities agree surprisingly well with the expectation for a Fermi liquid [see (*12*) and (*13*)]. Below about $T/T_F = 0.17$, the entropy starts to strongly fall off compared with that of a noninteracting Fermi gas, which we again interpret as the freezing out of single-particle excitations as a result of the formation of fermion pairs. Far below T_c, phonons dominate. They only have a minute contribution to the entropy (*23*), less than 0.02 k_B at $T/T_F = 0.1$, consistent with our measurements. At the critical point, we obtain $S_c = 0.73(13)$ Nk_B, in agreement with theory (*23*). It is encouraging for future experiments with fermions in optical lattices that we obtain entropies less than 0.04 N k_B, far below critical entropies required to reach magnetically ordered phases.

From the chemical potential μ/E_F and $T/T_F = \frac{4\pi}{(3\pi^2)^{2/3}}\frac{1}{(mk_BT/\hbar^2)^{3/2}}$, we finally obtain the density EoS $n(\mu,T) = \frac{1}{\lambda^3}f_n(\beta\mu)$, with the de Broglie wavelength $\lambda = \sqrt{\frac{2\pi\hbar^2}{mk_BT}}$. The pressure EoS follows as $P(\mu,T) \equiv \frac{k_BT}{\lambda^3}f_P(\beta\mu)$, with $f_P = \frac{2}{5}\frac{T_F}{T}\tilde{p}f_n(\beta\mu)$. Figure 4 shows the density and pressure normalized by their noninteracting counterparts at the same chemical potential and temperature. For the normal state, a concurrent theoretical calculation employing a new Monte Carlo method agrees excellently with our data (*34*). Our data deviate from a previous experimental determination of the pressure EoS (*12*) that was calibrated with an independently measured value of $\xi = 0.415(10)$ (*35*) and disagree with the energy measurement in (*11*) that used a thermometry inconsistent with the Virial expansion (*10*). Around

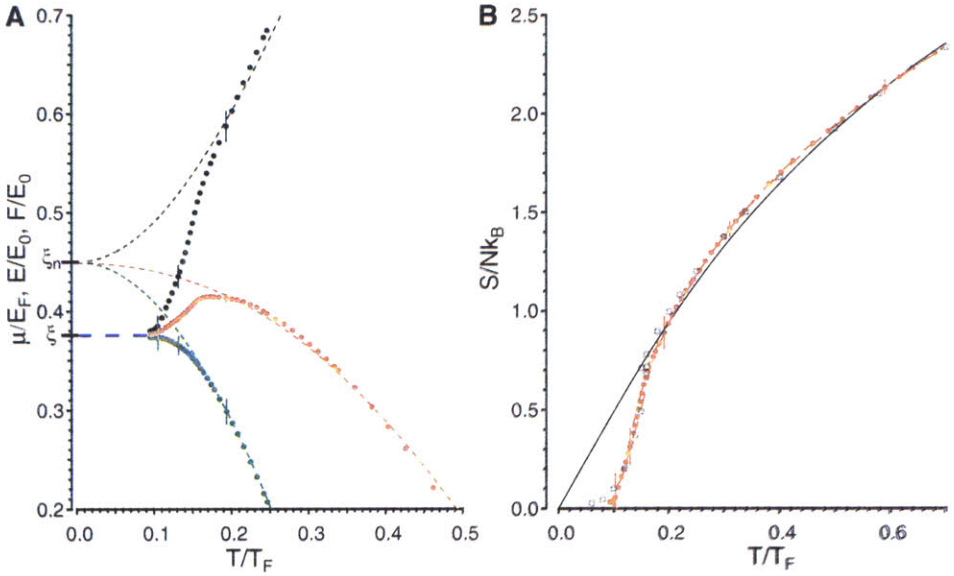

Fig. 3. (**A**) Chemical potential μ, energy E, and free energy F of the unitary Fermi gas versus T/T_F. μ (red solid circles) is normalized by the Fermi energy E_F, and E (black solid circle) and F (green solid circle) are normalized by $E_0 = \frac{3}{5}N\,E_F$. At high temperatures, all quantities approximately track those for a noninteracting Fermi gas, shifted by $\xi_n - 1$ (dashed curves). The peak in the chemical potential signals the onset of superfluidity. In the deeply superfluid regime at low temperatures, μ/E_F, E/E_0, and F/F_0 all approach ξ (blue dashed line). (**B**) Entropy per particle. At high temperatures, the entropy closely tracks that of a noninteracting Fermi gas (black solid curve). The open squares are from the self-consistent T-matrix calculation (*23*). A few representative error bars are shown, representing mean ± SD.

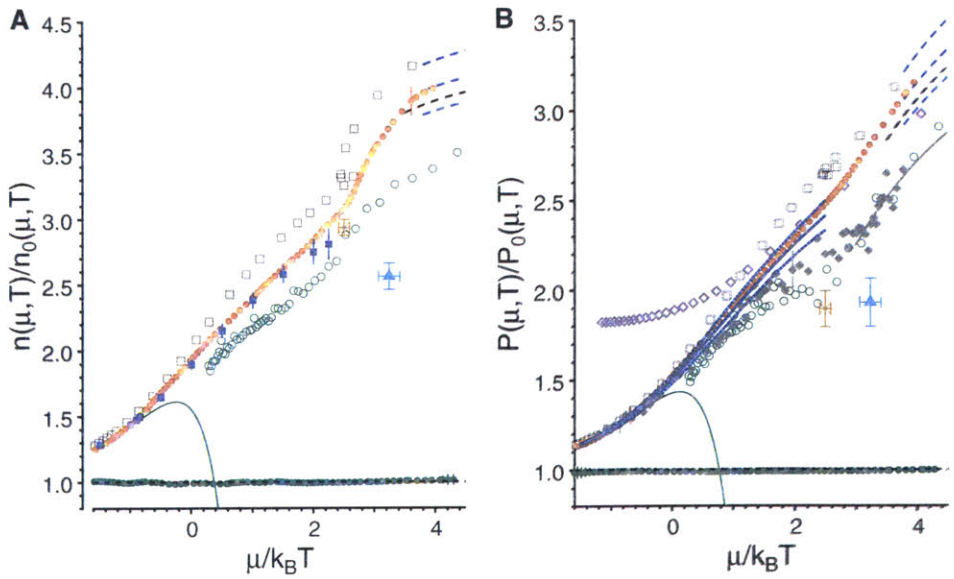

Fig. 4. (**A**) Density and (**B**) pressure of a unitary Fermi gas versus μ/k_BT, normalized by the density and pressure of a noninteracting Fermi gas at the same chemical potential μ and temperature T. Red solid circles: experimental EoS. Blue dashed curves: low-temperature behavior with $\xi = 0.364$ (upper), 0.376 (middle), and 0.388 (lower). Black dashed curve: low-temperature behavior with ξ at upper bound of 0.383 from (*30*). Green solid circles (black fine dashed line): MIT experimental data (theory) for the ideal Fermi gas. Blue solid squares (blue curve): diagrammatic Monte Carlo calculation (*34*) for density (pressure, with blue dashed curves denoting the uncertainty bands). Solid green line: third-order Virial expansion. Open black squares: self-consistent T-matrix calculation (*23*). Open green circles: lattice calculation (*36*). Orange star and blue triangle: critical point from the Monte Carlo calculations (*26*) and (*27*), respectively. Solid diamonds: Ecole Normale Supérieure experiment (*12*). Purple open diamonds: Tokyo experiment (*11*).

the critical point, the density shows a strong variation, whereas the pressure, the integral of the density over μ at constant T, is naturally less sensitive to the superfluid transition.

In conclusion, we have performed thermodynamic measurements of the unitary Fermi gas across the superfluid phase transition at the level of uncertainty of a few percent, without any fits or input from theory, enabling validation of theories for strongly interacting matter. Similar unbiased methods can be applied to other systems, for example, two-dimensional Bose and Fermi gases or fermions in optical lattices.

References and Notes

1. M. Tinkham, *Introduction to Superconductivity* (Dover, Mineola, New York, ed. 2, 2004).
2. D. Vollhardt, P. Wölfle, *The Superfluid Phases of Helium 3* (Taylor & Francis, London, 1990).
3. J. A. Lipa, J. A. Nissen, D. A. Stricker, D. R. Swanson, T. C. P. Chui, *Phys. Rev. B* **68**, 174518 (2003).
4. M. W. Zwierlein, J. R. Abo-Shaeer, A. Schirotzek, C. H. Schunck, W. Ketterle, *Nature* **435**, 1047 (2005).
5. W. Ketterle, M. Zwierlein, *Riv. Nuovo Cim.* **31**, 247 (2008).
6. S. Giorgini, L. P. Pitaevskii, S. Stringari, *Rev. Mod. Phys.* **80**, 1215 (2008).
7. I. Bloch, J. Dalibard, W. Zwerger, *Rev. Mod. Phys.* **80**, 885 (2008).
8. J. Kinast *et al.*, *Science* **307**, 1296 (2005).
9. J. T. Stewart, J. P. Gaebler, C. A. Regal, D. S. Jin, *Phys. Rev. Lett.* **97**, 220406 (2006).
10. L. Luo, B. Clancy, J. Joseph, J. Kinast, J. E. Thomas, *Phys. Rev. Lett.* **98**, 080402 (2007).
11. M. Horikoshi, S. Nakajima, M. Ueda, T. Mukaiyama, *Science* **327**, 442 (2010).
12. S. Nascimbène, N. Navon, K. J. Jiang, F. Chevy, C. Salomon, *Nature* **463**, 1057 (2010).
13. Materials and methods are available as supporting material on *Science* Online.
14. Y. Shin, M. W. Zwierlein, C. H. Schunck, A. Schirotzek, W. Ketterle, *Phys. Rev. Lett.* **97**, 030401 (2006).
15. G. B. Partridge *et al.*, *Phys. Rev. Lett.* **97**, 190407 (2006).
16. C.-H. Cheng, S.-K. Yip, *Phys. Rev. B* **75**, 014526 (2007).
17. T.-L. Ho, *Phys. Rev. Lett.* **92**, 090402 (2004).
18. X.-J. Liu, H. Hu, P. D. Drummond, *Phys. Rev. Lett.* **102**, 160401 (2009).
19. D. Rakshit, K. M. Daily, D. Blume, Thermodynamics of two-component Fermi gas with large scattering length: Fourth- and higher-order virial coefficients, preprint arXiv:1106.5958; available at http://arxiv.org/abs/1106.5958.
20. J. R. Ensher, D. S. Jin, M. R. Matthews, C. E. Wieman, E. A. Cornell, *Phys. Rev. Lett.* **77**, 4984 (1996).
21. L. Luo, J. Thomas, *J. Low Temp. Phys.* **154**, 1 (2009).
22. L. Pollet, N. V. Prokof'ev, B. V. Svistunov, *Phys. Rev. Lett.* **104**, 245705 (2010).
23. R. Haussmann, W. Rantner, S. Cerrito, W. Zwerger, *Phys. Rev. A* **75**, 023610 (2007).
24. C. A. Regal, M. Greiner, D. S. Jin, *Phys. Rev. Lett.* **92**, 040403 (2004).
25. M. W. Zwierlein *et al.*, *Phys. Rev. Lett.* **92**, 120403 (2004).
26. O. Goulko, M. Wingate, *Phys. Rev. A* **82**, 053621 (2010).
27. E. Burovski, N. Prokof'ev, B. Svistunov, M. Troyer, *Phys. Rev. Lett.* **96**, 160402 (2006).
28. J. P. Gaebler *et al.*, *Nat. Phys.* **6**, 569 (2010).
29. Y. Castin, F. Werner, *The BCS-BEC Crossover and the Unitary Fermi Gas*, W. Zwerger, ed. (Springer-Verlag, Berlin, 2012), chap. 5.
30. M. M. Forbes, S. Gandolfi, A. Gezerlis, *Phys. Rev. Lett.* **106**, 235303 (2011).
31. P. Arnold, J. E. Drut, D. T. Son, *Phys. Rev. A* **75**, 043605 (2007).
32. J. Carlson, S.-Y. Chang, V. R. Pandharipande, K. E. Schmidt, *Phys. Rev. Lett.* **91**, 050401 (2003).
33. G. E. Astrakharchik, J. Boronat, J. Casulleras, A. S. Giorgini, *Phys. Rev. Lett.* **93**, 200404 (2004).
34. K. Van Houcke *et al.*, Feynman diagrams versus Fermi-gas Feynman quantum emulator, preprint arXiv:1110.3747 (2011); available at http://arxiv.org/abs/1110.3747.
35. S. Nascimbène, Thermodynamics of ultracold Fermi gases, thesis, Ecole Normale Supérieure, Paris (2010).
36. A. Bulgac, J. E. Drut, P. Magierski, *Phys. Rev. Lett.* **96**, 090404 (2006).

Acknowledgments: We thank B. Svistunov, N. Prokof'ev, and F. Werner for fruitful discussions; Z. Hadzibabic for a critical reading of the manuscript; the authors of (*11*, *12*, *23*, *26*, *27*, *36*) for kindly providing us with their data; and André Schirotzek for help during the early stages of the experiment. M.J.H.K. acknowledges financial support from NSERC. This work was supported by the NSF, Air Force Office of Scientific Research (AFOSR) - Multidisciplinary Research Program of the University Research Initiative (MURI), Army Research Office (ARO) - MURI, Office of Naval Research, Defense Advanced Research Projects Agency (DARPA) Young Faculty Award, a grant from the ARO with funding from the DARPA Optical Lattice Emulator program, an AFOSR Presidential Early Career Award in Science and Engineering, the David and Lucile Packard Foundation, and the Alfred P. Sloan Foundation.

Supporting Online Material

www.sciencemag.org/cgi/content/full/science.1214987/DC1
Materials and Methods
Figs. S1 to S4
References (*37*–*45*)

7 October 2011; accepted 3 January 2012
Published online 12 January 2012;
10.1126/science.1214987

Iron Catalysts for Selective Anti-Markovnikov Alkene Hydrosilylation Using Tertiary Silanes

Aaron M. Tondreau,[1] Crisita Carmen Hojilla Atienza,[1] Keith J. Weller,[2] Susan A. Nye,[2] Kenrick M. Lewis,[3] Johannes G. P. Delis,[4] Paul J. Chirik[1]*

Alkene hydrosilylation, the addition of a silicon hydride (Si-H) across a carbon-carbon double bond, is one of the largest-scale industrial applications of homogeneous catalysis and is used in the commercial production of numerous consumer goods. For decades, precious metals, principally compounds of platinum and rhodium, have been used as catalysts for this reaction class. Despite their widespread application, limitations such as high and volatile catalyst costs and competing side reactions have persisted. Here, we report that well-characterized molecular iron coordination compounds promote the selective anti-Markovnikov addition of sterically hindered, tertiary silanes to alkenes under mild conditions. These Earth-abundant base-metal catalysts, coordinated by optimized bis(imino)pyridine ligands, show promise for industrial application.

Metal-catalyzed olefin hydrosilylation, which forms alkylsilanes by cleaving a silicon-hydrogen bond and adding the fragments across a carbon-carbon double bond (*1*, *2*), finds widespread application in the commercial manufacture of silicone-based surfactants, fluids, molding products, release coatings, and pressure-sensitive adhesives (*3*, *4*). Consequently, hydrosilylation has emerged as one of the largest-scale applications of homogeneous catalysis (*5*–*9*). For more than three decades, precious metal compounds with Pt, Pd, Ru, and Rh have been used almost exclusively as catalysts. Platinum compounds such as Karstedt's and Speier's catalysts, $Pt_2\{[(CH_2{=}CH)SiMe_2]_2O\}_3$ (Me, methyl) and $H_2PtCl_6{\cdot}6H_2O/^iPrOH$(^{i}Pr, isopropyl), respectively, are the most widely used industrial catalysts (*1*, *10*–*12*), though they suffer from chemical limitations such as intolerance to amino-substituted olefins and a tendency to catalyze competing isomerization of the terminal alkenes to internal isomers. Undesired isomerization often necessitates subsequent purification steps that are both energy and cost intensive. Furthermore, decomposition of the catalyst to colloidal platinum contributes to unwanted side reactions and also causes discoloration of the final products.

It has been estimated that the worldwide silicone industry consumed ~180,000 troy ounces (5.6 metric tons) of platinum in 2007 and most is not recovered (*13*). The high cost, coupled with the increasing demands on precious metals due to fuel-cell and other emerging technologies, has increased the volatility of the platinum market (*14*). The combination of chemical, economic, and political challenges inspires the exploration of inexpensive and Earth-abundant catalysts using iron, manganese, and cobalt (*15*). At the core of this challenge is suppressing tendencies of first-row transition metals toward one-electron redox processes in favor of the two-electron chemistry associated with the heavier metals that probably make up the fundamental steps in a catalytic cycle for alkene hydrosilylation.

[1]Department of Chemistry, Princeton University, Princeton, NJ 08544, USA. [2]Momentive Performance Materials, 260 Hudson River Road, Waterford, NY 12188, USA. [3]Momentive Performance Materials, 769 Old Saw Mill River Road, Tarrytown, NY 10591, USA. [4]Momentive Performance Materials bv, Plasticslaan 1, 4612PX Bergen op Zoom, Netherlands.

*To whom correspondence should be addressed. E-mail: pchirik@princeton.edu

Appendix E

Feynman diagrams versus Fermi-gas Feynman emulator

This appendix contains a reprint of Ref. [226]: K. Van Houcke, F. Werner, E. Kozik, N. Prokof'ev, B. Svistunov, M.J.H. Ku, A.T. Sommer, L.W. Cheuk, A. Schirotzek, and M.W. Zwierlein, *Feynman Diagrams versus Fermi-gas Feynman Emulator*, Nat. Phys., **8**, 366-370, (2012).

LETTERS
PUBLISHED ONLINE: 18 MARCH 2012 | DOI: 10.1038/NPHYS2273
nature physics

Feynman diagrams versus Fermi-gas Feynman emulator

K. Van Houcke[1,2*], F. Werner[1,3], E. Kozik[4,5], N. Prokof'ev[1,6], B. Svistunov[1,6], M. J. H. Ku[7], A. T. Sommer[7], L. W. Cheuk[7], A. Schirotzek[8] and M. W. Zwierlein[7]

Precise understanding of strongly interacting fermions, from electrons in modern materials to nuclear matter, presents a major goal in modern physics. However, the theoretical description of interacting Fermi systems is usually plagued by the intricate quantum statistics at play. Here we present a cross-validation between a new theoretical approach, bold diagrammatic Monte Carlo[1-3], and precision experiments on ultracold atoms. Specifically, we compute and measure, with unprecedented precision, the normal-state equation of state of the unitary gas, a prototypical example of a strongly correlated fermionic system[4-6]. Excellent agreement demonstrates that a series of Feynman diagrams can be controllably resummed in a non-perturbative regime using bold diagrammatic Monte Carlo.

In his seminal 1981 lecture[7], Richard Feynman argued that an arbitrary quantum system cannot be efficiently simulated with a classical universal computer, because generally, quantum statistics can only be imitated with a classical theory if probabilities are replaced with negative (or complex) weighting factors. For the majority of many-particle models this indeed leads to the so-called sign problem, which has remained an insurmountable obstacle. According to Feynman, the only way out is to employ computers made out of quantum-mechanical elements[7]. The recent experimental breakthroughs in cooling, probing and controlling strongly interacting quantum gases prompted a challenging effort to use this new form of quantum matter to realize Feynman's emulators of fundamental microscopic models[7,8]. Somewhat ironically, Feynman's arguments, which led him to the idea of emulators, may be defied by a theoretical method that he himself devised, namely Feynman diagrams. This technique organizes the calculation of a given physical quantity as a series of diagrams representing all the possible ways particles can propagate and interact (for example, ref. 9). For the many-body problem, this diagrammatic expansion is commonly used either in perturbative regimes or within uncontrolled approximations. However, the introduction of diagrammatic Monte Carlo recently allowed one to go well beyond the first few diagrams, and even reach convergence of the series in a moderately correlated regime[1,10].

In this Letter we show that for a strongly correlated system and down to a phase transition, the diagrammatic series can still be given a mathematical meaning and leads to controllable results within bold diagrammatic Monte Carlo (BDMC). This approach, proposed in refs 1–3, is first implemented here for the many-body problem. We focus on the unitary gas, that is, spin-1/2 fermions with zero-range interactions at infinite scattering length[4–6]. This system offers the unique possibility to stringently test our theory against a quantum emulator realized here with trapped ultracold ^{6}Li atoms at a broad Feshbach resonance[4–6]. This experimental validation is indispensable for our theory, based on resummation of a possibly divergent series: although the physical answer is shown to be independent of the applied resummation technique—suggesting that the procedure is adequate—its mathematical validity remains to be proven. In essence, nature provides the 'proof'. This presents the first—although long-anticipated—compelling example of how ultracold atoms can guide new microscopic theories for strongly interacting quantum matter.

At unitarity, the disappearance of an interaction-imposed length scale leads to scale invariance. This property renders the model relevant for other physical systems such as neutron matter. It also makes the balanced (that is, spin-unpolarized) unitary gas ideally suited for the experimental high-precision determination of the equation of state (EOS) described below. Finally, it implies the absence of a small parameter, making the problem notoriously difficult to solve.

In traditional Monte Carlo approaches, which simulate a finite piece of matter, the sign problem causes an exponential increase of the computing time with system size and inverse temperature. In contrast, BDMC simulates a mathematical answer in the thermodynamic limit. This radically changes the role of the fermionic sign. Diagrammatic contributions are sign-alternating with order, topology and values of internal variables. Because the number of graphs grows factorially with diagram order, a near-cancellation between these contributions is actually necessary for the series to be resummable by techniques requiring a finite radius of convergence. We find that this 'sign blessing' indeed takes place.

In essence, BDMC solves the full quantum many-body problem by stochastically summing all the skeleton diagrams for irreducible single-particle self-energy Σ and pair self-energy Π, expressed in terms of bold (that is, fully dressed) single-particle and pair propagators G and Γ which are determined self-consistently (Fig. 1). The density EOS (that is, the relation between total density n, chemical potential μ and temperature T) is given by G at zero distance and imaginary time, $n(\mu, T) = 2\,G(r = 0, \tau = 0^-)$. The thermodynamic limit can be taken analytically. The sum of ladder diagrams built on the bare single-particle propagator defines a partially dressed pair propagator Γ^0. As Γ^0 is well defined

[1]Department of Physics, University of Massachusetts, Amherst, Massachusetts 01003, USA, [2]Department of Physics and Astronomy, Ghent University, Proeftuinstraat 86, B-9000 Ghent, Belgium, [3]Laboratoire Kastler Brossel, Ecole Normale Supérieure, UPMC-Paris 6, CNRS, 24 rue Lhomond, 75005 Paris, France, [4]Theoretische Physik, ETH Zürich, CH-8093, Zürich, [5]Centre de Physique Théorique, Ecole Polytechnique, 91128 Palaiseau Cedex, France, [6]Russian Research Center "Kurchatov Institute", 123182 Moscow, Russia, [7]Department of Physics, MIT-Harvard Center for Ultracold Atoms, and Research Laboratory of Electronics, MIT, Cambridge, Massachusetts 02139, USA, [8]Advanced Light Source, Lawrence Berkeley National Laboratory, Berkeley, California 94720, USA. *e-mail: kris.vanhoucke@ugent.be.

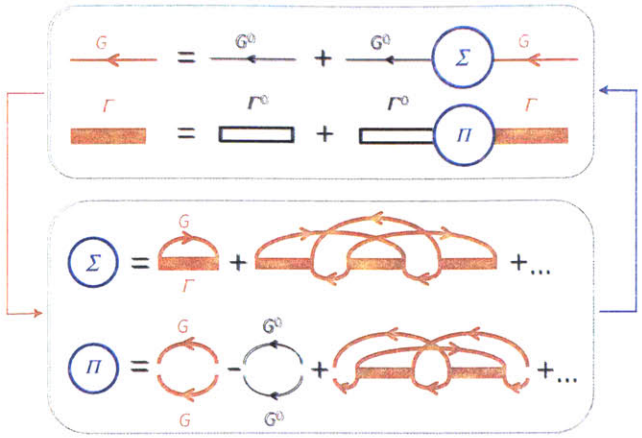

Figure 1 | Bold diagrammatic Monte Carlo The skeleton diagrammatic series for the self-energy Σ and the pair self-energy Π is evaluated stochastically (lower box). The diagrams are built on dressed one-body propagators G and pair propagators Γ, which themselves are the solution of the Dyson and Bethe-Salpeter equations (upper box). This cycle is repeated until convergence is reached. G^0 is the non-interacting propagator and Γ^0 is the partially dressed pair propagator obtained by summing the bare ladder diagrams.

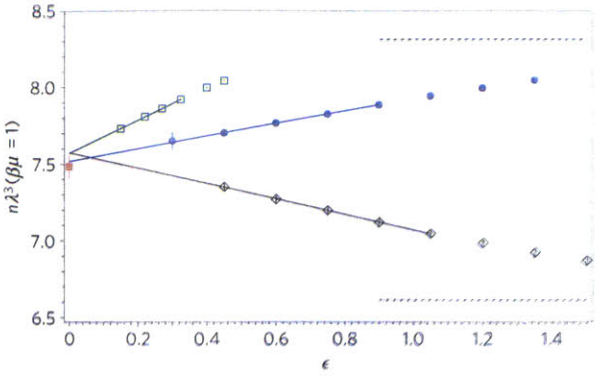

Figure 2 | Cross-validation between resummation procedure and experiment at $\beta\mu = +1$. Bold diagrammatic Monte Carlo data for the dimensionless density $n\lambda^3$, as a function of the parameter ϵ controlling the resummation procedure, for three different resummation methods: Lindelöf (blue circles), shifted Lindelöf (black diamonds), and Gauss (open green squares). The solid lines are linear fits to the Monte Carlo data, their $\epsilon \to 0$ extrapolation agrees within error bars with the experimental data point (filled red square). (In the opposite limit $\epsilon \to \infty$, the Lindelöf (resp. shifted Lindelöf) curves will asymptote to the first[15,21] (resp. third) order results, shown by the dashed (resp. dash-dotted) line.) Error bars for each ϵ represent the statistical error, together with the estimated systematic error coming from not sampling diagrams of order >9.

for the zero-range continuous-space interaction, the zero-range limit can also be taken analytically. This is in sharp contrast with other numerical methods[11–13], where taking the thermodynamic and zero-range limits is computationally very expensive. BDMC performs a random walk in the space of irreducible diagrams using local updates. The simulation is run in a self-consistent cycle (along the lines of ref. 2) until convergence is reached. Full details will be presented elsewhere. In essence, our approach upgrades the standard many-body theories based on one lowest-order diagram (for example, refs 14,15) to millions of graphs.

In the quantum degenerate regime, we do not observe convergence of the diagrammatic series for Σ and Π evaluated up to order 9. Here, order N means Σ-diagrams with N vertices (that is, N Γ-lines) and Π-diagrams with $N-1$ vertices. To extract the infinite-order result, we apply the following Abelian resummation methods[16]. The contribution of all diagrams of order N is multiplied by $e^{-\epsilon\lambda_{N-1}}$, where λ_n depends on the resummation method: (1) $\lambda_n = n \log n$ (with $\lambda_0 = 0$) for Lindelöf[16], (2) $\lambda_n = (n-1)\log(n-1)$ (with $\lambda_0 = \lambda_1 = 0$) for 'shifted Lindelöf', or (3) $\lambda_n = n^2$ for Gaussian[17]. A full simulation is performed for each ϵ, and the final result is obtained by extrapolating to $\epsilon = 0$ (Fig. 2).

This protocol relies on the following crucial mathematical assumptions: (1) the Nth order contribution of the diagrammatic expansion for Σ (for fixed external variables) is the Nth coefficient of the Taylor series at $z = 0$ of a function $g(z)$ which has a non-zero convergence radius, (2) the analytic continuation $g(1)$, performed by the above resummation methods[16,17], is the physically correct value of Σ. The same assumptions should hold for Π.

Proving these assumptions is an open mathematical challenge. Note that Dyson's collapse argument[18] is not applicable to immediately disprove the assumption (1) of a non-zero convergence radius: indeed, unlike QED, our skeleton series is not an expansion in powers of a coupling constant whose sign change would lead to an instability. The first important evidence for the validity of our mathematical assumptions is that the three different resummation methods yield consistent results. For an independent test, we turn to experiments.

The present experiment furnishes high-precision data for the density n as a function of the local value V of the trapping potential (Fig. 3 and Methods). We start the process by obtaining the EOS at high temperatures in the non-degenerate wings of the atom cloud, where the virial expansion is applicable. Once the temperature and the chemical potential have been determined from fits to the wings of the cloud, the data closer to the cloud centre provides a new prediction of the EOS. The process is iterated to access lower temperatures.

Scale invariance allows one to write the density EOS as $n(\mu,T)\lambda^3 = f(\beta\mu)$, with $\lambda = \sqrt{2\pi\hbar^2/(mk_BT)}$ the thermal de Broglie wavelength, $\beta = 1/(k_BT)$ the inverse temperature and f a universal function. A convenient normalization of the data is provided by the EOS of a non-interacting Fermi gas, $n_0\lambda^3 = f_0(\beta\mu)$. In Fig. 4a, we thus report the ratio $n(\mu,T)/n_0(\mu,T) = f(\beta\mu)/f_0(\beta\mu)$, bringing out the difference between the ideal and the strongly interacting Fermi gas. The Gibbs–Duhem relation allows us to also calculate the pressure at a given chemical potential, $P(\mu_0,T) = \int_{-\infty}^{\mu_0} d\mu\, n(\mu,T) = 1/(\beta\lambda^3)F(\beta\mu_0)$, where $F(x) = \int_{-\infty}^{x} dx' f(x')$. We normalize it by the pressure of the ideal Fermi gas and show $F(\beta\mu)/F_0(\beta\mu)$ (Fig. 4b). The agreement between BDMC and experiment is excellent. The comparison is sufficiently sensitive to validate the procedure of resumming and extrapolating (Fig. 2). The result was checked to be independent of the maximal sampled diagram order $N_{max} \in \{7; 8; 9\}$ within the error bars shown in Fig. 2 for each ϵ. The BDMC final error bar in Fig. 4 is the sum of the conservatively estimated systematic errors from the uncertainty of the $\epsilon \to 0$ extrapolation and from the dependence on numerical grids and cutoffs, the latter being reduced by analytically treating high-momentum short-time singular parts. The systematic error in the experiment is determined to be about 1% by the independent determination of the EOS of the non-interacting Fermi gas. The experimental error bars of Fig. 4 also include the statistical error, which is <0.5%, thanks to the scale invariance of the balanced unitary gas: irrespective of shot-to-shot fluctuations of atom number and temperature, all experimental profiles contribute to the same scaled EOS-function f. The dominant uncertainty on the experimental EOS stems from the uncertainty in the position of the ^{6}Li Feshbach resonance, known to be at 834.15 ± 1.5 G from spectroscopic measurements[19]. The change in energy, pressure and density with respect to the interaction strength is controlled by the so-called contact[20] that is obtained from Γ in the BDMC calculation.

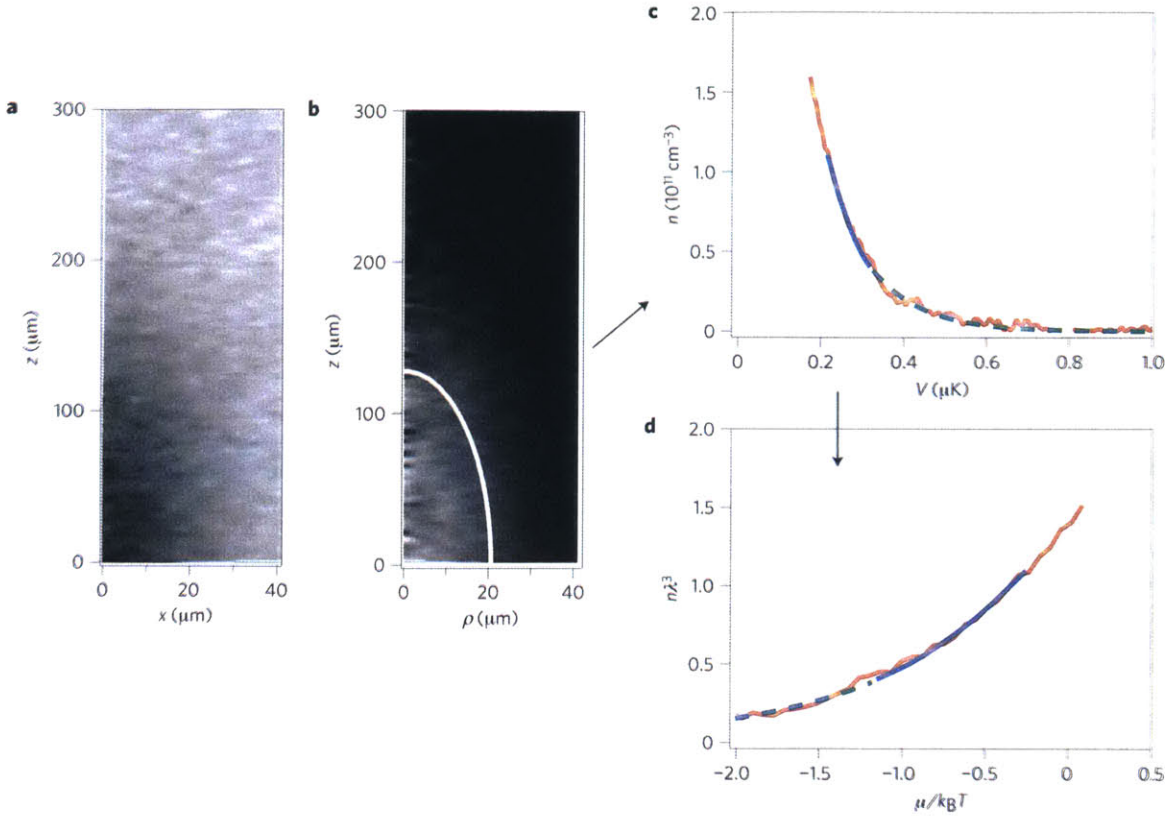

Figure 3 | Constructing the EOS from *in situ* imaging. The atom cloud shown contains $N = 8 \times 10^4$ atoms for each spin state, with a local Fermi energy of $E_F = 370$ nK at the centre. **a**, Absorption image of the atomic cloud after quadrant averaging. **b**, Reconstructed local density $n(\rho, z)$. **c**, Equipotential averaging produces a low-noise density profile, n versus V. Thermometry is performed by fitting the experimental data (red) to the known portion of the EOS (solid blue line), starting with the virial expansion for $\beta\mu < -1.25$ (green dashed line). In this example, the EOS is known for $\beta\mu \leq -0.25$, and the fit to the density profile yields $T = 113$ nK, and $\beta\mu = 1.63$. **d**, Given μ and T, the density profile can be rescaled to produce the EOS $n\lambda^3$ versus $\beta\mu$.

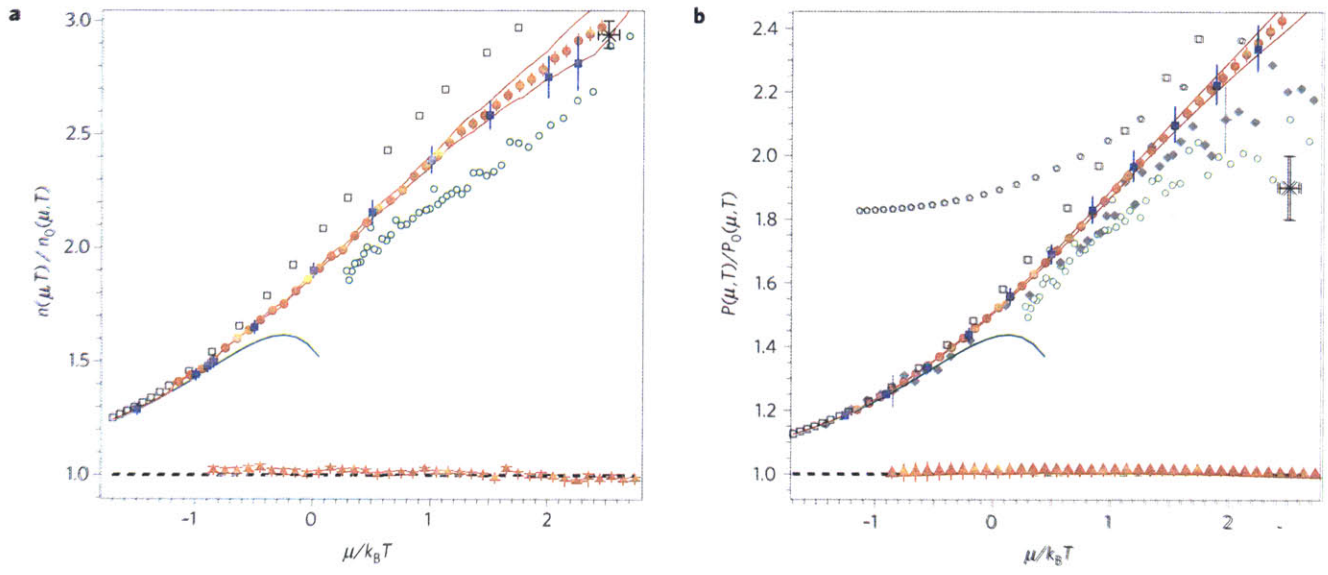

Figure 4 | Equation of state of the unitary Fermi gas in the normal phase. Density n (**a**) and pressure P (**b**) of a unitary Fermi gas, normalized by the density n_0 and the pressure P_0 of a non-interacting Fermi gas, versus the ratio of chemical potential μ to temperature T. Blue filled squares: BDMC (this work), red filled circles: experiment (this work). The BDMC error bars are estimated upper bounds on systematic errors. The error bars are one standard deviation systematic plus statistical errors, with the additional uncertainty from the Feshbach resonance position shown by the upper and lower margins as red solid lines. Black dashed line and red triangles: Theory and experiment (this work) for the ideal Fermi gas, used to assess the experimental systematic error. Green solid line: third order virial expansion. Open squares: first order bold diagram[15,21]. Green open circles: Auxiliary Field QMC (ref. 11). Star: superfluid transition point from Determinental Diagrammatic Monte Carlo[13]. Filled diamonds: experimental pressure EOS (ref. 22). Open pentagons: pressure EOS (ref. 23).

This allows us to define the uncertainty margins above and below the experimental data (Fig. 4) that give the prediction for the unitary EOS if the true Feshbach resonance lies 1.5 G below or above 834.15 G, respectively.

Our results clearly differ from previous theoretical and experimental results. Deviations from the theory based on the first-order Feynman diagrams[15,21] are expected, and rather remarkably moderate. Differences with lattice Monte Carlo data[11,13] may seem more surprising, as in the particular case of the balanced system these algorithms are free of the sign problem, allowing one in principle to approach the balanced unitary gas model in an unbiased way. However, eliminating systematic errors from lattice-discretization and finite volume requires extrapolations which are either not done[11] or difficult to control[12,13]. The ENS experimental pressure EOS (ref. 22) lies systematically below ours, slightly outside the reported error bar. The experimental results from Tokyo[23] do not agree with the virial expansion at high temperature. The BDMC results agree well with the present experimental data all the way down to the critical temperature for superfluidity (Fig. 4). On approaching $(\beta\mu)_c$, we observe the growth of the correlation length in the BDMC pair correlation function Γ. A protocol for extracting the critical temperature itself from the BDMC simulation will be presented elsewhere.

We are not aware of any system of strongly correlated fermions in nature where experimental and unbiased theoretical results were compared at the same level of accuracy. Even for bosons, the only analogue is liquid ^{4}He. This promotes the unitary gas to the major testing ground for unbiased theoretical treatments. The present BDMC implementation should remain applicable at finite polarization and/or finite scattering length, opening the way to rich physics which was already addressed by cold atoms experiments[6,24–27]. We also plan to extend BDMC to superfluid phases by introducing anomalous propagators. Moreover, as the method is generic, we expect numerous other important applications to long-standing problems across many fields.

Note added in proof: After a preprint of this work became available, new auxiliary-field quantum Monte Carlo data were presented[28], with undetermined systematic errors whose evaluation in future work is called for by the authors of ref. 28.

Methods

The experimental set-up has been described previously[24]. In short, ultracold fermionic ^{6}Li is brought to degeneracy by sympathetic cooling with ^{23}Na. A two-state mixture of the two lowest hyperfine states of ^{6}Li is further cooled in a hybrid magnetic and optical trap at the broad Feshbach resonance at 834 G. We employ high-resolution *in situ* absorption imaging to obtain the column density of the gas, that is converted into the full 3D density using the inverse Abel transform[29]. Equidensity lines provide equipotential lines that are precisely calibrated using the known axial, harmonic potential (axial frequency $\nu_z = 22.83 \pm 0.05$ Hz). Equipotential averaging yields low-noise profiles of density n versus potential V. Density is absolutely calibrated by imaging a highly degenerate, highly imbalanced Fermi mixture, and fitting the majority density profile to the ideal Fermi gas EOS (ref. 24). In contrast to previous studies[22,23], our analysis does not rely on the assumption of harmonic trapping.

Thermometry is performed by fitting the density profile to the EOS constructed thus far, restricting the fit to the portion of the density profile where the EOS is valid. In the high-temperature regime, the EOS is given by the virial expansion

$$n\lambda^3 = e^{\beta\mu} + 2b_2 e^{2\beta\mu} + 3b_3 e^{3\beta\mu} + \cdots \quad (1)$$

where the virial coefficients are $b_2 = 3\sqrt{2}/8$ (ref. 30), and $b_3 = -0.29095295$ (ref. 31). Fitting a high-temperature cloud to the virial expansion gives the temperature T and the chemical potential μ of the cloud, and the EOS $n\lambda^3 = f(\beta\mu)$ can be constructed. We have used equation (1) for $\beta\mu < (\beta\mu)_{max} = -1.25$ and we checked that our EOS did not change within statistical noise if we instead used $(\beta\mu)_{max} = -0.85$. Once a new patch of EOS has been produced, it can then in turn be used to fit colder clouds. Iteration of this method allows us to construct the EOS to arbitrarily low temperature. A total of ~1,000 profiles were used, with 10–100 profiles (50 on average) contributing at any given $\beta\mu$.

Received 14 October 2011; accepted 17 February 2012; published online 18 March 2012

References

1. Van Houcke, K., Kozik, E., Prokof'ev, N. & Svistunov, B. in *Computer Simulation Studies in Condensed Matter Physics XXI* (eds Landau, D. P., Lewis, S. P. & Schuttler, H. B.) (Springer, 2008).
2. Prokof'ev, N. & Svistunov, B. Bold diagrammatic Monte Carlo technique: When the sign problem is welcome. *Phys. Rev. Lett.* **99,** 250201 (2007).
3. Prokof'ev, N. V. & Svistunov, B. V. Bold diagrammatic Monte Carlo: A generic sign-problem tolerant technique for polaron models and possibly interacting many-body problems. *Phys. Rev. B* **77,** 125101 (2008).
4. Inguscio M., Ketterle, W. & Salomon, C. (eds) *Proc. Int. School of Physics Enrico Fermi*, Course CLXIV, Varenna, 20–30 June 2006 (IOS Press, 2008).
5. Giorgini, S., Pitaevskii, L. P. & Stringari, S. Theory of ultracold atomic Fermi gases. *Rev. Mod. Phys.* **80,** 1215–1274 (2008).
6. Zwerger, W. (ed.) in *BCS–BEC Crossover and the Unitary Fermi Gas* (Lecture Notes in Physics, Springer, 2012).
7. Feynman, R. Simulating physics with computers. *Int. J. Theoret. Phys.* **21,** 467–488 (1982).
8. Bloch, I., Dalibard, J. & Zwerger, W. Many-body physics with ultracold gases. *Rev. Mod. Phys.* **80,** 885–964 (2008).
9. Fetter, A. & Walecka, J. *Quantum Theory of Many-Particle Systems* (McGraw-Hill, 1971).
10. Kozik, E. *et al.* Diagrammatic Monte Carlo for correlated fermions. *Europhys. Lett.* **90,** 10004 (2010).
11. Bulgac, A., Drut, J. E. & Magierski, P. Spin 1/2 fermions in the unitary regime at finite temperature. *Phys. Rev. Lett.* **96,** 090404 (2006).
12. Burovski, E., Prokof'ev, N., Svistunov, B. & Troyer, M. Critical temperature and thermodynamics of attractive fermions at unitarity. *Phys. Rev. Lett.* **96,** 160402 (2006).
13. Goulko, O. & Wingate, M. Thermodynamics of balanced and slightly spin-imbalanced Fermi gases at unitarity. *Phys. Rev. A* **82,** 053621 (2010).
14. Strinati, G. C. in *BCS–BEC Crossover and the Unitary Fermi Gas* (ed. Zwerger, W.) (Lecture Notes in Physics, Springer, 2012).
15. Haussmann, R. Properties of a Fermi liquid at the superfluid transition in the crossover region between BCS superconductivity and Bose–Einstein condensation. *Phys. Rev. B* **49,** 12975–12983 (1994).
16. Hardy, G. *Divergent Series* (Oxford Univ. Press, 1949).
17. Fruchard, A. Prolongement analytique et systèmes dynamiques discrets. *Collect. Math.* **43,** 71–82 (1992).
18. Dyson, F. J. Divergence of perturbation theory in quantum electrodynamics. *Phys. Rev.* **85,** 631–632 (1952).
19. Bartenstein, M. *et al.* Precise determination of ^{6}Li cold collision parameters by radio-frequency spectroscopy on weakly bound molecules. *Phys. Rev. Lett.* **94,** 103201 (2004).
20. Braaten, E. in *BCS–BEC Crossover and the Unitary Fermi Gas* (ed. Zwerger, W.) (Lecture Notes in Physics, Springer, 2012).
21. Haussmann, R., Rantner, W., Cerrito, S. & Zwerger, W. Thermodynamics of the BCS–BEC crossover. *Phys. Rev. A* **75,** 023610 (2007).
22. Nascimbène, S., Navon, N., Jiang, K. J., Chevy, F. & Salomon, C. Exploring the thermodynamics of a universal Fermi gas. *Nature* **463,** 1057–1060 (2010).
23. Horikoshi, M., Nakajima, S., Ueda, M. & Mukaiyama, T. Measurement of universal thermodynamic functions for a unitary Fermi gas. *Science* **327,** 442–445 (2010).
24. Ketterle, W. & Zwierlein, M. Making, probing and understanding ultracold Fermi gases. *Rivista del Nuovo Cimento* **31,** 247–422 (2008).
25. Shin, Y., Schunck, C., Schirotzek, A. & Ketterle, W. Phase diagram of a two-component Fermi gas with resonant interactions. *Nature* **451,** 689–693 (2007).
26. Shin, Y. Determination of the equation of state of a polarized Fermi gas at unitarity. *Phys. Rev. A* **77,** 041603(R) (2008).
27. Navon, N., Nascimbène, S., Chevy, F. & Salomon, C. The equation of state of a low-temperature Fermi gas with tunable interactions. *Science* **328,** 729–732 (2010).
28. Drut, J. E., Lähde, T. A., Wlazłowski, G. & Magierski, P. The equation of state of the unitary Fermi gas: An update on lattice calculations. Preprint at http://arxiv.org/abs/1111.5079v1 (2011).
29. Shin, Y., Zwierlein, M., Schunck, C., Schirotzek, A. & Ketterle, W. Observation of phase separation in a strongly interacting imbalanced Fermi gas. *Phys. Rev. Lett.* **97,** 030401 (2006).
30. Ho, T-L. & Mueller, E. J. High temperature expansion applied to fermions near Feshbach resonance. *Phys. Rev. Lett.* **92,** 160404 (2004).
31. Liu, X-J., Hu, H. & Drummond, P. D. Virial expansion for a strongly correlated Fermi gas. *Phys. Rev. Lett.* **102,** 160401 (2009).

Acknowledgements

We thank R. Haussmann for providing propagator data from refs 15,21 for comparison, and the authors of refs 11,13,22,23 for sending us their data. This collaboration was supported by a grant from the Army Research Office with funding from the Defense Advanced Research Projects Agency (DARPA) Optical Lattice Emulator program. Theorists acknowledge the financial support of the Research Foundation Flanders (FWO) (K.V.H.), National Science Foundation (NSF) grant PHY-1005543 (University of Massachusetts group), Swiss National Science Foundation (SNF) Fellowship for Advanced Researchers (E.K.), and l'Institut Francilien de Recherche sur les Atomes Froids (IFRAF) (F.W.). Simulations ran on the clusters CM at UMass and Brutus at ETH. The MIT work was supported by the NSF, AFOSR-MURI, ARO-MURI, Office of Naval Research (ONR), DARPA Young Faculty Award, an AFOSR Presidential Early Career Award for Scientists and Engineers (PECASE), the David and Lucile Packard Foundation, and the Alfred P. Sloan Foundation.

Author contributions

K.V.H. (theory) and M.J.H.K. (experiment) contributed equally to this work. K.V.H., F.W., E.K., N.P. and B.S. developed the BDMC approach for unitary fermions; the computer code was written by K.V.H. assisted by F.W.; simulation data were produced by F.W., E.K. and K.V.H.; M.J.H.K., A.T.S., L.W.C., A.S. and M.W.Z. all contributed to the experimental work and the analysis. All authors participated in the manuscript preparation.

Additional information

The authors declare no competing financial interests. Reprints and permissions information is available online at www.nature.com/reprints. Correspondence and requests for materials should be addressed to K.V.H.

Appendix F

Collective Modes in a Unitary Fermi Gas across the Superfluid Phase Transition

This appendix contains a reprint of Ref. [222]: Meng Khoon Tey, Leonid A. Sidorenkov, Edmundo R. Saanchez Guajardo, Rudolf Grimm, Mark J. H. Ku, Martin W. Zwierlein, Yan-Hua Hou, Lev Pitaevskii, and Sandro Stringari, *Collective Modes in a Unitary Fermi Gas across the Superfluid Phase Transition*, Phys. Rev. Lett., **110**, 055303, (2013).

Collective Modes in a Unitary Fermi Gas across the Superfluid Phase Transition

Meng Khoon Tey, Leonid A. Sidorenkov, Edmundo R. Sánchez Guajardo, and Rudolf Grimm
Institut für Quantenoptik und Quanteninformation (IQOQI), Österreichische Akademie der Wissenschaften and Institut für Experimentalphysik, Universität Innsbruck, 6020 Innsbruck, Austria

Mark J. H. Ku and Martin W. Zwierlein
MIT-Harvard Center for Ultracold Atoms, Research Laboratory of Electronics, and Department of Physics, Massachusetts Institute of Technology, Cambridge, Massachusetts 02139, USA

Yan-Hua Hou,[1] Lev Pitaevskii,[1,2] and Sandro Stringari[1]
[1]*Dipartimento di Fisica, Universitá di Trento and INO-CNR BEC Center, I-38123 Povo, Italy*
[2]*Kapitza Institute for Physical Problems RAS, Kosygina 2, 119334 Moscow, Russia*
(Received 12 November 2012; published 29 January 2013)

We provide a joint theoretical and experimental investigation of the temperature dependence of the collective oscillations of first sound nature exhibited by a highly elongated harmonically trapped Fermi gas at unitarity, including the region below the critical temperature for superfluidity. Differently from the lowest axial breathing mode, the hydrodynamic frequencies of the higher-nodal excitations show a temperature dependence, which is calculated starting from Landau two-fluid theory and using the available experimental knowledge of the equation of state. The experimental results agree with high accuracy with the predictions of theory and provide the first evidence for the temperature dependence of the collective frequencies near the superfluid phase transition.

DOI: 10.1103/PhysRevLett.110.055303 PACS numbers: 67.85.Lm, 03.75.Ss, 05.30.Fk

Collective oscillations provide powerful tools to understand the physical behavior of quantum many-body systems from different points of view and to test fundamental theories. On one hand, collective modes can be used to explore different dynamical regimes of the system, such as superfluid, collisional, or collisionless regimes, for both Bose and Fermi statistics [1–4]. On the other hand, the mode frequencies allow us to probe the equation of state (EOS) of the system, including its temperature dependence. Major benefits result from the high accuracies attainable in the measurements of collective frequencies, which often enable refined investigations of subtle interaction effects.

The many-body physics of unitary Fermi gases, i.e., two-component Fermi gases with infinite scattering length, has attracted tremendous interest over the past decade [2–4]. The unitary Fermi gas is characterized by strong interaction effects in the EOS [5–8] and reveals a unique universal thermodynamic behavior [9]. Furthermore, at finite temperature, the strong interactions favor the collisional hydrodynamic regime, differently from the common situation in weakly interacting Bose gases. The low-frequency modes of a harmonically trapped Fermi gas have been the subject of intensive experimental [10–12] and theoretical (see Ref. [3] and references therein) efforts. The temperature dependence has been studied in Refs. [13–15]. Remarkably, at unitarity all modes observed so far turned out to be insensitive to the different nature of a superfluid and a classical gas, with their frequencies remaining independent of temperature throughout the hydrodynamic regime. Previous experiments have demonstrated the crossover from hydrodynamic to collisionless behavior, which typically occurs for temperatures approaching the Fermi temperature, without giving any further information on the regime of lower temperatures where the gas is deeply hydrodynamic and the superfluid phase transition occurs.

In this Letter, we report a joint effort of theory and experiment on higher-nodal collective modes in the unitary Fermi gas. We present a 1D hydrodynamic approach to describe axial modes in a trapped "cigar-shaped" cloud. Our experimental results confirm the predicted intrinsic sensitivity of higher-nodal modes to the EOS in the low-temperature regime, above and even well below the superfluid phase transition.

The macroscopic dynamic behavior of a superfluid is governed by the Landau two-fluid hydrodynamic equations [16] holding in the deep collisional regime $\omega\tau \ll 1$ where τ is a typical collisional time and ω is the frequency of the relevant sound mode in the trap. Landau's equations consist of the equation of continuity for the total density, the equation for the velocity of the superfluid component, the equation for the entropy density, and the equation for the current density. The physical ingredients entering these equations are the equation of state and the superfluid density. At zero temperature they reduce to the irrotational hydrodynamic equations of superfluids, above the critical point to the usual hydrodynamic equations of normal fluids. Below T_c these equations describe the propagation of first and second sound, the former being basically a density wave, with

the normal and superfluid components moving in phase, the latter being a temperature or entropy wave. For weakly compressible fluids the coupling between first and second sound is small [16]. This is the case of superfluid helium and also of the unitary Fermi gas [17]. Since in the present work we investigate the collective oscillations of density (first sound), we simplify the search for the solutions of Landau's equation by requiring that the velocity fields of the normal and superfluid components are equal. Under this approximation the equations of motion involve only the EOS, the superfluid density playing a role only in the propagation of second sound.

In the presence of a trapping potential, the solution of Landau's equations is highly nontrivial, due to the inhomogeneity of the density profile, and thus far has been calculated only for the simplest case of isotropic trapping [17,18]. Since the experimental excitation and observation of these modes are more easily accessible with very elongated traps, in the following we focus on such configurations. In [19] it was shown that under suitable conditions of radial trapping one can derive simplified 1D hydrodynamic equations starting from the more general 3D Landau's equations. The basic point for such a derivation is the assumption that both the velocity field v_z along the long axis and the temperature fluctuations during the propagation of sound do not depend on the radial coordinates. This 1D-like hydrodynamic formulation is justified under the condition that the viscosity and the thermal conductivity are sufficiently large to ensure, respectively, the absence of radial gradients in the velocity v_z and the temperature. The condition for the viscosity can be recast in the form $\eta \gg \rho_{n1}\omega$, where ρ_{n1} is the normal 1D mass density, obtained by radial integration of the 3D normal density. An analogous condition holds for the thermal conductivity. These conditions are better satisfied in the presence of tight radial confinement and for the lowest frequency oscillations. One can estimate the values of shear viscosity η using the experimental data of [20]. For the actual conditions of our experiments, both sides of the inequality are of the same order of magnitude and consequently the full applicability of the 1D hydrodynamic formulation can be justified only *a posteriori*. Violation of the 1D condition would result in a damping of the collective oscillations so that, to the extent that the observed damping is small, we expect that the assumption of velocity field and temperature being independent of the radial coordinate is a reasonable ansatz for our variational approach.

Under the above assumptions and focusing on the unitary Fermi gas, the equation for the velocity field, characterizing the density oscillations of the gas in a highly elongated harmonic trap, takes the form (see Ref. [21] for a complete and systematic derivation)

$$m(\omega^2 - \omega_z^2)v_z - \frac{7}{5}m\omega_z^2 z\partial_z v_z + \frac{7}{5}\frac{P_1}{n_1}\partial_z^2 v_z = 0, \quad (1)$$

where we have considered oscillations in time proportional to $e^{-i\omega t}$. Here, ω_z represents the trap frequency along the axial direction z and m is the atom's mass. Equation (1) explicitly points out the crucial role played by the equation of state $P_1(n_1, T)$, where $P_1 = \int P dxdy$ is the "1D pressure" (having units of force) and $n_1 = \int n dxdy$ is the atom number per unit length. In order to derive Eq. (1) we have explicitly used the adiabatic result $n_1(\partial P_1/\partial n_1)_{\bar{s}_1} = 7/5P_1$ holding at unitarity at all temperatures, where $\bar{s}_1 = (1/n_1)\int s dxdy$ is the entropy per atom with s the entropy density and we have assumed the validity of the local density approximation along both the axial and radial directions.

At zero temperature and in the classical limit of high temperature, the hydrodynamic equation (1) admits analytic solutions of polynomial form $v_z = a_k z^k + a_{k-2}z^{k-2} + \cdots$, with integer values of k. At $T = 0$, where $P_1(n_1)/n_1 = (2/7)[\mu_0 - (1/2)m\omega_z^2 z^2]$, with μ_0 the chemical potential at the center of the trap, the frequency of the kth mode is given by

$$\omega^2 = \frac{1}{5}(k+1)(k+5)\omega_z^2. \quad (2)$$

In the classical limit, where $P_1/n_1 = k_B T$, one finds the different k dependence

$$\omega^2 = \frac{1}{5}(7k+5)\omega_z^2. \quad (3)$$

It is worth noting that Eqs. (2) and (3) coincide for $k = 0$ (center of mass oscillation) and $k = 1$ (lowest axial breathing mode), while they predict different values for the higher nodal solutions. One can actually prove that not only the frequency of the center of mass but, at unitarity, also the frequency of the lowest axial breathing mode are independent of temperature, corresponding to an exact scaling solution of the two fluid hydrodynamic equations [21]. It then follows that only the $k \geq 2$ modes exhibit a temperature dependence.

In order to provide a simple quantitative prediction for the temperature dependence of the mode frequencies, we have developed a variational approach to the solution of the hydrodynamic equation (1) with the ansatz $v_z = a_2 z^2 + a_0$ for the $k = 2$ mode. This ansatz reproduces exactly the frequency of the $k = 2$ mode in the limits of $T = 0$ and high T. For intermediate temperatures we obtain [21]

$$\omega_{k=2}^2 = \frac{129t_2 - 25}{5(9t_2 - 5)}\omega_z^2, \quad (4)$$

where $t_2 = M_0 M_4/M_2^2$. We have introduced the dimensionless moments

$$M_\ell = \int_{-\infty}^{\beta\mu_0} dx(\beta\mu_0 - x)^{(\ell+1)/2} n(x)\lambda_T^3 \quad (5)$$

of the 3D number density $n(x)$, where x is the local chemical potential times $\beta = 1/k_B T$ and λ_T is the thermal

de Broglie wavelength. The temperature dependence of the moments M_ℓ can be evaluated using the experimentally determined EOS [8]. Approaching the classical regime, for $\beta\mu \lesssim -1.5$, the virial expansion of the EOS [22] holds [8] and allows us to extend the integral to $\beta\mu \to -\infty$. At low temperatures, corresponding to $\beta\mu > 4$, the EOS is governed by phonons and is solely determined by the Bertsch paramter ξ. The error of the quantity t_2 above resulting from the error in the density EOS is less than 1%. We have checked that our variational predictions are practically indistinguishable from the exact numerical solution of Eq. (1). Starting from the equation of continuity one can also calculate the shape of the density oscillations of each mode, proportional to $\partial_z(n_1 v_z)$.

Experimentally, we prepare an ultracold, resonantly interacting Fermi gas by evaporating a two-component spin mixture of fermionic ^{6}Li in an optical dipole trap [23]. The atomic cloud contains typically $N/2 = 1.5 \times 10^5$ atoms per spin state, and the magnetic field is set to 834 G, right on top of the well-known broad Feshbach resonance [24]. For the lowest temperatures, the trapping beam (wavelength 1075 nm) has a waist of 31 μm, the trap depth is about 2 μK, and the axial and radial trap frequencies are $\omega_z = 2\pi \times 22.52(2)$ Hz and $\omega_r = 2\pi \times 473(2)$ Hz, respectively. For experiments at higher temperatures, the beam waist is increased to 38 μm, and deeper traps are used (up to 16 μK depth) with trap frequencies of up to $\omega_z = 2\pi \times 23.31(3)$ Hz and $\omega_r = 2\pi \times 1226(6)$ Hz. The corresponding Fermi temperatures $T_F = \hbar(3N\omega_r^2\omega_z)^{1/3}/k_B$ vary between about 0.8 and 1.5 μK. We point out that essentially perfect harmonic confinement along the long trap axis (z axis) is ensured by the magnetic trapping that results from the curvature of the magnetic field used for Feshbach tuning [23]. Also, anharmonicities in the radial confinement remain negligibly small. To probe the ultracold gas we record one-dimensional axial density profiles $n_1(z)$ by near *in situ* absorption imaging [25].

The temperature T of the gas is set by controlled heating, always starting from a deeply cooled cloud ($T/T_F \approx 0.1$). In the low-temperature range ($T \lesssim 0.2T_F$), we simply introduce a variable hold time of up to 4 s in which residual trap heating slowly increases T. Higher temperatures are reached by parametric heating, modulating the trap power at about $2\omega_r$ and introducing a sufficient hold time to reach thermal equilibrium between the different degrees of freedom. We characterize the resulting temperature in a model-independent way that does not require any *a priori* knowledge of the EOS. Based on the virial theorem [26] we introduce the dimensionless parameter E/E_0, which represents the total energy $E = 3m\omega_z^2 \int_{-\infty}^{\infty} dz z^2 n_1(z)$ normalized to the energy of a noninteracting, zero-temperature Fermi gas, $E_0 = \frac{3}{4}Nk_BT_F$. For a given EOS, the energy scale (E/E_0) can be converted to a temperature scale (T/T_F). Alternatively, we obtain the cloud's temperature by fitting the experimental profiles $n_1(z)$ [7,27] with T-dependent profiles for a given EOS. For both methods, we use the EOS from Ref. [8]. We note that the temperatures obtained by both methods in general show satisfying agreement with each other. At very low temperatures the latter method shows a trend to give slightly lower values of T (up to ~10%), which indicates small systematic uncertainties of our measurements.

We selectively excite axial modes of order k by using a resonant excitation scheme. As illustrated in Fig. 1(a), a repulsive 532-nm laser beam perpendicularly intersects the trapping beam, with its position and size chosen in a way to provide best mode matching. Typically, the excitation pulse contains 8 cycles of sinusoidal modulation with a half-cycle sine envelope, and the maximum potential height of the excitation beam is kept to about $0.01k_BT_F$. The power, length, and shape of the excitation pulse are optimized in order to resonantly drive the desired small-amplitude oscillation. The amplitude of the corresponding density modulation stays well below 3% of the central density of the cloud.

We record axial density profiles $n_1(z, t)$ of the excited cloud for various time delays t after the excitation pulse.

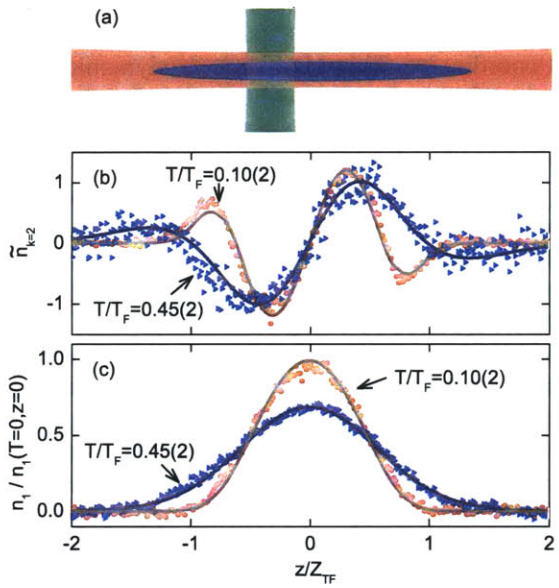

FIG. 1 (color online). Probing a higher-order first sound longitudinal mode at the example of $k = 2$. In (a), we illustrate the basic geometry of exciting the optically trapped cloud with a weak, power-modulated repulsive laser beam, which perpendicularly intersects the trapping beam. In (b), the experimental mode profiles (data points) are compared to theoretical curves based on the experimental EOS from Ref. [8] (solid lines) for two different temperatures. The corresponding cloud profiles in (c) are analyzed to extract the temperatures (see text). The solid lines show the density profiles obtained from the EOS [8] with $T/T_F = 0.10$ and 0.45. The parameter $Z_{\mathrm{TF}} = \xi^{1/4}\omega_z^{-1}\sqrt{2k_BT_F/m}$ represents the Thomas-Fermi radius of the zero-T interacting gas.

We then perform a Fourier transform. The resulting function $\tilde{n}(z, \omega)$ reveals the collective mode spectrum with eigenfrequencies ω_k and the corresponding spatial mode profiles $\tilde{n}_k(z)$. We extract the precise frequency of a particular mode k by projecting $n_1(z, t)$ onto the spatial profile $\tilde{n}_k(z)$ and analyzing the resulting oscillation in the time domain [25]. The high signal-to-noise ratio results in very low statistical uncertainties in the permille range.

In this way, we study the longitudinal modes with $k = 0$, 1, 2. The measured frequency ω_0 of the sloshing mode ($k = 0$) is an accurate measure of the axial trap frequency ($\omega_{k=0} = \omega_z$), and is therefore used for normalization purposes. The axial compression mode ($k = 1$) has been studied in previous work [11,28]. Here, in the full temperature range explored ($0.1 \leq T/T_F \leq 0.5$), we observe its frequency very close to $\omega_{k=1} = \sqrt{12/5}\omega_z$. Deviations from this value remain below 0.3% and no significant temperature dependence is observed. This confirms that this mode is insensitive to the temperature as long as the gas stays hydrodynamic. For the higher-nodal mode with $k = 2$, we observe the expected T-dependent frequency variations. Damping increases as compared to the $k = 1$ mode, but remains sufficiently small to observe many oscillations and thus to accurately determine the mode frequency. Typical observed damping times [25] are 2 s at $0.5T_c$, 0.2 s at T_c, and 0.12 s at $2T_c$. We note that the $k = 3$ mode [25] shows very similar behavior, with larger frequency variations but faster damping.

In Figs. 1(b) and 1(c), we show examples for the spatial profiles of the $k = 2$ mode for two different temperatures $T/T_F = 0.10$ and 0.45 along with the corresponding unperturbed density profiles of the cloud. The comparison of the experimental data (data points) with the theoretical results based on the experimental EOS in Ref. [8] (solid lines) shows excellent agreement.

Figure 2 presents the comparison between the experimental and theoretical frequencies for the $k = 2$ mode. In Fig. 2(a) the normalized mode frequencies $\omega_{k=2}/\omega_z$ are plotted versus the energy parameter E/E_0, while Fig. 2(b) displays the same data on a temperature scale T/T_F. The experimental data confirm the pronounced temperature dependence of the mode frequencies as predicted by our theory based on the EOS of Ref. [8] (solid line). In comparison, the disagreement with the dependence that would result from the EOS of the ideal Fermi gas (dashed line) highlights the important role of the EOS. At the lowest temperatures ($T/T_F \approx 0.1$) the frequency lies close to the $T = 0$ superfluid limit, but already shows a significant down-shift amounting to almost 1%. At the highest temperatures ($T/T_F \approx 0.45$) our data show a clear trend to go below the asymptotic high-temperature value, i.e., the classical hydrodynamic limit. The corresponding nonmonotonic temperature dependence can be understood based on the first-order correction to the EOS resulting from the virial expansion at high temperatures.

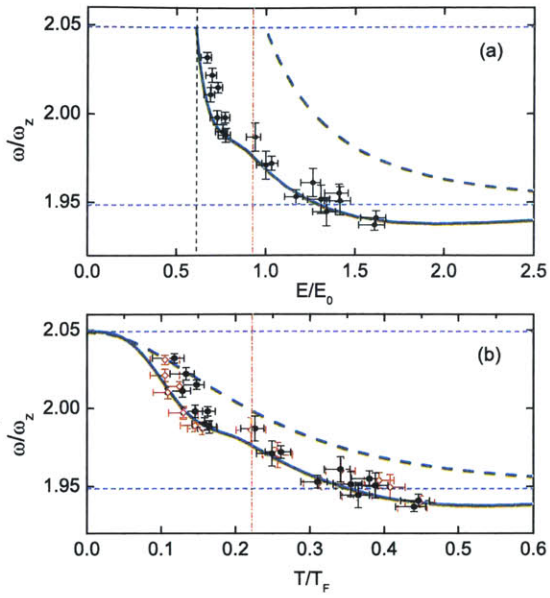

FIG. 2 (color online). Comparison between experimental and theoretical first sound frequencies of the $k = 2$ mode. In (a) the experimental data are plotted versus the energy parameter E/E_0, while in (b) we use a temperature scale T/T_F. The theoretical curves (solid lines) are based on the EOS of Ref. [8]. This EOS is also used to extract T/T_F from the measured profile in two different ways: The filled symbols in (b) result from a direct conversion of E/E_0 to T/T_F, while the open symbols result from fitting the cloud profiles (see text). For comparison, we also show the mode frequencies (dashed curves) that would result from the EOS of the ideal Fermi gas. The thin horizontal dashed lines mark the zero-T superfluid limit ($\omega/\omega_z = \sqrt{21/5}$) and the classical hydrodynamic limit ($\omega/\omega_z = \sqrt{19/5}$) according to Eqs. (2) and (3), respectively. In (a) the dashed vertical line indicates the $T = 0$ ground state with $E/E_0 = \sqrt{\xi} = 0.613(3)$, while the dash-dotted vertical lines in (a) and (b) indicate the critical energy $E_c/E_0 = 0.934(39)$ and temperature $T_c/T_F = 0.223(15)$.

In conclusion, our combined theoretical and experimental work on higher-nodal axial collective modes of a unitary Fermi gas reveals a pronounced temperature dependence below and near the superfluid phase transition. The observed temperature dependence is a unique feature of higher-nodal modes, not present for any other collective mode studied in Fermi gases so far. Our theoretical approach is based on a 1D two-fluid hydrodynamic model describing the frequently used elongated cigar-shaped trap geometry. The excellent agreement with the experimental results provides a stringent test for the validity of this 1D approach and highlights its potential power to accurately describe second sound modes. Moreover, our measurements provide an independent confirmation of the recently measured EOS of a unitary Fermi gas.

We would like to thank John Thomas for useful discussions and Florian Schreck for discussion and experimental support. The Innsbruck team acknowledges support from the Austrian Science Fund (FWF) within SFB FoQuS

(Project No. F4004-N16). The Trento team acknowledges support from the European Research Council through the project QGBE. The MIT work was supported by the NSF, AFOSR, ONR, ARO with funding from the DARPA OLE program, and the David and Lucile Packard Foundation.

[1] L. Pitaevskii and S. Stringari, *Bose-Einstein Condensation* (Oxford University Press, 2003).
[2] M. Inguscio, W. Ketterle, and C. Salomon, *Proceedings of the International School of Physics "Enrico Fermi", Course CLXIV* (IOS Press, Amsterdam, 2008).
[3] S. Giorgini, L. P. Pitaevskii, and S. Stringari, Rev. Mod. Phys. **80**, 1215 (2008).
[4] I. Bloch, J. Dalibard, and W. Zwerger, Rev. Mod. Phys. **80**, 885 (2008).
[5] J. Kinast, A. Turlapov, J. E. Thomas, Q. Chen, J. Stajic, and K. Levin, Science **307**, 1296 (2005).
[6] M. Horikoshi, S. Nakajima, M. Ueda, and T. Mukaiyama, Science **327**, 442 (2010).
[7] S. Nascimbène, N. Navon, K. J. Jiang, F. Chevy, and C. Salomon, Nature (London) **463**, 1057 (2010).
[8] M. J. H. Ku, A. T. Sommer, L. W. Cheuk, and M. W. Zwierlein, Science **335**, 563 (2012).
[9] T.-L. Ho, Phys. Rev. Lett. **92**, 090402 (2004).
[10] J. Kinast, S. L. Hemmer, M. E. Gehm, A. Turlapov, and J. E. Thomas, Phys. Rev. Lett. **92**, 150402 (2004).
[11] M. Bartenstein, A. Altmeyer, S. Riedl, S. Jochim, C. Chin, J. Hecker Denschlag, and R. Grimm, Phys. Rev. Lett. **92**, 203201 (2004).
[12] A. Altmeyer, S. Riedl, C. Kohstall, M. J. Wright, R. Geursen, M. Bartenstein, C. Chin, J. Hecker Denschlag, and R. Grimm, Phys. Rev. Lett. **98**, 040401 (2007).
[13] J. Kinast, A. Turlapov, and J. E. Thomas, Phys. Rev. Lett. **94**, 170404 (2005).
[14] M. J. Wright, S. Riedl, A. Altmeyer, C. Kohstall, E. R. Sánchez Guajardo, J. Hecker Denschlag, and R. Grimm, Phys. Rev. Lett. **99**, 150403 (2007).
[15] S. Riedl, E. R. Sánchez Guajardo, C. Kohstall, A. Altmeyer, M. J. Wright, J. Hecker Denschlag, R. Grimm, G. M. Bruun, and H. Smith, Phys. Rev. A **78**, 053609 (2008).
[16] I. M. Khalatnikov, *An Introduction to the Theory of Superfluidity* (Benjamin, New York, 1965).
[17] E. Taylor, H. Hu, X.-J. Liu, L. P. Pitaevskii, A. Griffin, and S. Stringari, Phys. Rev. A **80**, 053601 (2009).
[18] Y. He, Q. Chen, C.-C. Chien, and K. Levin, Phys. Rev. A **76**, 051602 (2007).
[19] G. Bertaina, L. Pitaevskii, and S. Stringari, Phys. Rev. Lett. **105**, 150402 (2010).
[20] C. Cao, E. Elliott, H. Wu, and J. E. Thomas, New J. Phys. **13**, 075007 (2011).
[21] Y.-H. Hou, L. Pitaevskii, and S. Stringari arXiv:1301.4419.
[22] X.-J. Liu, H. Hu, and P. D. Drummond, Phys. Rev. Lett. **102**, 160401 (2009).
[23] S. Jochim, M. Bartenstein, A. Altmeyer, G. Hendl, S. Riedl, C. Chin, J. Hecker Denschlag, and R. Grimm, Science **302**, 2101 (2003).
[24] C. Chin, R. Grimm, P. S. Julienne, and E. Tiesinga, Rev. Mod. Phys. **82**, 1225 (2010).
[25] E. R. Sánchez Guajardo, M. K. Tey, L. A. Sidorenkov, and R. Grimm (to be published).
[26] J. E. Thomas, J. Kinast, and A. Turlapov, Phys. Rev. Lett. **95**, 120402 (2005).
[27] T.-L. Ho and Q. Zhou, Nat. Phys. **6**, 131 (2010).
[28] S. Nascimbène, N. Navon, K. J. Jiang, L. Tarruell, M. Teichmann, J. McKeever, F. Chevy, and C. Salomon, Phys. Rev. Lett. **103**, 170402 (2009).

Appendix G

Heavy Solitons in a Fermionic Superfluid

This appendix contains a reprint of Ref. [243]: Tarik Yefsah, Ariel T. Sommer, Mark J. H. Ku, Lawrence W. Cheuk, Wenjie Ji, Waseem S. Bakr, and Martin W. Zwierlein, *Heavy Solitons in a Fermionic Superfluid*, Nature, **499**, 426Ũ430, (2013).

ARTICLE

doi:10.1038/nature12338

Heavy solitons in a fermionic superfluid

Tarik Yefsah[1], Ariel T. Sommer[1], Mark J. H. Ku[1], Lawrence W. Cheuk[1], Wenjie Ji[1], Waseem S. Bakr[1] & Martin W. Zwierlein[1]

Solitons—solitary waves that maintain their shape as they propagate—occur as water waves in narrow canals, as light pulses in optical fibres and as quantum mechanical matter waves in superfluids and superconductors. Their highly nonlinear and localized nature makes them very sensitive probes of the medium in which they propagate. Here we create long-lived solitons in a strongly interacting superfluid of fermionic atoms and directly observe their motion. As the interactions are tuned from the regime of Bose–Einstein condensation of tightly bound molecules towards the Bardeen–Cooper–Schrieffer limit of long-range Cooper pairs, the solitons' effective mass increases markedly, to more than 200 times their bare mass, signalling strong quantum fluctuations. This mass enhancement is more than 50 times larger than the theoretically predicted value. Our work provides a benchmark for theories of non-equilibrium dynamics of strongly interacting fermions.

Solitonic excitations are found throughout nature, in proteins and DNA, in crystals as dislocations, and generally in the wake of symmetry-breaking phase transitions[1]. In fermionic systems, solitonic defects may provide bound states for fermions that often play a crucial role in the system's transport properties. Famous examples are Andreev bound states inside vortex cores[2], fractionally charged solitons in relativistic quantum field theory[3,4], and the spinless charged solitons responsible for the high conductivity of polymers[5]. However, the free motion of such defects in electronic systems is hindered by pinning at impurities[5,6]. Fermionic superfluids of ultracold atomic gases provide a paradigmatic form of quantum matter[7–9] that is free of impurities, where—as we show here—real-time dynamics of solitonic excitations can be directly observed.

Superfluids are described by a complex macroscopic wavefunction that is rigid against twists of its phase. The ground state of the superfluid thus has uniform phase, and small perturbations propagate as sound waves. A nonlinear excitation—the dark soliton—occurs when the phase is twisted substantially over a short range. In the extreme case of a phase jump by 180°, the wavefunction changes sign and crosses zero at the location of the jump, creating a stationary black soliton. In weakly interacting Bose–Einstein condensates (BECs) all bosons reside in the condensate, so the particle density vanishes at a black soliton, and is reduced for a moving dark soliton. Solitons in BECs have been studied extensively both theoretically and experimentally[10]. In a series of pioneering experiments, dark solitons have been created via phase-imprinting[11–14] or in the wake of shock waves[15–17]. Collisions of two dark solitons[17] and soliton oscillations[14,17] were observed. Solitons in weakly interacting BECs are well described as solutions to the Gross–Pitaevskii equation, known in other contexts as the cubic nonlinear Schrödinger equation.

In fermionic superfluids[7–9], solitons are phase twists in the wavefunction of fermion pairs[18,19]. For *s*-wave superfluids, the pair wavefunction is also known as the pairing gap $\Delta(r)$, which in general can depend on the spatial location r. By tuning the interactions between fermions, one can access the crossover from Bose–Einstein condensation of molecules to the Bardeen–Cooper–Schrieffer (BCS) state of long-range Cooper pairs. In the limit of tight molecular pairing, interactions between molecules are weak and the molecular condensate is still described by the Gross–Pitaevskii equation. Stationary solitons are thus again devoid of particles. In this limit, the wavefunction for a stationary soliton, shown in Fig. 1a, depends on position along the z axis as $\Delta(z) = \Delta_0 \tanh(z/\xi)$, where Δ_0 is the magnitude of the wavefunction in the bulk, far away from the soliton, and the soliton width ξ is equal to the healing length of the condensate[20]. The repulsive interactions between the molecular bosons can be increased by means of a Feshbach resonance, allowing the study of strongly interacting Bose gases[7]. Strong interactions increase the importance of quantum fluctuations that are present even at zero temperature, leading to a depletion of the condensate. The uncondensed bosons are expected to fill in the soliton notch, the void at the soliton's position, in order to minimize their repulsive interaction with the condensate[10,21–24]. Figure 1a shows the density profile of the bosons localized at the soliton, the so-called anomalous mode that is predicted to be the main contribution to the density inside the soliton notch[21–23]. Similar soliton filling has been predicted for BECs in optical lattices, where the effect of interactions and thus the role of quantum fluctuations is enhanced by reducing the particles' kinetic energy[25].

Description of solitons in the BEC–BCS crossover

When the interaction strength in the pair condensate becomes of the order of the Fermi energy (E_F), the composite nature of the molecules is revealed. The fermion pair size is now of the order of the interparticle spacing, and the system is a crossover superfluid in between the BEC and BCS limits of superfluidity[7–9]. A unified description for solitons in fermionic superfluids throughout the BEC–BCS crossover has been found within mean-field theory via the Bogoliubov-de Gennes (BdG) equation for a spatially varying gap $\Delta(z)$ (refs 19, 26–28):

$$\left\{\left(-\frac{\hbar^2\nabla^2}{2m}-\mu\right)\sigma_z+\Delta(z)\sigma_x\right\}\begin{pmatrix}u_n\\v_n\end{pmatrix}=E_n\begin{pmatrix}u_n\\v_n\end{pmatrix} \qquad (1)$$

where $\hbar$ is Planck's constant h divided by 2π, m is the atomic mass, μ is the chemical potential, $\sigma_{x,y,z}$ are Pauli matrices, and $u_n(z)$ and $v_n(z)$ are the amplitudes describing the particle and hole character of Bogoliubov quasi-particles of energy E_n (we omit spin indices). The order parameter $\Delta(z)$ is related to the quasi-particle amplitudes by the self-consistency relation $\Delta(z) = -g\sum_n u_n(z)v_n^*(z)$, where g is the coupling strength, tunable via the scattering length a between fermions, and * denotes complex conjugation. The BdG equations have been shown to reduce to the Gross–Pitaevskii equation for bosonic molecules in the BEC limit[29], where stationary solitons are devoid of particles. As the interactions are tuned from the BEC to the BCS regime, the BdG equations predict an increasing filling of the soliton[19]. At the

[1]MIT-Harvard Center for Ultracold Atoms, Research Laboratory of Electronics, Department of Physics, Massachusetts Institute of Technology, Cambridge, Massachusetts 02139, USA.

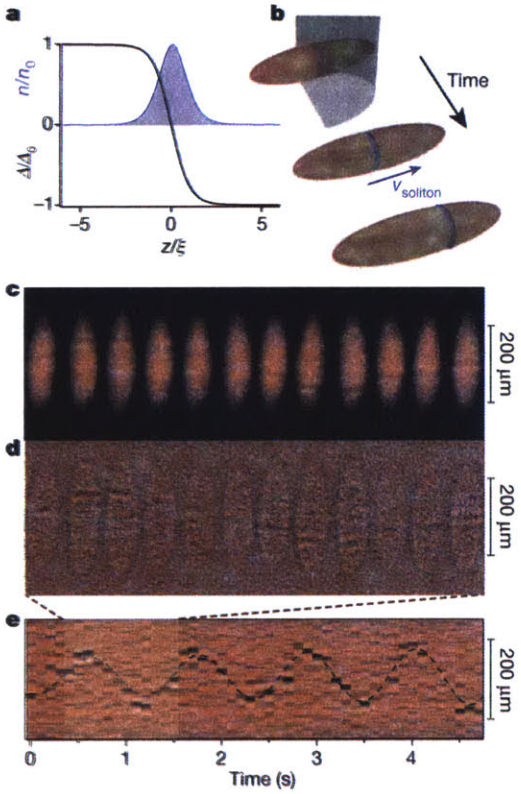

Figure 1 | Creation and observation of solitons in a fermionic superfluid. **a**, Superfluid pairing gap $\Delta(z)$ for a stationary soliton, normalized by the bulk pairing gap Δ_0, and density $n(z)$ of the localized bosonic (fermionic) state versus position z, in the BEC (BCS) regime of the crossover, in units of the BEC healing length (BCS coherence length) ξ. **b**, Diagram of the experiment. A phase-imprinting laser beam twists the phase of one-half of the trapped superfluid by approximately π. The soliton generally moves at non-zero velocity $v_{soliton}$. **c**, Optical density and **d**, residuals (optical density minus a smoothed copy of the same image) of atom clouds at 815 G, imaged via the rapid ramp method[34], showing solitons at various hold times after creation. One period of soliton oscillation is shown. The in-trap aspect ratio was $\lambda = 6.5(1)$. **e**, Radially integrated residuals as a function of time revealing long-lived soliton oscillations. The soliton period is $T_s = 12(2)T_z$, much longer than the trapping period of $T_z = 93.76(5)$ ms, revealing an extreme enhancement of the soliton's relative effective mass, M^*/M.

Feshbach resonance, in the unitarity limit where the scattering length diverges, a substantial part of this filling is due to so-called Andreev bound states, localized fermionic states bound to the soliton, also known to reside inside vortex cores[2]. Here, the gas density in the vicinity of the soliton is predicted to be suppressed by 80% of the bulk density, as opposed to 100% for solitons in BECs.

In the BCS limit of weak attractive interactions, the BdG equations reduce to the Andreev equation, a Dirac equation where the pairing gap $\Delta(z)$ plays the role of a spatially varying mass coupling particles and holes[3] (see Supplementary Information). The same equation describes solitons in conducting polymers[5]. The solution for the pairing gap is known[5] to be $\Delta(z) = \Delta_0 \tanh(z/\xi_{BCS})$, as in the BEC limit, that is, it is again represented by Fig. 1a but with $\xi = \xi_{BCS}$, the BCS coherence length. The density profile of the localized state in Fig. 1a here represents the fermionic Andreev bound state, as opposed to the density of uncondensed bosons in the BEC regime. Solitons in the BCS regime are expected to be essentially completely filled in. Indeed, in this limit of long-range overlapping Cooper pairs, only a minute fraction of particles near the Fermi surface takes part in pairing, and the reduction of the pairing gap at the soliton affects the density only very weakly.

Creating solitons in a fermionic superfluid

The creation of solitons in a strongly interacting fermionic superfluid poses several challenges. First, a superfluid with a soliton is not in its ground state, so the temperature of the gas has to be low enough for the soliton not to decay rapidly into thermal excitations. Such dissipation can proceed through collisions of the soliton with sound waves, leading to its acceleration. When the soliton reaches a critical velocity, it is expected to decay into phonons or, in the case of fermionic superfluids, pair excitations[27,28,30]. Second, solitons can generally decay into vortices via the so-called snake instability[13,15,31,32]. In the case of weakly interacting BECs in elongated traps, stability requires the chemical potential μ of the condensate to be not much larger than the transverse confinement energy[31]. For a Fermi gas, this would require a quasi-one-dimensional geometry where the transverse cloud width is one inter-particle spacing. As we show below, this is not necessary. Last, for strongly interacting superfluids, it is a priori not obvious that solitons are stable against quantum fluctuations[10,21–25,33].

Here we create and observe long-lived solitons in a strongly interacting fermionic superfluid of ^{6}Li atoms near a Feshbach resonance. Solitons are created via phase imprinting (see Fig. 1b), a technique successfully employed for weakly interacting Bose condensates[11,12,14]. The superfluid containing typically $\sim 2 \times 10^5$ atom pairs is prepared in an elongated trap with cylindrical symmetry (axial and radial trapping period respectively $T_z = 45$–210 ms and $T_\perp = 14$ ms) and tunable aspect ratio $\lambda = T_z/T_\perp$ (ref. 7). A green laser beam far detuned from the atomic resonance is masked to shine on one half of the superfluid. In a time t, the applied potential U, as experienced by a single fermion, advances the phase of the superfluid order parameter in the exposed region by $\Delta\phi = 2Ut/\hbar$ relative to the unexposed region. The time $t \approx 35$ μs is experimentally adjusted in order to create one high-contrast soliton.

In the strongly interacting regime, the soliton does not cause a density depletion within our resolution. However, it is tied to a phase twist in the pair wavefunction. As in the case of vortices[34], the pair wavefunction can be directly observed via a rapid ramp to the BEC side of the Feshbach resonance. The ramp converts large fermion pairs into tightly bound molecules, empties out the soliton cores and increases the soliton width to the final healing length $\propto 1/\sqrt{n_M a_f}$, where a_f is the scattering length at the final magnetic field and n_M the density of molecules. The rapid ramp followed by time-of-flight expansion thus enhances the soliton contrast and acts as a magnifying glass (for details, see Supplementary Information).

Figure 1c and d report the observation of solitons in a fermionic superfluid prepared at 815 G (close to the 832 G Feshbach resonance) for various hold times following the phase imprint. Here, the interaction parameter at the cloud centre is $1/k_F a = 0.30(2)$, where a is the scattering length and $k_F = (3\pi^2 n)^{1/3}$ is the Fermi wavevector, related to the total central fermion density n and the Fermi energy $E_F = \hbar^2 k_F^2/2m$. Figure 1c shows the optical density in absorption images taken after time of flight and the rapid ramp to ~580 G, while Fig. 1d displays residuals obtained by subtracting a smoothed copy of the same absorption image. The optical density contrast of solitons is about 10% (see Supplementary Information). A sequence of radially integrated residuals as a function of time is displayed in Fig. 1e, demonstrating the soliton to be stable for more than 4 s or 100,000 times the microscopic timescale $\hbar/E_F$, the Fermi time. This establishes that solitons in fermionic superfluids can exist as stable and long-lived excitations that do not decay despite strong quantum fluctuations.

Soliton oscillations

The solitons are observed to undergo oscillations in the harmonically trapped superfluid, demonstrating their emergent particle nature. The motion is to a high degree deterministic, as soliton positions for different realizations of the experiment at varying wait times lie on the same classical sinusoidal trajectory. The force on the soliton is provided by the trapping force experienced by the atoms missing in the soliton, $N_s m\omega_z^2 z \equiv M\omega_z^2 z$, where $\omega_z = 2\pi/T_z$, $|N_s|$ is the number of missing atoms, and $M = N_s m < 0$ the bare mass of the soliton. M is negative as the soliton is a density depletion. Introducing the effective, or

inertial mass of the soliton M^*, this force causes an acceleration $\ddot{z} = -\frac{M}{M^*}\omega_z^2 z$. Because we observe oscillations, M^* must be negative as well, implying that the soliton is an effective particle that decreases its kinetic energy as it speeds up. One obtains a direct relation[26] between the relative effective mass M^*/M and the normalized soliton period T_s/T_z:

$$\frac{M^*}{M} = \left(\frac{T_s}{T_z}\right)^2 \quad (2)$$

The observed soliton period of oscillation T_s is about one order of magnitude longer than the trapping period T_z for single atoms. This directly indicates an extreme enhancement of the relative effective mass. In general, the difference between the effective mass M^* and the bare mass M of the soliton arises from the phase slip $\Delta\phi$ across the soliton, which implies a superfluid counterflow[26]. For the soliton to move, an entire sheet of atoms thus has to flow past it. The difference $M - M^*$ is the mass of that sheet, given by the mass density multiplied by the entire soliton volume. In contrast, the soliton's bare mass M is only due to the mass deficit of $|N_s|$ atoms and can become much smaller in magnitude than M^* when the soliton is filled. For weakly interacting BECs, where solitons are devoid of particles, the effective mass is still of the same order of the bare mass, $(M^*/M)_{BEC} = 2$. This leads to an oscillation period that is only $\sqrt{2}$ times longer than T_z (refs 20, 35), as has been observed in experiments[14,17]. In the BCS limit, where only a minute fraction Δ_0/E_F of the gas contributes to Cooper pairing, $|N_s| \propto \Delta_0/E_F \propto \exp[-\pi/(2k_F|a|)]$ and thus the soliton's relative effective mass can be expected to become exponentially large.

Indeed, as shown in Fig. 2, we find that the soliton period, and hence the relative effective mass, increases dramatically as the interactions are tuned from the limit of Bose–Einstein condensation (Fig. 2a) towards the BCS limit. At 700 G, where $1/k_Fa = 2.6(2)$, the system represents a strongly interacting Bose gas of molecules[7]. The soliton period is $T_s = 4.4(5)T_z$, already three times longer than in the case of a weakly interacting BEC. At the Feshbach resonance (Fig. 2d), we measure a soliton period of $T_s = 14(2)T_z$, corresponding to a relative effective mass of $M^*/M = 200(50)$. This is more than 50 times larger than the result of mean-field BdG theory in three dimensions[26,36] that predicts $M^*/M = 3$. Note that the superfluid is fully three-dimensional: on resonance, the chemical potential $\mu \approx 35\hbar\omega_\perp$, where $\omega_\perp$ is the radial trapping frequency. Still, for very elongated traps, one expects to reach a universal quasi-one-dimensional regime where the tight radial confinement is irrelevant for propagation along the long axis[37]. This prompted us to study the dependence of the soliton period on the aspect ratio of our trap.

Figure 3 summarizes our measurements for the soliton period and the relative effective mass as a function of the interaction parameter $1/k_Fa$ throughout the BEC–BCS crossover, for aspect ratios $\lambda = 3.3$, 6.2 and 15. The strong increase of M^*/M towards the BCS regime is observed for all trap geometries. The normalized soliton period T_s/T_z appears to converge to a limiting value for the most elongated trap: the normalized period changes by only 15% as the aspect ratio is increased by more than a factor of two from 6.2 to 15. This indicates that the soliton dynamics approach a universal quasi-one-dimensional limit. Even in a much less elongated trap with $\lambda = 3.3(1)$, the soliton period is only slightly increased by about 30% compared to $\lambda = 6.2$, accompanied by an increased susceptibility of the soliton towards bending or 'snaking'[10,13,15] (for examples, see Supplementary Information).

We attribute the large relative effective mass M^*/M in the strongly interacting regime to the filling of the soliton with uncondensed fermion pairs resulting from strong quantum fluctuations. Similar filling with uncondensed particles has been predicted for solitons in strongly interacting Bose condensates[10,22–25,33]. A substantial filling of the soliton will reduce the number $|N_s|$ of atoms missing inside the soliton, therefore considerably weaken the restoring harmonic force from the trap and strongly increase M^*/M. At the Feshbach resonance, our *in situ* density profiles provide a lower bound on the soliton filling of 90%, compared to the expected 20% from mean-field theory (see Supplementary Information). Mean-field theory for the BEC–BCS crossover heavily underestimates the role of quantum fluctuations already on the BEC side, where it predicts a fraction of uncondensed bosons that scales as na^3 instead of the correct $\sqrt{na^3}$ scaling[7]. Our experiment thus directly reveals the importance of beyond mean-field effects for the dynamics of strongly interacting fermionic superfluids. Significant soliton filling was found theoretically in a strongly interacting relativistic superfluid using methods from string theory[38–40]. For the resonantly interacting Fermi gas, a theoretical study based on a

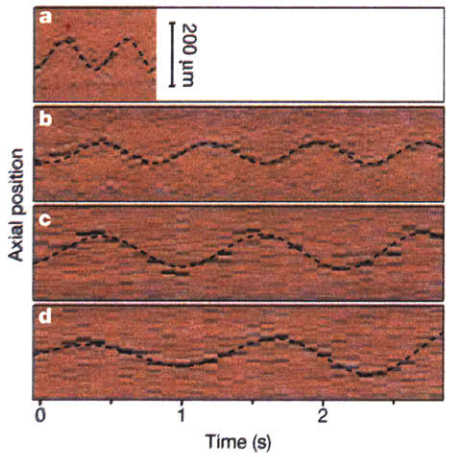

Figure 2 | Soliton oscillations in the BEC–BCS crossover. Shown are soliton oscillations in a trapped fermionic superfluid for various magnetic fields B around the Feshbach resonance. **a–d**, The soliton period is observed to markedly increase as the system is tuned from the BEC regime (**a**) to the Feshbach resonance (**d**). The measured period (T_s/T_z), magnetic field (B in G) and interaction parameter at the cloud centre $1/k_Fa$ were respectively: **a**, 4.4(5), 700, 2.6(2); **b**, 7.5(9), 760, 1.4(1); **c**, 12(2), 815, 0.30(2); **d**, 14(2), 832, 0. The initial atom number per spin state (N_0), its decay rate (τ in s) and Thomas-Fermi radius after time of flight (R_{TF} in μm) range respectively from: 1.1×10^5, 1.2(2), 135 at $B = 700$ G to 2.3×10^5, 12(1) and 200 on resonance. The aspect ratio is $\lambda = 6.2(7)$. Note that at $B = 700$ G, the superfluid is short lived due to enhanced three-body loss. At 760 G (**b**), the soliton survived for more than 6 s, comparable to the lifetime of the superfluid at that field.

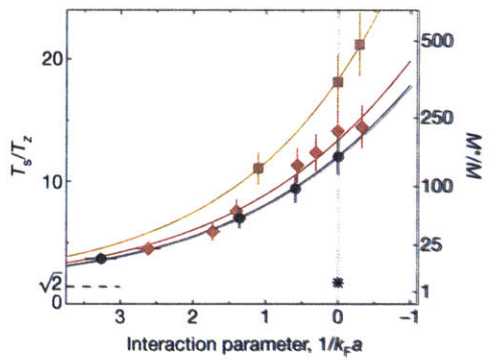

Figure 3 | Soliton period and effective mass versus interaction strength in the BEC–BCS crossover. The normalized soliton period T_s/T_z is shown as a function of the interaction parameter $1/k_Fa$ in the cloud centre, for three different trap aspect ratios: $\lambda = 15(1)$ (black circles), 6.2(7) (red diamonds) and 3.3(1) (orange squares). The error bars correspond to the typical spread over five measurements, and the solid lines are guides to the eye. The soliton period strongly increases from the BEC regime towards the Feshbach resonance (vertical dotted line), where $T_s/T_z = 12(2)$ for $\lambda = 15(1)$, and to the BCS side. This directly reflects an extreme enhancement of the relative effective mass $M^*/M = T_s^2/T_z^2$, which we attribute to strong quantum fluctuations and filling of Andreev bound states. The result for a weakly interacting BEC, $T_s/T_z = \sqrt{2}$, is shown as the dashed line. The star marks the mean-field prediction[26] at unitarity $M^*/M = T_s^2/T_z^2 = 3$.

density functional approach found solitons with clear filling in the wake of shock waves[41]. The strong increase of the soliton period is reminiscent of the situation for dark-bright solitons in weakly interacting BECs, where a distinguishable atomic species or another spin state resides inside the soliton notch[14,42,43]. For fermions, mean-field theory in the strongly interacting regime attributes a substantial part of the soliton filling to Andreev bound states[19,26–28]. These are also predicted to carry the dominant fraction of the superfluid flow across the soliton, which can be regarded, in its rest frame, as a Josephson junction of vanishing barrier height[29]. It will be an interesting topic for future experiments to determine the contribution of Andreev states to the soliton filling.

Temperature dependence

To demonstrate that the slow soliton oscillations are a truly quantum effect and not due to the finite temperature of our gas, we investigated the soliton motion as a function of temperature for the unitary Fermi gas at the Feshbach resonance (Figs 4 and 5). A measure of temperature is provided by the thermal fraction, the number of uncondensed molecules observed after the rapid ramp. The soliton period is found to be insensitive to changes in temperature within the measurement uncertainty (Fig. 5a).

The stability of solitons is, however, strongly affected by thermal effects. At low temperatures, the soliton oscillation occurs essentially without energy loss, demonstrating dissipationless flow (Fig. 4a). For increasing temperature, we observe anti-damping of soliton oscillations (Fig. 4b). This is characteristic of a particle with negative mass that can lower its energy by accelerating. To our knowledge, such anti-damping of solitons has not been directly observed previously in a quantum gas experiment. The energy loss is likely to be due to collisions with thermally induced phonons[10], and we indeed observe a strong decrease in the anti-damping time constant as the temperature is raised (Fig. 5b). At even higher temperatures, the soliton's position becomes less reproducible (Fig. 4c) and its lifetime is strongly reduced (Fig. 5c). Concurrently, we observe increased axial fluctuations in the superfluid (see Fig. 4d–f), some of which appear to have comparable contrast to the imprinted soliton. These additional solitons might be 'thermal solitons', predicted to occur even in equilibrium in weakly interacting Bose condensates[44]. Similar to vortex–anti-vortex pairs in two dimensions, soliton–anti-soliton pairs can be expected to spontaneously break in one dimension and proliferate.

We note that on resonance, the fastest solitons we observe move at the exceedingly slow speed of 0.50 mm s^{-1} or 5% of the (independently measured) speed of sound on resonance. Their sudden disappearance, observed for example in Fig. 4c, can thus not be related to motion close to the Landau critical speed. Instead, their decay might be tied to inelastic collisions with thermal solitons, as soliton collisions have been found to become increasingly inelastic towards the BCS side in theoretical simulations[28]. Another possibility for their decay at such low speeds is that the soliton's energy dispersion has a minimum at an unexpectedly small fraction of the critical velocity[28]. One might expect fermion pairs to break at finite temperatures and fill in the soliton, in addition to quantum fluctuations. However, even for the highest thermal fraction where solitons have been observed, the actual temperature is determined to be below $T = 0.10E_F/k_B$ (k_B is the Boltzmann constant), while the bulk pairing gap is about $\Delta_0 = 0.4E_F$ (ref. 45). Pair breaking should thus still be exponentially suppressed, explaining the insensitivity of the soliton period to the thermal fraction.

Conclusion and outlook

We have created and observed long-lived solitons in a strongly interacting fermionic superfluid. Their period of oscillation and thus their relative effective mass increases markedly as the interactions are tuned from the BEC limit of tightly bound molecules towards the BCS limit of long-range Cooper pairs. This signals strong, beyond mean-field, effects, which are likely to be due to uncondensed fermion pairs filling the soliton, in addition to purely fermionic Andreev bound states. Our study provides an important quantitative benchmark for theories of non-equilibrium dynamics of strongly interacting Fermi gases. An exciting prospect is to directly detect the Andreev bound states spectroscopically[19,46]. Although they are not topologically protected, their lifetime should equal that of the soliton—many seconds or 100,000

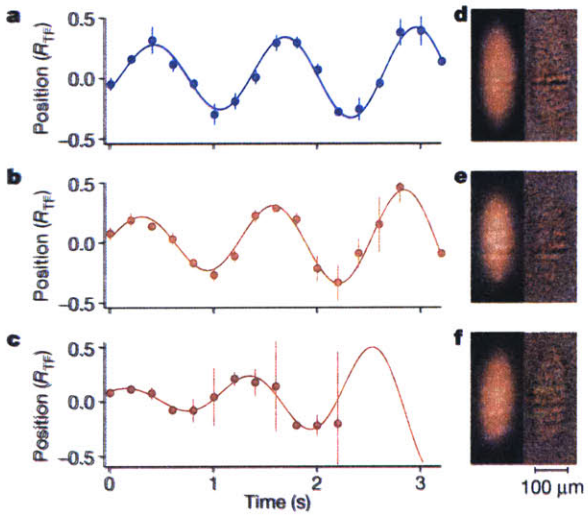

Figure 4 | Soliton motion in the unitary Fermi gas at various temperatures. **a**–**c**, Soliton trajectories for increasing temperature, with thermal fractions **a**, 7(2)%, **b**, 9(2)% and **c**, 15(3)%. The error bars indicate the standard deviation of typically five repetitions and the solid lines are fits to the data to the anti-damped sinusoidal function $f(t) \propto \exp(t/\tau_s)\sin(2\pi t/T_s + \phi)$. Whereas the period is found to be independent of temperature within our uncertainty, the anti-damping time decreases from $\tau_s/T_s = 5(2)$ for the coldest clouds (**a**) to $\tau_s/T_s = 1.3(5)$ for the hottest ones (**c**). **d**–**f**, Representative optical densities (left) and residuals (right) of the superfluid after the rapid ramp. Whereas at low temperatures, the soliton is the only significant density variation, at higher temperatures transverse stripes appear that we tentatively interpret as thermal solitons.

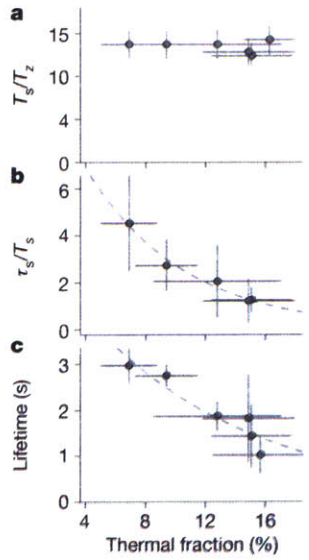

Figure 5 | Effect of finite temperature on soliton motion. **a**, The soliton period is found to be insensitive to temperature. **b**, The 1/*e* anti-damping time and **c**, the soliton lifetime, are found to be strongly dependent on the thermal fraction. The soliton lifetime is defined as the time when the probability of observing a soliton decreased to 50%. The dashed lines are guides to the eye. The horizontal error bars indicate the standard deviation of the thermal fraction within a data set. The vertical error bars in **a** represent the typical spread over five measurements, those in **b** result from the contribution of the fitting error on τ_s and the error on T_s, and those in **c** reflect the time difference between having 90% and 10% survival probability.

Fermi times—so that they might become a useful quantum resource. In the presence of spin imbalance, the soliton represents a limiting case of the long-sought Fulde–Ferrell–Larkin–Ovchinnikov state of moving Cooper pairs[46–49]. Indeed, it is energetically favourable for an excess fermion to reside inside a soliton rather than inside the bulk superfluid. Although it is difficult to realize the Fulde–Ferrell–Larkin–Ovchinnikov state in equilibrium, direct engineering of soliton trains might produce a long-lived metastable analogue.

METHODS SUMMARY

Preparation. The atomic gas is composed of a balanced mixture of the two lowest hyperfine states of ^{6}Li initially prepared at 760 G (ref. 7). The trapping potential results from the combination of a magnetic field curvature providing harmonic confinement in the axial direction and an optical dipole trap (wavelength 1,064 nm) providing tighter radial confinement. The axial periods are $T_z = 210$ ms, 95 ms and 45 ms, respectively, for the three aspect ratios considered here.

Phase imprinting. A step-like intensity profile is imprinted on a laser beam (wavelength 532 nm, power ~200 mW) by means of an opaque mask. A 3-μm-resolution imaging system projects the intensity distribution at the mask location onto the atoms (the beam waist at the atoms is 60 μm). A phase twist of π corresponds to a pulse time of about 30 μs, much shorter than the timescale $\hbar/\mu$ associated with a typical chemical potential, of the order of few 100 μs. The pulse duration is finely adjusted to yield exactly one soliton with high contrast observed after the rapid ramp. Because we imprint only a phase step but not a density depletion, sound waves must be generated in addition to the soliton[11,12]. The sound waves are found to die out in a quarter axial trapping period when they have reached the edge of the atom cloud (see Supplementary Information). For the data above 760 G, the soliton is created at 760 G and the magnetic field is subsequently ramped (in about $2T_z$) to the final magnetic field where the soliton motion is studied. For final magnetic fields below 760 G, the soliton is created at that field. We found that solitons can be created directly at the Feshbach resonance as well.

Thermometry. Thermometry from fits of density profiles at the Feshbach resonance to the known equation of state[50] yielded an upper limit of $T = 0.05E_F/k_B = 10\,\mathrm{nK} \approx 3\hbar\omega_\perp$ for our lowest temperatures, where $\omega_\perp = 2\pi/T_\perp$. At such low temperatures, far below the critical temperature for superfluidity, thermometry via fitting is less sensitive to small changes in temperature[7]. We therefore use the thermal fraction of molecules observed after a rapid ramp to the BEC side of the Feshbach resonance as a robust thermometer[7].

Received 19 February; accepted 28 May 2013.
Published online 17 July 2013.

1. Zurek, W. Cosmological experiments in condensed matter systems. *Phys. Rep.* **276,** 177–221 (1996).
2. Caroli, C., Gennes, P. d. & Matricon, J. Bound fermion states on a vortex line in a type II superconductor. *Phys. Lett.* **9,** 307–309 (1964).
3. Jackiw, R. & Rebbi, C. Solitons with fermion number 1/2. *Phys. Rev. D* **13,** 3398–3409 (1976).
4. Goldstone, J. & Wilczek, F. Fractional quantum numbers on solitons. *Phys. Rev. Lett.* **47,** 986–989 (1981).
5. Heeger, A. J., Kivelson, S., Schrieffer, J. R. & Su, W. P. Solitons in conducting polymers. *Rev. Mod. Phys.* **60,** 781–850 (1988).
6. Monceau, P. Electronic crystals: an experimental overview. *Adv. Phys.* **61,** 325–581 (2012).
7. Ketterle, W. & Zwierlein, M. Making, probing and understanding ultracold Fermi gases. *Riv. Nuovo Cim.* **31,** 247–422 (2008).
8. Giorgini, S., Pitaevskii, L. P. & Stringari, S. Theory of ultracold atomic Fermi gases. *Rev. Mod. Phys.* **80,** 1215–1274 (2008).
9. Zwerger, W. (ed.) *The BCS-BEC Crossover and the Unitary Fermi Gas* (Lecture Notes in Physics Vol. 836, Springer, 2011).
10. Frantzeskakis, D. J. Dark solitons in atomic Bose-Einstein condensates: from theory to experiments. *J. Phys. A* **43,** 213001 (2010).
11. Burger, S., Bongs, K., Dettmer, S., Ertmer, W. & Sengstock, K. Dark solitons in Bose-Einstein condensates. *Phys. Rev. Lett.* **83,** 5198–5201 (1999).
12. Denschlag, J. *et al.* Generating solitons by phase engineering of a Bose-Einstein condensate. *Science* **287,** 97–101 (2000).
13. Anderson, B. P. *et al.* Watching dark solitons decay into vortex rings in a Bose-Einstein condensate. *Phys. Rev. Lett.* **86,** 2926–2929 (2001).
14. Becker, C. *et al.* Oscillations and interactions of dark and dark-bright solitons in Bose-Einstein condensates. *Nature Phys.* **4,** 496–501 (2008).
15. Dutton, Z., Budde, M., Slowe, C. & Hau, L. V. Observation of quantum shock waves created with ultra-compressed slow light pulses in a Bose-Einstein condensate. *Science* **293,** 663–668 (2001).
16. Engels, P. & Atherton, C. Stationary and nonstationary fluid flow of a Bose-Einstein condensate through a penetrable barrier. *Phys. Rev. Lett.* **99,** 160405 (2007).
17. Weller, A. *et al.* Experimental observation of oscillating and interacting matter wave dark solitons. *Phys. Rev. Lett.* **101,** 130401 (2008).
18. Dziarmaga, J. & Sacha, K. Gap soliton in superfluid Fermi gas at zero and finite temperature. *Laser Phys.* **15,** 674–678 (2005).
19. Antezza, M., Dalfovo, F., Pitaevskii, L. P. & Stringari, S. Dark solitons in a superfluid Fermi gas. *Phys. Rev. A* **76,** 043610 (2007).
20. Busch, T. & Anglin, J. R. Motion of dark solitons in trapped Bose-Einstein condensates. *Phys. Rev. Lett.* **84,** 2298–2301 (2000).
21. Dziarmaga, J., Karkuszewski, Z. P. & Sacha, K. Quantum depletion of an excited condensate. *Phys. Rev. A* **66,** 043615 (2002).
22. Dziarmaga, J. & Sacha, K. Depletion of the dark soliton: the anomalous mode of the Bogoliubov theory. *Phys. Rev. A* **66,** 043620 (2002).
23. Law, C. K., Leung, P. T. & Chu, M. C. Quantum fluctuations of coupled dark solitons in a trapped Bose-Einstein condensate. *J. Phys. At. Mol. Opt. Phys.* **35,** 3583–3590 (2002).
24. Martin, A. D. & Ruostekoski, J. Quantum and thermal effects of dark solitons in a one-dimensional Bose gas. *Phys. Rev. Lett.* **104,** 194102 (2010).
25. Mishmash, R. V. & Carr, L. D. Quantum entangled dark solitons formed by ultracold atoms in optical lattices. *Phys. Rev. Lett.* **103,** 140403 (2009).
26. Scott, R. G., Dalfovo, F., Pitaevskii, L. P. & Stringari, S. Dynamics of dark solitons in a trapped superfluid Fermi gas. *Phys. Rev. Lett.* **106,** 185301 (2011).
27. Spuntarelli, A., Carr, L. D., Pieri, P. & Strinati, G. C. Gray solitons in a strongly interacting superfluid Fermi gas. *New J. Phys.* **13,** 035010 (2011).
28. Scott, R. G. *et al.* The decay and collisions of dark solitons in superfluid Fermi gases. *New J. Phys.* **14,** 023044 (2012).
29. Spuntarelli, A., Pieri, P. & Strinati, G. C. Solution of the Bogoliubov–de Gennes equations at zero temperature throughout the BCS-BEC crossover: Josephson and related effects. *Phys. Rep.* **488,** 111–167 (2010).
30. Fedichev, P. O., Muryshev, A. E. & Shlyapnikov, G. V. Dissipative dynamics of a kink state in a Bose-condensed gas. *Phys. Rev. A* **60,** 3220–3224 (1999).
31. Muryshev, A. E., van Linden van den Heuvell, H. B. & Shlyapnikov, G. V. Stability of standing matter waves in a trap. *Phys. Rev. A* **60,** R2665–R2668 (1999).
32. Feder, D. L., Pindzola, M. S., Collins, L. A., Schneider, B. I. & Clark, C. W. Dark-soliton states of Bose-Einstein condensates in anisotropic traps. *Phys. Rev. A* **62,** 053606 (2000).
33. Walczak, P. B. & Anglin, J. R. Back-reaction of perturbation wave packets on gray solitons. *Phys. Rev. A* **86,** 013611 (2012).
34. Zwierlein, M. W., Abo-Shaeer, J. R., Schirotzek, A., Schunck, C. H. & Ketterle, W. Vortices and superfluidity in a strongly interacting Fermi gas. *Nature* **435,** 1047–1051 (2005).
35. Konotop, V. V. & Pitaevskii, L. Landau dynamics of a grey soliton in a trapped condensate. *Phys. Rev. Lett.* **93,** 240403 (2004).
36. Liao, R. & Brand, J. Traveling dark solitons in superfluid Fermi gases. *Phys. Rev. A* **83,** 041604 (2011).
37. Bertaina, G., Pitaevskii, L. & Stringari, S. First and second sound in cylindrically trapped gases. *Phys. Rev. Lett.* **105,** 150402 (2010).
38. Keränen, V., Keski-Vakkuri, E., Nowling, S. & Yogendran, K. P. Dark solitons in holographic superfluids. *Phys. Rev. D* **80,** 121901 (2009).
39. Keränen, V., Keski-Vakkuri, E., Nowling, S. & Yogendran, K. P. Inhomogeneous structures in holographic superfluids. I. Dark solitons. *Phys. Rev. D* **81,** 126011 (2010).
40. Adams, A., Lincoln, D. C., Thomas, S., Peter, S. & John, E. T. Strongly correlated quantum fluids: ultracold quantum gases, quantum chromodynamic plasmas and holographic duality. *New J. Phys.* **14,** 115009 (2012).
41. Bulgac, A., Luo, Y.-L. & Roche, K. J. Quantum shock waves and domain walls in the real-time dynamics of a superfluid unitary Fermi gas. *Phys. Rev. Lett.* **108,** 150401 (2012).
42. Busch, T. & Anglin, J. R. Dark-bright solitons in inhomogeneous Bose-Einstein condensates. *Phys. Rev. Lett.* **87,** 010401 (2001).
43. Middelkamp, S. *et al.* Dynamics of dark-bright solitons in cigar-shaped Bose-Einstein condensates. *Phys. Lett. A* **375,** 642–646 (2011).
44. Karpiuk, T. *et al.* Spontaneous solitons in the thermal equilibrium of a quasi-1d Bose gas. *Phys. Rev. Lett.* **109,** 205302 (2012).
45. Schirotzek, A., Shin, Y., Schunck, C. H. & Ketterle, W. Determination of the superfluid gap in atomic Fermi gases by quasiparticle spectroscopy. *Phys. Rev. Lett.* **101,** 140403 (2008).
46. Lutchyn, R. M., Dzero, M. & Yakovenko, V. M. Spectroscopy of the soliton lattice formation in quasi-one-dimensional fermionic superfluids with population imbalance. *Phys. Rev. A* **84,** 033609 (2011).
47. Yoshida, N. & Yip, S. K. Larkin-Ovchinnikov state in resonant Fermi gas. *Phys. Rev. A* **75,** 063601 (2007).
48. Bulgac, A. & Forbes, M. M. Unitary Fermi supersolid: the Larkin-Ovchinnikov phase. *Phys. Rev. Lett.* **101,** 215301–215304 (2008).
49. Radzihovsky, L. Fluctuations and phase transitions in Larkin-Ovchinnikov liquid-crystal states of a population-imbalanced resonant Fermi gas. *Phys. Rev. A* **84,** 023611 (2011).
50. Ku, M. J. H., Sommer, A. T., Cheuk, L. W. & Zwierlein, M. W. Revealing the superfluid lambda transition in the universal thermodynamics of a unitary Fermi gas. *Science* **335,** 563–567 (2012).

Supplementary Information is available in the online version of the paper.

Acknowledgements We thank L. Pitaevskii, S. Stringari, F. Dalfovo, W. Zwerger and D. Huse for discussions. This work was supported by the NSF, the ARO MURI on Atomtronics, AFOSR PECASE, ONR, a grant from the Army Research Office with funding from the DARPA OLE programme, and the David and Lucile Packard Foundation.

Author Contributions T.Y. and A.T.S. contributed equally to the experimental work. All authors contributed extensively to the work presented in this paper.

Author Information Reprints and permissions information is available at www.nature.com/reprints. The authors declare no competing financial interests. Readers are welcome to comment on the online version of the paper. Correspondence and requests for materials should be addressed to M.W.Z. (zwierlein@mit.edu).

Appendix H

Motion of a Solitonic Vortex in the BEC-BCS Crossover

This appendix contains a reprint of Ref. [127]: Mark J.-H. Ku, Wenjie Ji, Biswaroop Mukherjee, Elmer Guardado Sanchez, Lawrence T. Cheuk, Tarik Yefsah, and Martin W. Zwierlein, *Motion of a Solitonic Vortex in the BEC-BCS Crossover*, Phys. Rev. Lett., **113**, 065301, (2014).

Motion of a Solitonic Vortex in the BEC-BCS Crossover

Mark J. H. Ku, Wenjie Ji, Biswaroop Mukherjee, Elmer Guardado-Sanchez, Lawrence W. Cheuk, Tarik Yefsah, and Martin W. Zwierlein
MIT-Harvard Center for Ultracold Atoms, Research Laboratory of Electronics, and Department of Physics, Massachusetts Institute of Technology, Cambridge, Massachusetts 02139, USA
(Received 27 February 2014; published 4 August 2014)

We observe a long-lived solitary wave in a superfluid Fermi gas of ^{6}Li atoms after phase imprinting. Tomographic imaging reveals the excitation to be a solitonic vortex, oriented transverse to the long axis of the cigar-shaped atom cloud. The precessional motion of the vortex is directly observed, and its period is measured as a function of the chemical potential in the BEC-BCS crossover. The long period and the correspondingly large ratio of the inertial to the bare mass of the vortex are in good agreement with estimates based on superfluid hydrodynamics that we derive here using the known equation of state in the BEC-BCS crossover.

DOI: 10.1103/PhysRevLett.113.065301 PACS numbers: 67.85.-d, 03.75.Kk, 03.75.Lm, 03.75.Ss

Solitary waves that do not spread as they propagate are ubiquitous in nonlinear systems, from classical fluids and fiber optics to superfluids and superconductors. These waves are localized objects with defined energy and mass, and as such they can be described as an effective single particle emerging from a many-body environment. This distinguishes them from larger-scale collective excitations such as shape oscillations of a superfluid, or from perturbative linear excitations such as phonons. Paradigmatic examples of solitary waves in superfluids are planar solitons that separate regions of differing phase, as well as vortex rings or single vortex lines [see Fig. 1(a)]. The direct creation of such localized and highly nonlinear objects "on demand" in ultracold quantum gases allows for an excellent dynamical probe of novel superfluids, such as strongly interacting Fermi gases [1] or spin-orbit coupled Bose-Einstein condensates [2,3].

In a recent experiment on fermionic superfluids at MIT [1], long-lived solitary waves were produced that featured a large ratio of inertial to bare (missing) mass of over 200, evidenced by an oscillation period over 15 times longer than the period for a single atom. The observed absorption images suggested the interpretation of the waves as planar solitons, but the longevity as well as the large effective mass ratio were unexpected for this type of defect [4–7]. Indeed, the nodal plane of a soliton is energetically more costly than the nodal line of a vortex, and planar solitons can decay into lower energy excitations via the snake instability, the undulation of the soliton plane [4]. Several recent works therefore suggested that these solitary waves are vortex rings [8–10]. For weakly interacting Bose-Einstein condensates, solitons have been created [11,12] and observed to decay into vortex rings [13,14]. The latter further decay into a vortex-antivortex pair that eventually breaks up, leaving behind a single remnant vortex [15–17]. The exact process was recently elucidated in a discussion of apparent soliton oscillations observed in weakly interacting BECs [18,19]. In the case of strongly interacting fermionic superfluids, the understanding of such nontrivial dynamics presents a challenging nonequilibrium many-body problem [8,20].

In this Letter, we investigate the nature of the long-lived solitary wave observed in Ref. [1] via tomographic imaging and identify the wave to be a solitonic vortex [15–17]. The term describes a vortex placed in an elongated geometry, such as the cigar-shaped superfluid of the present experiment, where the transverse Thomas-Fermi cloud radius $R_\perp$ is much smaller than the axial radius R_z. In this case, a vortex deforms the superfluid phase only in a restricted region of axial extent $\sim R_\perp$. The vortex together with the surrounding flow field thus constitutes an effective particle localized to within $R_\perp \ll R_z$. Its far-field phase profile resembles that of a dark soliton. In particular, the phase difference across a stationary solitonic vortex in the axial direction is π, the same as for a stationary dark soliton. A vortex moving in the axial direction at a critical speed converts into a gray, moving soliton [17]. In the tightly confining limit where $R_\perp$ approaches ξ, the vortex core size, a stationary solitonic vortex becomes energetically degenerate with a dark soliton [16,17]. In the limit of an isotropic system where $R_\perp \sim R_z$, one recovers a conventional vortex. A solitonic vortex thus represents the link between the topologically protected excitations in one and three dimensions. The precessional motion of the vortex, projected onto the long axis of the cigar-shaped atom cloud, appears as the oscillation of a particle of inertial mass M^* and bare mass M. As we show below, the bare mass scales as the missing mass inside the vortex core, $M \propto mn\xi^2 R_\perp \mathcal{L}$, while the inertial mass $M^* \propto mnR_\perp^3/\mathcal{L}$ is proportional to the volume $R_\perp^3$ in which flow is perturbed by the vortex. Here, n is the gas density and $\mathcal{L} = \ln(R_\perp/\xi)$ is a logarithmic correction that is on the order of 3 to 5 in our

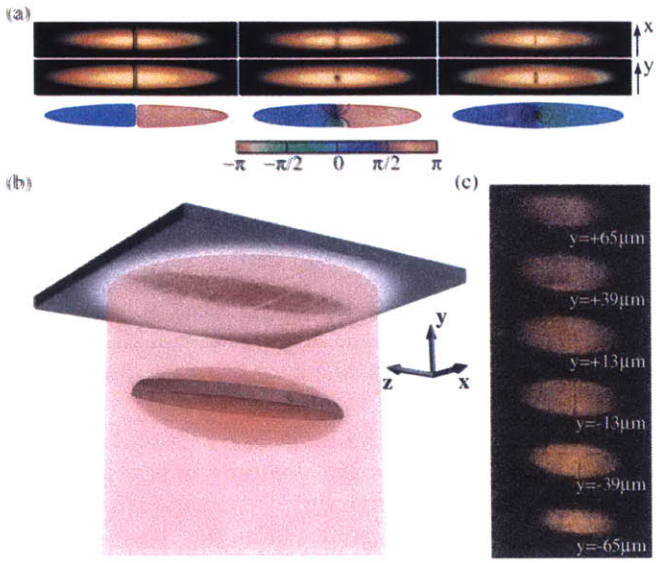

FIG. 1 (color online). (a) Examples of solitary waves in 3D Bose-Einstein condensates. Shown are simulated column density profiles in the (z-x) plane (upper row), the local density of the cloud in a central layer in the (z-y) plane (middle row), and the phase (lower row) for a soliton (left), a solitonic vortex (center), and a vortex ring (right). The images correspond to $\mu/\hbar\omega_\perp = 7.31$, 7.14, and 10.66. (b) Schematic of the experimental tomographic imaging technique. A partially masked optical pumping beam propagating along z (not shown) selects a 23 μm thick slice within the expanded atom cloud for absorption imaging along the vertical y direction. (c) Tomography of a unitary fermionic superfluid of ^{6}Li atoms containing a solitary wave. Shown are density distributions of horizontal slices selected at different y positions. Tomography reveals a single solitonic vortex.

experiment. Thus, $M^*/M \propto R_\perp^2/\xi^2/\mathcal{L}^2$, which can easily approach 200 for our experimental parameters, thus explaining the experimental findings in Ref. [1].

We create fermionic superfluids using a balanced mixture of the two lowest hyperfine states of ^{6}Li, $|1\rangle$ and $|2\rangle$. A Feshbach resonance allows us to tune the interparticle interactions from the limit of Bose-Einstein condensation of tightly bound molecules towards the regime of BCS superfluidity [1,21]. The atom cloud contains $1\text{–}10 \times 10^5$ atoms per spin state and is cigar shaped due to a tight radial confinement from an optical dipole trapping beam propagating along the (horizontal) z direction, in combination with a weaker, harmonic confinement along z provided by a magnetic field curvature. The radial and axial trapping frequencies are varied in the range of $\omega_\perp/2\pi \approx$ 55–75 Hz and $\omega_z/2\pi = 5\text{–}23$ Hz. Gravity slightly weakens the trapping potential along the vertical y direction, causing a residual anharmonicity and an anisotropy $\omega_y/\omega_x - 1 \approx -5\%$.

The solitary wave is created as in Refs. [1,11,12,18] via phase imprinting, whereby one half of the superfluid is exposed to a blue-detuned laser beam for a duration that causes a phase shift of the order parameter close to π. To observe the magnitude of the superfluid wave function, we employ a rapid ramp to the BEC side of the Feshbach resonance during time of flight [1,21,22]. In addition to emptying out defects such as vortex cores [22], the ramp effectively increases the healing length ξ of the superfluid to observable values (typically $\sim$20 μm). The observed width of the defect after the rapid ramp and time of flight thus does not reflect the in-trap width, which is expected to be on the order of one interparticle spacing $\sim$1 μm [23]. Absorption images are taken along the vertical direction [see Fig. 1(b)].

In order to lift the ambiguity on the nature of the observed excitation, we employ a tomographic technique whereby only a chosen slice of the full atom cloud is imaged after time of flight [see Fig. 1(b)]. This method gives direct access to the local density of the 3D cloud. Tomography is achieved by optically pumping within 10 μs all atoms outside the desired slice into hyperfine states that are off resonant with the imaging transition for state $|1\rangle$, predominantly state $|6\rangle$. The slice is selected by masking part of the optical pumping light with a thin wire, and projecting the wire's shadow onto the atom cloud. The slice thickness is measured to be 23(1) μm ($= 2\sigma$ of a Gaussian fit), comparable to the width of the observed solitary wave after time of flight, and about one sixth of the transverse cloud diameter after expansion. Since the imaging procedure is destructive, each run of the experiment provides a single slice at a given time of the defect's motion. Thanks to the high degree of stability of our experiment, reliable tomography can be built up from many repetitions of the experiment.

Representative tomographic images for the unitary fermionic superfluid are shown in Fig. 1(c), taken 1.6 s after the phase imprint. A line of depletion with about 40% contrast cuts across the entire cloud in one particular slice. This immediately demonstrates that the solitary wave is not a vortex ring. On average, only a specific one of the six slices imaged features the depletion. The strong depletion is thus not a planar soliton, as we interpreted in our previous paper [1] . Instead, our observation is consistent with a single, solitonic vortex. For the present experimental conditions we observe the vortex to be horizontal in every single repetition of the experiment. Due to the slight anisotropy of the trap, the vortex can minimize its energy by aligning along the short axis, while orientation along the longer, intermediate axis is unstable [19,24,25]. Slight tilts of the vortex into the vertical direction cause partial vortex lines to be detected in a given slice, as seen for slice position $y = -39$ μm in Fig. 1(c).

In a fully 3D setting where the radial cloud size $R_\perp$ is much larger than the vortex core size ξ, an off-center transverse vortex will undergo precessional motion along equipotential lines [26,27]. Tomographic imaging enables a measurement of the vortex position in the z-y plane [see

Figs. 1(b) and 1(c)]. The vortex's z coordinate is readily obtained from the images. The y coordinate is given by the position of the slice that contains the vortex (e.g., in Fig. 1(c), the vortex is observed at $y = -13$ μm). In order to refine the determination of the y position of the vortex, a histogram of occurrence as a function of the slice position is built up from several (~7 runs per slice position) repetitions of the experiment, and for each time of the vortex's motion. Representative images and density profiles of slices containing the vortex are shown in Fig. 2, along with histograms of the occurrence of vortex observations in each slice. The z-y coordinates of the vortex lie on an ellipse with the same aspect ratio (after expansion) as the atom cloud, as expected for vortex precession along equipotential lines.

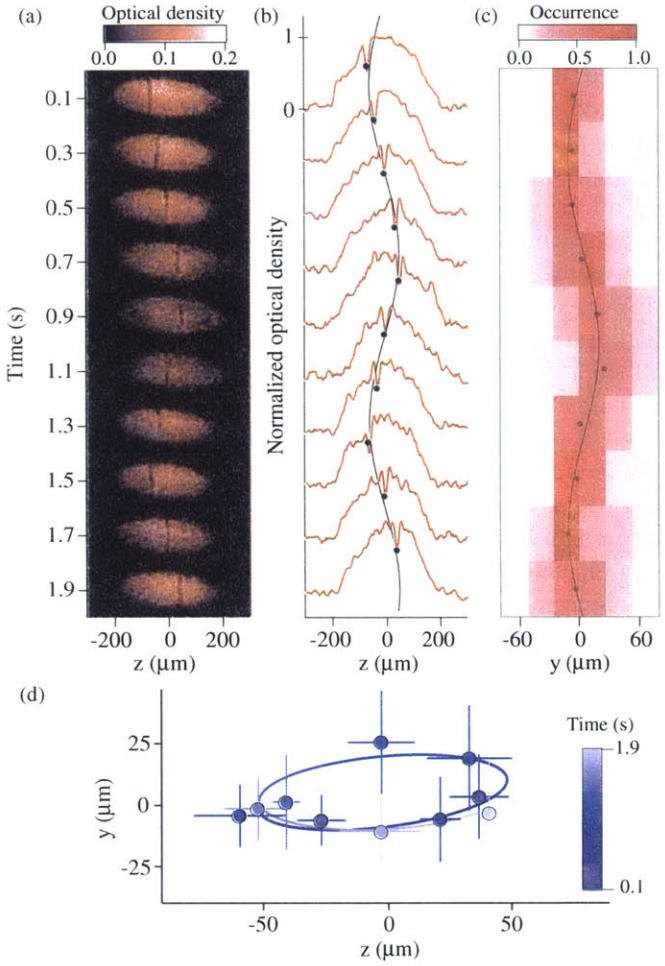

FIG. 2 (color online). Observation of vortex precession in a unitary fermionic superfluid via tomographic imaging. (a) Representative horizontal slices showing the oscillation of the vortex along the z axis. Time $t = 0$ s marks 600 ms after the phase imprint. The y position of each slice can be inferred from (c). (b) Density profiles normalized by the peak density, showing a depletion of typically 30% contrast. The solid line is a sine fit to the vortex positions (black dots). (c) Average occurrence of the vortex at a given y position of the slice as function of time, showing the vortex oscillation along the y axis. Red dots: average y position of the vortex from Gaussian fit at the given time. Solid red line: sine fit. (d) Reconstructed precessional motion in the z-y plane.

The period of the vortex motion can be estimated from superfluid hydrodynamics and the equation of state in the BEC-BCS crossover [28]. Our Hamiltonian approach is analogous to that used to describe the motion of vortex rings in Ref. [29]. We take the vortex to be aligned in the transverse x direction, and located at $\vec{r}_0 = (y_0, z_0)$ in the y-z plane. The free energy E_V of the vortex is dominated by the kinetic energy of its flow field $\vec{v} = \hbar\nabla\phi/m_B$, where $\phi = \arctan((y - y_0)/(z - z_0))$ is the phase profile near the vortex, and $m_B = 2m$ the boson mass. One finds $E_V \approx \int \frac{1}{2} mnv^2 \mathrm{d}^3 r = (\pi\hbar^2 m/m_B^2) n_{2D}(y_0, z_0) \ln(R_\perp/\xi)$ to logarithmic accuracy, i.e., in the limit $\ln(R_\perp/\xi) \gg 1$. Here, n is the gas density, n_{2D} is the column density along the vortex line, $R_\perp$ is the transverse Thomas-Fermi radius, much smaller than the axial radius R_z, and ξ is the characteristic size of the vortex core. In the crossover we may take $\xi = \frac{1}{\sqrt{2}}\hbar/m_B c$, with c the speed of sound, a definition that recovers the healing length in the BEC regime. At unitarity, this yields $\xi \approx 1/k_F$ where $k_F = (3\pi^2 n)^{1/3}$ is the Fermi wave vector, a reasonable estimate [23], especially within logarithmic accuracy.

The canonical momentum of the vortex along the axial z direction is given by $P_z = \int mnv_z \mathrm{d}^3 r = (m/m_B) \int \hbar n \partial_z \phi \, \mathrm{d}^3 r$. Since $R_\perp \ll R_z$, the phase gradient is concentrated in the neighborhood of the vortex in a range of size $\sim R_\perp$ along the z direction, allowing us to set $n(x, y, z) \approx n(x, y, z_0)$. The integral of $\partial_z \phi$ over the z direction thus simply equals π or $-\pi$, depending on whether the path runs along $y < y_0$ or $y > y_0$. One thus has $P_z \simeq (m/m_B)\hbar\pi(\int_{-R_\perp}^{y_0} \mathrm{d}y - \int_{y_0}^{R_\perp} \mathrm{d}y) n_{2D}(y, z_0) = (m/m_B)\hbar\pi \int_{-y_0}^{y_0} \mathrm{d}y n_{2D}(y, z_0)$. Assuming harmonic trapping and the local density approximation, we deduce the axial velocity of the vortex from Hamilton's equation

$$\dot{z}_0 = \frac{\partial E_V}{\partial P_z} = \frac{\partial E_V/\partial y_0}{\partial P_z/\partial y_0} = -\frac{\omega_\perp}{\omega_z}\Omega y_0,$$

and similarly $\dot{y}_0 = (\omega_z/\omega_\perp)\Omega z_0$, with the angular frequency

$$\frac{\Omega}{\omega_z} = \frac{2\gamma + 1}{8}\frac{\hbar\omega_\perp}{\mu}\ln\left(\frac{R_\perp}{\xi}\right).$$

Here, $\gamma \equiv (\mu/n)(\partial n/\partial\mu)$ is a polytropic index determined by the equation of state, and μ is evaluated at the vortex position. $\gamma = 1$ in the BEC regime, while $\gamma = 3/2$ at unitarity and in the BCS regime. The equations describe the precessional motion of the vortex with angular frequency Ω along an equipotential line of the trap with $\mu = \text{const}$, i.e., $y_0^2/R_\perp^2 + z_0^2/R_z^2 = \text{const}$. The result is identical to what one finds by equating the Magnus force [30] $hn_{2D}\hat{x} \times \dot{\vec{r}}_0$ to the force $-\nabla E_V$ acting on the vortex, and it generalizes the known result for vortex motion in

trapped, weakly interacting Bose-Einstein condensates [26,27] to superfluids with arbitrary equation of state. We find the inertial mass of the vortex [5]

$$M^* = \frac{\partial P_z}{\partial \dot{z}_0} = \frac{\partial P_z/\partial y_0}{\partial \dot{z}_0/\partial y_0} = -\frac{4\pi}{2\gamma+1}\frac{n_{2D}R_\perp^2}{\ln(R_\perp/\xi)}m,$$

which is proportional to the total mass of atoms contained in the volume $R_\perp^3$, while the bare mass

$$M = -\frac{\partial E_V}{\partial \mu}m = -\pi\frac{2\gamma+1}{4\gamma}n_{2D}\xi^2\ln\left(\frac{R_\perp}{\xi}\right)m$$

is only proportional to the mass of "missing" atoms contained in the vortex core. Here we have used $\mu = \gamma mc^2 = \gamma\hbar^2/2m\xi^2$. The ratio $M^*/M \propto R_\perp^2/\xi^2/[\ln(R_\perp/\xi)]^2$ thus depends on the transverse size of the system and can become large. In contrast, the bare and inertial mass of a planar soliton are both on the order of the mass of "missing" atoms in the soliton plane, $\propto n\xi R_\perp^2$, and their ratio is bound to be on the order of unity in the crossover regime close to resonance. Using the experimental parameters of $\mu/\hbar\omega_\perp \approx 25$–$35$ [1], the hydrodynamical model yields a normalized vortex period $T_V/T_z \approx 11$–15 and effective mass ratio $M^*/M = 130$–220, in close agreement with the measured values.

We have taken extensive data for the vortex period in the BEC-BCS crossover exploring a wide range of chemical potentials. Figure 3 shows the normalized period T_V/T_z versus $\mu/\hbar\omega_\perp$ including data for several aspect ratios, interaction strengths, and atom numbers. Chemical potentials were extracted from the measured axial Thomas-Fermi radius of the cloud and the known axial trapping frequency. The inset in Fig. 3 shows the data from Ref. [1] along with the theoretical prediction for a fixed, characteristic atom number of $N/2 = 3\times10^5$ per spin state, using the known equation of state in the BEC-BCS crossover [28]. The data are in good agreement with the approximate theory, from the BEC regime towards resonance and into the BCS regime. Corrections beyond logarithmic accuracy could be important as $\ln(R_\perp/\xi)$ is only 3–5, but they are not known in the crossover beyond the weakly interacting BEC regime, and are the subject of debate [31]. Generally, there will be a contribution to the vortex's inertial mass from superfluid backflow, the Baym-Chandler mass [32]. For a strongly interacting Bose gas, quantum depletion localized inside vortex cores will modify the inertial and bare mass [33,34]. In the BCS regime, one expects a contribution due to fermions trapped in Andreev bound states inside the vortex core [35], the Kopnin mass [36]. For a molecular BEC, the prediction from the Gross-Pitaevskii equation is [26,27] $\frac{\Omega}{\omega_z} = \frac{3}{8}(\hbar\omega_\perp/\mu)[\ln(R_\perp/\xi)+\frac{3}{4}]$ and is shown in Fig. 3 to agree well with the data.

An interesting future investigation concerns the early times a few milliseconds after the phase imprinting. Is the single observed vortex a result of multiple decay processes, in which an initial planar soliton decays into a vortex ring, that further decays into vortex-antivortex pairs, followed by a "sling-shot" event [19] by which one of the vortices is ejected? Or does the phase imprint rather directly create vortices of a given circulation? For example, solitons that are slightly tilted with respect to the transverse direction can efficiently convert into solitonic vortices of one type of charge, removing the required angular momentum from a collective mode of the gas cloud [37].

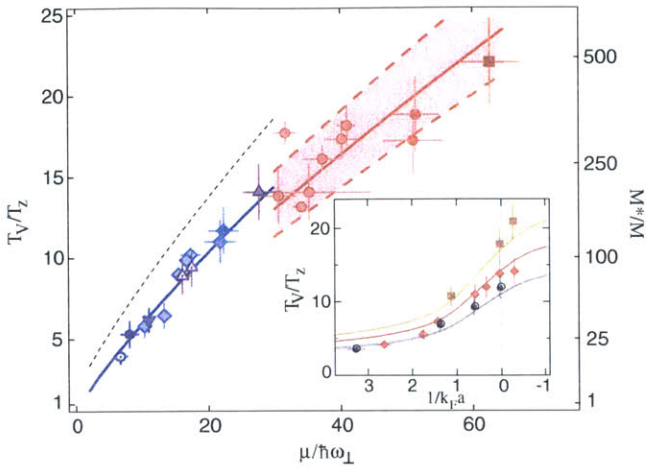

FIG. 3 (color online). Normalized period of the solitonic vortex T_V/T_z, as a function of the normalized chemical potential $\mu/\hbar\omega_\perp$. Experimental data are for magnetic fields B = 850 G (BCS side, square) and 832 G (unitarity, circle), and for the BEC side at 800 G (triangle), 760 G (diamond), 740 G (inverted triangle), and 700 G (hexagon). $\omega_z/2\pi$ was 23 Hz (solid symbols), 10 Hz (framed), 5 Hz (dotted). Predictions in the BEC regime: solid blue line from Ref. [26], dashed black line from Ref. [27]. Red solid curve: hydrodynamic prediction on resonance, assuming $\xi = 1/k_F$. The error band is bounded by the choice $\xi = 1/2k_F$ (lower bound) and $\xi = 2/k_F$ (upper bound). Inset: T_V/T_z as a function of the interaction parameter $1/k_Fa$, data from Ref. [1]. Square, diamond, and circle are for $\omega_z/2\pi = 23$, 10, and 5 Hz, respectively. Atom numbers range from $N/2 = 1\times10^5$ per spin state in the BEC regime to 3×10^5 around resonance. Solid curves: hydrodynamic prediction fixing $N/2 = 3\times10^5$, and $\omega_z/2\pi = 23$ Hz (gold), 10 Hz (red), and 5 Hz (black).

In conclusion, we have implemented a tomographic imaging technique that allowed us to conclusively demonstrate that a long-lived solitary wave observed in our fermionic superfluid is a solitonic vortex. The vortex is topologically protected, explaining the long lifetime of the wave, and its theoretical inertial to bare mass ratio agrees with that found experimentally. Solitonic vortices can be expected to occur as persistent defects created via a Kibble-Zurek mechanism [38,39], via phase imprinting [18,19] or even via thermal excitations, as hinted at by the observation of thermally induced defects in Ref. [1]. They also correspond to the "N"-shaped vortices created via rotation

in Ref. [40], in the limit of zero rotation frequency (called "*S*" shaped in Ref. [41]). Further studies on this topological excitation created "on demand" concern the interaction of multiple solitonic vortices in fermionic superfluids, a measurement of the current-phase relation of solitonic vortices [17], their contribution to flow resistance of the superfluid [42], and the observation of Andreev states bound to vortex cores [35].

We would like to thank David Huse, Lev Pitaevskii, and Joachim Brand for fruitful discussions. This work was supported by the NSF, the ARO MURI on Atomtronics, AFOSR PECASE, ONR, a grant from the Army Research Office with funding from the DARPA OLE program and the David and Lucile Packard Foundation.

Note added.—Recently, two related manuscripts [43,44] have been posted online.

[1] T. Yefsah, A. T. Sommer, M. J. H. Ku, L. W. Cheuk, W. Ji, W. S. Bakr, and M. W. Zwierlein, Nature (London) **499**, 426 (2013).
[2] Y-J. Lin, K. Jiménez-García, and I. B. Spielman, Nature (London) **471**, 83 (2011).
[3] A. L. Fetter, Phys. Rev. A **89**, 023629 (2014).
[4] A. E. Muryshev, H. B. van Linden van den Heuvell, and G. V. Shlyapnikov, Phys. Rev. A **60**, R2665 (1999).
[5] R. G. Scott, F. Dalfovo, L. P. Pitaevskii, and S. Stringari, Phys. Rev. Lett. **106**, 185301 (2011).
[6] R. Liao and J. Brand, Phys. Rev. A **83**, 041604 (2011).
[7] A. Cetoli, J. Brand, R. G. Scott, F. Dalfovo, and L. P. Pitaevskii, Phys. Rev. A **88**, 043639 (2013).
[8] A. Bulgac, M. M. Forbes, M. M. Kelley, K. J. Roche, and G. Wlazłowski , Phys. Rev. Lett. **112**, 025301 (2014).
[9] M. D. Reichl and E. J. Mueller, Phys. Rev. A **88**, 053626 (2013).
[10] W. Wen, C. Zhao, and X. Ma, Phys. Rev. A **88**, 063621 (2013).
[11] S. Burger, K. Bongs, S. Dettmer, W. Ertmer, K. Sengstock, A. Sanpera, G. V. Shlyapnikov, and M. Lewenstein, Phys. Rev. Lett. **83**, 5198 (1999).
[12] J. Denschlag, J. E. Simsarian, D. L. Feder, C. W. Clark, L. A. Collins, J. Cubizolles, L. Deng, E. W. Hagley, K. Helmerson, W. P. Reinhardt, S. L. Rolston, B. I. Schneider, and W. D. Phillips, Science **287**, 97 (2000).
[13] B. P. Anderson, P. C. Haljan, C. A. Regal, D. L. Feder, L. A. Collins, C. W. Clark, and E. A. Cornell, Phys. Rev. Lett. **86**, 2926 (2001).
[14] Z. Dutton, M. Budde, C. Slowe, and L. V. Hau, Science **293**, 663 (2001).
[15] J. Brand and W. P. Reinhardt, J. Phys. B **34**, L113 (2001).
[16] J. Brand and W. P. Reinhardt, Phys. Rev. A **65**, 043612 (2002).
[17] S. Komineas and N. Papanicolaou, Phys. Rev. A **68**, 043617 (2003).
[18] C. Becker, S. Stellmer, P. Soltan-Panahi, S. Dörscher, M. Baumert, E. M. Richter, J. Kronjäger, K. Bongs, and K. Sengstock, Nat. Phys. **4**, 496 (2008).
[19] C. Becker, K. Sengstock, P. Schmelcher, P. G. Kevrekidis, and R. Carretero-Gonzalez, New J. Phys. **15**, 113028 (2013).
[20] P. Scherpelz, K. Padavić, A. Rançon, A. Glatz, I. S. Aranson, and K. Levin, arXiv:1401.8267.
[21] W. Ketterle and M. Zwierlein, Riv. Nuovo Cimento Soc. Ital. Fis. **31**, 247 (2008).
[22] M. W. Zwierlein, J. R. Abo-Shaeer, A. Schirotzek, C. H. Schunck, and W. Ketterle, Nature (London) **435**, 1047 (2005).
[23] A. Bulgac and Y. Yu, Phys. Rev. Lett. **91**, 190404 (2003).
[24] A. A. Svidzinsky and A. L. Fetter, Phys. Rev. A **62**, 063617 (2000).
[25] Following submission of the present work, this question was investigated numerically in Ref. [43], where the slight anharmonicity was shown to also play an important role in stabilizing the vortex orientation.
[26] E. Lundh and P. Ao, Phys. Rev. A **61**, 063612 (2000).
[27] A. L. Fetter and J.-k. Kim, J. Low Temp. Phys. **125**, 239 (2001).
[28] N. Navon, S. Nascimbene, F. Chevy, and C. Salomon, Science **328**, 729 (2010).
[29] L. P. Pitaevskii, arXiv:1311.4693.
[30] P. Ao and D. J. Thouless, Phys. Rev. Lett. **70**, 2158 (1993).
[31] E. B. Sonin, Phys. Rev. B **87**, 134515 (2013).
[32] G. Baym and E. Chandler, J. Low Temp. Phys. **50**, 57 (1983).
[33] A. L. Fetter, Phys. Rev. Lett. **27**, 986 (1971).
[34] A. L. Fetter, Ann. Phys. (N.Y.) **70**, 67 (1972).
[35] C. Caroli, P. G. De Gennes, and J. Matricon, Phys. Lett. **9**, 307 (1964).
[36] N. B. Kopnin, JETP Lett. **27**, 390 (1978);
[37] N. Parker, Numerical Studies of Vortices and Dark Solitons in Atomic Bose-Einstein Condensates, Ph.D. thesis, University of Durham, 2004.
[38] C. N. Weiler, T. W. Neely, D. R. Scherer, A. S. Bradley, M. J. Davis, and B. P. Anderson, Nature (London) **455**, 948 (2008).
[39] G. Lamporesi, S. Donadello, S. Serafini, F. Dalfovo, and G. Ferrari, Nat. Phys. **9**, 656 (2013).
[40] P. Rosenbusch, V. Bretin, and J. Dalibard, Phys. Rev. Lett. **89**, 200403 (2002).
[41] S. Komineas, N. R. Cooper, and N. Papanicolaou, Phys. Rev. A **72**, 053624 (2005).
[42] B. I. Halperin, G. Refael, and E. Demler, Int. J. Mod. Phys. B **24**, 4039 (2010).
[43] G. Wlazłowski , A. Bulgac, M. M. Forbes, and K. J. Roche, arXiv:1404.1038.
[44] S. Donadello, S. Serafini, M. Tylutki, L. P. Pitaevskii, F. Dalfovo, G. Lamporesi, and G. Ferrari, Phys. Rev. Lett. **113**, 065302 (2014).

Bibliography

[1] J.R. Abo-Shaeer, C. Raman, J.M. Vogels, and W. Ketterle. Observation of vortex lattices in Bose-Einstein condensates. *Science*, 292:476–479, 2001.

[2] M. Aidelsburger, M. Atala, M. Lohse, J. T. Barreiro, B. Paredes, and I. Bloch. Realization of the Hofstadter Hamiltonian with ultracold atoms in optical lattices. *Phys. Rev. Lett.*, 111:185301, 2013.

[3] M. Aidelsburger, M. Atala, S. NascimbÃĺne, S. Trotzky, Y. A. Chen, and I. Bloch. Experimental realization of strong effective magnetic fields in an optical lattice. *Phys. Rev. Lett.*, 107:255301, 2011.

[4] B. P. Anderson, P. C. Haljan, C. A. Regal, D. L. Feder, L. A. Collins, C. W. Clark, and E. A. Cornell. Watching dark solitons decay into vortex rings in a Bose-Einstein condensate. *Phys. Rev. Lett.*, 86:2926–2929, 2001.

[5] M. H. Anderson, J. R. Ensher, M. R. Matthews, C. E. Wieman, and E. A. Cornell. Observation of Bose-Einstein condensation in a dilute atomic vapor. *Science*, 269:198–201, 1995.

[6] A. F. Andreev. The thermal conductivity of the intermediate state in superconductors. *Sov. Phys. JETP, 19, 1228 (1964)*, 46:1823, 1964.

[7] M. Antezza, F. Dalfovo, L.P. Pitaevskii, and S. Stringari. Dark solitons in a superfluid Fermi gas. *Phys. Rev. A*, 76:043610, 2007.

[8] P. Ao and D.J. Thouless. Berry's phase and the Magnus force for a vortex line in a superconductor. *Phys. Rev. Lett.*, 70:2158–2161, 1993.

[9] P. Arnold, J. E. Drut, and D. T. Son. Next-to-next-to-leading-order ϵ expansion for a Fermi gas at infinite scattering length. *Phys. Rev. A*, 75:043605, 2007.

[10] G. E. Astrakharchik, J. Boronat, J. Casulleras, and S. Giorgini. Equation of state of a Fermi gas in the BEC-BCS crossover: A Quantum Monte-Carlo study. *Phys. Rev. Lett.*, 93:200404, 2004.

[11] G. A. Baker. Neutron matter model. *Phys. Rev. C*, 60:054311, 1999.

[12] W. S. Bakr, J. I. Gillen, A. Peng, S. Folling, and M. Greiner. A quantum gas microscope for detecting single atoms in a Hubbard-regime optical lattice. *Nature*, 462:74–77, 2009.

[13] J. Bar-Sagi and C. G. Kuper. Self-consistent pair potential in an inhomogeneous superconductor. *Phys. Rev. Lett.*, 28:1556–1559, 1972.

[14] J. Bardeen, L. N. Cooper, and J. R. Schrieffer. Theory of superconductivity. *Phys. Rev.*, 108:1175, 1957.

[15] J. T. Barreiro, M. Müller, P. Schindler, D. Nigg, T. Monz, M. Chwalla, M. Hennrich, C. F. Roos, P. Zoller, and R. Blatt. An open-system quantum simulator with trapped ions. *Nature*, 470:486–491, 2011.

[16] M. Bartenstein, A. Altmeyer, S. Riedl, R. Geursen, S. Jochim, C. Chin, J. Hecker-Denschlag, R. Grimm, A. Simoni, E. Tiesinga, C. J. Williams, and P. S. Julienne. Precise determination of ^{6}Li cold collision parameters by radio-frequency spectroscopy on weakly bound molecules. *Phys. Rev. Lett.*, 94:103201, 2005.

[17] M. Bartenstein, A. Altmeyer, S. Riedl, S. Jochim, R. Geursen, C. Chin, J. Hecker Denschlag, and R. Grimm. Exploring the BEC-BCS crossover with an ultracold gas of ^{6}Li atoms. *AIP Conference Proceedings*, 770:278–288, 2005.

[18] G. Baym and E. Chandler. The hydrodynamics of rotating superfluids. i. zero-temperature, nondissipative theory. *J. Low Temp. Phys.*, 50:57–87, 1983.

[19] C. Becker, K. Sengstock, P. Schmelcher, P. G. Kevrekidis, and R. Carretero-González. Inelastic collisions of solitary waves in anisotropic Bose-Einstein condensates: sling-shot events and expanding collision bubbles. *New Journal of Physics*, 15:113028, 2013.

[20] C. Becker, S. Stellmer, P. Soltan-Panahi, S. Dörscher, M. Baumert, E. M. Richter, J. Kronjäger, K. Bongs, and K. Sengstock. Oscillations and interactions of dark and dark-bright solitons in Bose-Einstein condensates. *Nature Physics*, 4:496–501, 2008.

[21] V. L. Berezinskii. Destruction of long-range order in one-dimensional and two-dimensional systems possessing a continuous symmetry group. II. Quantum systems. *Sov. Phys. JETP*, 34:610, 1972.

[22] G. Bertaina, L. Pitaevskii, and S. Stringari. First and second sound in cylindrically trapped gases. *Phys. Rev. Lett.*, 105:150402, 2010.

[23] G. Bertsch. Many-body X challenge. In R.F. Bishop, K. A. Gernoth, N. R. Walet, and Y. Xian, editors, *Proceedings of the Tenth International Conference on Recent Progress in Many-Body Theories*, Seattle, 2000. World Scientific.

[24] I. Bloch, J. Dalibard, and W. Zwerger. Many-body physics with ultracold gases. *Rev. Mod. Phys.*, 80:885–80, 2008.

[25] J. Brand and W. P. Reinhardt. Solitonic vortices and the fundamental modes of the snake instability: Possibility of observation in the gaseous Bose-Einstein condensate. *Phys. Rev. A*, 65:043612, 2002.

[26] J. Brand and W.P. Reinhardt. Generating ring currents, solitons and svortices by stirring a Bose-Einstein condensate in a toroidal trap. *J. Phys. B: At. Mol. Opt. Phys.*, 34:L113.

[27] A. Bulgac, J. E. Drut, and P. Magierski. Spin 1/2 fermions in the unitary regime at finite temperature. *Phys. Rev. Lett.*, 96:090404, 2006.

[28] A. Bulgac and M. M. Forbes. Unitary Fermi supersolid: The Larkin-Ovchinnikov phase. *Phys. Rev. Lett.*, 101:215301–4, 2008.

[29] A. Bulgac and M. M. Forbes. *Quantum Gases: Finite Temperature and Non-Equilibrium Dynamics (Vol. 1 Cold Atoms Series).* Imperial College Press, London, 2013.

[30] A. Bulgac, M. M. Forbes, M. M. Kelley, K. J. Roche, and G. Wlazlowski. Quantized superfluid vortex rings in the unitary Fermi gas. *Phys. Rev. Lett.*, 112:025301, 2014.

[31] A. Bulgac, Y-L. Luo, P. Magierski, K. Roche, and Y. Yu. Real-time dynamics of quantized vortices in a unitary Fermi superfluid. *Science*, 332:1288, 2011.

[32] A. Bulgac and Y. Yu. The vortex state in a strongly coupled dilute atomic fermionic superfluid. *Phys. Rev. Lett.*, 91:190404, 2003.

[33] I. Buluta and F. Nori. Quantum simulators. *Science*, 326:108–111, 2009.

[34] S. Burger, K. Bongs, S. Dettmer, W. Ertmer, and K. Sengstock. Dark solitons in Bose-Einstein condensates. *Phys. Rev. Lett.*, 83:5198–5201, 1999.

[35] E. Burovski, N. Prokof'ev, B. Svistunov, and M. Troyer. Critical temperature and thermodynamics of attractive fermions at unitarity. *Phys. Rev. Lett.*, 96:160402, 2006.

[36] T. Busch and J. R. Anglin. Motion of dark solitons in trapped Bose-Einstein condensates. *Phys. Rev. Lett.*, 84:2298–2301, 2000.

[37] J. Carlson, S.-Y. Chang, V. R. Pandharipande, and K. E. Schmidt. Superfluid Fermi gases with large scattering length. *Phys. Rev. Lett.*, 91:050401, 2003.

[38] J. Carlson, S. Gandolfi, K. E. Schmidt, and S. Zhang. Auxiliary-field quantum Monte Carlo method for strongly paired fermions. *Phys. Rev. A*, 84:061602, 2011.

[39] J. Carlson and S. Reddy. Asymmetric two-component fermion systems in strong coupling. *Phys. Rev. Lett.*, 95:060401, 2005.

[40] C. Caroli, P.G. de Gennes, and J. Matricon. Bound fermion states on a vortex line in a type II superconductor. *Phys. Lett.*, 9:307, 1964.

[41] Y. Castin. Exact scaling transform for a unitary quantum gas in a time dependent harmonic potential. *Comptes Rendus Physique*, 5:407–410, 2004.

[42] Y. Castin and F. Werner. The unitary gas and its symmetry properties. In Wilhelm Zwerger, editor, *BEC-BCS Crossover and the Unitary Fermi Gas*, pages 127–191. Springer, Heidelberg, 2012.

[43] A. Cetoli, J. Brand, R. G. Scott, F. Dalfovo, and L. P. Pitaevskii. Snake instability of dark solitons in fermionic superfluids. *Phys. Rev. A*, 88:043639, 2013.

[44] K. J. Challis, R. J. Ballagh, and C. W. Gardiner. Bragg scattering of cooper pairs in an ultracold fermi gas. *Phys. Rev. Lett.*, 98:093002, 2007.

[45] L. W. Cheuk, M. A. Nichols, M. Okan, T. Gersdorf, V. V. Ramasesh, W. S. Bakr, T. Lompe, and M. W. Zwierlein. Quantum-gas microscope for fermionic atoms. *Phys. Rev. Lett.*, 114:193001, 2015.

[46] L. W. Cheuk, A. T. Sommer, Z. Hadzibabic, T. Yefsah, W. S. Bakr, and M. W. Zwierlein. Spin-injection spectroscopy of a spin-orbit coupled fermi gas. *Phys. Rev. Lett.*, 109:095302, 2012.

[47] A. Chikkatur. *Colliding and Moving Bose-Einstein Condensates: Studies of superfluidity and optical tweezers for condensate transport.* Ph.D. thesis, Massachusetts Institute of Technology, 2002.

[48] C. Chin, R. Grimm, P. Julienne, and E. Tiesinga. Feshbach resonances in ultracold gases. *Rev. Mod. Phys.*, 82:1225, 2010.

[49] J.-Y. Choi, S. W. Seo, and Y.-I. Shin. Observation of thermally activated vortex pairs in a quasi-2D Bose gas. *Phys. Rev. Lett.*, 110:175302, 2013.

[50] B. Clancy, L. Luo, and J. E. Thomas. Observation of nearly perfect irrotational flow in normal and superfluid strongly interacting Fermi gases. *Phys. Rev. Lett.*, 99:140401, 2007.

[51] R. Combescot, M. Yu. Kagan, and S. Stringari. Collective mode of homogeneous superfluid Fermi gases in the BEC-BCS crossover. *Phys. Rev. A*, 74:042717–14, 2006.

[52] K. B. Davis, M.-O. Mewes, M. R. Andrews, N. J. van Druten, D. S. Durfee, D. M. Kurn, and W. Ketterle. Bose-Einstein condensation in a gas of sodium atoms. *Phys. Rev. Lett.*, 75:3969–3973, 1995.

[53] B. DeMarco and D.S. Jin. Onset of Fermi degeneracy in a trapped atomic gas. *Science*, 285:1703–1706, 1999.

[54] J. Denschlag, J. E. Simsarian, D. L. Feder, Charles W. Clark, L. A. Collins, J. Cubizolles, L. Deng, E. W. Hagley, K. Helmerson, W. P. Reinhardt, S. L. Rolston, B. I. Schneider, and W. D. Phillips. Generating solitons by phase engineering of a Bose-Einstein condensate. *Science*, 287:97–101, 2000.

[55] R. Desbuquois, L. Chomaz, T. Yefsah, J. Léonard, J. Beugnon, C. Weitenberg, and J. Dalibard. Superfluid behaviour of a two-dimensional Bose gas. *Nature Physics*, 8:645–648, 2012.

[56] R. Desbuquois, T. Yefsah, L. Chomaz, C. Weitenberg, L. Corman, S. Nascimbène, and J. Dalibard. Determination of scale-invariant equations of state without fitting parameters: Application to the two-dimensional Bose gas across the Berezinskii-Kosterlitz-Thouless transition. *Phys. Rev. Lett.*, 113:020404, 2014.

[57] K. Dieckmann, C. A. Stan, S. Gupta, Z. Hadzibabic, C. Schunck, and W. Ketterle. Decay of an ultracold fermionic lithium gas near a Feshbach resonance. *Phys. Rev. Lett.*, 89:203201, 2002.

[58] S. Donadello, S. Serafini, M. Tylutki, L. P. Pitaevskii, F. Dalfovo, G. Lamporesi, and G. Ferrari. Observation of solitonic vortices in Bose-Einstein condensates. *Phys. Rev. Lett.*, 113:065302, 2014.

[59] T. E. Drake, Y. Sagi, R. Paudel, J. T. Stewart, J. P. Gaebler, and D. S. Jin. Direct observation of the Fermi surface in an ultracold atomic gas. *Phys. Rev. A*, 86:031601, 2012.

[60] J. E. Drut, T. A. Lahde, G. Wlazłowski, and P. Magierski. Equation of state of the unitary Fermi gas: An update on lattice calculations. *Phys. Rev. A*, 85:051601, 2012.

[61] Z. Dutton, M. Budde, C. Slowe, and L. V. Hau. Observation of quantum shock waves created with ultra-compressed slow light pulses in a Bose-Einstein condensate. *Science*, 293:663–668, 2001.

[62] J. Dziarmaga, Z. P. Karkuszewski, and K. Sacha. Quantum depletion of an excited condensate. *Phys. Rev. A*, 66:043615, 2002.

[63] J. Dziarmaga and K. Sacha. Depletion of the dark soliton: The anomalous mode of the Bogoliubov theory. *Phys. Rev. A*, 66:043620, 2002.

[64] J. Dziarmaga and K. Sacha. Gap soliton in superfluid Fermi gas at zero and finite temperature. *Laser physics*, 15:674–678, 2005.

[65] D. M. Eagles. Possible pairing without superconductivity at low carrier concentrations in bulk and thin-film superconducting semiconductors. *Phys. Rev.*, 186:456, 1969.

[66] D. K. Efimkin and V. Galitski. Moving solitons in a one-dimensional fermionic superfluid. *Phys. Rev. A*, 91:023616, 2015.

[67] M. G. Endres, D. B. Kaplan, J.-W. Lee, and A. N. Nicholson. Lattice Monte Carlo calculations for unitary fermions in a finite box. *Phys. Rev. A*, 87:023615, 2013.

[68] P. Engels and C. Atherton. Stationary and nonstationary fluid flow of a Bose-Einstein condensate through a penetrable barrier. *Phys. Rev. Lett.*, 99:160405, 2007.

[69] J.R. Ensher, D.S. Jin, M.R. Matthews, C.E. Wieman, and E.A. Cornell. Bose-Einstein condensation in a dilute gas: Measurement of energy and ground-state occupation. *Phys. Rev. Lett.*, 77:4984–4987, 1996.

[70] D. L. Feder, M. S. Pindzola, L. A. Collins, B. I. Schneider, and C. W. Clark. Dark-soliton states of Bose-Einstein condensates in anisotropic traps. *Phys. Rev. A*, 62:053606, 2000.

[71] P. O. Fedichev, A. E. Muryshev, and G. V. Shlyapnikov. Dissipative dynamics of a kink state in a Bose-condensed gas. *Phys. Rev. A*, 60:3220–3224, 1999.

[72] M. Feld, B. Frohlich, E. Vogt, M. Koschorreck, and M. Kohl. Observation of a pairing pseudogap in a two-dimensional Fermi gas. *Nature*, 480:75–78, 2011.

[73] A. L. Fetter. Core structure of a quantized vortex. *Phys. Rev. Lett.*, 27:986–988, 1971.

[74] A. L. Fetter. Nonuniform states of an imperfect Bose gas. *Annals of Physics*, 70:67 – 101, 1972.

[75] A. L. Fetter and J. k Kim. Vortex precession in a rotating nonaxisymmetric trapped Bose-Einstein condensate. *J. Low Temp. Phys.*, 125:239–248, 2001.

[76] R. Feynman. Simulating physics with computers. *International Journal of Theoretical Physics*, 21:467–488, 1982.

[77] M. M. Forbes, S. Gandolfi, and A. Gezerlis. Resonantly interacting fermions in a box. *Phys. Rev. Lett.*, 106:235303, 2011.

[78] D. J. Frantzeskakis. Dark solitons in atomic Bose-Einstein condensates: from theory to experiments. *Journal of Physics A: Mathematical and Theoretical*, 43:213001, 2010.

[79] P. Fulde and R.A. Ferrell. Superconductivity in a strong spin-exchange field. *Phys. Rev.*, 135:A550, 1964.

[80] S. Gandolfi, K. E. Schmidt, and J. Carlson. BEC-BCS crossover and universal relations in unitary Fermi gases. *Phys. Rev. A*, 83:041601, 2011.

[81] S. Giorgini, L. P. Pitaevskii, and S. Stringari. Theory of ultracold atomic Fermi gases. *Rev. Mod. Phys.*, 80:1215–60, 2008.

[82] J. Goldstone and F. Wilczek. Fractional quantum numbers on solitons. *Phys. Rev. Lett.*, 47:986–989, 1981.

[83] D. E. Gonzalez Trotter, F. Salinas Meneses, W. Tornow, C. R. Howell, Q. Chen, A. S. Crowell, C. D. Roper, R. L. Walter, D. Schmidt, H. Witała, W. Glöckle, H. Tang, Z. Zhou, and I. Šlaus. Neutron-deuteron breakup experiment at E_n = 13 MeV: Determination of the $^1S_0$ neutron-neutron scattering length a_{nn}. *Phys. Rev. C*, 73:034001, 2006.

[84] O. Goulko and M. Wingate. Thermodynamics of balanced and slightly spin-imbalanced Fermi gases at unitarity. *Phys. Rev. A*, 82:053621, 2010.

[85] S. R. Granade, M. E. Gehm, K. M. O'Hara, and J. E. Thomas. All-optical production of a degenerate Fermi gas. *Phys. Rev. Lett.*, 88:120405, 2002.

[86] M. Greiner, O. Mandel, T. Esslinger, T. W. Hänsch, and I. Bloch. Quantum phase transition from a superfluid to a Mott insulator in a gas of ultracold atoms. *Nature*, 415:39–44, 2002.

[87] M. Greiner, C. A. Regal, and D. S. Jin. Emergence of a molecular Bose-Einstein condensate from a Fermi gas. *Nature*, 426:537, 2003.

[88] Z. Hadzibabic. *Studies of a Quantum Degenerate Fermionic Lithium Gas.* Ph.d. thesis, Massachusetts Institute of Technology, 2003.

[89] Z. Hadzibabic and J. Dalibard. Two-dimensional Bose fluids: An atomic physics perspective. *Rivista del Nuovo Cimento*, 34:389, 2011.

[90] Z. Hadzibabic, C. A. Stan, K. Dieckmann, S. Gupta, M.W. Zwierlein, A. Goerlitz, and W. Ketterle. Two species mixture of quantum degenerate Bose and Fermi gases. *Phys. Rev. Lett.*, 88:160401, 2002.

[91] E. Haller, J. Hudson, D. A. Kelly, A. Cotta, B. Peaudecerf, G. D. Bruce, and S. Kuhr. Single-atom imaging of fermions in a quantum-gas microscope. *preprint arXiv:1503.02005.*

[92] Bertrand I. Halperin, Gil Refael, and Eugene Demler. Resistance in superconductors. *International Journal of Modern Physics B: Condensed Matter Physics; Statistical Physics; Applied Physics*, 24:4039–4080, 2010.

[93] R. Haussmann, W. Rantner, S. Cerrito, and W. Zwerger. Thermodynamics of the BCS-BEC crossover. *Phys. Rev. A*, 75:023610, 2007.

[94] R. Haussmann and W. Zwerger. Thermodynamics of a trapped unitary Fermi gas. *Phys. Rev. A*, 78:063602, 2008.

[95] A. J. Heeger, S. Kivelson, J. R. Schrieffer, and W. P. Su. Solitons in conducting polymers. *Rev. Mod. Phys.*, 60:781–850, 1988.

[96] H. Heiselberg. Fermi systems with long scattering lengths. *Phys. Rev. A*, 63:043606, 2001.

[97] T.-L. Ho and E. J. Mueller. High temperature expansion applied to fermions near feshbach resonance. *Phys. Rev. Lett.*, 92:160404, 2004.

[98] Tin-Lun Ho and Qi Zhou. Obtaining the phase diagram and thermodynamic quantities of bulk systems from the densities of trapped gases. *Nat Phys*, 6:131–134, 2010.

[99] E. Hodby, G. Hechenblaikner, S. A. Hopkins, O. M. Maragò, and C. J. Foot. Vortex nucleation in Bose-Einstein condensates in an oblate, purely magnetic potential. *Phys. Rev. Lett.*, 88:010405, 2001.

[100] S. Hoinka, M. Lingham, M. Delehaye, and C. J. Vale. Dynamic spin response of a strongly interacting Fermi gas. *Phys. Rev. Lett.*, 109:050403, 2012.

[101] M. Horikoshi, S. Nakajima, M. Ueda, and T. Mukaiyama. Measurement of universal thermodynamic functions for a unitary Fermi gas. *Science*, 327:442–445, 2010.

[102] Y.-H. Hou, L. P. Pitaevskii, and S. Stringari. First and second sound in a highly elongated Fermi gas at unitarity. *Phys. Rev. A*, 88:043630, 2013.

[103] Y.-H. Hou, L. P. Pitaevskii, and S. Stringari. Scaling solutions of the two-fluid hydrodynamic equations in a harmonically trapped gas at unitarity. *Phys. Rev. A*, 87:033620, 2013.

[104] K. Van Houcke, F. Werner, E. Kozik, N. Prokof'ev, and B. Svistunov. Contact and momentum distribution of the unitary Fermi gas by bold diagrammatic monte carlo. *preprint arXiv:1303.6245*, 2013.

[105] C.-L. Hung, X. Zhang, N. Gemelke, and C. Chin. Observation of scale invariance and universality in two-dimensional Bose gases. *Nature*, 470:236–239, 2012.

[106] R. Islam, E. E. Edwards, K. Kim, S. Korenblit, C. Noh, H. Carmichael, G.-D. Lin, L.-M. Duan, C.-C. J. Wang, J.K. Freericks, and C. Monroe. Onset of a quantum phase transition with a trapped ion quantum simulator. *Nature communications*, 2:377, 2011.

[107] R. Jackiw and C. Rebbi. Solitons with fermion number 1/2. *Phys. Rev. D*, 13:3398–3409, 1976.

[108] S. Jochim, M. Bartenstein, A. Altmeyer, G. Hendl, S. Riedl, C. Chin, J. Hecker-Denschlag, and R. Grimm. Bose-Einstein condensation of molecules. *Science*, 302:2101, 2003.

[109] S. Jochim, M. Bartenstein, G. Hendl, J. Hecker-Denschlag, R. Grimm, A. Mosk, and M. Weidemüller. Magnetic field control of elastic scattering in a cold gas of fermionic lithium atoms. *Phys. Rev. Lett.*, 89:273202, 2002.

[110] J. Joseph, B. Clancy, L. Luo, J. Kinast, A. Turlapov, and J. E. Thomas. Measurement of sound velocity in a Fermi gas near a Feshbach resonance. *Phys. Rev. Lett.*, 98:170401, 2007.

[111] J. A. Joseph, J. E. Thomas, M. Kulkarni, and A. G. Abanov. Observation of shock waves in a strongly interacting Fermi gas. *Phys. Rev. Lett.*, 106:150401, 2011.

[112] A. M. Kamchatnov and L. P. Pitaevskii. Stabilization of solitons generated by a supersonic flow of Bose-Einstein condensate past an obstacle. *Phys. Rev. Lett.*, 100:160402, 2008.

[113] T. Karpiuk, P. Deuar, P. Bienias, E. Witkowska, K. Pawlowski, M. Gajda, K. Rzazewski, and M. Brewczyk. Spontaneous solitons in the thermal equilibrium of a quasi-1D Bose gas. *Phys. Rev. Lett.*, 109:205302, 2012.

[114] V. A. Kashurnikov, N. V. Prokof'ev, and B. V. Svistunov. Critical temperature shift in weakly interacting Bose gas. *Phys. Rev. Lett.*, 87:120402, 2001.

[115] L.V. Keldysh and A.N. Kozlov. Collective properties of excitons in semiconductors. *Sov. Phys. JETP, 19, 1228 (1964)*, 54:978, 1968.

[116] W. Ketterle and M.W. Zwierlein. Making, probing and understanding ultracold Fermi gases. *Rivista del Nuovo Cimento*, 31:247–422, 2008.

[117] K. Kim, M.-S. Chang, S. Korenblit, R. Islam, E. E. Edwards, J. K. Freericks, G.-D. Lin, L.-M. Duan, and C. Monroe. Quantum simulation of frustrated ising spins with trapped ions. *Nature*, 465:590–593, 2010.

[118] J. Kinast, A. Turlapov, and J. E. Thomas. Damping of a unitary Fermi gas. *Phys. Rev. Lett.*, 94:170404, 2005.

[119] J. Kinast, A. Turlapov, J. E. Thomas, Q. Chen, J. Stajic, and K. Levin. Heat capacity of a strongly-interacting Fermi gas. *Science*, 307:1296–1299, 2005.

[120] P. F. Kolb, U. Heinz, R. C. Hwa, and X. N. Wang. Hydrodynamic description of ultrarelativistic heavy-ion collisions. In R.C. Hwa and X.-N. Wang, editors, *Quark gluon plasma 3*, page 634. World Scientific, Singapore, 2004.

[121] S. Komineas, N. R. Cooper, and N. Papanicolaou. Single vortex states in a confined Bose-Einstein condensate. *Phys. Rev. A*, 72:053624, 2005.

[122] S. Komineas and N. Papanicolaou. Solitons, solitonic vortices, and vortex rings in a confined bose-einstein condensate. *Phys. Rev. A*, 68:043617, 2003.

[123] V. V. Konotop and L. Pitaevskii. Landau dynamics of a grey soliton in a trapped condensate. *Phys. Rev. Lett.*, 93:240403, 2004.

[124] N. B. Kopnin. Frequency singularities of the dissipation in the mixed state of pure type-ii superconductors at low temperatures. *JETP Letters, 27, 390 (1978)*, 27:417–420, 1978.

[125] J. M. Kosterlitz and D. J. Thouless. Ordering, metastability and phase transitions in two-dimensional systems. *Journal of Physics C: Solid State Physics*, 6:1181, 1973.

[126] M. J. H. Ku, L. W Cheuk, and M. W. Zwierlein. Thermodynamics of trapped gases from the column density. *Manuscript in preparation*, 2015.

[127] M. J. H. Ku, W. Ji, B. Mukherjee, E. Guardado-Sanchez, L. W. Cheuk, T. Yefsah, and M. W. Zwierlein. Motion of a solitonic vortex in the BEC-BCS crossover. *Phys. Rev. Lett.*, 113:065301, 2014.

[128] M. J. H. Ku, B. Mukherjee, T. Yefsah, and M. W. Zwierlein. From planar solitons to vortex rings and lines: Cascade of solitonic excitations in a superfluid Fermi gas. *Manuscript in preparation*, 2015.

[129] M. J. H. Ku, A. T. Sommer, L. W. Cheuk, and M. W. Zwierlein. Revealing the superfluid lambda transition in the universal thermodynamics of a unitary Fermi gas. *Science*, 335:563–567, 2012.

[130] H. Lamb. *Hydrodynamics.* Dover, New York, 6nd edition edition.

[131] L. D. Landau and E. M. Lifshitz. *Quantum Mechanics: Non-Relativistic Theory.* Pergamon Press, New York, 1987.

[132] A. J. Larkin and Y. N. Ovchinnikov. Inhomogeneous state of superconductors. *Sov. Phys. JETP, 19, 1228 (1964)*, 47:1136, 1964.

[133] C. K. Law, P. T. Leung, and M. C. Chu. Quantum fluctuations of coupled dark solitons in a trapped Bose-Einstein condensate. *Journal of Physics B: Atomic, Molecular and Optical Physics*, 35:3583, 2002.

[134] P. A. Lee, N. Nagaosa, and X.-G. Wen. Doping a Mott insulator: Physics of high-temperature superconductivity. *Rev. Mod. Phys.*, 78:17, 2006.

[135] A. J. Leggett. Diatomic molecules and Cooper pairs. In *Modern Trends in the Theory of Condensed Matter. Proceedings of the XVIth Karpacz Winter School of Theoretical Physics, Karpacz, Poland*, pages 13–27. Springer-Verlag, Berlin, 1980.

[136] R. Liao and J. Brand. Traveling dark solitons in superfluid Fermi gases. *Phys. Rev. A*, 83:041604, 2011.

[137] Y. J. Lin, R. L. Compton, K. Jimenez-Garcia, W. D. Phillips, J. V. Porto, and I. B. Spielman. A synthetic electric force acting on neutral atoms. *Nat. Phys.*, 7:531–534, 2011.

[138] Y. J. Lin, K. Jimenez-Garcia, and I. B. Spielman. Spin-orbit-coupled Bose-Einstein condensates. *Nature*, 471:83–86, 2011.

[139] J. A. Lipa, J. A. Nissen, D. A. Stricker, D. R. Swanson, and T. C. P. Chui. Specific heat of liquid helium in zero gravity very near the lambda point. *Phys. Rev. B*, 68:174518, 2003.

[140] X.-J. Liu, H. Hu, and P. D. Drummond. Virial expansion for a strongly correlated fermi gas. *Phys. Rev. Lett.*, 102:160401, 2009.

[141] T. Loftus, C. A. Regal, C. Ticknor, J. L. Bohn, and D. S. Jin. Resonant control of elastic collisions in an optically trapped Fermi gas of atoms. *Phys. Rev. Lett.*, 88:173201, 2002.

[142] E. Lundh and P. Ao. Hydrodynamic approach to vortex lifetimes in trapped Bose condensates. *Phys. Rev. A*, 61:063612, 2000.

[143] L. Luo, B. Clancy, J. Joseph, J. Kinast, and J. E. Thomas. Measurement of the entropy and critical temperature of a strongly interacting Fermi gas. *Phys. Rev. Lett.*, 98:080402, 2007.

[144] L. Luo and J. Thomas. Thermodynamic measurements in a strongly interacting Fermi gas. *J. Low Temp. Phys.*, 154:1–29, 2009.

[145] R. M. Lutchyn, M. Dzero, and V. M. Yakovenko. Spectroscopy of the soliton lattice formation in quasi-one-dimensional fermionic superfluids with population imbalance. *Phys. Rev. A*, 84:033609, 2011.

[146] K. W. Madison, F. Chevy, W. Wohlleben, and J. Dalibard. Vortex formation in a stirred Bose-Einstein condensate. *Phys. Rev. Lett.*, 84:806–809, 2000.

[147] M. Marini, F. Pistolesi, and G. C. Strinati. Evolution from BCS superconductivity to Bose condensation: analytic results for the crossover in three dimensions. *Eur. Phys. J. B*, 1:151–159, 1998.

[148] A. D. Martin and J. Ruostekoski. Quantum and thermal effects of dark solitons in a one-dimensional Bose gas. *Phys. Rev. Lett.*, 104:194102, 2010.

[149] S. Matsuo, S. Higashitani, Y. Nagato, and K. Nagai. Phase diagram of the Fulde-Ferrell-Larkin-Ovchinnikov state in a three-dimensional superconductor. *J. Phys. Soc. Jap.*, 67:280, 1998.

[150] M. R. Matthews, B. P. Anderson, P. C. Haljan, D. S. Hall, C. E. Wieman, and E. A. Cornell. Vortices in a Bose-Einstein condensate. *Phys. Rev. Lett.*, 83:2498–2501, 1999.

[151] D. E. Miller, J. K. Chin, C. A. Stan, Y. Liu, W. Setiawan, C. Sanner, and W. Ketterle. Critical velocity for superfluid flow across the BEC-BCS crossover. *Phys. Rev. Lett.*, 99:070402, 2007.

[152] R. V. Mishmash and L. D. Carr. Quantum entangled dark solitons formed by ultracold atoms in optical lattices. *Phys. Rev. Lett.*, 103:140403, 2009.

[153] H. Miyake, G. A. Siviloglou, C. J. Kennedy, W. C. Burton, and W. Ketterle. Realizing the harper hamiltonian with laser-assisted tunneling in optical lattices. *Phys. Rev. Lett.*, 111:185302, 2013.

[154] P. Monceau. Electronic crystals: an experimental overview. *Advances in Physics*, 61:325–581, 2012.

[155] A. Muñoz Mateo and J. Brand. Chladni solitons and the onset of the snaking instability for dark solitons in confined superfluids. *Phys. Rev. Lett.*, 113:255302, 2014.

[156] A. E. Muryshev, H. B. van Linden van den Heuvell, and G. V. Shlyapnikov. Stability of standing matter waves in a trap. *Phys. Rev. A*, 60:R2665–R2668, 1999.

[157] S. Nascimbène. *Thermodynamics of ultracold Fermi gases.* Ph.D. thesis, Laboratoire Kastler Brossel, Ecole Normale Supérieure, 2010.

[158] S. Nascimbène, N. Navon, K. J. Jiang, F. Chevy, and C. Salomon. Exploring the thermodynamics of a universal Fermi gas. *Nature*, 463:1057–1060, 2010.

[159] N. Navon, S. Nascimbene, F. Chevy, and C. Salomon. The equation of state of a low-temperature Fermi gas with tunable interactions. *Science*, 328:729–732, 2010.

[160] K. K. Ni, S. Ospelkaus, M. H. G. de Miranda, A. Pe'er, B. Neyenhuis, J. J. Zirbel, S. Kotochigova, P. S. Julienne, D. S. Jin, and J. Ye. A high phase-space-density gas of polar molecules. *Science*, 322:231–235, 2008.

[161] P. Nozières and S. Schmitt-Rink. Bose condensation in an attractive fermion gas: from weak to strong coupling superconductivity. *J. Low Temp. Phys.*, 59:195–211, 1985.

[162] K. M. O'Hara, S. L. Hemmer, M. E. Gehm, S. R. Granade, and J. E. Thomas. Observation of a strongly interacting degenerate Fermi gas of atoms. *Science*, 298:2179, 2002.

[163] K. M. O'Hara, S. L. Hemmer, S. R. Granade, M. E. Gehm, J. E. Thomas, V.Venturi, E. Tiesinga, and C.J. Williams. Measurement of the zero crossing in a Feshbach resonance of fermionic ^{6}Li. *Phys. Rev. A*, 66:041401(R), 2002.

[164] G. Ortiz and J. Dukelsky. BCS-to-BEC crossover from the exact BCS solution. *Phys. Rev. A*, 72:043611, 2005.

[165] M. S. Paoletti and D. P. Lathrop. Quantum turbulence. *Annual Review of Condensed Matter Physics*, 2:213–234, 2011.

[166] J. W. Park, S. A. Will, and M. W. Zwierlein. Ultracold dipolar gas of fermionic $^{23}Na^{40}K$ molecules in their absolute ground state. *Phys. Rev. Lett.*, 114:205302, 2015.

[167] M. F. Parsons, F. Huber, A. Mazurenko, C. S. Chiu, W. Setiawan, K. Wooley-Brown, S. Blatt, and M. Greiner. Site-resolved imaging of fermionic Lithium-6 in an optical lattice. *preprint arXiv:1504.04397.*

[168] G. B. Partridge, W. Li, R. I. Kamar, Y. Liao, and R. G. Hulet. Pairing and phase separation in a polarized Fermi gas. *Science*, 311:503, 2006.

[169] W. Pauli. The connection between spin and statistics. *Phys. Rev.*, 58:716, 1940.

[170] A. Perali, P. Pieri, and G. C. Strinati. Quantitative comparison between theoretical predictions and experimental results for the BCS-BEC crossover. *Phys. Rev. Lett.*, 93:100404, 2004.

[171] C.J. Pethick and H. Smith. *Bose-Einstein Condensation in Dilute Gases.* Cambridge University Press, Cambridge, 2002.

[172] D. S. Petrov. Three-boson problem near a narrow Feshbach resonance. *Phys. Rev. Lett.*, 93:143201, 2004.

[173] D. S. Petrov, C. Salomon, and G. V. Shlyapnikov. Weakly bound dimers of fermionic atoms. *Phys. Rev. Lett.*, 93:090404, 2004.

[174] P. Pieri and G. C. Strinati. Derivation of the Gross-Pitaevskii equation for condensed bosons from the Bogoliubov de-Gennes equations for superfluid fermions. *Phys. Rev. Lett.*, 91:030401, 2003.

[175] F. Pistolesi and G. C. Strinati. Evolution from BCS superconductivity to Bose condensation: Role of the parameter $k_F\xi$. *Phys. Rev. B*, 49:6356, 1994.

[176] L. P. Pitaevskii. Hydrodynamic theory of motion of quantized vortex rings in trapped superfluid gases. *preprint arXiv:1311.4693*, 2013.

[177] L. Pollet, N. V. Prokof'ev, and B. V. Svistunov. Criticality in trapped atomic systems. *Phys. Rev. Lett.*, 104:245705, 2010.

[178] V. N. Popov. Theory of a Bose gas produced by bound states of Fermi particles. *Sov. Phys. JETP, 19, 1228 (1964)*, 50:1550, 1966.

[179] N. Prokof'ev and B. Svistunov. Bold diagrammatic Monte Carlo technique: When the sign problem is welcome. *Phys. Rev. Lett.*, 99:250201, 2007.

[180] N. Prokof'ev and B. Svistunov. Fermi-polaron problem: Diagrammatic Monte Carlo method for divergent sign-alternating series. *Phys. Rev. B*, 77:020408, 2008.

[181] N. V. Prokof'ev and B. V. Svistunov. Bold diagrammatic monte carlo: A generic sign-problem tolerant technique for polaron models and possibly interacting many-body problems. *Phys. Rev. B*, 77:125101, 2008.

[182] L. Radzihovsky. Fluctuations and phase transitions in Larkin-Ovchinnikov liquid-crystal states of a population-imbalanced resonant Fermi gas. *Phys. Rev. A*, 84:023611, 2011.

[183] D. Rakshit, K. M. Daily, and D. Blume. Natural and unnatural parity states of small trapped equal-mass two-component Fermi gases at unitarity and fourth-order virial coefficient. *Phys. Rev. A*, 85:033634, 2012.

[184] M. Randeria. Ultracold fermi gases: Pre-pairing for condensation. *Nat Phys*, 6:561–562, 2010.

[185] G. W. Rayfield and F. Reif. Quantized vortex rings in superfluid helium. *Phys. Rev.*, 136:A1194–A1208, 1964.

[186] C. A. Regal, M. Greiner, and D. S. Jin. Observation of resonance condensation of fermionic atom pairs. *Phys. Rev. Lett.*, 92:040403, 2004.

[187] C. A. Regal, C. Ticknor, J. L. Bohn, and D. S. Jin. Creation of ultracold molecules from a Fermi gas of atoms. *Nature*, 424:47, 2003.

[188] M. D. Reichl and E. J. Mueller. Vortex ring dynamics in trapped Bose-Einstein condensates. *Phys. Rev. A*, 88:053626, 2013.

[189] G. Reinaudi, T. Lahaye, Z. Wang, and D. Guéry-Odelin. Strong saturation absorption imaging of dense clouds of ultracold atoms. *Opt. Lett.*, 32:3143–3145, 2007.

[190] S. Riedl, E. R. Sanchez Guajardo, C. Kohstall, J. Hecker Denschlag, and R. Grimm. Lifetime of angular momentum in a rotating strongly interacting Fermi gas. *Phys. Rev. A*, 79:053628, 2009.

[191] S. Riedl, E. R. Sánchez Guajardo, C. Kohstall, A. Altmeyer, M. J. Wright, J. Hecker Denschlag, R. Grimm, G. M. Bruun, and H. Smith. Collective oscillations of a Fermi gas in the unitarity limit: Temperature effects and the role of pair correlations. *Phys. Rev. A*, 78:053609, 2008.

[192] G. Roati, F. Riboli, G. Modugno, and M. Inguscio. Fermi-Bose quantum degenerate ^{40}K - ^{87}Rb mixture with attractive interaction. *Phys. Rev. Lett.*, 89:150403, 2002.

[193] P. Rosenbusch, V. Bretin, and J. Dalibard. Dynamics of a single vortex line in a bose-einstein condensate. *Phys. Rev. Lett.*, 89:200403, 2002.

[194] C. A. R. Sá de Melo, M. Randeria, and J. R. Engelbrecht. Crossover from BCS to Bose superconductivity: Transition temperature and time-dependent Ginzburg-Landau theory. *Phys. Rev. Lett.*, 71:3202, 1993.

[195] P. Saffman. *Vortex Dynamics.* Cambridge University Press, Cambridge, England, 1992.

[196] E. R. Sánchez Guajardo, M. K. Tey, L. A. Sidorenkov, and R. Grimm. Higher-nodal collective modes in a resonantly interacting Fermi gas. *Phys. Rev. A*, 87:063601, 2013.

[197] P. Scherpelz, K. Padavić, A. Murray, A. Glatz, I. S. Aranson, and K. Levin. Universal Behavior of Perturbation-Induced Defects in Trapped Superfluids. *preprint arXiv:1410.0067.*

[198] P. Scherpelz, K. Padavić, A. Rançon, A. Glatz, I. S. Aranson, and K. Levin. Phase imprinting in equilibrating fermi gases: The transience of vortex rings and other defects. *Phys. Rev. Lett.*, 113:125301, 2014.

[199] A. Schirotzek, Y. Shin, Ch. H. Schunck, and W. Ketterle. Determination of the superfluid gap in atomic Fermi gases by quasiparticle spectroscopy. *Phys. Rev. Lett.*, 101:140403, 2008.

[200] A. Schirotzek, C.-H. Wu, A. Sommer, and M. W. Zwierlein. Observation of Fermi polarons in a tunable Fermi liquid of ultracold atoms. *Phys. Rev. Lett.*, 102:230402–4, 2009.

[201] F. Schreck, L. Khaykovich, K. L. Corwin, G. Ferrari, T. Bourdel, J. Cubizolles, and C. Salomon. Quasipure Bose-Einstein condensate immersed in a Fermi sea. *Phys. Rev. Lett.*, 87:080403, 2001.

[202] C. Schunck. *Study of an ultracold cloud of fermionic ^{6}Li atoms near a Feshbach resonance.* Diploma thesis, University of Heidelberg, 2002.

[203] R. G. Scott, F. Dalfovo, L. P. Pitaevskii, and S. Stringari. Dynamics of dark solitons in a trapped superfluid Fermi gas. *Phys. Rev. Lett.*, 106:185301, 2011.

[204] R. G. Scott, F. Dalfovo, L. P. Pitaevskii, S. Stringari, O. Fialko, R. Liao, and J. Brand. The decay and collisions of dark solitons in superfluid Fermi gases. *New J. Phys.*, 14:023044, 2012.

[205] Jacob F. Sherson, Christof Weitenberg, Manuel Endres, Marc Cheneau, Immanuel Bloch, and Stefan Kuhr. Single-atom-resolved fluorescence imaging of an atomic mott insulator. *Nature*, 467:68–72, 2010.

[206] Y. Shin, C.H. Schunck, A. Schirotzek, and W. Ketterle. Phase diagram of a two-component Fermi gas with resonant interactions. *Nature*, 451:689–693, 2007.

[207] E. Shuryak. Why does the quark gluon plasma at RHIC behave as a nearly ideal fluid? *Prog. Part. Nucl. Phys.*, 53:273–303, 2004.

[208] L. A. Sidorenkov, M. K. Tey, R. Grimm, Y.-H. Hou, L. Pitaevskii, and S. Stringari. Second sound and the superfluid fraction in a Fermi gas with resonant interactions. *Nature*, 498:78–81, 2013.

[209] A. Sommer, M. Ku, G. Roati, and M. W. Zwierlein. Universal spin transport in a strongly interacting Fermi gas. *Nature*, 472:201–204, 2011.

[210] A. Sommer, M. Ku, and M. W. Zwierlein. Spin transport in polaronic and superfluid Fermi gases. *New J. Phys.*, 13:055009, 2011.

[211] Ariel T. Sommer, Lawrence W. Cheuk, Mark J. H. Ku, Waseem S. Bakr, and Martin W. Zwierlein. Evolution of fermion pairing from three to two dimensions. *Phys. Rev. Lett.*, 108:045302, 2012.

[212] E. B. Sonin. Transverse force on a vortex and vortex mass: Effects of free bulk and vortex-core bound quasiparticles. *Phys. Rev. B*, 87:134515, 2013.

[213] A. Spuntarelli, L. D. Carr, P. Pieri, and G. C. Strinati. Gray solitons in a strongly interacting superfluid Fermi gas. *New J. Phys.*, 13:035010, 2011.

[214] A. Spuntarelli, P. Pieri, and G. C. Strinati. Solution of the Bogoliubo-de Gennes equations at zero temperature throughout the BCS-BEC crossover: Josephson and related effects. *Phys. Rep.*, 488:111–167, 2010.

[215] D. M. Stamper-Kurn. *Peeking and poking at a new quantum fluid: Studies of gaseous Bose-Einstein condensates in magnetic and optical traps.* Ph.d., Massachusetts Institute of Technology, 1999.

[216] C. A. Stan. *Experiments with Interacting Bose and Fermi Gases.* Ph.d. thesis, Massachusetts Institute of Technology, 2005.

[217] J. T. Stewart, J. P. Gaebler, and D. S. Jin. Using photoemission spectroscopy to probe a strongly interacting fermi gas. *Nature*, 454:744–747, 2008.

[218] J. T. Stewart, J. P. Gaebler, C. A. Regal, and D. S. Jin. Potential energy of a ^{40}K Fermi gas in the BCS-BEC crossover. *Phys. Rev. Lett.*, 97:220406, 2006.

[219] A. A. Svidzinsky and A. L. Fetter. Dynamics of a vortex in a trapped Bose-Einstein condensate. *Phys. Rev. A*, 62:063617, 2000.

[220] S. Tan. Energetics of a strongly correlated Fermi gas. *Annals of Physics*, 323:2952–2970, 2008.

[221] L. Tarruell, M. Teichmann, J. McKeever, T Bourdel, J Cubizolles, N. Navon, F. Chevy, C. Salomon, L. Khaykovich, and J. Zhang. Expansion of an ultracold lithium gas in the BEC-BCS crossover. In M. Inguscio, W. Ketterle, and C. Salomon, editors, *Ultracold Fermi Gases, Proceedings of the International School of Physics "Enrico Fermi", Course CLXIV, Varenna, 20 - 30 June 2006.* IOS Press, Amsterdam., 2008.

[222] M. K. Tey, L. A. Sidorenkov, E. R. Sánchez Guajardo, R. Grimm, M. J. H. Ku, M. W. Zwierlein, Y.-H. Hou, L. Pitaevskii, and S. Stringari. Collective modes in a unitary Fermi gas across the superfluid phase transition. *Phys. Rev. Lett.*, 110:055303, 2013.

[223] M. Tinkham. *Introduction to Superconductivity.* Dover, Mineola, New York, second edition edition, 2004.

[224] A. G. Truscott, K. E. Strecker, W. I. McAlexander, G. B. Partridge, and R. G. Hulet. Observation of Fermi pressure in a gas of trapped atoms. *Science*, 291:2570–2572, 2001.

[225] M. Tsubota. Quantum turbulence. *Journal of the Physical Society of Japan*, 77:111006, 2008.

[226] K. Van Houcke, F. Werner, E. Kozik, N. Prokof'ev, B. Svistunov, M. J. H. Ku, A. T. Sommer, L. W. Cheuk, A. Schirotzek, and M. W. Zwierlein. Feynman diagrams versus Fermi-gas Feynman emulator. *Nat. Phys.*, 8:366–370, 2012.

[227] W. F. Vinen and J. J. Niemela. Quantum turbulence. *J. Low Temp. Phys.*, 128:167–231, 2002.

[228] W.F. Vinen. An introduction to quantum turbulence. *J. Low Temp. Phys.*, 145:7–24, 2006.

[229] W.F. Vinen. Quantum turbulence: Achievements and challenges. *J. Low Temp. Phys.*, 161:419–444, 2010.

[230] D. Vollhardt and P. Wölfle. *The Superfluid Phases of Helium 3.* Taylor & Francis, London, 1990.

[231] I. Šlaus, Y. Akaishi, and H. Tanaka. Neutron-neutron effective range parameters. *Physics Reports*, 173(5):257 – 300, 1989.

[232] P. B. Walczak and J. R. Anglin. Back-reaction of perturbation wave packets on gray solitons. *Phys. Rev. A*, 86:013611, 2012.

[233] P. Wang, Z.-Q. Yu, Z. Fu, J. Miao, L. Huang, S. Chai, H. Zhai, and J. Zhang. Spin-orbit coupled degenerate Fermi gases. *Phys. Rev. Lett.*, 109:095301, 2012.

[234] C. N. Weiler, T. W. Neely, D. R. Scherer, A. S. Bradley, M. J. Davis, and B. P. Anderson. Spontaneous vortices in the formation of Bose-Einstein condensates. *Nature*, 455:948–951, 2008.

[235] A. Weller, J. P. Ronzheimer, C. Gross, J. Esteve, M. K. Oberthaler, D. J. Frantzeskakis, G. Theocharis, and P. G. Kevrekidis. Experimental observation of oscillating and interacting matter wave dark solitons. *Phys. Rev. Lett.*, 101:130401, 2008.

[236] W. Wen and G. Huang. Dynamics of dark solitons in superfluid Fermi gases in the BCS-BEC crossover. *Phys. Rev. A*, 79:023605, 2009.

[237] Wen Wen, Changqing Zhao, and Xiaodong Ma. Dark-soliton dynamics and snake instability in superfluid Fermi gases trapped by an anisotropic harmonic potential. *Phys. Rev. A*, 88:063621, 2013.

[238] F. Werner and Y. Castin. Exact relations for quantum-mechanical few-body and many-body problems with short-range interactions in two and three dimensions. *Preprint arXiv:1001.0774*, 2010.

[239] F. Werner, L. Tarruell, and Y. Castin. Number of closed-channel molecules in the BEC-BCS crossover. *The European Physical Journal B - Condensed Matter and Complex Systems*, 68:401–415, 2009.

[240] G. Wlazłowski, A. Bulgac, M. M. Forbes, and K. J. Roche. Life cycle of superfluid vortices and quantum turbulence in the unitary Fermi gas. *Phys. Rev. A*, 91:031602, 2015.

[241] M. J. Wright, S. Riedl, A. Altmeyer, C. Kohstall, E. R. Sanchez Guajardo, J. Hecker-Denschlag, and R. Grimm. Finite-temperature collective dynamics of a Fermi gas in the BEC-BCS crossover. *Phys. Rev. Lett.*, 99:150403, 2007.

[242] T. Yefsah, R. Desbuquois, L. Chomaz, K. J. Günter, and J. Dalibard. Exploring the thermodynamics of a two-dimensional Bose gas. *Phys. Rev. Lett.*, 107:130401, 2011.

[243] Tarik Yefsah, Ariel T. Sommer, Mark J. H. Ku, Lawrence W. Cheuk, Wenjie Ji, Waseem S. Bakr, and Martin W. Zwierlein. Heavy solitons in a fermionic superfluid. *Nature*, 499:426–430, 2013.

[244] N. Yoshida and S. K. Yip. Larkin-Ovchinnikov state in resonant Fermi gas. *Phys. Rev. A*, 75:063601, 2007.

[245] G. Zürn, T. Lompe, A. N. Wenz, S. Jochim, P. S. Julienne, and J. M. Hutson. Precise characterization of ^{6}Li Feshbach resonances using trap-sideband-resolved RF spectroscopy of weakly bound molecules. *Phys. Rev. Lett.*, 110:135301, 2013.

[246] W. Zwerger, editor. *The BCS-BEC crossover and the unitary Fermi gas*, volume 836. Springer, 2011.

[247] M. W. Zwierlein. *Cooling and Trapping a Bose-Fermi Mixture of Dilute Atomic Gases.* PhD thesis, Stage de Recherche, Magistère Interuniversitaire de Physique, Paris.

[248] M. W. Zwierlein. *High-temperature superfluidity in an Ultracold Fermi Gas.* PhD thesis, Massachusetts Institute of Technology, 2006.

[249] M. W. Zwierlein, J. R. Abo-Shaeer, A. Schirotzek, C. H. Schunck, and W. Ketterle. Vortices and superfluidity in a strongly interacting Fermi gas. *Nature*, 435:1047–1051, 2005.

[250] M. W. Zwierlein, C. A. Stan, C. H. Schunck, S. M. F. Raupach, S. Gupta, Z. Hadzibabic, and W. Ketterle. Observation of Bose-Einstein condensation of molecules. *Phys. Rev. Lett.*, 91:250401, 2003.

[251] M. W. Zwierlein, C. A. Stan, C. H. Schunck, S. M. F. Raupach, A. J. Kerman, and W. Ketterle. Condensation of pairs of fermionic atoms near a Feshbach resonance. *Phys. Rev. Lett.*, 92:120403, 2004.